Arbeitsbericht
NAB 16-17

FEBEX-DP Post-mortem THM/THG Analysis Report

August 2017

María Victoria Villar

Contributors:
Ana María Fernández, Enrique Romero, Ann Dueck,
Jaime Cuevas, Michael Plötze, Stephan Kaufhold,
Reiner Dohrmann, Rubén J. Iglesias, Toshihiro Sakaki,
Marco Voltolini, Liange Zheng, Ken Kawamoto, Florian Kober

**National Cooperative
for the Disposal of
Radioactive Waste**

Hardstrasse 73
P.O. Box 280
5430 Wettingen
Switzerland
Tel. +41 56 437 11 11

www.nagra.ch

Arbeitsbericht
NAB 16-17

FEBEX-DP Post-mortem THM/THG Analysis Report

August 2017

María Victoria Villar

Contributors:
Ana María Fernández[1], Enrique Romero[2], Ann Dueck[3],
Jaime Cuevas[4], Michael Plötze[5], Stephan Kaufhold[6],
Reiner Dohrmann[6], Rubén J. Iglesias[1], Toshihiro Sakaki[7],
Marco Voltolini[8], Liange Zheng[8], Ken Kawamoto[9], Florian Kober[7]

1) Centro de Investigaciones Energéticas Medioambientales y Tecnológicas, Madrid, Spain
2) Universitat Politècnica de Catalunya, Spain
3) Clay Technology, Sweden
4) Universidad Autónoma de Madrid, Spain
5) Eidgenössische Technische Hochschule Zürich, Switzerland
6) Bundesanstalt für Geowissenschaften und Rohstoffe, Germany
7) Nagra, Switzerland
8) Lawrence Berkeley National Laboratory, Department of Energy, USA
9) Saitama University, Japan

KEYWORDS

Bentonite, large-scale test, geological disposal, engineered barrier, long term, thermo-hydraulic gradient, smectite, permeability, swelling, alteration, microstructure, geochemistry

**National Cooperative
for the Disposal of
Radioactive Waste**

Hardstrasse 73
P.O. Box 280
5430 Wettingen
Switzerland
Tel. +41 56 437 11 11

www.nagra.ch

Table of Contents

List of Tables

List of Figures

1 Introduction

FEBEX (Full-scale Engineered Barrier Experiment in Crystalline Host Rock) was a research and demonstration project that was initiated by Enresa (Spain). The aim of FEBEX (Full-scale Engineered Barrier Experiment) was to study the behaviour of components in the near-field for a high-level radioactive waste (HLW) repository in crystalline rock. The project was based on the Spanish reference concept for disposal of radioactive waste in crystalline rock (AGP Granito): the waste canisters are placed horizontally in drifts and surrounded by a clay barrier constructed from highly-compacted bentonite blocks (Enresa 1995).

The main objectives of the project were:

- Demonstration of the feasibility of constructing the engineered barrier system in a horizontal configuration according to the Spanish concept for deep geological storage (AGP), and analysis of the technical problems to be solved for this type of disposal method.
- Better understanding of the thermo-hydro-mechanical (THM) and thermo-hydro-geochemical (THG) processes in the near field, and development and validation of the modelling tools required for interpretation and prediction of the evolution of such processes.

To fulfil these objectives the project included two large-scale tests shown in Fig. 1 (Enresa 2000, 2006). The "mock-up" is managed by CIEMAT in Spain and the *in-situ* test was performed at the Grimsel underground laboratory in Switzerland, also known as Grimsel Test Site (GTS) or Felslabor Grimsel (FLG in German).

The *in-situ* test, done under natural conditions and at full scale, is the focus of this document. The thermal effect of the waste was simulated by means of heaters, whereas hydration was natural. The test was monitored using a comprehensive suite of sensors, allowing to obtain the evolution of the temperature, total pressure, water content, water pressure, displacements and other parameters continuously in different parts of the barrier and the host rock. This information was used to validate the predictions of the thermo-hydro-mechanical (THM) and thermo-hydro-geochemical (THG) models.

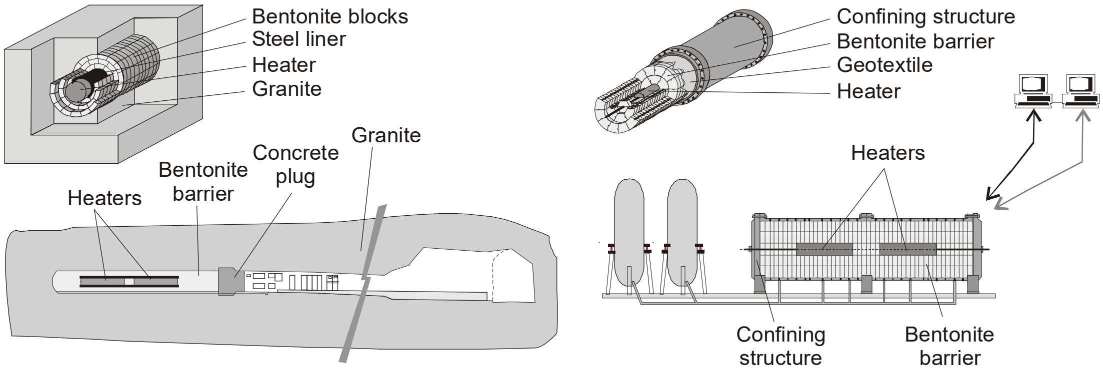

Fig. 1: Overall layout of FEBEX *in situ* test (left) and "mock-up" test (right).

The project started in 1994 and has been supported by the European Commission through consecutive contracts, identified as FEBEX I for the period January 1996 to June 1999, and FEBEX II, from September 2000 to December 2004. Afterwards, NF-PRO continued the project from January 2005 to December 2007. Finally, in January 2008, the *in-situ* test was transferred from Enresa to the FEBEXe Consortium, composed by SKB (Sweden), Posiva (Finland), CIEMAT (Spain), Nagra (Switzerland) and more recently KAERI (South Korea), which supported it until final dismantling was completed.

The final *in-situ* experiment excavation was carried out in 2015 and new partners, interested in taking part in the planned sampling and analysis operations, were incorporated to the Consortium (from then on called FEBEX-DP) for that purpose, namely US DOE (USA), Obayashi (Japan), RWM (UK), Andra (France), BGR (Germany) and SÚRAO (Czech Republic).

1.1 Test configuration during FEBEX I

The installation of the *in-situ* test was carried out at the GTS. A horizontal drift with a diameter of 2.28 m was excavated in the Grimsel granodiorite especially for this experiment using a tunnel boring machine (TBM). Two electrical heaters, of the same size and of a similar weight as the reference canisters, were placed in the axis of the drift. Fig. 2 shows the dimensions and layout of the test components schematically. The gap between the heaters and the rock was backfilled with compacted bentonite blocks, for a distance of 17.40 m and this required a total 115'716 kg of bentonite. The blocks were arranged in vertical slices consisting of concentric rings. In the heater areas, the interior ring was in contact with the steel liner, whereas in the non-heater areas a core of bentonite blocks replaced the heaters (Fig. 3). The thickness of the bentonite barrier in the heater areas was 65 cm (distance from liner to granite). The bentonite slices were numbered from the back of the gallery towards the front, and those in which sensors were installed were called "instrumented section" and given a distinctive reference letter. The backfilled area was sealed with a plain concrete plug placed into a recess excavated in the rock and having a length of 2.70 m and a volume of 17.8 m^3.

A total of 632 instruments, located in both the bentonite buffer and the host rock, were installed in a number of instrumented sections. They monitored relevant parameters such as temperature, humidity, total and pore pressure, displacements, etc. The instruments were of many different kinds and their characteristics and positions were fully described in Fuentes-Cantillana & García-Siñeriz (1998).

A Data Acquisition and Control System (DACS) located in the service area of the FEBEX drift collected the data provided by the instruments. This system recorded and stored information from the sensors and also controlled the power applied to the electrical heaters, in order to maintain a constant temperature at the heaters/bentonite interface. The DACS allowed the experiment to be run in an automated mode, with remote supervision from Madrid. Data stored at the local DACS were periodically downloaded in Madrid and used to build the experimental Master Data Base.

The construction of the concrete plug was completed in October 1996, and the heating operation started on February 28, 1997. A constant temperature of 100°C was maintained at the heater/bentonite interfaces, while the bentonite buffer was slowly hydrating with water naturally flowing from the rock.

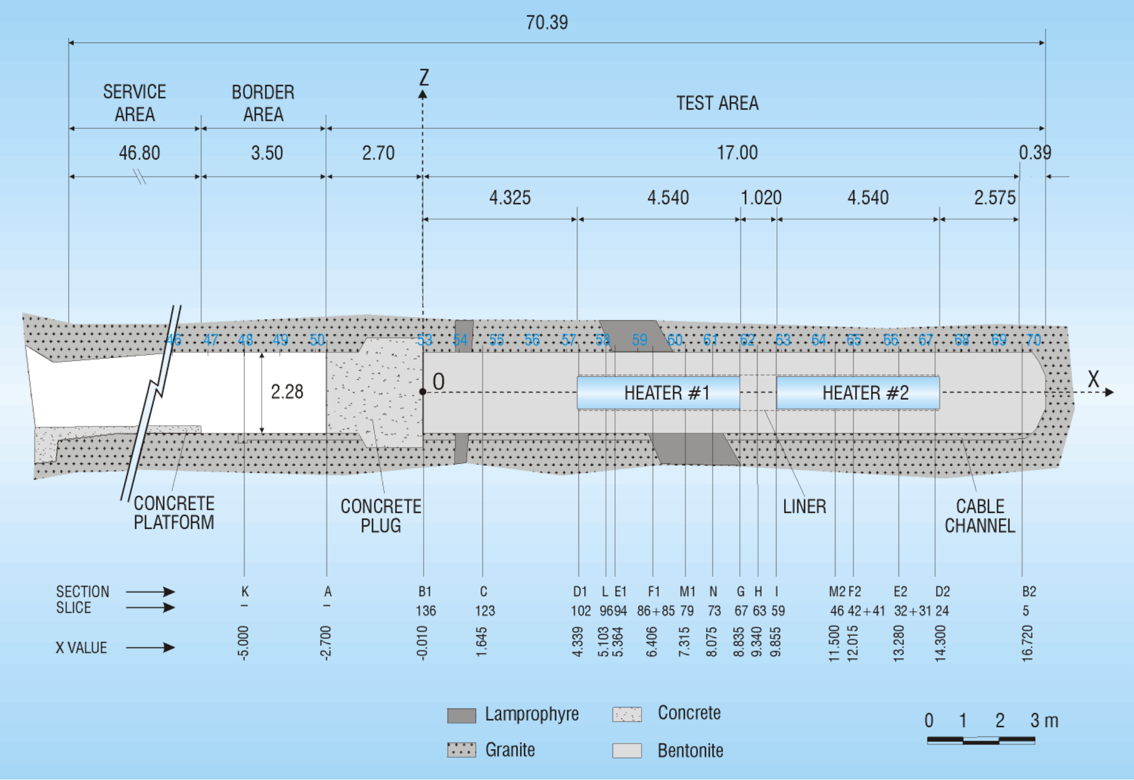

Fig. 2: Initial general layout of the FEBEX *in-situ* test (dimensions in m).

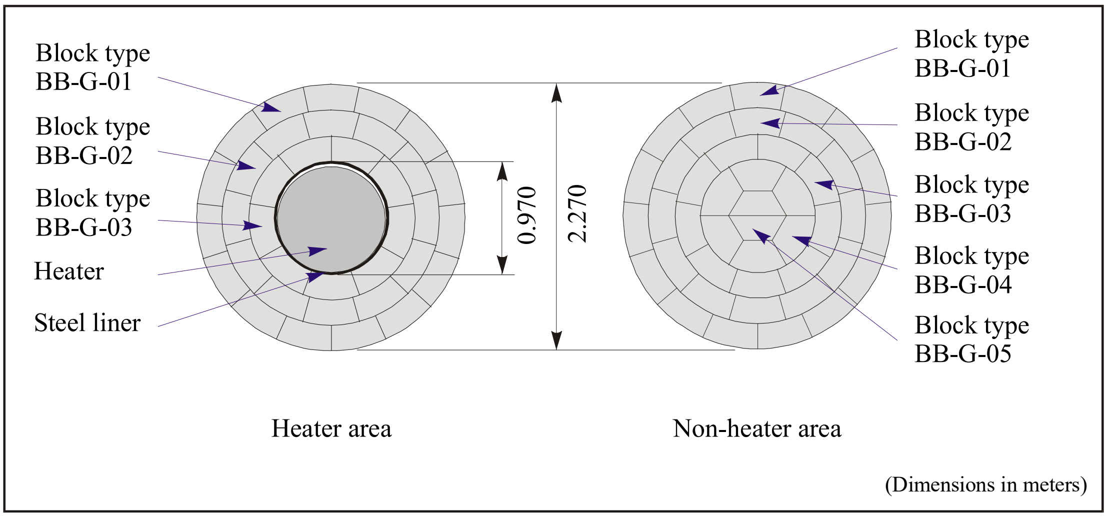

Fig. 3: Geometry of the clay barrier in the FEBEX *in-situ* test at GTS (Enresa 2000).

1.2 Dismantling of Heater #1 and test configuration afterwards (FEBEX II)

A partial dismantling of the FEBEX *in-situ* test was carried out during the summer of 2002, after 5 years of continuous heating. The operation included the demolition of the concrete plug, the removal of the section of the test corresponding to the first heater, and the resealing of the remaining tunnel with a new shotcrete plug. A large number of samples from all types of materials were taken for analysis during this partial dismantling. A number of instruments were also subsequently dismantled and inspected. The description of the partial dismantling operation is given in Bárcena et al. (2003).

The configuration of the test, after completing the partial dismantling operation and construction of the full plug length, is shown in Fig. 4. It shows how the buffer and all components were removed up to a distance of 2 metres from Heater #2 to minimise disturbance of the non-dismantled area. A dummy steel cylinder with a length of 1 m was inserted in the void left by Heater #1 in the centre of the buffer.

Additional sensors were also introduced in boreholes drilled in the buffer parallel to the drift. To simplify this operation, the new shotcrete plug was constructed in two phases: an initial temporary plug measuring just 1 m in length, that was built immediately after dismantling, and a second section to complete the plug up to a length of 3 m as planned in the experimental design. The new plug differed from the FEBEX I plug in that it was constructed without a recess excavated in the rock and was installed by shotcreting.

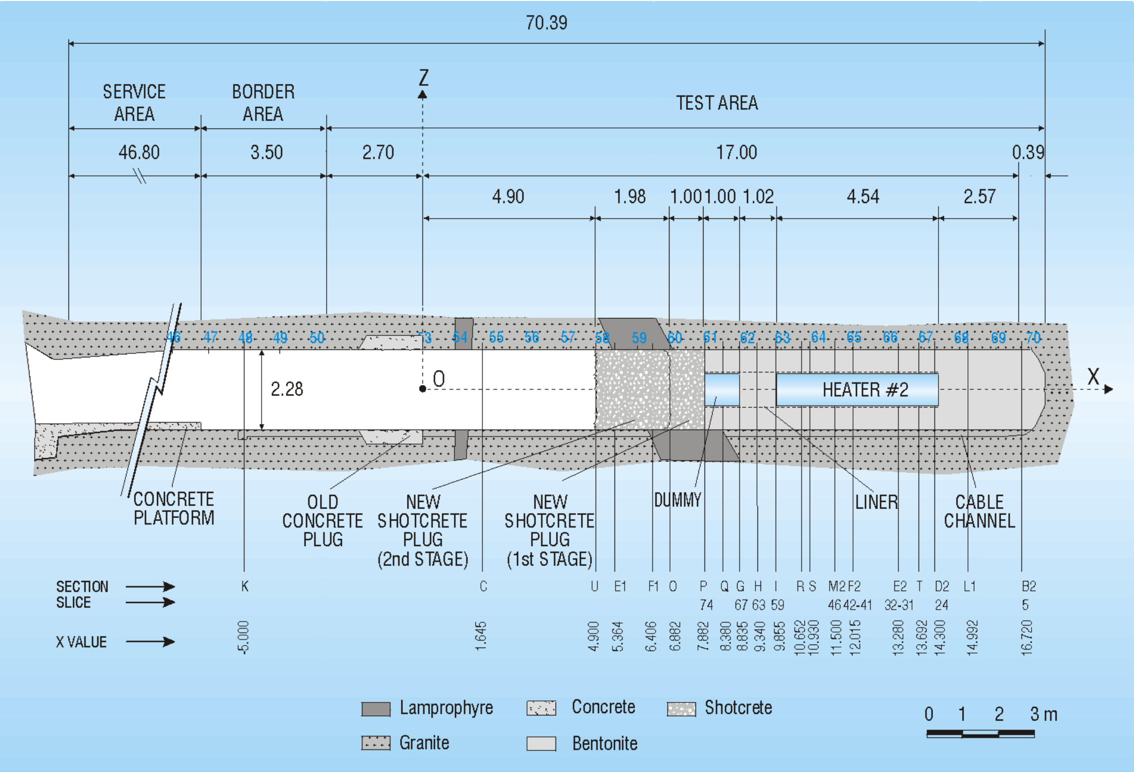

Fig. 4: Layout of the FEBEX *in-situ* test after the partial dismantling (dimensions in m).

The characterisation of the bentonite samples retrieved during the partial dismantling and performed by several laboratories is described in Villar et al. (2006), and a more complete report that describes the test from the conception up to two years of operation after the partial dismantling is given in Enresa (2006).

1.3 Concept of the dismantling of Heater #2

The objective of the second dismantling operation, carried out throughout 2015, was to dismantle all the remaining parts of the *in-situ* test, including Heater #2. Many sensors were in operation until the end of the experiment, which allowed to follow the evolution of some thermo-hydro-mechanical variables during the second operational phase (Martínez et al. 2016). In particular, the temperatures measured at the different instrumented sections indicated in Fig. 4 just before dismantling are shown in Tab. 1, along with those measured just before the partial dismantling in 2002. The location of sensors in the bentonite rings is given according to Fig. 3.

Tab. 1: Temperatures measured in the bentonite barrier before dismantling.

(1: 2002, Bárcena et al. 2006) and 2015 (2: 2015, Martínez et al. 2016).

	Date	**Section G** (1 m from heater)	**Section I** (heater front)	**Section S** (1 m into heater zone)	**Section F2** (middle of heater)	**Section D2** (heater rear end)	**Section B2** (gallery end)
Outer ring (BB-G-01)	1	44 – 46	44 – 45			36 – 38	21 – 23
	2	30 – 34	37 – 39			36 – 37	22
Intermediate ring (BB-G-02)	1	58 – 60	58 – 61			51 – 53	
	2	34 – 39	54 – 63	72	71 – 73	54 – 56	
Inner ring 1 (BB-G-03)	1	80 – 84	84 – 88		95 – 100	82 – 90	
	2	36 – 43	84 – 87	93	94 – 99	83 – 88	
Inner ring 2 (BB-G-04)							21 – 23
							20 – 22
Core (BB-G-05)	1	100 – 104					21 – 23
	2						22

The dismantling operation included carrying out a complete sampling of the bentonite, rock, relevant interfaces, sensors, metallic components and tracers to allow the analysis of the barriers' condition after 18 years of heating and natural hydration, as described in NAB 16-11 (García-Siñeriz et al. 2016).

All details about the sampling program are given in NAB 15-14 (Bárcena & García-Siñeriz 2015) and all sample logs of the dismantling operation are documented in AN 15-578 Sample Log Book 34 to 62 FEBEX-DP (Abós & Martínez 2015).

Following the same terminology used during installation of the experiment and during the first dismantling, the term bentonite "slice" refers to the vertical slices of bentonite blocks as they were installed. These were numbered during the installation of the barrier in 1997 as they were put in place: from slice 1, at the back of the gallery, to slice 136, at the front of the barrier in contact with the first concrete plug, the last one installed. The term "section" refers to the vertical sampling sections in which samples of any kind were taken during dismantling. They were numbered from the entrance of the gallery towards the back of it, and the numbering started in the first dismantling. Hence, sampling Sections S1 to S30 were sampled in 2002, and sampling Sections S31 to S61 were sampled in 2015. For this reason, there were more slices than sampling sections, because not all the bentonite slices were sampled. A sampling section could also include two or three slices.

The analytical results obtained from the different samples retrieved during the final dismantling will be compared with data obtained from the partial dismantling (Enresa 2006), the monitoring data (AITEMIN 2014, Martínez et al. 2016) as well as with the results derived from modelling efforts (Lanyon & Gaus 2016). The results are expected to increase the current knowledge and confidence for the FEBEX-DP partners in bentonite performance with a focus on thermo-hydro-mechanical (THM) and thermo-hydro-geochemical (THG) processes as well as on corrosion and microbial activity. In addition to this report, other laboratory analysis and dismantling results are detailed in Wersin & Kober (2017) for the corrosion studies, Turrero & Cloet (2017) for the concrete interactions, and Bengtsson et al. (2017) for the microbiology.

1.4 Objectives and contents

This report is intended for documenting the activities carried out and the main results obtained by different laboratories in the analyses performed with bentonite samples retrieved from the FEBEX *in-situ* test and sent to them. The following contributions of the different organisations are summarised, compared and evaluated in this report:

- Villar, M.V., Iglesias, R.J., Gutiérrez-Álvarez, C., Carbonell, B., Campos, R., Campos, G., Martín, P.L. & Castro, B. (2018): FEBEX-DP: Thermo-hydro-mechanical postmortem analysis of bentonite performed at CIEMAT. Technical report CIEMAT/DMA/2G216/2/16. NAB 16-24. Madrid.
- Fernández, A.M., Sánchez-Ledesma, D.M., Melón, A., Robredo, L. M., Rey, J.J., Labajo, M., Clavero, M.A., Carretero, S. & González, A.E. (2018): Thermo-hydro-geochemical behaviour of a Spanish bentonite after of the FEBEX in situ test at the Grimsel Test Site. Technical report CIEMAT/DMA/2G216/03/16. NAB 16-25. Madrid, 256 pp.
- Romero, E., Alvarado, C., Lloret, A. & Mirsalehi, S. (2017): Laboratory tests on the post mortem hydro-mechanical characterisation of FEBEX bentonite. CIMNE-UPC-GEOLAB, 62 pp.
- Dueck, A., Nilsson, U. & Åkesson, M. (2016): FEBEX-DP, Hydro-mechanical analyses of the bentonite buffer. Clay Technology AB, 33 pp.
- Cuevas, J., Ruiz, A.I., Ortega, A. & Fernández, R. (2016): Bentonite laboratory program and report. Contribution to (3) mineralogical and geochemical characterization: S45, mineralogy, crystal-chemistry. UAM, Madrid, 30 pp.
- Plötze, M. (2015): FEBEX DP Bentonite characterization. IGT Report CL 1053/1. 15 pp.
- Plötze, M. (2017): FEBEX DP Bentonite characterization. IGT Report CL 1053/2. 13 pp.
- Kaufhold, S., Dohrmann, R. & Ufer, K. (2016): FEBEX Experiment – Geochemistry and Mineralogy. 20 pp.
- Sakaki, T. (2016): FEBEX-DP: In-situ measurement of thermal conductivity of bentonite blocks during dismantling and a comparison with CIEMAT laboratory results. Nagra AN 16-05 (included in NAB 16-68). 25 pp.

- Kawamoto, K. (2016): Microfocus X-Ray Computerized Tomography on selected FEBEX-DP samples at Saitama University. Internal Report.
- Zheng, L., Voltolini, M. & Birkholzer, J. (2017): Characterization of the microscopic structure of bentonite samples: Quantitative characterization of the fracture network in the FEBEX samples via Synchrotron X-ray MicroCT. In: Zheng L., Rutqvist J., Xu H., Kim K., Voltolini M., Cao X. 2017. Investigation of coupled processes and impact of high temperature limits in argillite rock: FY17 Progress. Lawrence Berkeley National Laboratory, June 23, 2017, SFWD-SFWST-2017-000040, LBNL No. 2001014.
- Cervinka, R. & Kolomá, K. (2016): Determination of CEC and exchangeable cations on sample B-S-36-3. Technical Report XY/2015. Prague, 14 pp.

These reports are collectively stored in a Nagra internal report (Kober 2018), except for the detailed studies performed at CIEMAT, which are included in the two additional NABs mentioned above.

The current report is organised in the following chapters, in which the results obtained by the different laboratories are presented together and compared:

- Three introductory chapters, including this one, a chapter on the material considered by the different laboratories as reference one (the FEBEX bentonite) and a chapter identifying which samples were analysed as well as the state in which they were received by the laboratories.
- A chapter on the physical state of the bentonite (water content and dry density), its microstructure (texture, pore size distribution) and the physico-chemical properties related to them (surface properties, suction and water adsorption capacity).
- A chapter on the mineralogical and geochemical characteristics of the solid bulk and fine fractions of the bentonite and of its pore water, as analysed using different techniques.
- A chapter on the thermo-hydro-mechanical properties of the bentonite, analysed in situ (thermal conductivity) and in the laboratory, both in the "as-retrieved" and in "remoulded" samples.
- A final chapter discussing the results obtained concerning the three areas identified above and drawing some conclusions.
- An Annex including the numerical data obtained by the different groups organised in tables, except CIEMAT's results, which are included in the documents NAB 16-24 and NAB 16-25.

2 The reference FEBEX bentonite

The FEBEX bentonite was a 900-t batch of bentonite that was extracted from the Cortijo de Archidona deposit and processed in 1996 for the FEBEX project. The processing consisted in homogenisation, air-drying and manual removing of volcanic pebbles on-site and, at the factory, crumbling, drying in a rotary oven at temperatures between 50 and 60 °C and sieving through a 5-mm mess. The blocks for the FEBEX *in-situ* test at Grimsel as well as those for the FEBEX mock-up test at CIEMAT were manufactured from this material. During packaging, an approximately 9-kg bentonite sample was taken for every 2.5 t. These subsamples were mixed at CIEMAT facilities to obtain a very homogeneous material that was used for a comprehensive characterisation and different laboratory tests during the FEBEX I and FEBEX II projects. These initial studies can be found in the final report of the project (Enresa 2006) and in Villar (2002) and Fernández (2004). This material was also used for the NF-PRO and PEBS projects (Villar & Gómez-Espina 2009) and was distributed over the years to different laboratories to be used in different projects (e.g. ABM [Svensson et al. 2011], ESDRED [Alonso et al. 2008]).

In addition to this well characterised "reference" FEBEX material, that was used to identify any changes in the bentonite properties caused by the operation, each organisation involved in FEBEX-DP independently characterised samples of untreated FEBEX bentonite and provided their results for comparison. This was done because the values of some of the parameters and properties analysed will depend on the methodology used to determine them, and it is advisable to evaluate changes among parameters determined under the same conditions. This was clearly shown during the round-robin performed before dismantling (Kober & Van Meir 2017).

- CIEMAT used the homogeneous batch described above, prepared at the beginning of the FEBEX project as a reference material. The main mineralogical, geochemical and thermos-hydro-mechanical characteristics of this material can be found in Enresa (2006).
- UPC and ClayTech used a FEBEX bentonite block compacted in 1996 along with those used in the FEBEX in situ tests at the GTS as reference material.
- BGR used the Febex bentonite used for the ABM test (Dohrmann et al. 2013, Kaufhold et al. 2013) as reference material. In addition, 22 samples of those investigated in the present study were selected and the values were averaged to calculate a reference (Ref. Avg.). These selected samples were taken at a distance of more than 10 cm from the heater and from the granite. The chemical composition, CEC and exchangeable cations of the Ref. ABM and Ref. Avg. were similar, but in this report only the values for the ABM material have been used.

3 Samples analysed

The different laboratories received samples between May and December 2015 in the form of cores, blocks or irregular shapes, packed according to the conditions previously demanded by the groups, although most of them were wrapped in plastic film and packed in double vacuumed aluminium foil bags (Fig. 5, Fig. 6). The description of the sampling operations and the sampling plan –which includes information about the samples taken and the organisations they were sent to– is given in NAB 16-11 (García-Siñeriz et al. 2016) and NAB 15-14 (Bárcena & García-Siñeriz 2015), respectively. Tab. 2 summarises the samples sent to the laboratories for THM-THG analyses from the different sampling sections. The analyses included basic and microstructural characterisation (dry density, water content, suction measurement, pore size distribution (PSD), specific surface area), determination of thermal (thermal conductivity), hydraulic (gas and water permeability, water retention capacity), and mechanical (swelling pressure and swelling capacity, consolidation, strength) properties, and complete mineralogical and geochemical (solid and water) characterisation. The location of the sampling sections along the gallery is shown in Fig. 7.

Fig. 5: Vacuum-packing of blocks at the GTS (left) and packed cores ready for shipment (right).

Fig. 6: Packed blocks received in the laboratories.

Tab. 2: Summary of samples received and analysed for THM-THG determinations by each laboratory.

Section	**Slice**	**Institution**	**Sample type**	**Analyses**
S36	74	CIEMAT	9 blocks 5 cores	Water content, dry density, suction, PSD, thermal conductivity, swelling, permeability, water retention, solid and liquid geochemistry, mineralogy
S36	74	SÚRAO	1 irregular	CEC, exchangeable cations
S42	59	BGR	2 irregular	Geochemistry, mineralogy
S45	49	UAM	10 cores	Geochemistry, mineralogy
S45	49	BGR	14 cores	Geochemistry, mineralogy
S46	45	Nagra	On-site	Thermal conductivity
S46 – S47	44 – 46	ETH	10 cores	Water content, dry density, PSD, thermal conductivity, specific surface, mineralogy, geochemistry
S47	44	CIEMAT	9 blocks 6 cores	Water content, dry density, suction, PSD, thermal conductivity, swelling, permeability, water retention, solid and liquid geochemistry, mineralogy
S47	44	ClayTech	3 blocks	Water content, dry density, swelling, permeability, water retention, unconfined compression tests
S48	42	BGR	2 irregular	Geochemistry, mineralogy
S48	42	DOE	9 cubes	Microstructure (SXR-μCT)
S49	40	SAITAMA	27 cores	Specific weight, analysis of interfaces by MFX-CT
S50	37	UPC	3 blocks	Water content, dry density, suction, PSD, thermal conductivity, high-stress oedometer tests, high-stress isotropic tests
S50	37	BGR	10 cores	Geochemistry, mineralogy
S53	28	Nagra	On-site	Thermal conductivity
S53	28	CIEMAT	9 blocks 6 cores	Water content, dry density, suction, PSD, thermal conductivity, swelling, permeability, water retention, solid and liquid geochemistry, mineralogy
S53	28	BGR	7 cores	Geochemistry, mineralogy
S57	19	CIEMAT	13 blocks 6 cores	Water content, dry density, suction, PSD, thermal conductivity, swelling, permeability, water retention, solid and liquid geochemistry, mineralogy
S57	19	UPC	4 blocks	Water content, dry density, suction, PSD, thermal conductivity, high-stress oedometer tests, high-stress isotropic tests
S58	9, 13	Nagra	On-site	Thermal conductivity
S59	8	DOE	15 cubes	Microstructure (SXR-μCT)
S61	4	ETH		Water content, dry density, PSD, thermal conductivity, specific surface, mineralogy, geochemistry
S61	4	Nagra	On-site	Thermal conductivity

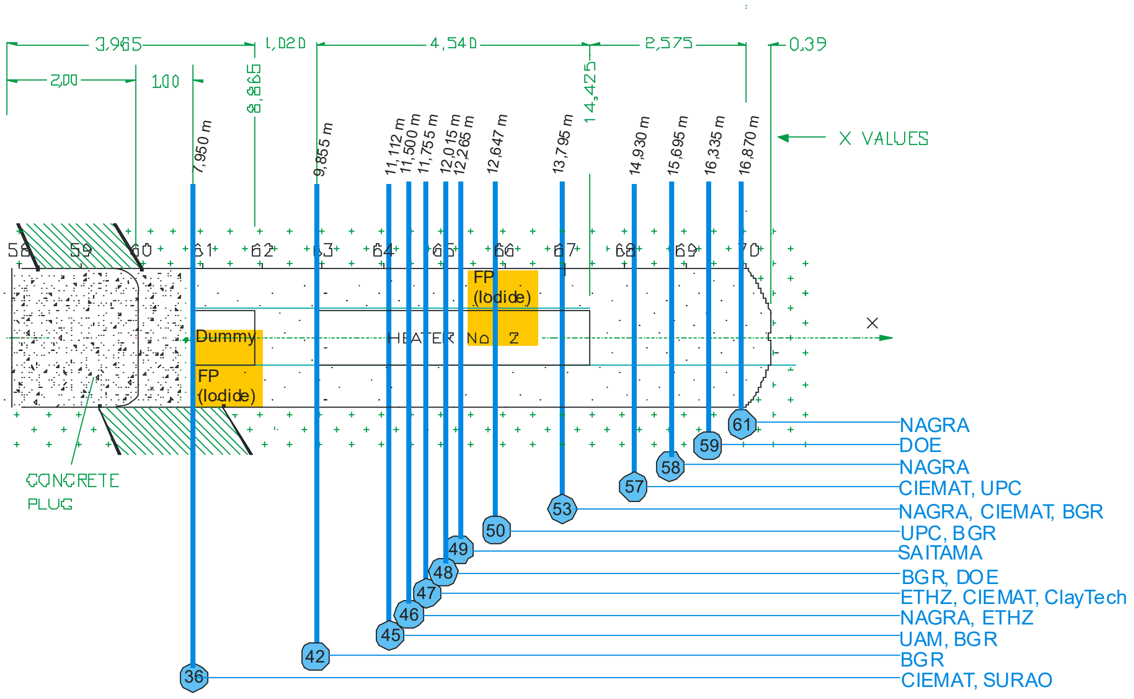

Fig. 7: Location of the sampling sections used by each organisation for bentonite characterisation (see location of $x = 0$ coordinate in Fig. 2).

The on-site determinations performed during dismantling showed that the physical conditions of the bentonite along the barrier had changed during operation, as a result of hydration and of the different temperatures to which the bentonite had been subjected (Tab. 1). Water content and dry density gradients, both across the vertical sections and along the gallery, had been generated (Villar et al. 2016a). Fig. 8 to Fig. 10 show the final distribution of dry density, water content and degree of saturation along the barrier obtained from the on-site determinations. It is clear that the initial conditions of the samples received by the different laboratories depended on the exact location along the barrier of the sampling section from which they were taken, as well as on the position of a particular sample with respect to the axis of the gallery. The main differences occurred between sections located around the heater (Sections 42 to 53) or in cool areas.

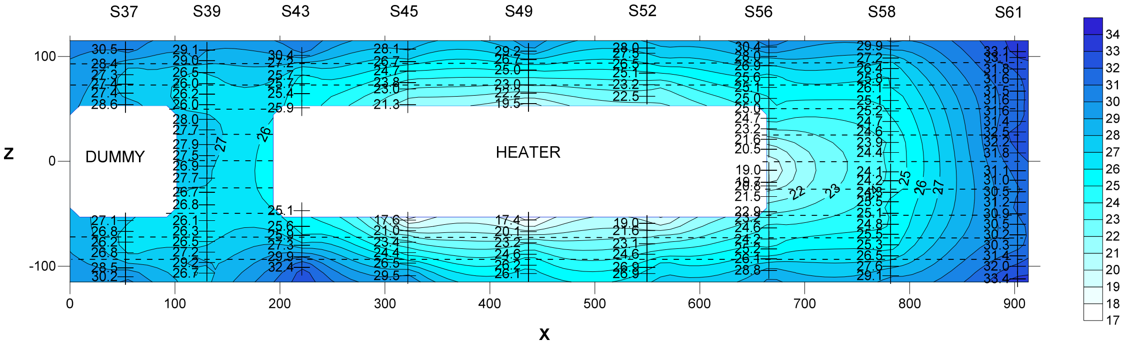

Fig. 8: Water content distribution in a vertical longitudinal section (Villar et al. 2016a).

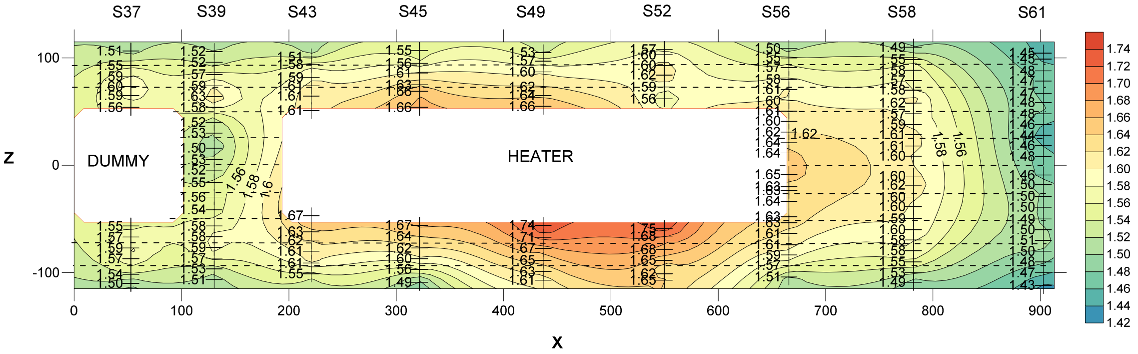

Fig. 9: Dry density distribution in a vertical longitudinal section (Villar et al. 2016).

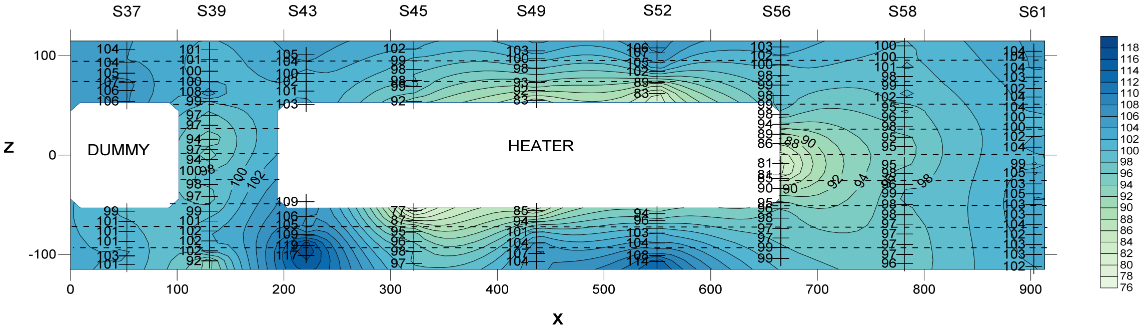

Fig. 10: Degree of saturation distribution in a vertical longitudinal section (Villar et al. 2016) (inexact values because of solid specific weight and water density uncertainties).

4 Characterisation of the physical state and microstructure

The complete characterisation of the physical state of the barrier was performed on-site by AITEMIN during the dismantling operation. Water content and dry density were determined in samples taken along six evenly distributed radii over the surface of nine vertical sampling sections. The results obtained were reported in NAB 16-12 (Villar et al. 2016a) and are partly summarised in Fig. 8 to Fig. 10. Most of the organisations receiving bentonite samples from the GTS also determined water content and dry density in their laboratories, and the results obtained are given in Annex I and presented below, along with comparisons with the values obtained on-site. Additionally, the microstructure of the samples was analysed by X-ray diffraction (determination of the smectite basal spacing), mercury intrusion porosimetry (determination of the pore size distribution) and tomography (texture and state of interfaces). Surface properties such as the external specific surface area and the water adsorption isotherms were also determined and are reported in this Chapter.

4.1 Water content, dry density

The water content and dry density of the bentonite was determined by several organisations on the samples they received. The characteristics of these determinations are shown in Tab. 3. To determine water content all the groups dried the samples at temperatures between 105 and 110 °C, but the drying times varied from 1 to 7 days. Nevertheless, and despite the fact that there was a large range in analysis time periods since retrieval at GTS, the values obtained were consistent, as shown in Fig. 11 for sections around the heater. Fig. 12 also highlights the consistency of the results obtained in the laboratories and on site for the sections around the heater. This suggests that the packing and transport conditions were appropriate to maintain the *in-situ* state of the blocks even several months after their retrieval. The results by ClayTech tended to be in the lower range, but only the innermost block analysed in this laboratory yielded lower water contents than those expected at this position (crosses for distances around and below 60 cm in Fig. 12), which could indicate that some drying took place between retrieval and sampling in the laboratory.

Fig. 13 shows the results obtained for cool sections by CIEMAT and UPC. The differences found in the determined values (the water contents determined by CIEMAT were higher and the dry densities lower) can be justified by the exact location of the sections analysed (*x*-coordinate): Section S59 was located closer to the back of the gallery, and the on-site determinations showed that the dry density of the barrier decreased towards it while the water content increased (Fig. 8, Fig. 9). In fact, if the results are plotted along with those obtained on site for an intermediate section, the differences are placed in context (Fig. 13, right). ETH also analysed samples taken from the back of the gallery (S61) and they found consistently higher water contents and lower dry densities than the other groups, which agrees with the results obtained on site.

The determination of dry density was performed following several different methodologies to measure the volume of the sample, and these are indicated in Tab. 3. CIEMAT determined the water content in the same samples used to determine the bulk volume, which allowed direct determination of the dry density of the samples. The other groups determined the water content in samples taken close to those used for the bulk density determination and then computed their dry density from that value. The two methodologies gave overall similar results (Fig. 14), if we take into account the dispersion that is usually found in this kind of determination and the one to be expected from the longitudinal changes along the barrier (Fig. 9). Only the results by ETH, obtained with a commercial instrument, were significantly lower than those obtained by the rest of participants. Fig. 15 shows the dry density values measured on site and in the laboratory in sections around the heater. The results obtained on site showed considerable dispersion, and most of the laboratory results lay inside the most frequent range found on site. Hence, there is a good consistency between the results obtained on site and in the laboratory. The dry densities obtained by ClayTech tended to be in the upper range of those found by the other laboratories, particularly for the innermost block, which is consistent with the lower water contents measured in it. Nevertheless, when these values are plotted along with the on-site results, they are seen to fit in the range of variation. The results obtained by ETH in Sections S46 and S47 lay in the lower range of the values measured on site, which correspond to one sampling radius of Section S52.

In the cool sections the consistency between on-site and lab results was also good (Fig. 16, right). The fact that the dry densities determined by CIEMAT were lower than those determined by UPC can be explained –as in the case of the differences found in water content– by the particular location of the sections analysed (Fig. 9): Section S59, analysed by CIEMAT, was closer to the back of the gallery (where the dry density was lower) than Section S57, analysed by UPC.

Tab. 3: Characteristics of the water content and dry density determinations performed in the laboratory.

Organisation	**Reception date**	**Sample type**	**Quantity of sample** (g)	**Heating *T*** (°C)	**Heating time** (days)	**Method for volume determination**
CIEMAT	Aug-15	Block	4 – 47	110	2	Immersion in mercury
UAM	Aug-15	Core	2.5	110	2	Not determined
UPC	Sep-15	Block		105	> 2	Wax paraffin (ASTM D4531-15)
ClayTech	Dec-15	Block		105	1	Weighing the specimen above and submerged in paraffin oil
ETH	Jul-15	Core		105 – 110	7	Immersion in silica nano powder (5 g)

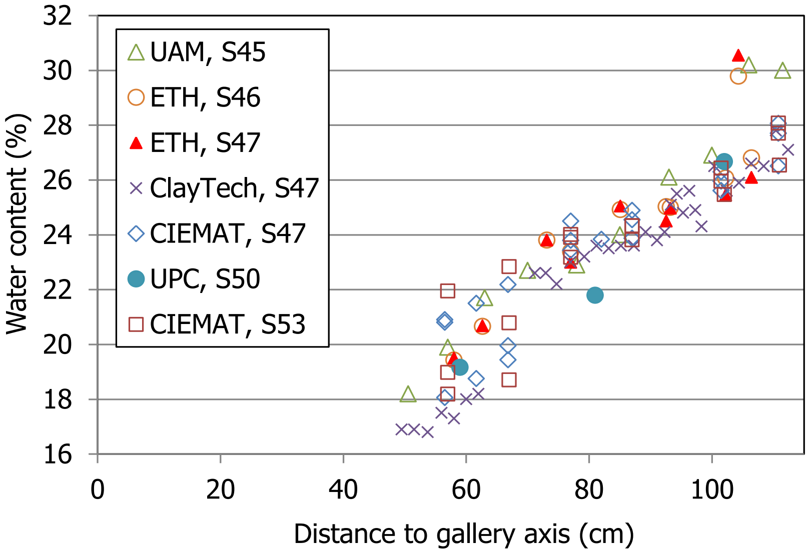

Fig. 11: Water content determined in different laboratories for samples of various sections located around the heater.

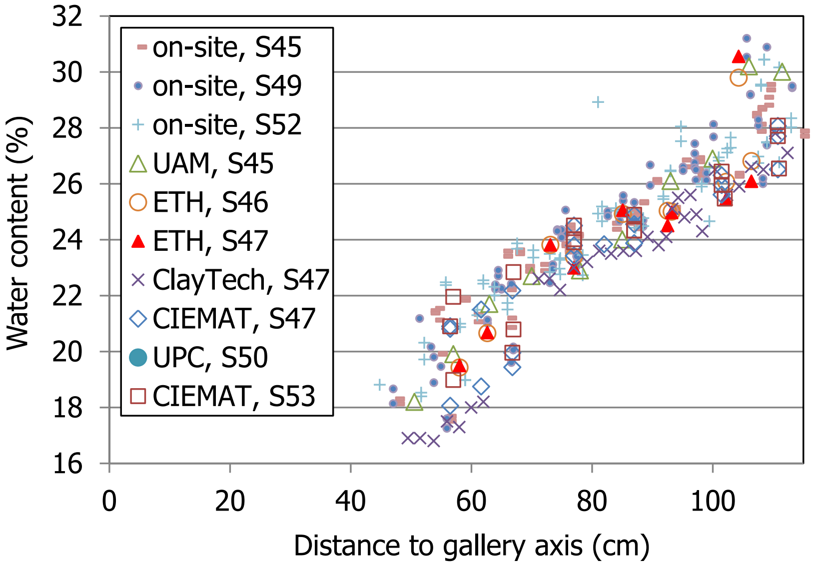

Fig. 12: Comparison of water content for sections around the heater determined on site and in different laboratories

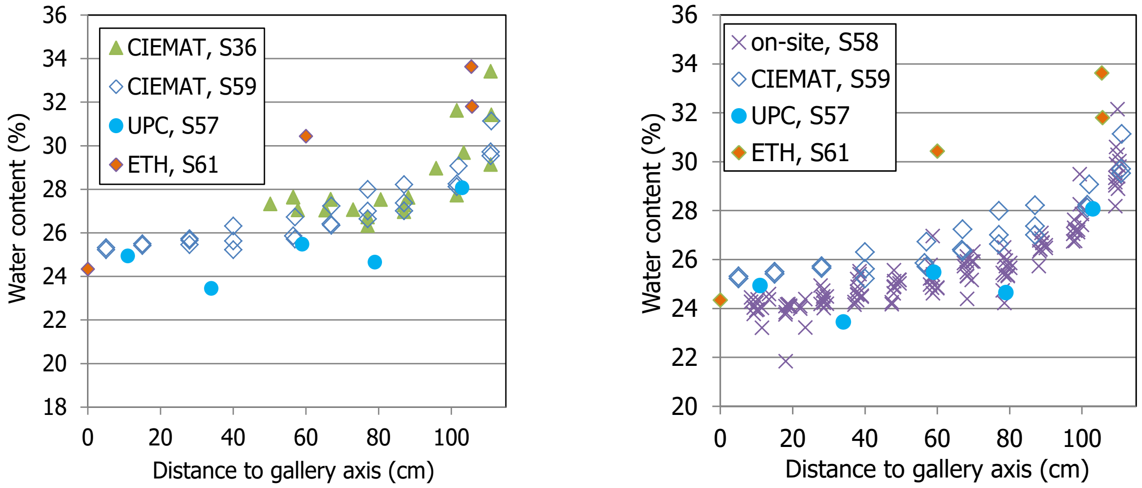

Fig. 13: Water content for cool sections determined in different laboratories and on site.

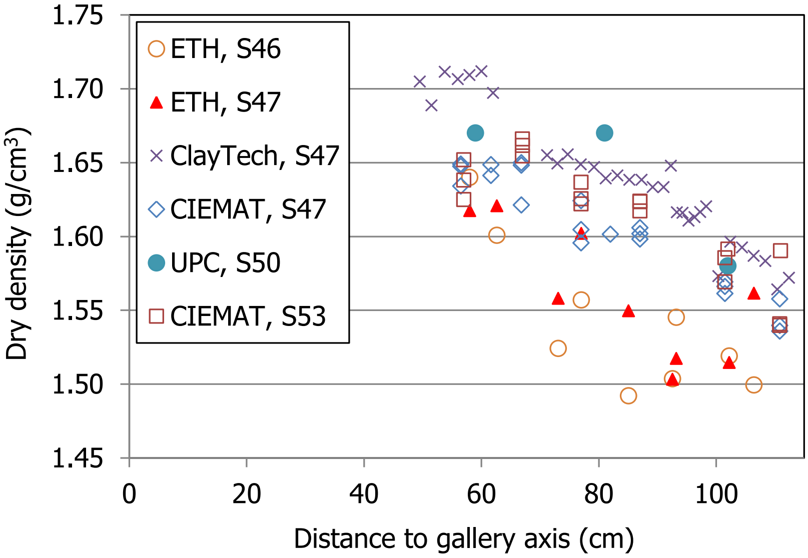

Fig. 14: Dry density determined in different laboratories for samples of various sections located around the heater.

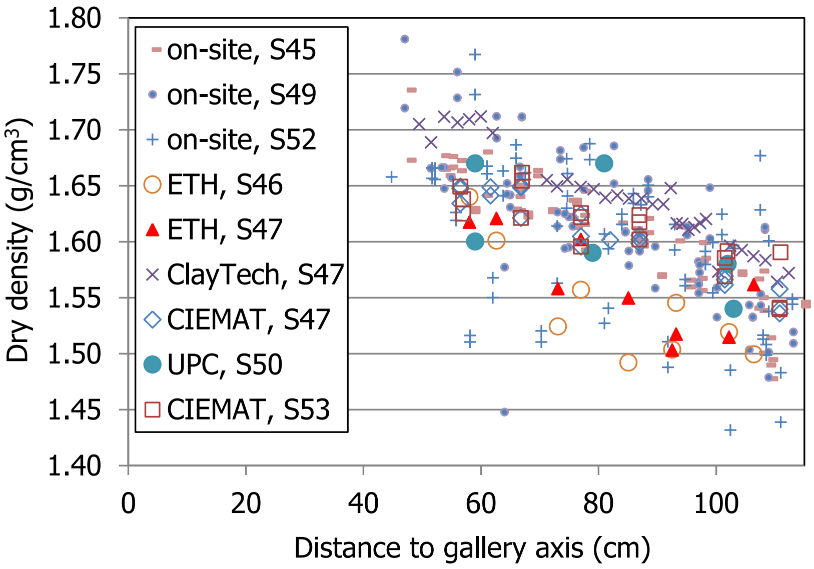

Fig. 15: Comparison of dry density for sections around the heater determined on site and in different laboratories.

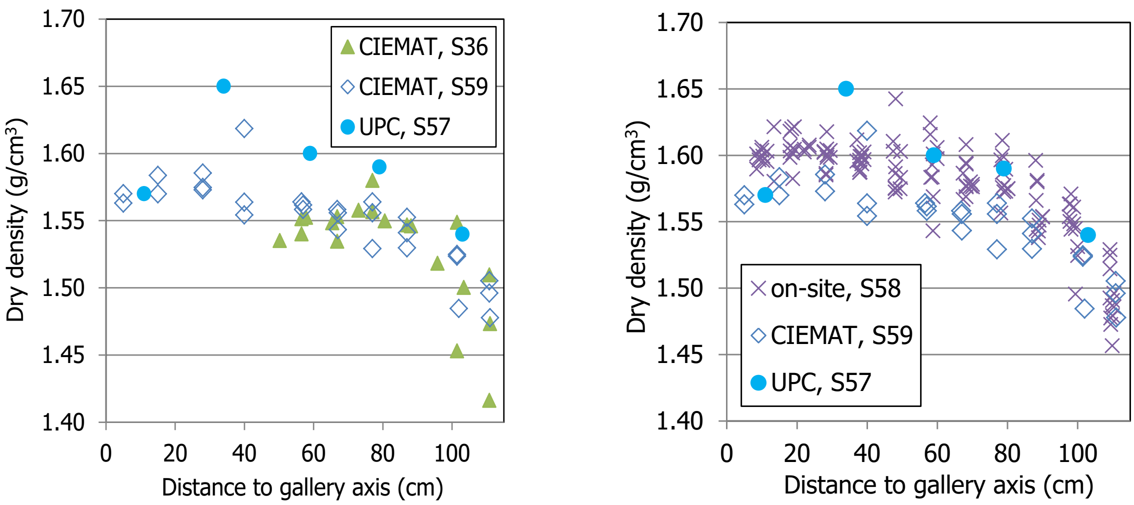

Fig. 16: Dry density for cool sections determined in different laboratories and on site.

The degree of saturation of the samples was computed assuming a water density of 1 g/cm^3 and different solid specific weights, depending on the organisation:

- CIEMAT and UPC used 2.70 ± 0.04 g/cm^3 for the solid component, which is the average of 20 measurements performed in pycnometers using water for soil suspension (Villar 2002, Enresa 2000, 2006). In 22 samples taken from Grimsel during the 2015 dismantling, this parameter was determined again and the same average value was found (Villar et al. 2018).
- ClayTech used 2.735 g/cm^3, taken from Svensson et al. (2011).
- ETH obtained an average value of 2.565 g/cm^3 for determinations performed in several samples with a helium pycnometer.
- Saitama determined with pycnometers a solid specific weight of 2.68 g/cm^3 in three samples from Section S49.

The values used by ClayTech and determined by Saitama fit in the range of variation of the determinations performed by CIEMAT, but the value obtained by ETH is considerably lower, probably because the helium molecule is not able to enter the collapsed smectite interlayer, which gives a larger solid volume than when water is used as suspension medium. Nevertheless, agreeing in homogeneous values for all the laboratories was beyond the scope of the report.

The degree of saturation computed for the samples retrieved and also at the end of the hydromechanical tests reported below (Chapter 6) can be inaccurate not only because of the uncertainties in the solid specific weight value determination, but also because of the assumption that the density of water is 1 g/cm^3. There is increasing evidence from the fields of neutron diffraction, Monte Carlo computer simulations and quasi-elastic neutron scattering that the density of water attached to clay minerals may be greater than 1.0 g/cm^3 (Skipper et al. 1991, Monsalvo et al. 2006, Chávez-Páez et al. 2001, Tambach et al. 2004, Huang et al. 1994), with values of water density in phylosilicates of up to 1.38 g/cm^3, higher in smectites with divalent cations in the interlayer (such as FEBEX) than with monovalent ones (Jacinto et al., 2012). This fact becomes especially evident in highly compacted expansive clays close to water saturation, in which degrees of saturation much higher than 100 % can be computed if a water density value of 1.0 g/cm^3 is considered (Villar 2002, Marcial 2003, Lloret & Villar 2007). Thus, a computed degree of saturation of 115 % for a saturated sample would indicate that the average density of the water in it is 1.15 g/cm^3. Besides, the proportion of adsorbed water (with a density higher than 1 g/cm^3) over free water (with a density of 1 g/cm^3) increases as the dry density of the bentonite is higher. Consequently, for low-density bentonite the average water density would be close to 1 g/cm^3 or even lower.

Since there is no accurate knowledge of the values that the density of water can take (which would depend on the particular bentonite, its density and water content), the customary value of 1 g/cm^3 was used in the calculations presented in the following subchapters and Annex, which would partially explain the degree of saturation higher than 100 % found in some cases.

4.2 Texture by tomography

Two different techniques based on the use of X-ray Computerised Tomography were used to study the texture of the bentonite, in particular the larger pores/fractures and the interfaces between blocks.

4.2.1 Crack network by Synchrotron X-ray Micro Computerised Tomography (SXR-µCT)

To study the microstructure of the retrieved bentonite, and in particular its fracture network, the Lawrence Berkeley National Laboratory (LBNL) used the non-destructive Synchrotron X-ray Micro-Computed Tomography (SXR-µCT) technique to look at the interior of samples as undisturbed as possible. The final aim was to associate a quantitative parameter to each sample so that the variation of the fracture network for samples at different locations could be understood. This should serve as additional evidence to delineate the right permeability change functions and increase the predictability of models.

The experiments were carried out on the 8.3.2 Beamline at the Advanced Light Source (ALS) at LBNL (MacDowell et al. 2012). The experiment consisted in placing the sample on a rotating stage and taking radiographs over 180 degrees of rotation at given angular intervals. From these radiographs, a software based on the concept of the filtered-back projection provided a virtual volume of the sample in the form of a stack of horizontal "slices".

In these experiments the samples were measured with monochromatic X-rays (34 keV), 650 ms of exposure time, collecting 2049 projections, with a continuous tomography and "local area" (sample larger than the field of view) setup. The advantage of using a sample larger than the field of view is that the outer part of the sample, more affected by sample preparation, is not actually measured. The resulting voxel (vx, value on a regular grid in three-dimensional space) size of these measurements was 3.22 µm and the usable datasets were cylinders of 1'820 vx (= 5.86 mm) diameter and 500 vx (= 1.61 mm) height. Two measurements at higher resolution (0.633 µm voxel size) were carried out as well to check the presence of smaller fractures, which would be missed at the lower resolution.

Cylindrical samples were drilled on site and delivered in vacuum-sealed aluminium foil bags. Three samples from Section S48 around the heater and two samples from the cool Section S59 close to the back of the gallery were used (Fig. 7). The characteristics of these samples, as estimated from the on-site measurements (Villar et al. 2016a), are shown in Tab. 4. From the internal part of each sample three roughly cylindrical pieces of ~ 1.5 cm in height were cut and immediately sealed in plastic film to minimise the loss of moisture as much as possible during determinations. This means a total of 15 subsamples were analysed. Smaller fragments (~ 4 mm) were used for the higher resolution measurements.

Tab. 4: Characteristics of the samples used for the SXR-µCT tests.

Sample	**Distance to gallery axis** (cm)	***T* during operation*** (°C)	**Water content** (%)	**Dry density** (g/cm^3)	**Degree of saturation** (%)
BD-48-3	51	92 – 96 (S48)	20.6	1.66	89
BD-48-7	96	32 – 36 (S54)	27.5	1.53	97
BD-59-15	35	21 – 23 (S62)	24.4	1.59	94
BD-59-8	73	21 – 23 (S62)	25.6	1.58	98
BD-59-3	111	21 – 23 (S62)	28.9	1.52	101

* Estimated from the closest instrumented section indicated in parenthesis.

The analysis of the tomographic datasets was carried out using an automated Fiji script (Schindelin et al. 2012) with the aim of obtaining volumes where the medial axis of the fractures was labelled, in each point, with the local thickness (LT), a value related to the aperture (Dougherty & Kunzelmann 2007). The resulting volumes for some of the subsamples (Fig. 17, Fig. 18) include all the information about the frequency and size distributions of the fracture network. The samples were pervaded by a network of thin fractures, with sizes in the order of a few tens of microns. The volume renderings show that the fractures were present in the clay matrix (pure desiccation cracks), some cut across larger crystalline particles (quartz, feldspar, etc.) and some fractures were located along the interfaces of the crystals with the clay-rich matrix (aggregate-matrix detaching). From these observations, it seems reasonable to assume that there were different mechanisms involved in the development of these fractures. There was also a small amount of microporosity apparently not related to modifications in the microstructure of the material, but with the nature of the aggregate particles in the bentonite (for example on the left side of sample BD-59-15 in Fig. 18).

The middle part of the Figures, which shows the superimposing of the medial axes of the fractures (labelled with the values of the local thickness in each voxel) served as a check to confirm that the script found all the fractures above the actual resolution and the labelling with the LT values was correct. In the lower part of the Figures only the rendering of the labelled medial axes is shown. A colour log scale for the aperture values has been chosen since the majority of the aperture values were small, so in a log scale it is easier to appreciate the small variations in aperture in the fracture network.

More details about the characteristics of the fracture network can be seen in Fig. 19, where a thin horizontal slice of a sample (BD-59-3) is shown superimposed with a smaller volume of the fractures (as a white isosurface) to emphasize the structure and provide context for the fracture network. A zoom of a detail of the slice, but with the LT-labelled medial axes, is also shown to highlight the different kinds of fractures present. Fractures ran inside broken aggregate particles (e.g. top right) and connected different aggregate particles, but thin fractures were also present in the clay matrix.

For each of the 15 subsamples analysed, a frequency plot of apertures was calculated and the results are shown in Fig. 20. At the largest LT-values the samples were very different, in a seemingly chaotic fashion, but also the largest values of LT (i.e. large cracks) were very uncommon. In the range from 25 to 45 µm there seems to be two groups with common trends (Fig. 21). For smaller than 25-µm size bins (intervals), the size starts to be too close to the resolution, and the morphometric parameters start to be less reliable. The number of points in the medial axes of the fractures below the 45 µm size is very large, making the analysis more reliable from a purely statistical point of view. Obtaining statistically reliable results would be more challenging for the larger fractures, with bins larger than 100 µm, for example.

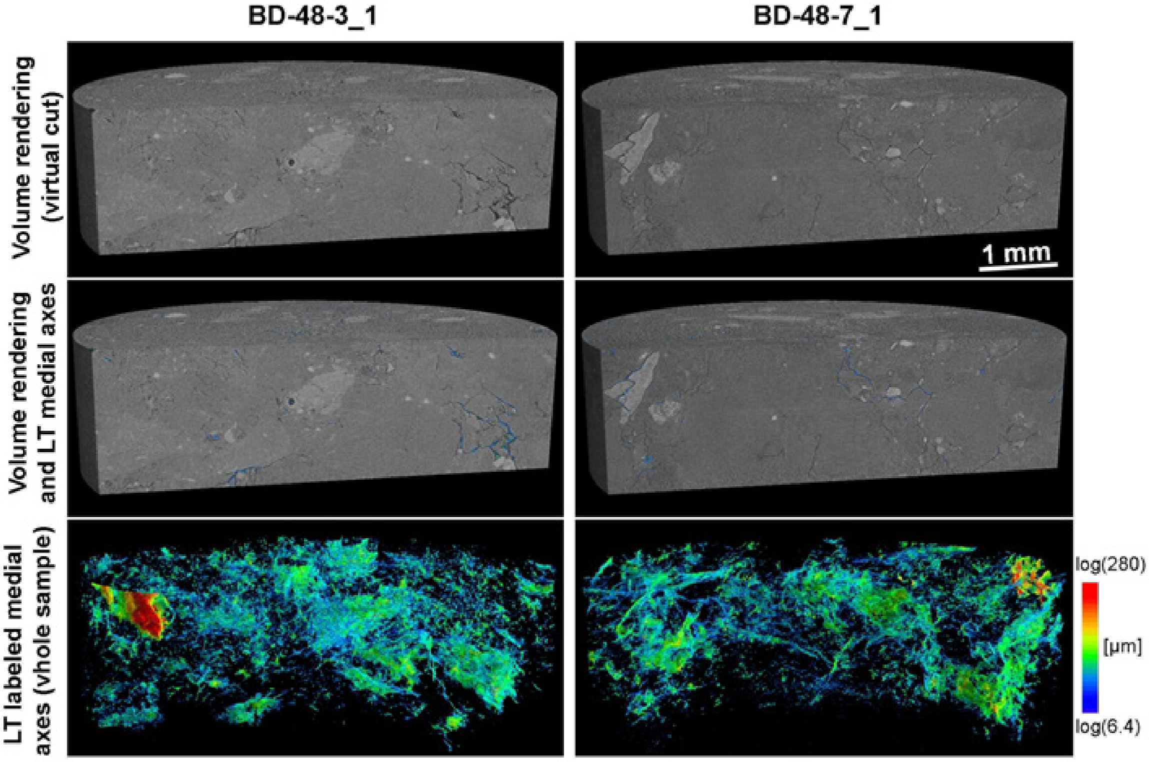

Fig. 17: Graphical results of the SXR-µCT of samples from Section S48: BD-48-3 (near the heater) and BD-48-7 (near the granite).

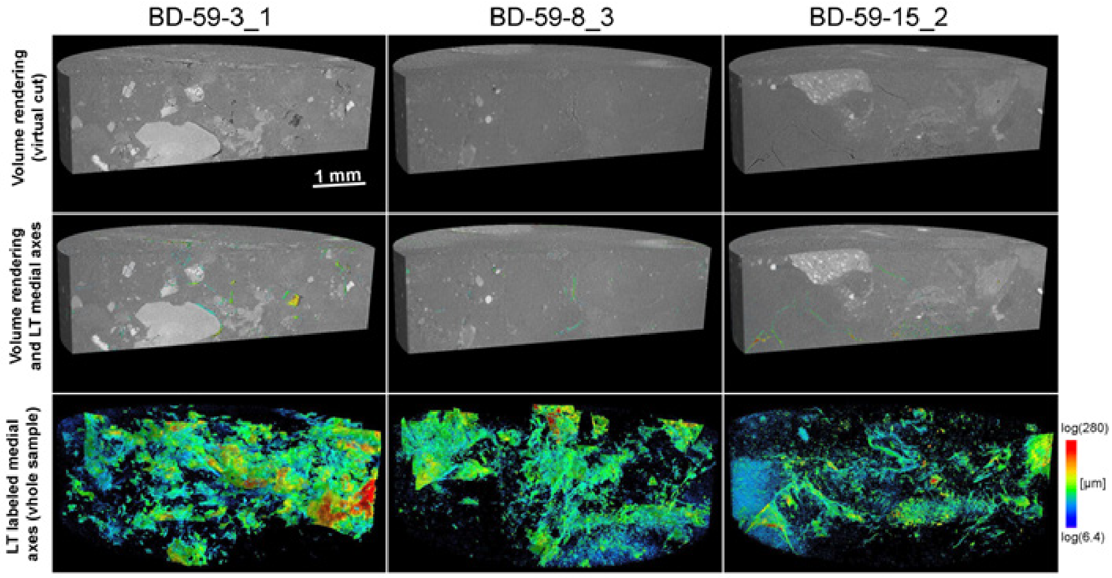

Fig. 18: Graphical results of the SXR-µCT of samples from Section S59: BD-59-3 sample (near the granite), BD-59-8 (half radius) and BD-59-15 (center).

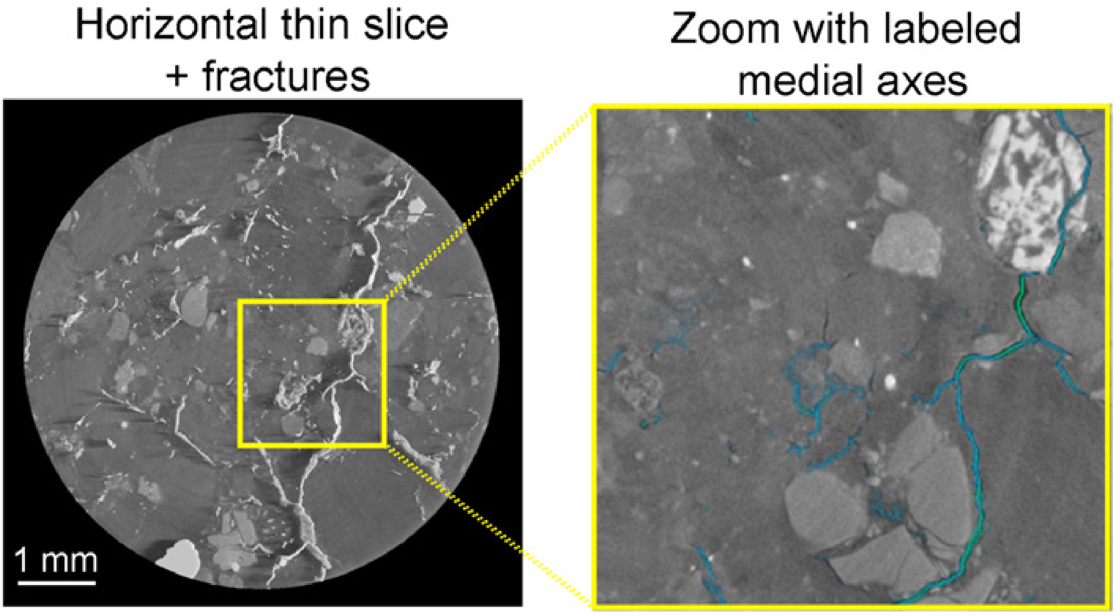

Fig. 19: Different features of the fracture network obtained by SXR-µCT in sample BD-59-3.

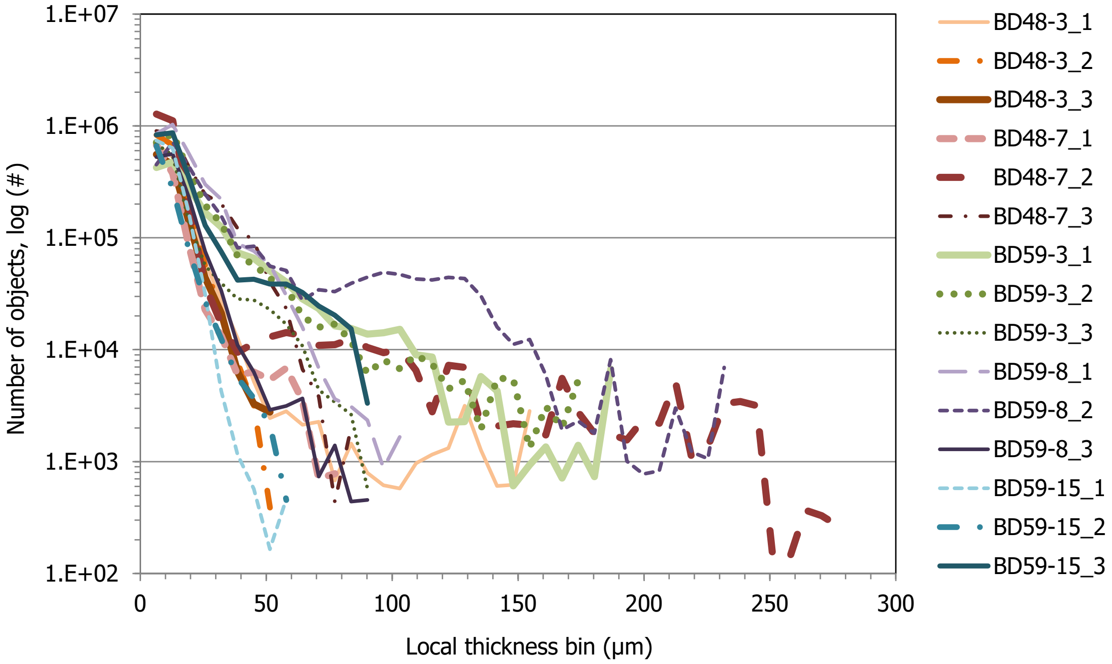

Fig. 20: Local thickness frequency plots (in absolute values) for all the 15 samples analysed by SXR-µCT.

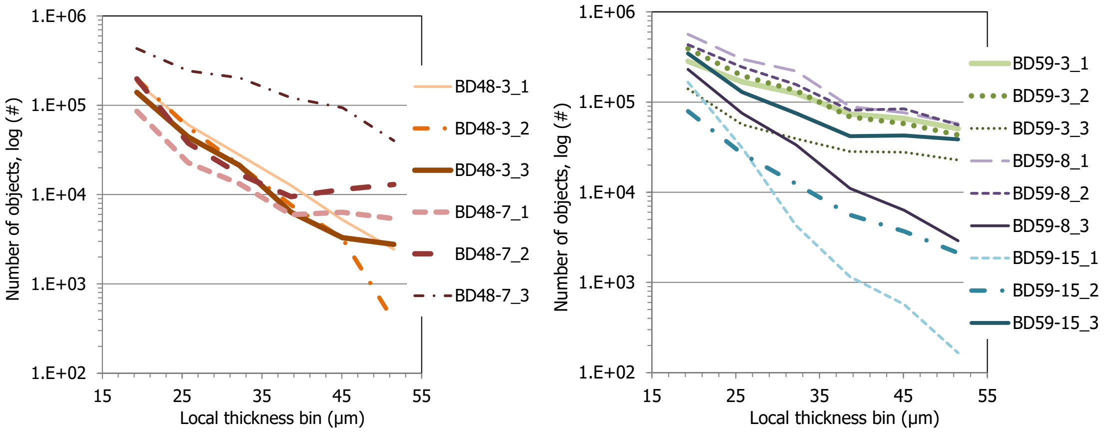

Fig. 21: Local thickness frequency plots in a smaller interval for samples of Sections S48 and S59.

The fracture aperture distributions in this interval (25 – 45 µm) were roughly linear (in log scale), and a linear regression for each sample was calculated. The slope of the fitted line (angular coefficient) provided direct information about the ratios of small *vs*. large fractures: smaller values of the angular coefficient mean that a large amount (exponentially proportional) of microfractures (close to the resolution of the measurements) was present in the sample, whereas higher values highlight the presence of larger cracks. The average of the values for the volumes of the three subsamples was calculated and plotted in Fig. 22, which consequently refers to a total volume of

~ 130 mm^3 for each position sampled. There seems to be a correlation of the angular coefficient relative to the distance to the granite contact: the slope of the linear regression curve increased with the distance from the wall, which would indicate that the samples closer to the granite tended to have a larger number of large voids compared to the samples close to the heater or to the centre of the section. The sample closest to the heater (BD-48-3) had the largest relative amount of the smallest microfractures of all the samples. This suggests that either the decrease in humidity promoted the relative creation of smaller microfractures or the increase in water content brought about the creation of larger voids, while no evident trend was observed looking at the absolute values. However, there was a large variability among the subsamples of a given sampling position, so while the trend found shows some consistency, a much larger number of measurements should be carried out to fully validate this finding.

The analyses presented so far used a resolution of 3.22 µm, trying to balance the sample size and the imaging resolution. However, such a resolution may not allow to detect nanoscale features, which are known to be important for clay-rich materials. For this reason, and to assess how much of the smaller features were missed using the lower resolution scans, a measurement at much higher resolution (633 nm per voxel) was carried out on sample BD-48-7. Given the higher resolution the usable volume investigated was a ~ 1 mm long cylinder. The graphical results obtained are shown in Fig. 23, where the segmented volume of the voids (fractures + micropores) has been highlighted in red. From a qualitative point of view, it seems that the amount of fractures with aperture values close to the resolution was relatively low, which could mean that the number of voids below this size (3.22 µm) was small. The nanoporosity present in some specific aggregate particles became visible and measurable at this resolution.

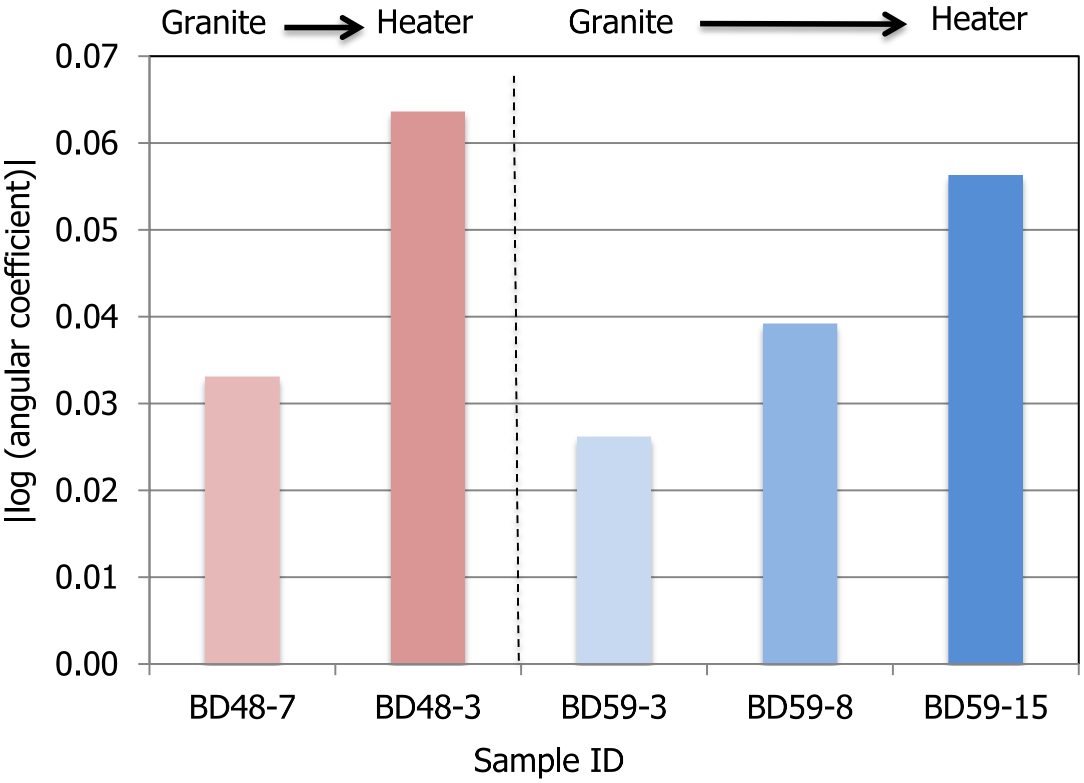

Fig. 22: Angular coefficients (average of the 3 subsamples) of the linear regressions of the plots shown in Fig. 21.

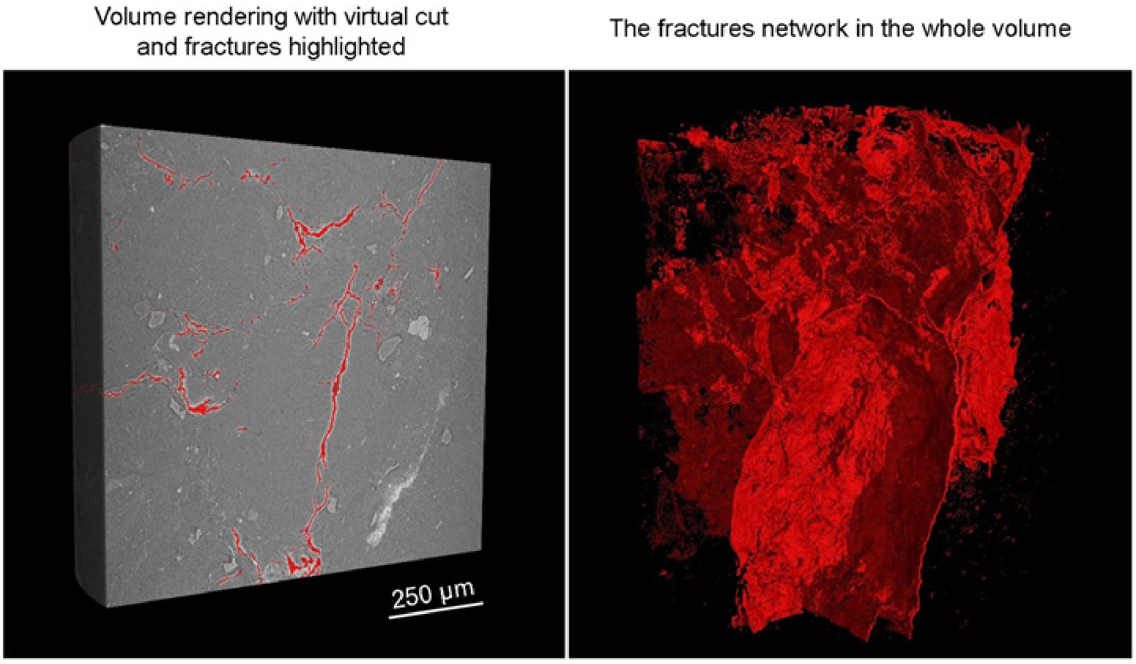

Fig. 23: Results from the high-resolution SXR-µCT measurement on sample BD-48-7 (the voids have been highlighted in red).

4.2.2 Analysis of interfaces between blocks by Microfocus X-ray Computerised Tomography (MFX-CT)

Observations during the dismantling indicated that the interfaces between the bentonite blocks that had various openings at the time of their installation had completely closed during operation due to hydration and swelling (Villar et al. 2016a, Kober & Van Meir 2017). A set of samples with and without the block joints were collected from Section S49 (slice 40) and their conditions were visualized at Saitama University by means of a Microfocus X-Ray Computerized Tomography (MFX-CT) system.

The samples were obtained by drilling on site, vacuum-packed and sent to Saitama's facilities. The samples were not preserved in resin, therefore, deformation was not constrained. A set of six samples, whose characteristics are shown in Tab. 5, was analysed. Their exact locations did not always correspond to those indicated in the Sampling Book (Bárcena & García-Siñeriz 2015), and samples that should have been drilled through an interface were actually not (Fig. 24).

Tab. 5: Characteristics of the samples analysed by Saitama by MXR-CT (according to the on-site measurements (Villar et al. 2016a), photographic record and MFX-CT observations).

Reference	**Distance to gallery axis** (cm)	**Transect**	**Water content** (%)	**Dry density** (g/cm^3)	**Remarks**
BC-49-67	56	Left	20.2	1.68	No joint
BC-49-64	89	Left	25.6	1.60	No joint
BC-49-62	112	Left	27.7	1.56	Joint
BC-49-23	66	Right	22.3	1.63	Joint and cracks perpendicular to it
BC-49-21	88	Right	25.6	1.57	Joint and cracks
BC-49-19	108	Right	28.1	1.53	No joint visible

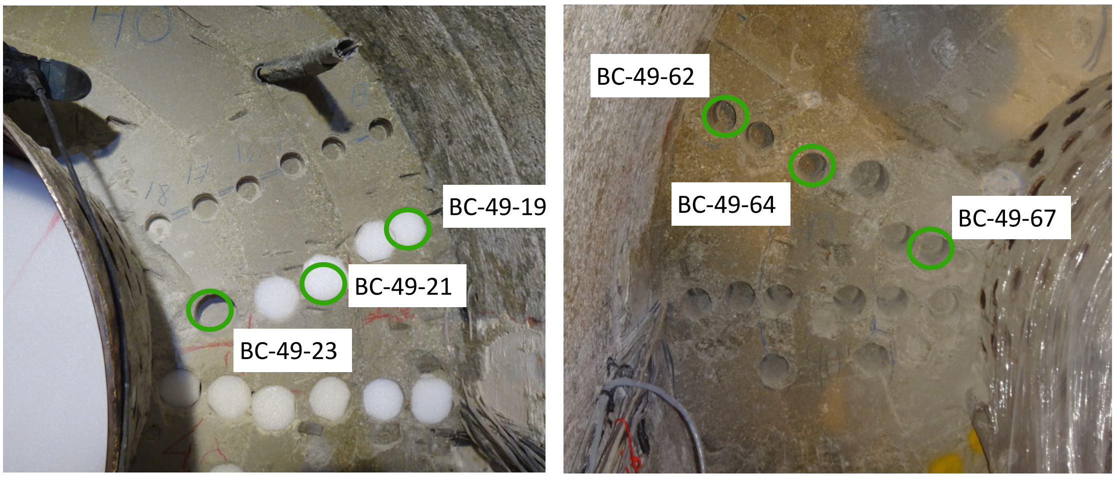

Fig. 24: Location in Section S49 of samples analysed by Saitama by MFX-CT: radius B-C (left) and E-F (right).

Once in the laboratory the samples were taken out of the sealed bags and trimmed with a knife into cylinders of about 5 cm diameter that were put inside acrylic columns of 5.5 cm diameter and 4 cm height. The gap between the sample and the acrylic column was filled with wax and the column was transferred to the CT device. The time of sample processing was 10 – 15 min and the CT scanning took 30 min.

A MFX-CT system, inspeXio SMX-90CT (Shimadzu Co Ltd, Japan) was used to scan the samples. The CT-images were reconstructed to visualize the samples in three dimensions using VGStudioMAX software (Volume Graphics GmbH, Germany). Four kinds of resolution, from 12 to 52 µm/voxel, were used. A typical scanned image (MPR: Multiplanar Reconstruction) is shown in Fig. 25.

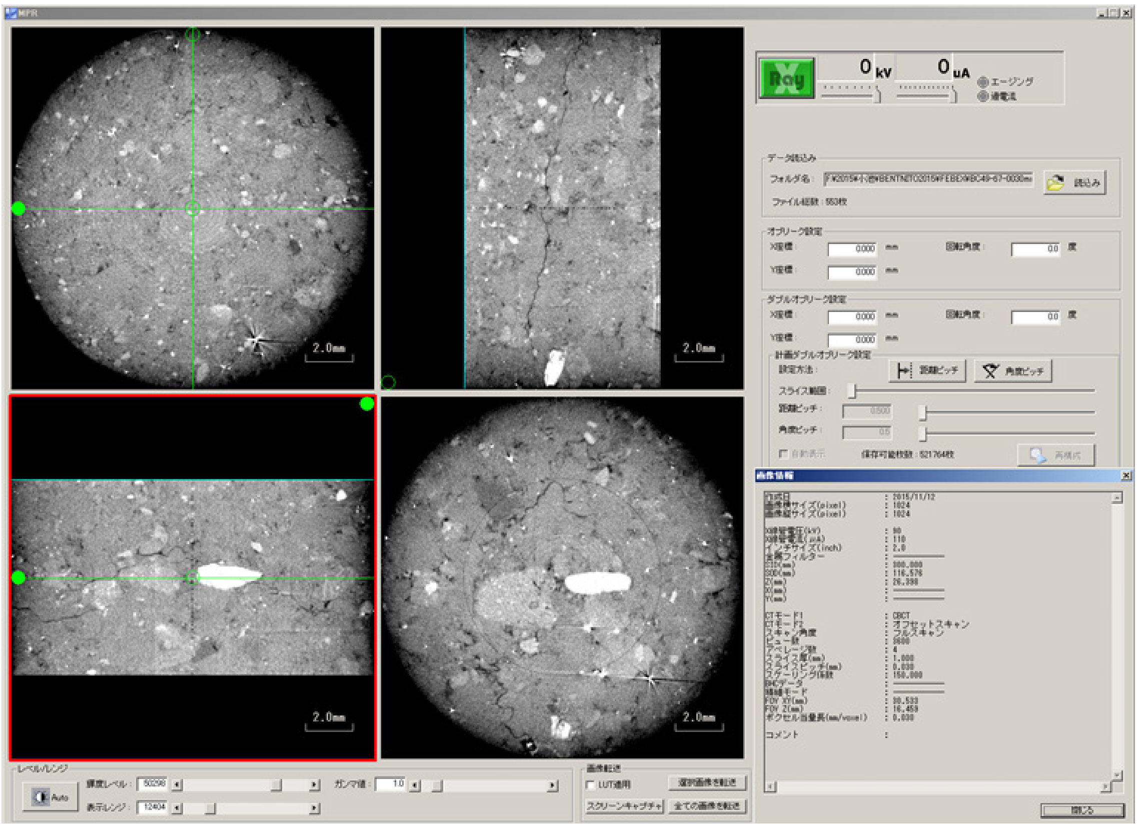

Fig. 25: MPR image for B-C-49-67 (near heater), resolution: 30 µm.

As an example, the scanned images (resolution = 52 µm) for samples BC-49-23 (near the heater) and BC-49-19 (near the tunnel wall) are shown in Fig. 26 and Fig. 27. A clear block joint was observed in sample BC-49-23. The observed joint was confirmed to be slightly open due to the stress relief as the deformation of the samples had not been constrained during sampling. The images also showed a crack that was not associated with the joint: whereas the joint resulted in a very straight line, the crack exhibited a more random opening. On the other hand, no joint was clearly confirmed on BC-49-21 (middle) and BC-49-19 (near tunnel wall). This indicates that the original block joints had closed tightly during the long period of water adsorption in the barrier.

As shown in Tab. 5, the samples from radius E-F, on the left transect, did not seem to have been taken across the interface between blocks. In fact, the scanned images did not show any indication of joint in samples BC-49-67 (near heater) and BC-49-64 (middle). However, sample BC-49-62 (near the tunnel wall) showed a straight successive crack-like opening near the edge of the sample (Fig. 28) with a straightness indicating that it was a block joint. A closer look at this sample showed that, at approximately *z* = ~ 80 mm (Fig. 28, right), a block joint between the bentonite block slices 40 and 41, i.e. an in-situ vertical joint, was detected (Fig. 29). Although it is difficult to distinguish whether or not the joint was about to open or fully intact, no significant heterogeneity was observed near the joint.

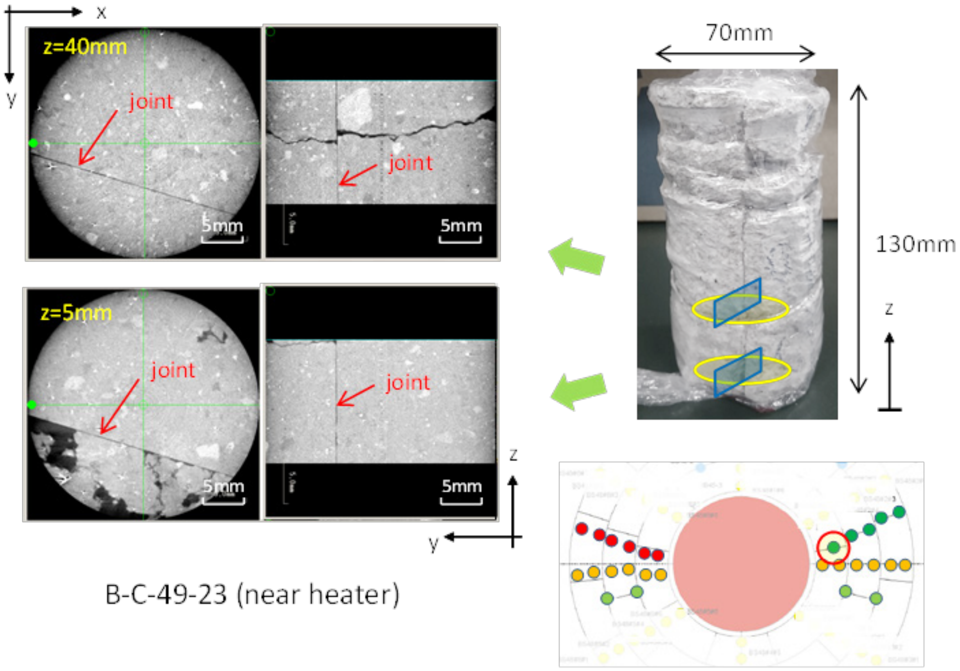

Fig. 26: Scanned images for sample BC-49-23, near heater (the yellow ellipses and blue rectangles on the picture indicate the position of the transversal and longitudinal scans of the sample, respectively).

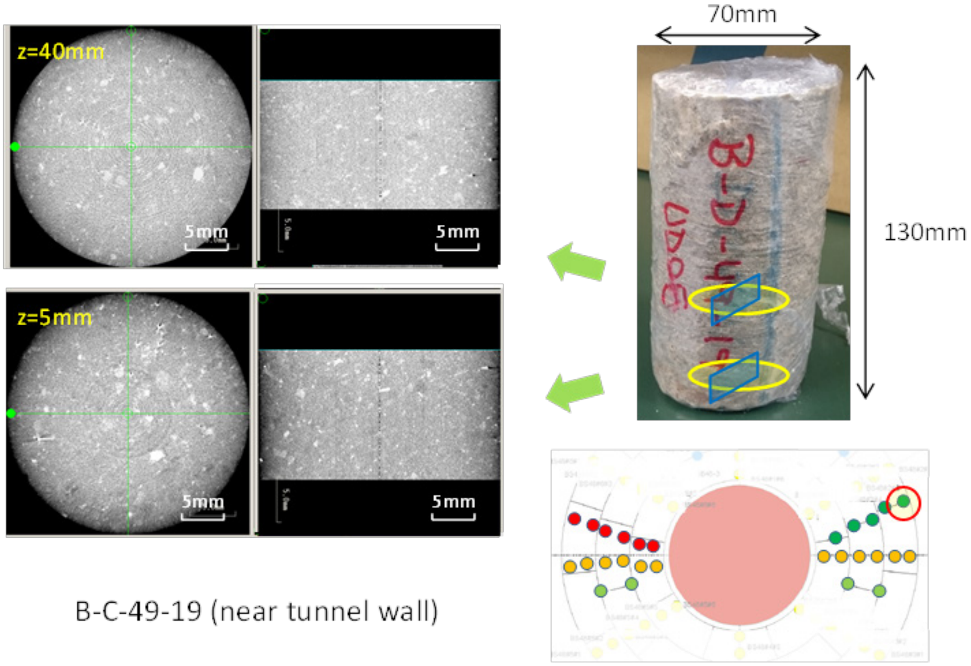

Fig. 27: Scanned images for sample BC-49-19, near tunnel wall (the yellow ellipses and blue rectangles on the picture indicate the position of the transversal and longitudinal scans of the sample, respectively).

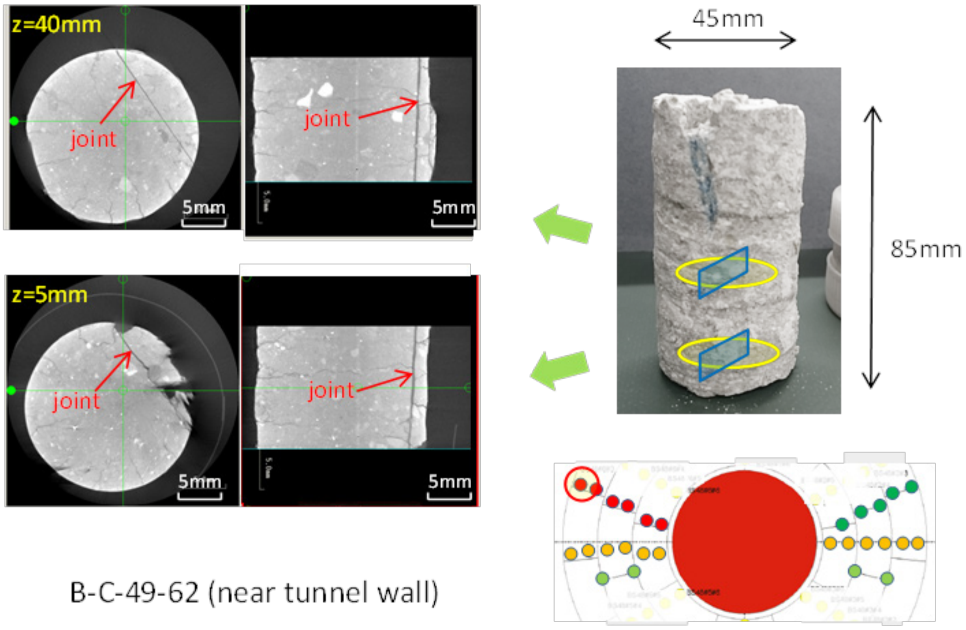

Fig. 28: Scanned images for sample BC-49-62, near tunnel wall (the yellow ellipses and blue rectangles on the picture indicate the position of the transversal and longitudinal scans of the sample, respectively).

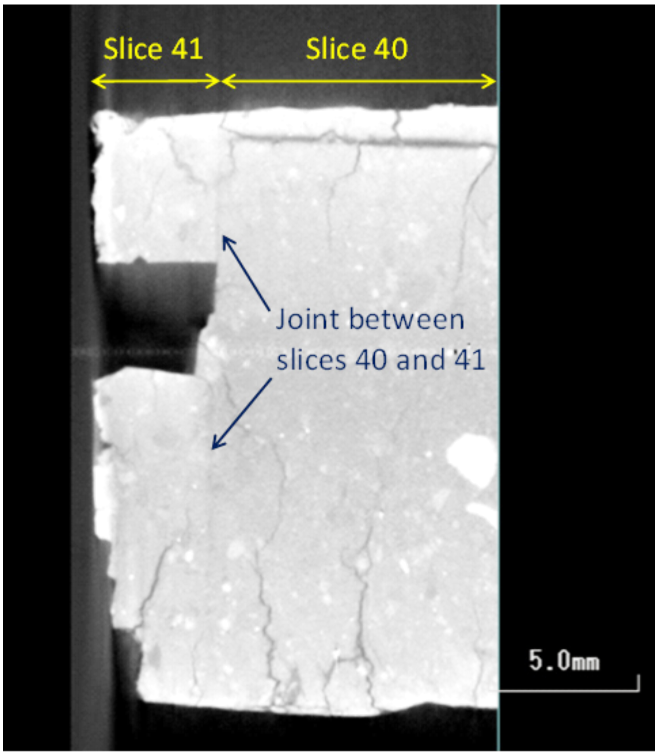

Fig. 29: Block joint detected between bentonite vertical slices of bentonite blocks 40 and 41 in sample BC-49-62.

Aperture widths (*D*) of observed block joints were estimated using the scanned images. The *D* values were measured at 10 cross-sectional views from each section (upper, middle, lower) of the samples. For sample BC-49-23 the values were between 0.38 and 0.47 mm and for sample BC-49-62 between 0.36 and 0.43 mm. Nevertheless, these values do not necessarily reflect those the joints had in the barrier, since the stress relief upon extraction was not constrained.

Additionally, the measured CT-brightness reflects material density in the X-ray scanning: higher CT-brightness becomes higher material bulk density and lower CT-brightness becomes lower material bulk density. Histograms of CT-brightness inside the scanned image were obtained for two different ROI (Regions of Interest), 1024x1024x550 voxels and 500x500x550 voxels. The mean values of CT brightness varied only slightly depending on the target ROIs and scanned resolutions. Hence, the strong gradients measured on site as a function of distance from the heater in dry and bulk density and water content (Villar et al. 2016a) were not observed in the brightness. The reason was probably that the size of the bentonite particles and pores was significantly smaller than the spatial resolution of the MFX-CT system.

4.3 Microstructure

4.3.1 Interlayer space

The basal reflection (*d*001 value) gives a measure of the interlayer distance between smectite particles, a minimum value of about 1 nm corresponding to a collapsed interlayer with no water in it. It is considered that smectites display basal reflections of about 1.25, 1.55 and 1.85 nm for the homogeneous 1, 2 and 3 water layers' hydration states, respectively, the exact values mainly depending, for a given smectite type, on the exchangeable cations. Under hygroscopic water content (14 %), which was the condition of the bentonite used to manufacture the blocks in 1996, the basal spacing of the FEBEX bentonite is about 1.48 nm (Villar et al. 2012).

The smectite basal reflection of the FEBEX-DP samples was determined by CIEMAT from X-ray profiles recorded on a sufficiently flat surface at room temperature, without any previous treatment of the samples. The values obtained are plotted in Fig. 30 as a function of the distance to the gallery axis and in Fig. 31 as a function of the water content. All the values measured were above the initial ones and corresponded mostly to a completely developed 2-layer hydrate, except for those samples of Sections S47 and S53 that were taken at less than 20 cm from the heater. Fig. 31 shows that these samples were those with water content below 25 %. Above this water content the basal reflection tended to increase with water content, i.e. as the distance from the axis of the gallery increased. A few samples had basal reflections close to those corresponding to the 3-layer hydrate.

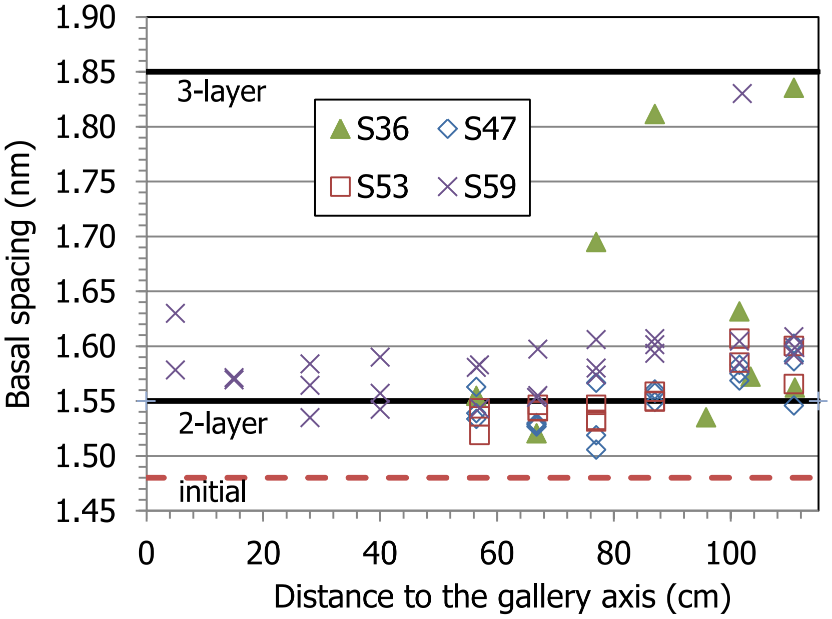

Fig. 30: Interlayer space of the smectite in FEBEX-DP samples of different sections as a function of the distance to the axis.

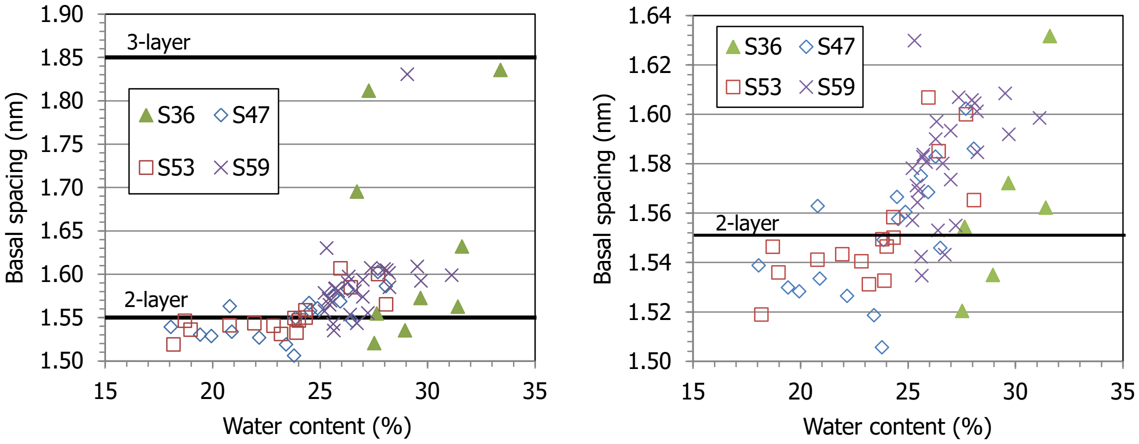

Fig. 31: Interlayer space of the smectite in FEBEX-DP samples of different sections as a function of water content (the figure on the right is an enlargement).

For most of the samples the 001-reflection peak was a double one that could be decomposed into two peaks, the one plotted in the previous Figures and another one towards lower angles, i.e. higher spacings. The two peaks could be separated by profile fitting of the XRD pattern. An example of this is shown in Fig. 32 for radius B of Section S47. The average value of the main peak was 1.562 ± 0.028 nm and of the second one 1.724 ± 0.89 nm, the first one corresponding to the full development of the 2-layer hydrate and the second one to the transition between the 2- and 3-layer hydrate. Overall, the ratio between the intensities of the main and the secondary peaks was higher for the drier samples, i.e. those closer to the heater, which would indicate a predominance of the 2-layer hydrate in these samples.

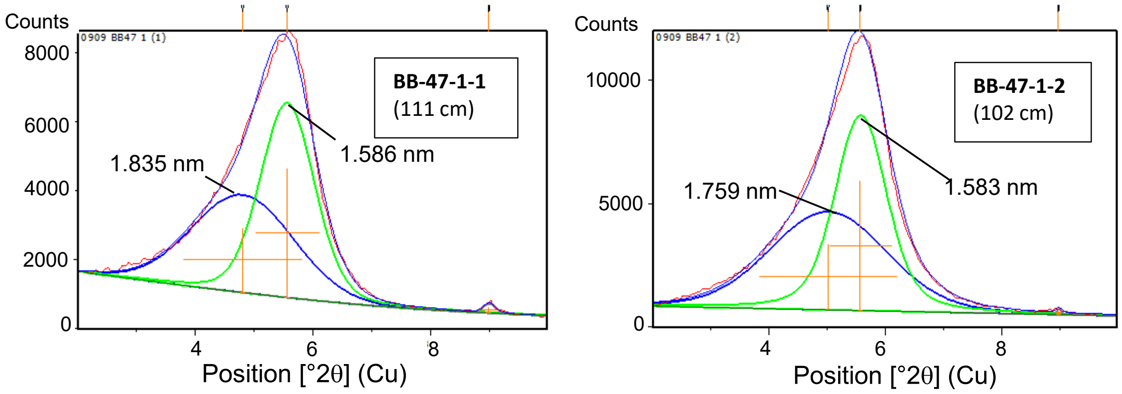

Fig. 32: Profile fitting of the XRD pattern of samples from radius B in Section S47 (Villar et al. 2018). The distance to the axis of the gallery is indicated in parentheses.

The values of the maximum intensity peaks have been plotted along with values obtained for the FEBEX bentonite saturated in different ways with deionised water (Villar et al. 2012, 2016b and other unpublished data) and are shown in Fig. 33. Most of them were samples obtained from compaction to a wide range of dry densities (from 1.1 to 1.75 g/cm^3) saturated either prior to compaction or afterwards. The values obtained for the FEBEX-DP samples for water contents below 27 % were similar to those measured in FEBEX bentonite samples of the same water content saturated with deionised water. For higher water contents, there is a larger dispersion, both among the samples from the dismantling and among the other FEBEX samples.

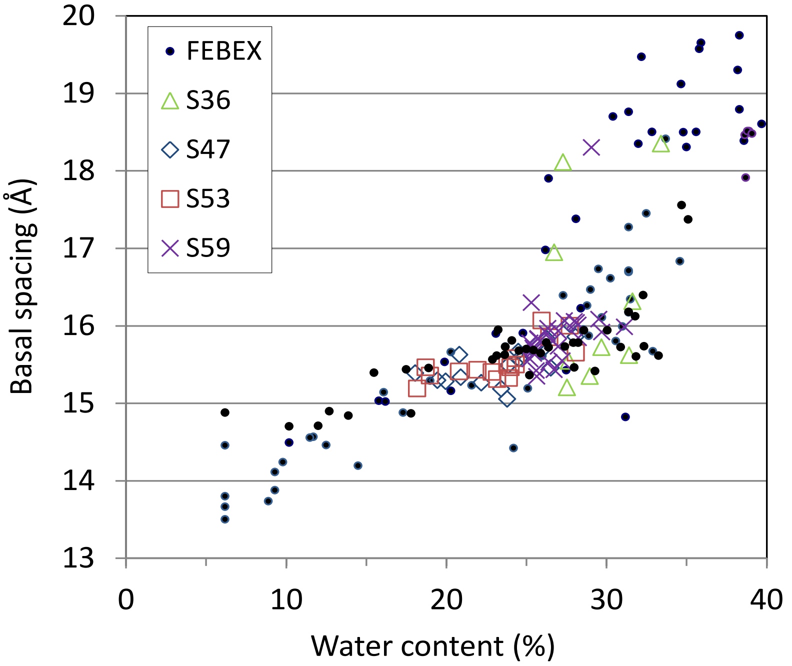

Fig. 33: Interlayer space of FEBEX samples saturated in different ways with deionised water (Villar et al. 2012, 2016b) and of samples from the FEBEX-DP.

4.3.2 Pore size distribution

The pore size distribution was determined by CIEMAT (S36, S47, S53, S59), UPC (S50, S57) and ETH (S46-S47, S61) using mercury intrusion porosimetry (MIP). This technique allows the determination of the pore size distribution by injecting mercury into the sample at different pressures while controlling the volume intruded. The pressure applied may be related to the minimum pore diameter intruded, taking into account the characteristics of the fluid (Washburn equation). The relationship between the volume of mercury intruded (pore volume) and the applied pressure (which conditions the minimum pore diameter) allows distribution curves to be obtained establishing the percentage of pores of a size included within a given range. Prior to testing, the water in the samples must be removed causing minimum disturbance to the shape and size of the pores (avoiding namely shrinkage). To accomplish this, freeze-drying/lyophilisation were used by the three laboratories.

The equipment used by CIEMAT and UPC could get access to pores between 540 µm and 7 nm, whereas the equipment used by ETH analysed pores between 120 µm and 4 nm. Hence, the mercury intrusion method allows access to be gained only to the macroporosity (pores of sizes between $5.4 \cdot 10^5$ and 50 nm) and to part of the mesopores (those of sizes between 50 and 7 nm, 50 and 4 nm in the case of ETH), since mercury does not intrude the microporosity (pores of a size of less than 2 nm, according to the classification of Sing et al. 1985). In the high-density clay materials retrieved from the FEBEX-DP, pores larger than those that can be quantified by MIP are not expected. However, the pores connected to the external surface by narrow openings will not be intruded until sufficient pressure is applied to intrude the entryways. All of the volume of such pores will be allocated to the threshold radius class of the most restricted part of the entryway (bottleneck effect). Nevertheless, considering that most of the non-intruded porosity corresponds to the pores of a size smaller than the limit of the apparatus, an estimation of the percentage of pores actually intruded can be made by comparing the actual void ratio of the samples (e, computed from their dry density and density of solid particles) and the apparent void ratio calculated from mercury intrusion (e_{nw}, mercury being a non-wetting ($_{nw}$) fluid).

CIEMAT analysed samples from eight blocks in Section S36, six samples along three radii in Sections S47 and S53 and nine samples along three radii in Section S59 (Villar et al. 2018). UPC analysed three samples along a radius in Sections S50 and S57 (Romero et al. 2017). ETH analysed samples along a radius in Section S46, and four samples in Section S61 (two close to the granite, one in the middle of the barrier and another one close to the heater). Fig. 34 shows the results obtained by CIEMAT in representative samples taken at three different distances from the axis of the gallery in a section around the heater (S47). The results are plotted in terms of pore size density function (PSD), which is defined as $f(\log \phi) = -d\, e_{nw}/d(\log \phi)$, where e_{nw} is the intruded void ratio (nw = non-wetting fluid) and ϕ is the diameter in nm. Since three radii were analysed there are triplicates for each distance. The results obtained for samples taken at the same distance from different radii agree very well. Fig. 35 and Fig. 36 show results for samples from sections around the heater analysed by UPC and ETH. ETH applied many small pressure steps during the tests and that is why the curves have a lot of noise, even though the values plotted are the moving averages of the data. The results obtained by the three groups showed two major pore families in all the samples consistently: a macropore family, with sizes between 10 and 60 µm, and a mesopore family, with sizes between 8 and 20 nm. Whereas CIEMAT and UPC's results showed no spatial changes in the mean pore size of the mesopores, ETH found an increase towards mean sizes between 10 and 60 nm in the samples taken closest to the granite, whereas the size of the macropores decreased.

For samples taken in cool Sections (S57, S59 and S61) the same results are plotted in Fig. 37 to Fig. 39. The same pore families described above could be observed. In this case, ETH's results reflected changes in the mode of the mesopore family along the barrier radii: samples taken at 60 cm from the axis of the gallery and some of the samples taken near the granite showed an increase in the size of the mesopores. In contrast, CIEMAT and UPC did not find changes in the mesopore size along the radii. The results of CIEMAT, and to a lesser extent those of UPC, showed a decrease in the percentage of macropores towards the gallery axis. CIEMAT's result also indicated the presence of a new pore family of larger size in the more saturated samples taken in the external part of the barrier.

From these results, the percentage of pores larger and smaller than a given size value can be computed, although the separate quantification of mesopores and micropores cannot be accurately done, because the limit of the two pore sizes is 2 nm, whereas the lower limit of the equipments is 7 or 4 nm. Hence, Fig. 40 and Fig. 41 show the percentage of macropores (> 50 nm) and of pores of diameter smaller than 50 nm (i.e. mesopores along with micropores) for samples taken in sections around the heater and in cool sections, respectively. The horizontal lines in the Figures indicate the average void-ratio percentages determined by CIEMAT in samples compacted at dry density 1.6 g/cm^3 with their hygroscopic water content, which represents approximately the original state of the blocks. In the original material 46 % of the void ratio corresponded to pores in the range of the macropore size.

The results for the cool sections showed an increase in the percentage of void ratio corresponding to pores smaller than 50 nm with respect to the reference material. The difference between the void-ratio percentage of pores larger and smaller than 50 nm increased on the whole from the granite towards the internal part of the barrier (40). In particular, there was an overall increase in the micropore void ratio and a significant decrease in the macropore void ratio with distance from the granite. It must be remembered that the total void ratio was higher for the samples from the external part of the barrier than for those in the internal part, because by the end of FEBEX operation, the dry density clearly increased with distance from the granite surface (see for example Fig. 15).

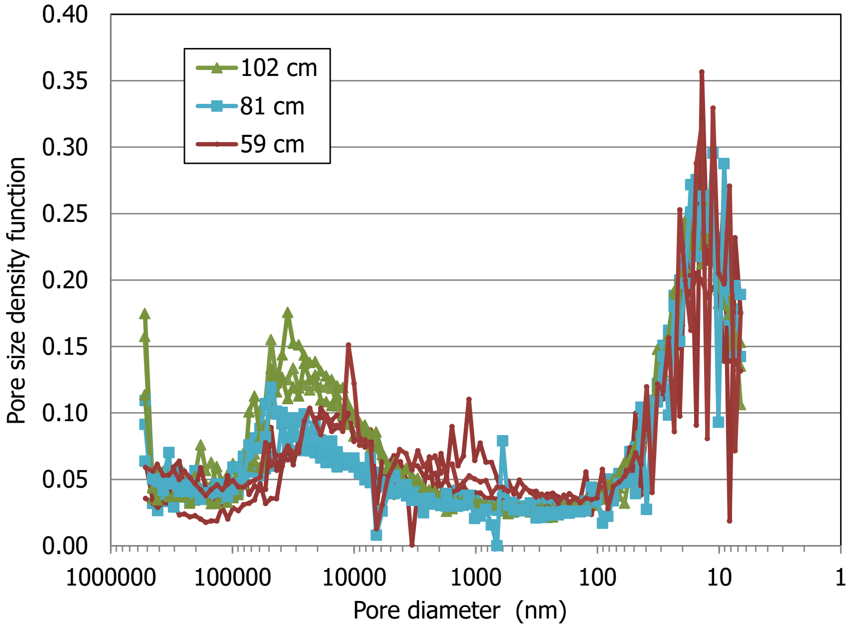

Fig. 34: Pore size density functions obtained with MIP by CIEMAT in samples of Section S47 taken at different distances from the gallery axis (section around the heater).

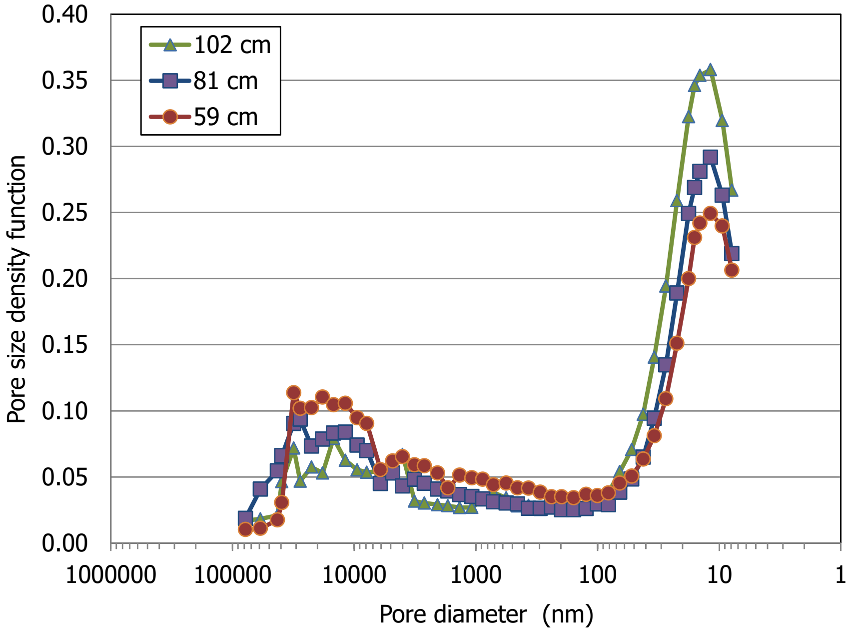

Fig. 35: Pore size density functions obtained with MIP by UPC in samples of Section S50 taken at different distances from the gallery axis (section around the heater).

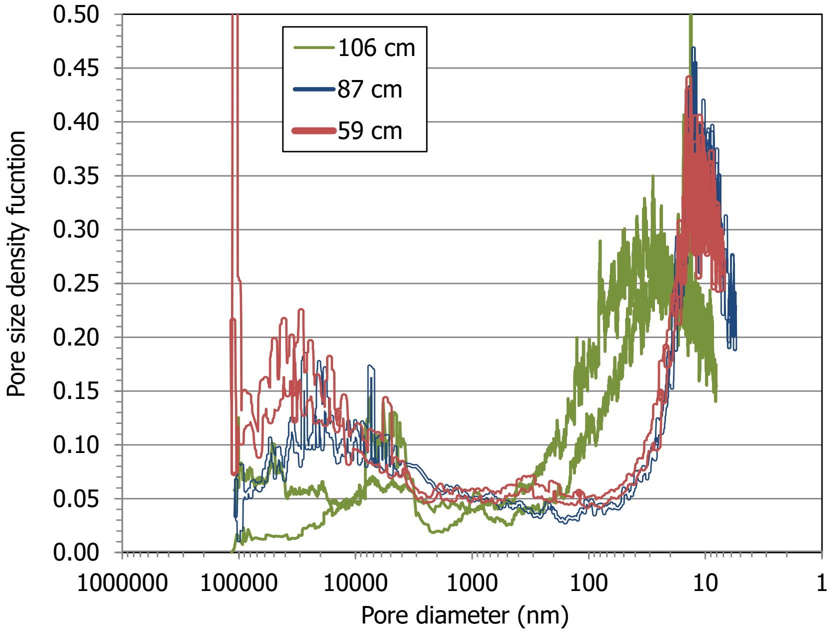

Fig. 36 Pore size density functions obtained with MIP by ETH in samples of Section S46 – S47 taken at different distances from the gallery axis (section around the heater).

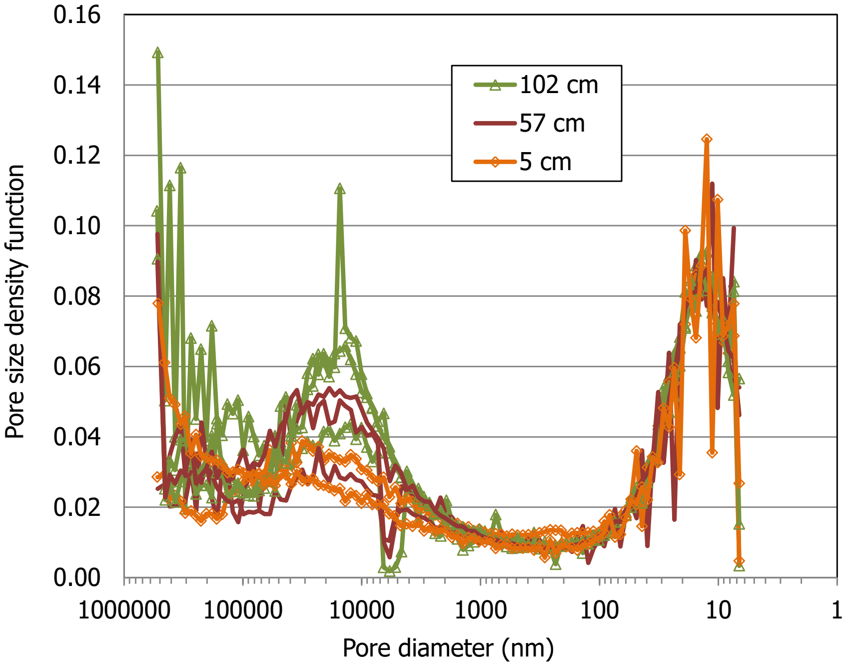

Fig. 37: Pore size density functions obtained with MIP by CIEMAT in samples of Section S59 taken at different distances from the gallery axis (cool section).

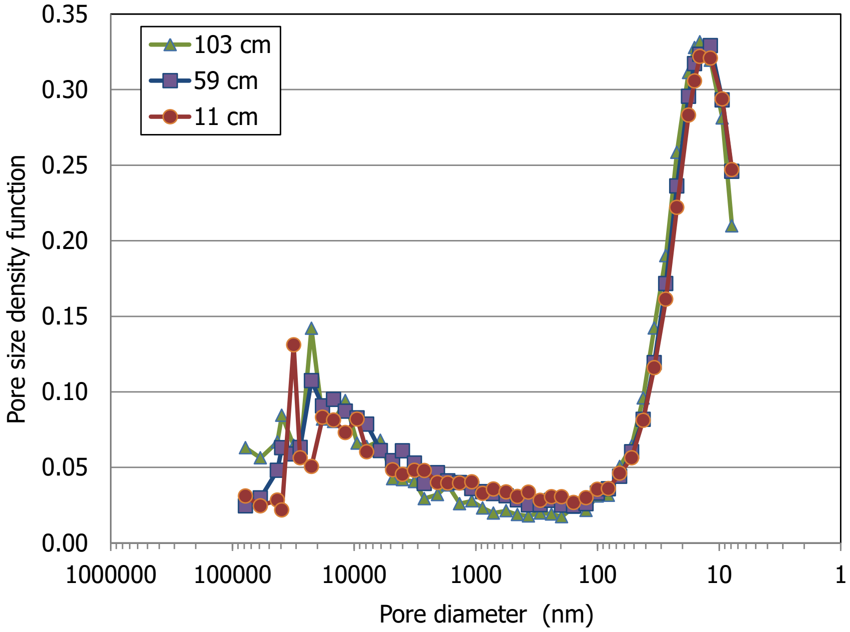

Fig. 38: Pore size density functions obtained with MIP by UPC in samples of Section S57 taken at different distances from the gallery axis (cool section).

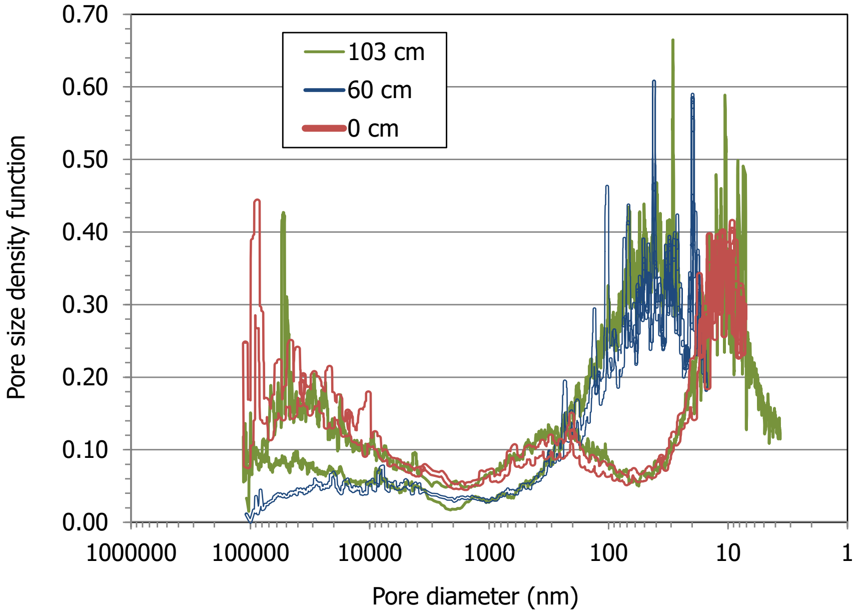

Fig. 39: Pore size density functions obtained with MIP by ETH in samples of Section S61 taken at different distances from the gallery axis (cool section).

In the sections around the heater the proportion of pores smaller than 50 nm also increased with respect to those in the reference sample, while the proportion of pores larger than 50 nm decreased. In fact, more than 65 % of the void ratio corresponded to pores smaller than 50 nm in the end-of-test samples (Fig. 41). This would point to the homogenisation of the pore sizes during operation, with average size decreasing. Close to the heater there was a small relative increase in the macropore void ratio, maybe as a consequence of drying.

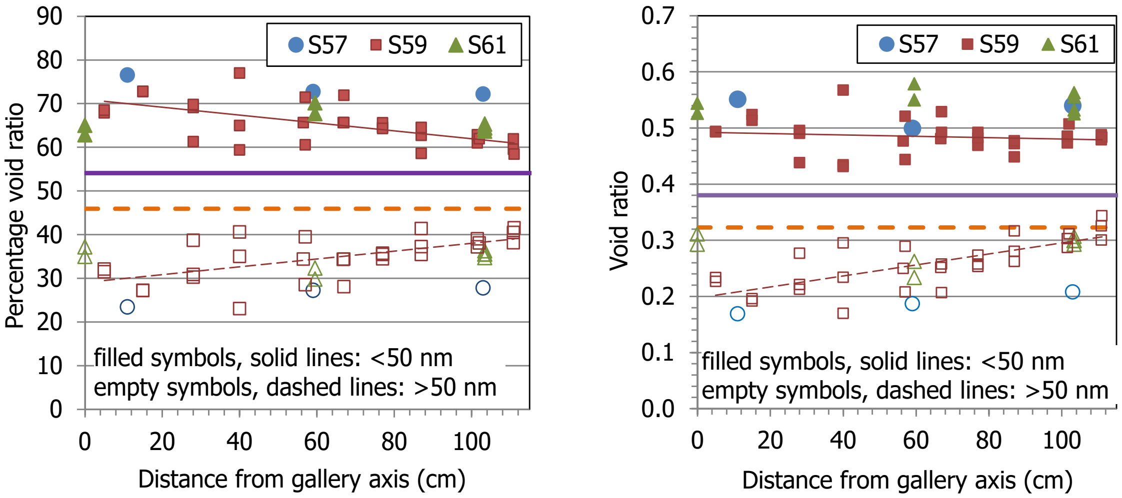

Fig. 40: Distribution of void ratio in samples of Sections S57 (UPC), S59 (CIEMAT) and S61 (ETH). The thick horizontal lines indicate the values for the reference FEBEX compacted at 1.6 g/cm^3 with 14 % water content as determined by CIEMAT.

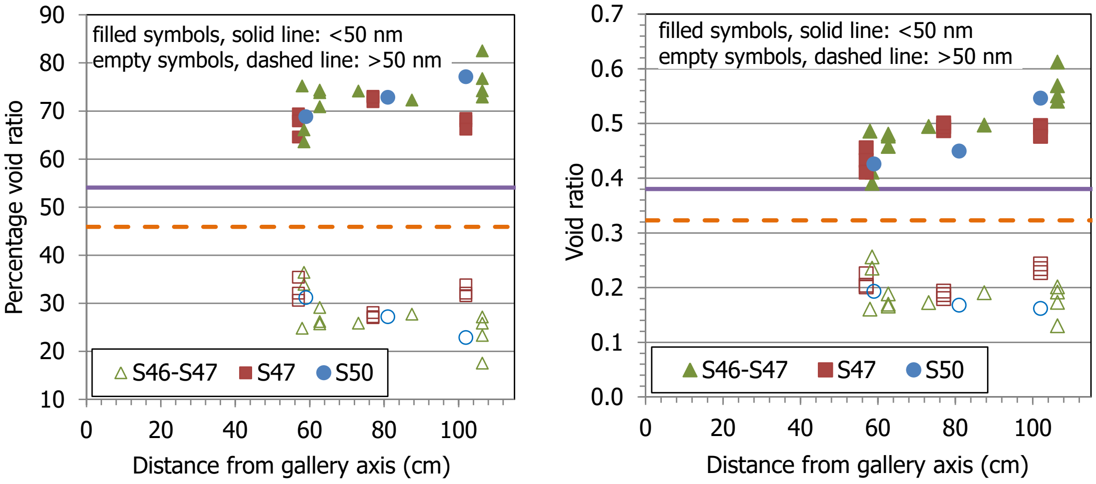

Fig. 41: Distribution of void ratio in samples of Sections S46 – S47 (ETH), S47 (CIEMAT) and S50 (UPC). The thick horizontal lines indicate the values for the reference FEBEX compacted at 1.6 g/cm^3 with 14 % water content as determined by CIEMAT.

There was also a systematic increase in the diameter mode of the macropores and the mesopores with respect to the reference material recorded by the three laboratories (according to CIEMAT's measurements, the macropore mode size of the reference material was 17 ± 3 µm and the mesopore mode size 9 ± 2 nm). This was probably related to the overall decrease in the bentonite dry density (from the initial block dry density of 1.7 g/cm^3), which gave place to a more open structure.

The percentage of mesopores and micropores (diameter < 50 nm) as a whole increased over the course of the experiment and the average size of the mesopores (diameter 50 – 7 nm) increased. Consequently, it is assumed that the hydration occurring during operation also brought about an increase in the percentage of micropores, i.e. those that cannot be intruded by mercury. These conclusions are consistent with the average increase in basal spacing reported in the previous section.

4.4 Surface properties

4.4.1 Specific surface area

The external specific surface area (a_s) of the bentonite samples was determined by CIEMAT, ETH and UAM using the BET method (Brunauer et al. 1938) to analyse the adsorption isotherms of nitrogen gas. This parameter represents the external surface, i.e. the surface of the intra-aggregate and inter-aggregate voids but not that of the interlayer space. Thus, it is a measure of the available area for solute transport in the compacted bentonite and of the degree of coherent stacking of smectite platelets (Sposito 1992).

- ETH determined the a_s of bulk samples of 0.3 – 0.7 g that were ground to < 400 µm particle size. The 11-point method in the range of P/P_0 relative pressure 0.05 – 0.3 was used. The samples were previously degassed for 15 h at 150 °C under vacuum of 0.2 mbar.
- UAM performed the analyses on a bulk sample ground to < 5 µm. Samples of 0.2 g were degassed by heating to 90 °C for 18 hours prior to analysis, which consisted in determining an isotherm of five points (0.05 – 0.25 P/P_0 relative pressure).
- CIEMAT did not grind the samples, which were lyophilised prior to degassing. Samples of between 0.8 and 1.8 g were degassed at 90 °C during a time period necessary to reach a vacuum of 0.07 mbar, which was kept for 10 min. Afterwards the samples were kept at 90 °C under vacuum for 8 h. The isotherms obtained had 32 points in the range of relative pressures between 0.01 and 0.995 and 23 points in the range 0.995 and 0.14. The BET method was applied in the range of P/P_0 0.06 – 0.2.

The samples analysed by ETH were taken from Sections S46 – S47 and S61; the samples analysed by UAM were taken along one radius in Section S45; and those analysed by CIEMAT were taken along one radius in Sections S36, S47, S53 and S59. The results obtained by all the laboratories are shown in Fig. 42. This Figure also shows the value for the reference untreated bentonite as determined by two laboratories. The reference values found by the two laboratories were similar (55 – 56 m^2/g). UAM and ETH found values close to the reference one in the samples located in cold sections and in the external part of the barrier in sections around the heater. However, in the 15 cm closest to the heater, a decrease in surface area was detected, to values as low as 22 m^2/g. This effect was observed repeatedly in experiments conducted with FEBEX bentonite under thermal gradients (Cuevas et al. 2002, Villar et al. 2008) and was attributed to aggregation of smectite particles under shrinkage induced by the initial thermal impact. Lower values of a_s were also found in samples taken close to the heater during the first dismantling (Villar et al. 2006).

The values found by CIEMAT in the proximity to the granite were higher than the reference one in the four sections analysed, and then tended to decrease towards the internal part of the barrier. The decrease recorded was not as sharp as that found by UAM and ETH, maybe because no samples at less than 17 cm to the heater were analysed. In the cool Section S59 the specific surface area was slightly higher than the reference one, particularly in the external part of the barrier (approximately the 30 cm closest to the granite), where it was noticeably higher. Hence, it seems the specific surface area was related to the water content the samples had before being analysed. This becomes clear in Fig. 43, where the specific surface area values have been plotted as a function of water content of the samples after dismantling. The samples with water content values above 22 % had specific surface areas that in the case of CIEMAT increased slightly with water content but kept in the same range as observed for the reference material. All the samples analysed by CIEMAT were in this water content range, and they had on average an a_s -value 7 % higher than the reference value. However, for water content values below this value the a_s decreased sharply to very low values as water content decreased. It is remarkable that the values obtained by the three laboratories were so similar, given that the way in which the samples were prepared was not the same and this is known to affect the results.

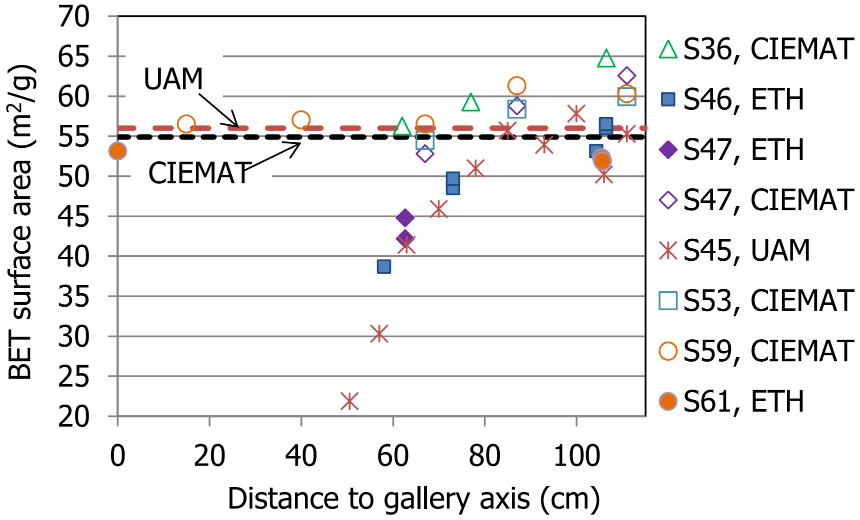

Fig. 42: BET specific surface area measured by CIEMAT, ETH and UAM in samples taken from different sections (the dashed lines indicate the values for the reference sample as determined by two CIEMAT and UAM).

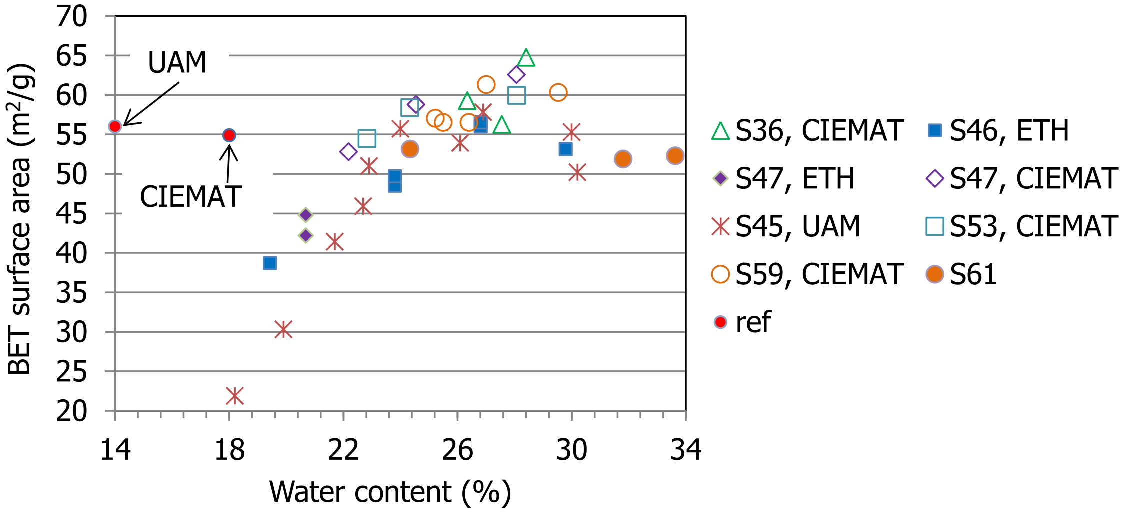

Fig. 43: BET specific surface area measured by CIEMAT, ETH and UAM in samples taken from different sections as a function of their initial water content.

In addition to the external specific surface area discussed above, CIEMAT and ETH determined the total specific surface area, which is a parameter related to the water absorption and swelling capacity of bentonite. It determines the amount of water needed for hydrating all the clay particles. In contrast to nitrogen, which is only adsorbed on the external surface of the stacks of the layers, water molecules can be adsorbed on the whole surface, including both the internal (interlayer) and external surfaces of the clay minerals. The amount of adsorbed water at the interlayers depends on the type of adsorbed cations.

CIEMAT determined this parameter by means of the Keeling's hygroscopic method (Keeling 1961, Keeling et al. 1980) at relative humidity 75 % in samples taken along three radii in Sections S47, S53 and S59 and along two radii in Section S36. ETH used the same method. The results obtained by CIEMAT are plotted in Fig. 44. All the values were below the total specific surface area of the reference sample (which was determined at the same time as the other samples), and there was a slight trend for the total a_s to decrease towards the axis of the gallery, although the dispersion was large, even amongst radii of the same section. ETH analysed two samples from Section S46 and two other from Section S61 and the values obtained for all of them were alike, with an average of 666 ± 6 m^2/g.

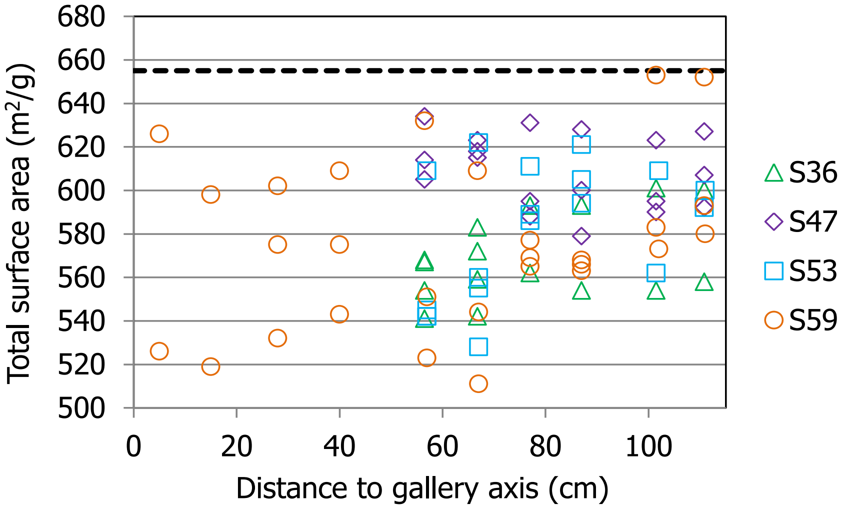

Fig. 44: Total specific surface area measured by CIEMAT in samples taken along different radii of different sections (the dashed line indicates the values for the reference sample).

Additionally, ETH determined the water uptake capacity of three samples from Section S46 and one sample from Section S61 using the Enslin-Neff method (DIN 18312), which gives an indication of the exchangeable sodium content, and hence of plasticity and swelling capacity. The values obtained for the external part of the barrier were in the order of those found by other authors for Ca/Mg bentonites (Kaufhold & Dohrmann 2008) and decreased clearly towards the heater (Fig. 45). This decrease would agree with the decrease in exchangeable sodium reported in Section 5.4.

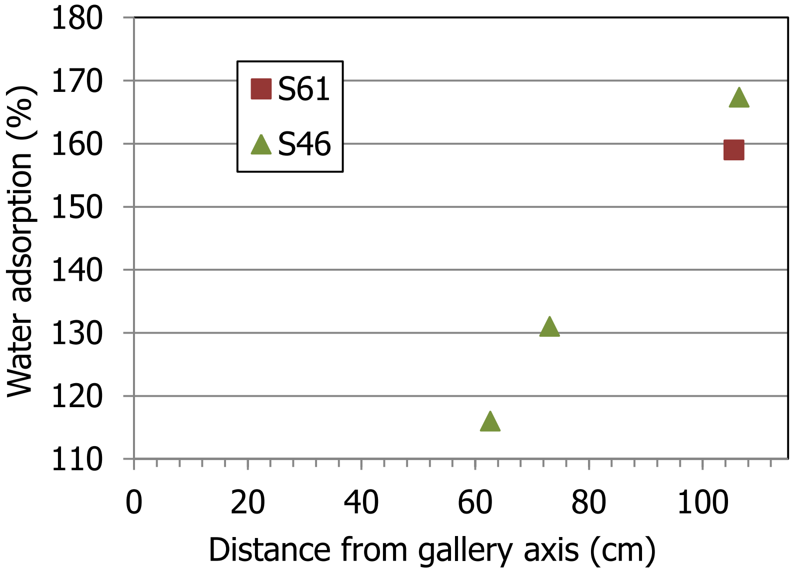

Fig. 45: Water adsorption capacity measured by ETH with the Enslin-Neff method.

4.4.2 Suction measurement on blocks

The relative humidity and temperature of the bentonite was measured at CIEMAT either with thermocouple psychrometers or with capacitive sensors, depending on the bentonite water content. Psychrometers were used for the highest relative humidities (lower suctions) and capacitive sensors had to be used when suction was higher than 7 MPa. The measurements were performed before unpacking the blocks by inserting the sensors in holes of the appropriate size previously drilled in the bentonite (Fig. 46, left). The relative humidity values were converted to suction using Kelvin's law. UPC used a dew point psychrometer in the total suction range from 1 to 100 MPa. In this case, a small sample (4 cm in diameter and 1 cm high) trimmed from the block was placed in a round cup which was set in the equipment chamber (Fig. 46, right). After about 5 minutes, the final water potential reading was directly shown.

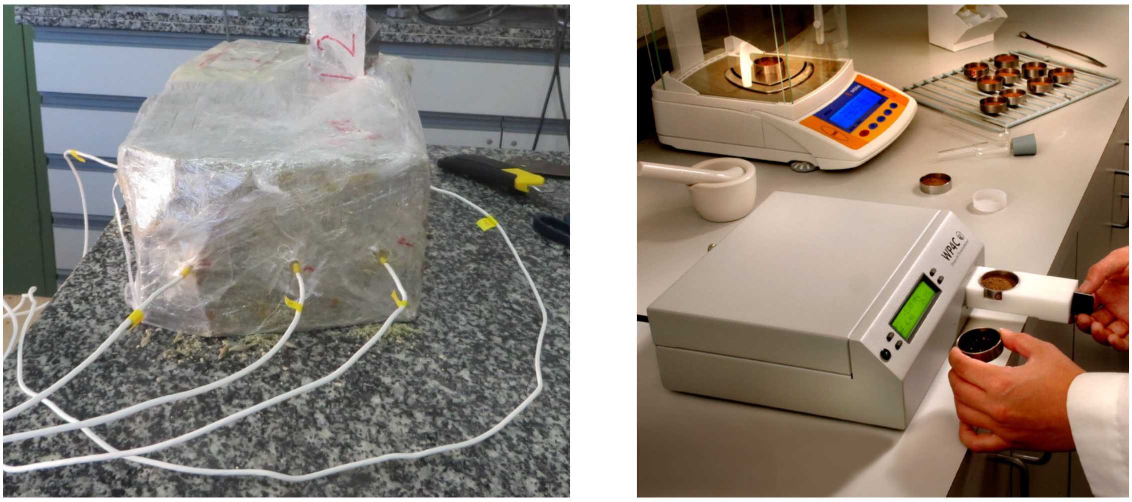

Fig. 46: Psychrometers inserted into a block prior to unpacking (CIEMAT, left) and sample placed in the dew point psychrometer (UPC, right).

The suction values obtained by the two laboratories are plotted in Fig. 47 as a function of the position in the barrier, indicated as distance to the gallery axis. The three sections around the heater (S47, S50 and S53) showed a clear increase of suction from the external part of the barrier towards the heater. In fact, capacitive sensors had to be used at CIEMAT to measure the suction in the two internal rings of the barrier, because it was above the range suitable for psychrometers. Although the suctions were much lower, they also increased from the external part of the barrier towards the internal one in S36.

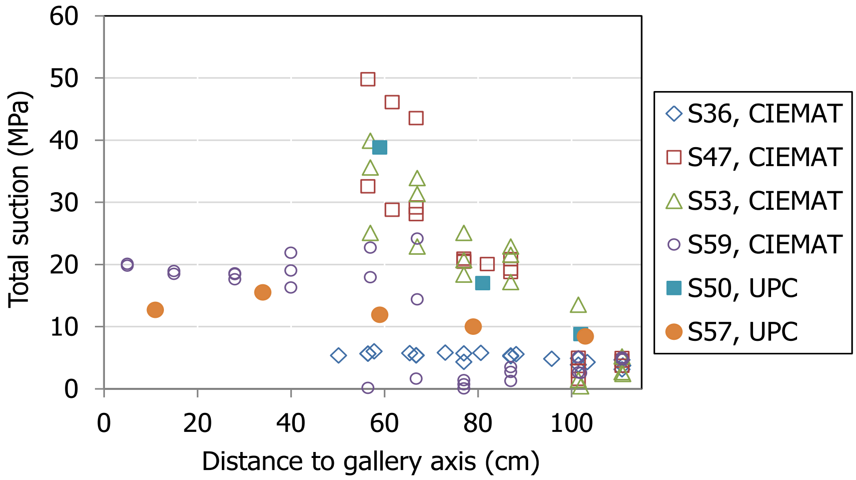

Fig. 47: Total suction values measured in blocks from different sampling sections at CIEMAT and UPC.

The suction values measured in the laboratory are plotted versus the degree of saturation determined in the same blocks and in the same position in Fig. 48 as water retention curves (WRC). For degrees of saturation lower than approximately 95 % (i.e. for suctions above 10 MPa), suction decreased lineally as degree of saturation increased. Nevertheless, suction did not vanish when approaching full saturation. This remaining total suction was mainly a consequence of the block retrieval operation (undrained unloading). The relationship between suction and degree of saturation for the lowest suctions (those below 7 MPa) does not seem clear in these Figures. To analyse the lower suction range, the values were grouped according to the dry density of the samples in Fig. 49 (Villar et al. 2018). The relationship between suction and water content or degree of saturation for suctions below 7 MPa (those measured with psychrometers) was basically dependent on dry density: the higher the dry density the lower the water content for a given suction, because samples of lower density have higher porosity. However, in terms of degree of saturation, the effect of density on the WRC was not noticeable. The coherence between the results obtained by the two laboratories is highlighted in these figures.

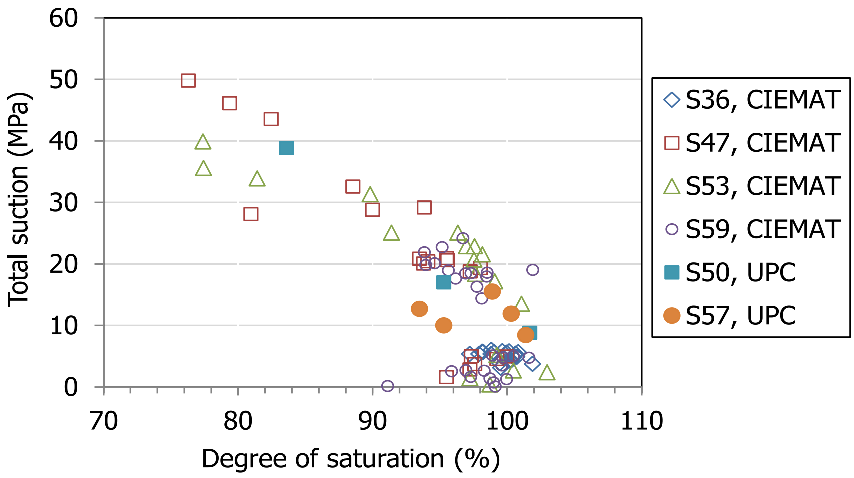

Fig. 48: Relationship between suction and degree of saturation (or water content) in the blocks sampled at CIEMAT's laboratory.

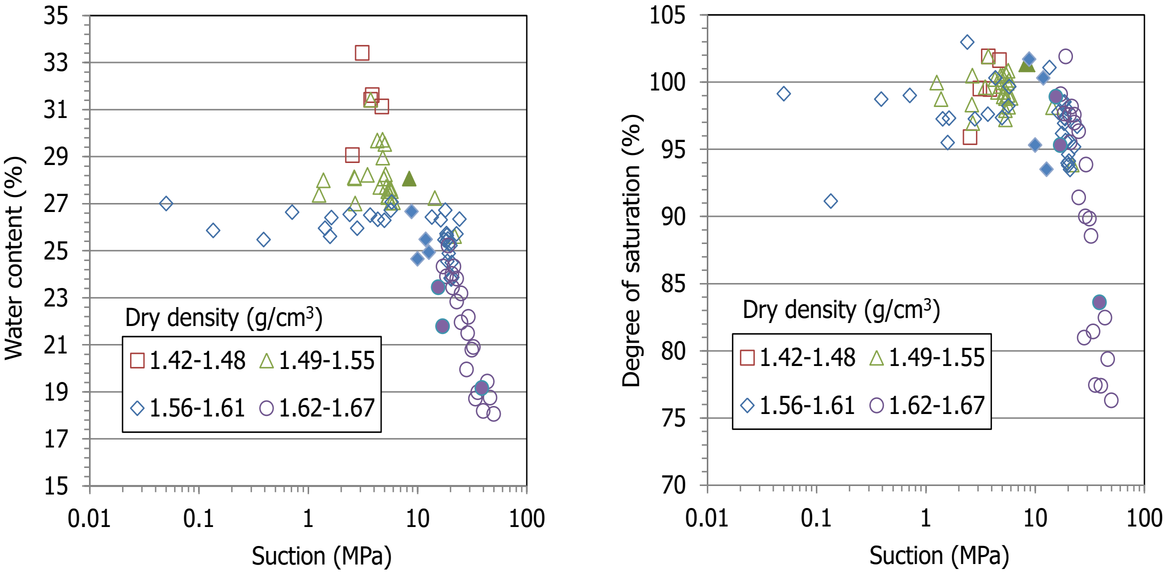

Fig. 49: Relationship between suction measured and water content and degree of saturation in the blocks sampled at CIEMAT (empty symbols) and UPC (filled symbols).

Fig. 50 shows all the results, along with the water retention curve for the FEBEX reference bentonite obtained previously using several methods for the same density as the average dry density of the barrier (1.6 g/cm^3). During operation, the bentonite blocks were exposed to high temperatures, and consequently the suction pressures during operation could have been lower than those measured in the laboratory. On the other hand, the samples retrieved experienced relaxation during dismantling and this possibly increased their suction, because of the changes in porosity. Nevertheless, the comparison of the WRC of the blocks retrieved with that of the reference material points to the preservation of the water retention capacity during operation (Villar et al. 2018), which agrees with the results of the water sorption isotherms (4.4.2) and interlayer space (4.3.1).

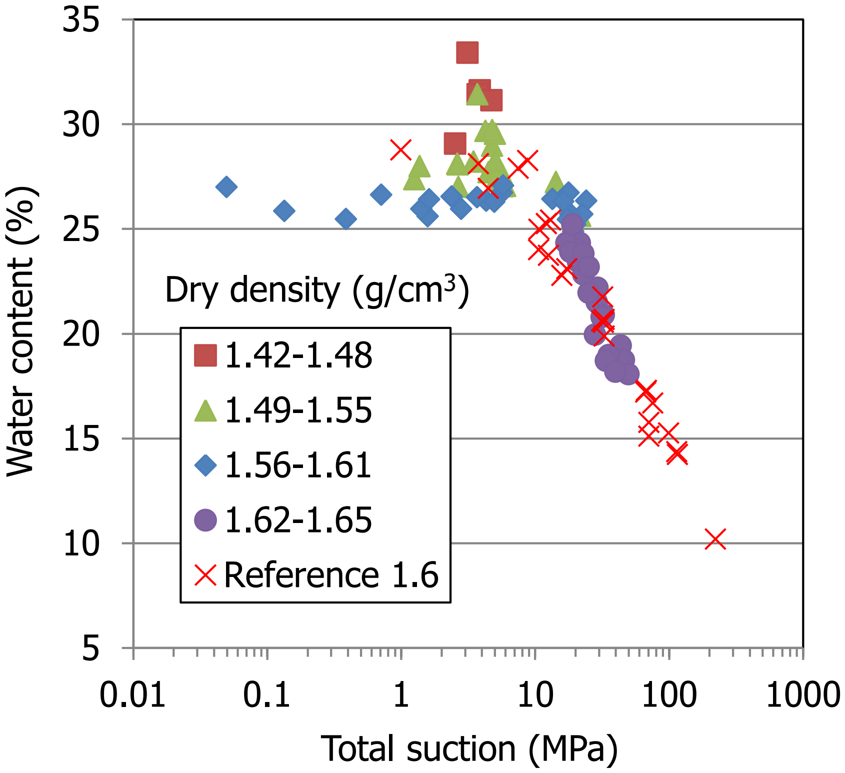

Fig. 50: Water retention curve of samples from the FEBEX-DP experiment determined with sensors and of the reference FEBEX bentonite determined with the vapour transfer technique and capacitive sensors (crosses).

4.4.3 Water adsorption isotherms

CIEMAT and ClayTech determined the water sorption isotherms of ground samples using the vapour transfer technique, a simple diffusion static method. From each sample different subsamples were obtained, and each of them was introduced in a hermetic glass container (CIEMAT used desiccators and ClayTech used jars) in which a salt solution generated a given relative humidity (RH). The bentonite sample exchanged water with the container atmosphere until equilibrium between both was reached. Thus, the relation between different water potentials (given by the relative humidity or partial vapour pressure in the container, P/P_0=RH/100) and sample water content was determined, and with the pairs of points obtained the water sorption isotherm could be defined. The range of relative humidity explored by ClayTech was from 0 to 97 % and by CIEMAT from 9 to 99 %. The temperature during the determinations was 25 °C for ClayTech and 21 °C for CIEMAT.

Three samples taken along a radius of Sections S36, S47, S53 and S59 and the FEBEX reference were tested by CIEMAT in 1-g duplicates after grinding the bentonite and drying to 105 °C. ClayTech tested 7-g ground samples. One of them was from a block of the inner ring in Section S47 (BB47-12), taken at a distance of 49 cm from the axis of the gallery, with its original water content (16 %). Three others were samples from the reference bentonite (taken from a block compacted in 1996 along with those installed in the in-situ test), one with hygroscopic water content (14 %), another one which was wetted (initial w = 62 %) and another one which was dried (initial w = 1 %). The samples were left to equilibrate for between one and three months (2 months for most samples) by CIEMAT and for 72 days by ClayTech, although for most samples equilibrium was reached earlier, after approximately 40 days.

Fig. 51 shows the results obtained by ClayTech. The curves for the reference material show the expected hysteresis: the water content values reached during drying (i.e. for the sample with initial water content 62 %) were higher than those obtained during wetting (sample with initial water content 1 %), whereas the sample with hygroscopic initial water content (14 %) reached, for a given relative humidity, an intermediate water content. The sample retrieved from the barrier, which had an initial water content of 16 %, reached consistent water content values that were between the wetting and the drying branches of the isotherms. Thus, for the relative humidities that dried the sample the water content values were close to those of the drying branch of the reference bentonite, while for relative humidities higher than 60 % (implying increase in water content), the equilibrium water content values approached those of the wetting branch of the reference bentonite. For the highest relative humidities (i.e. lowest suctions) the water content taken by the sample from the inner ring of the barrier was considerably higher than that reached by the reference samples.

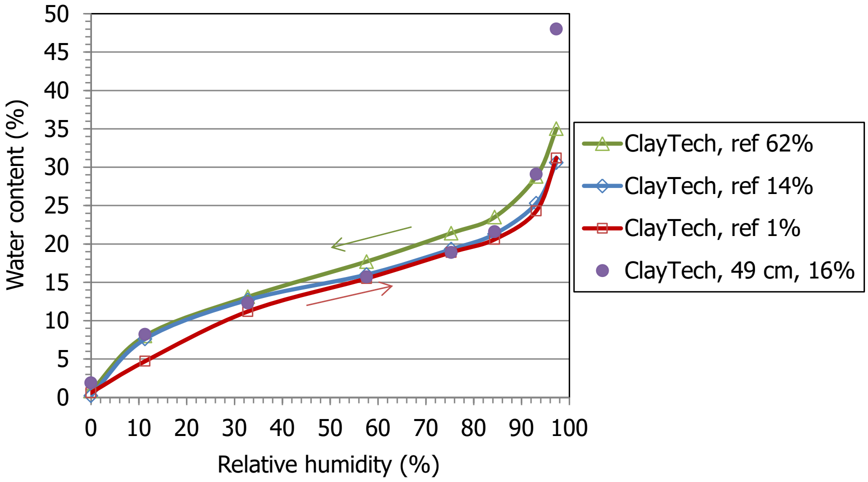

Fig. 51: Water adsorption isotherms determined by ClayTech in ground specimens of the reference FEBEX bentonite and of a sample taken close to the liner in Section S47.

The initial water content values are indicated in the legend.

The results obtained by CIEMAT for the retrieved and the reference samples are shown in Fig. 52. The water adsorption capacity was similar for all the samples, it seemed to be independent of the position of the sample along the radius and similar values were also found for the four sections sampled. These values followed the same trend as the reference sample.

The results shown above indicate that the water sorption capacity of the bentonite was preserved during operation.

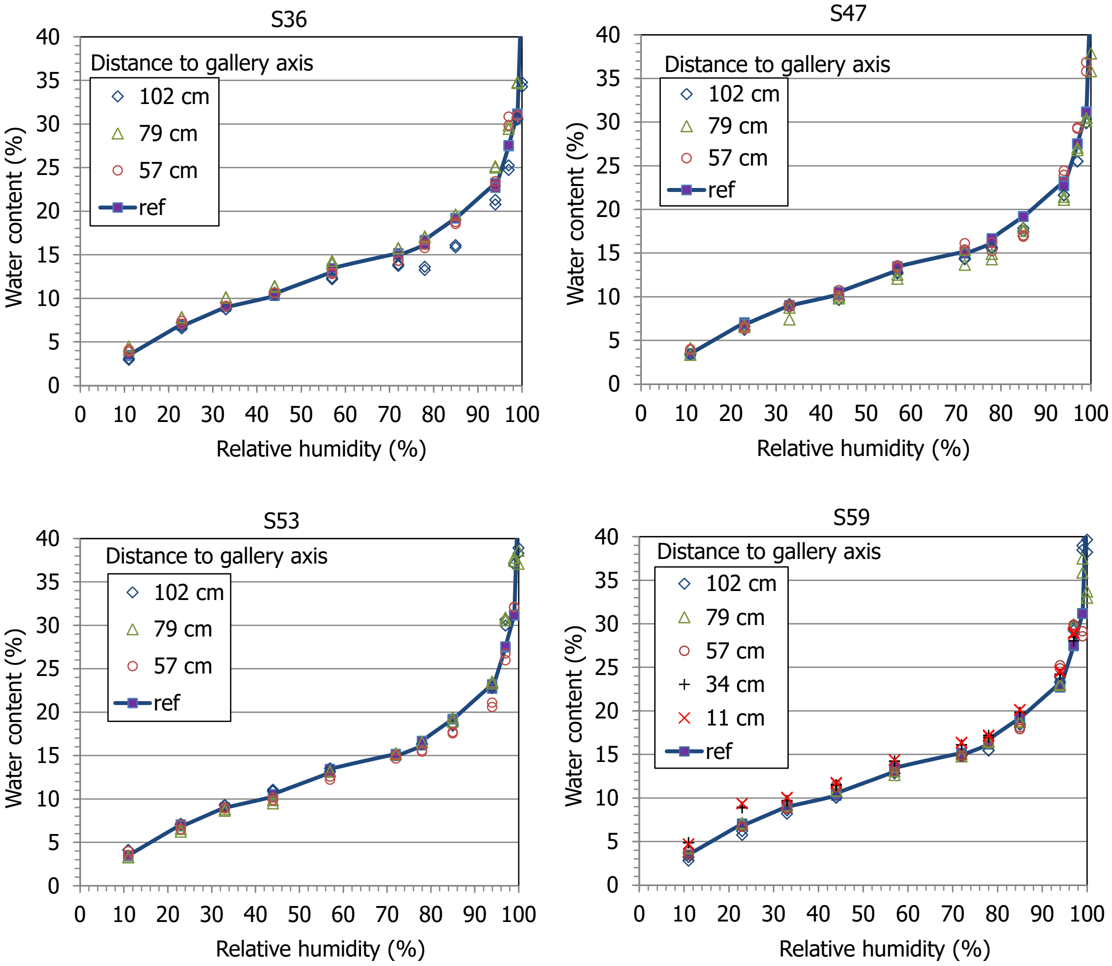

Fig. 52: Water adsorption isotherms determined by CIEMAT in ground and dried specimens taken along a radius of different sampling sections and of the reference FEBEX bentonite.

5 Mineralogical and geochemical characterisation

CIEMAT, BGR, UAM and ETH performed the mineralogical and geochemical characterisation of the samples retrieved.

- CIEMAT analysed samples along three radii of Section S36, in contact with the shotcrete plug, of Sections S47 and S53 around the heater and along three radii of Section S59 in the cool area at the back of the gallery. The samples were obtained from the blocks sent to CIEMAT facilities.
- BGR analysed samples from the sections around the heater S42, S45, S48, S50 and S53.
- UAM analysed ten cores taken on-site along a radius of Section S45 around the heater. About 50 – 100 g of each core were disaggregated and kept stored in polypropylene bottles to be used for the different determinations.
- ETH analysed core samples drilled across the sections around the heater S46 and S47. These cores were taken at the same time and exactly the same position in the two sections, hence they have been considered as the same set of samples, S46-S47. Cores taken in Section S61 were also analysed.
- SÚRAO analysed the cation exchange capacity of a sample from Section S36.

5.1 Mineralogy

The mineralogical characterisation of the samples retrieved was carried out by:

- CIEMAT in samples from Sections S36, S47, S53 and S59
- ETH, in samples from Section S46-S47 and S61
- UAM, in samples from Section S45

The three laboratories used X-ray diffraction as main analysis technique, but CIEMAT and ETH used a combination of other techniques to refine the results, since the accuracy of X-ray diffraction, which gives mineral weight percentages, is below 5 %.

5.1.1 X-ray diffraction

X-ray diffraction (XRD) analyses were carried out by CIEMAT, UAM and ETH to identify and quantify the mineralogical composition of the ground bulk material (air-dried in the case of CIEMAT and dried at 60 °C in the case of UAM and ETH).

The retrieved bentonite samples contained smectite (82 – 96 %, depending on the sample and laboratory) as their major mineral phase, the same as the reference sample, whose smectite content is, according to CIEMAT's determinations, 92 ± 4 % (UAM determined a smectite content for the reference sample of 94 ± 1 %). Other minerals appearing systematically in all the samples were K-feldspars, quartz, cristobalite, calcite and plagioclase, all of them in proportions lower than 5 %. These are also the minerals composing the reference bentonite, and from that point of view it can be said that the overall mineralogical composition of the bentonite did not change during operation. Fig. 53 shows an example of the XRD patterns determined by CIEMAT in the FEBEX reference sample and in some retrieved samples. ETH found also contents of illite around 3 % in all the samples, whereas UAM found traces of illite in the reference sample and in those samples taken at less than 30 cm from the granite. UAM found albite in the samples closest to the heater. CIEMAT identified dolomite and iron sulphides in a few samples, without a clear spatial pattern.

Fig. 54 and Fig. 55 show the smectite content in samples taken from sections around the heater and in cooler areas, respectively. The changes in the smectite content of the samples did not seem to follow any particular spatial trend, except in the samples of Sections S46 – S47 analysed by ETH, where smectite content seemed to increase slightly towards the heater. Also, the contents measured by ETH were lower overall than those determined by the other laboratories. The smectite had a basal spacing around 1.5 nm, typical of a predominantly divalent montmorillonite. The fact that the interlayer was occupied by various cations gave rise to a broadening of the (002) reflection, which was also observed in the reference material.

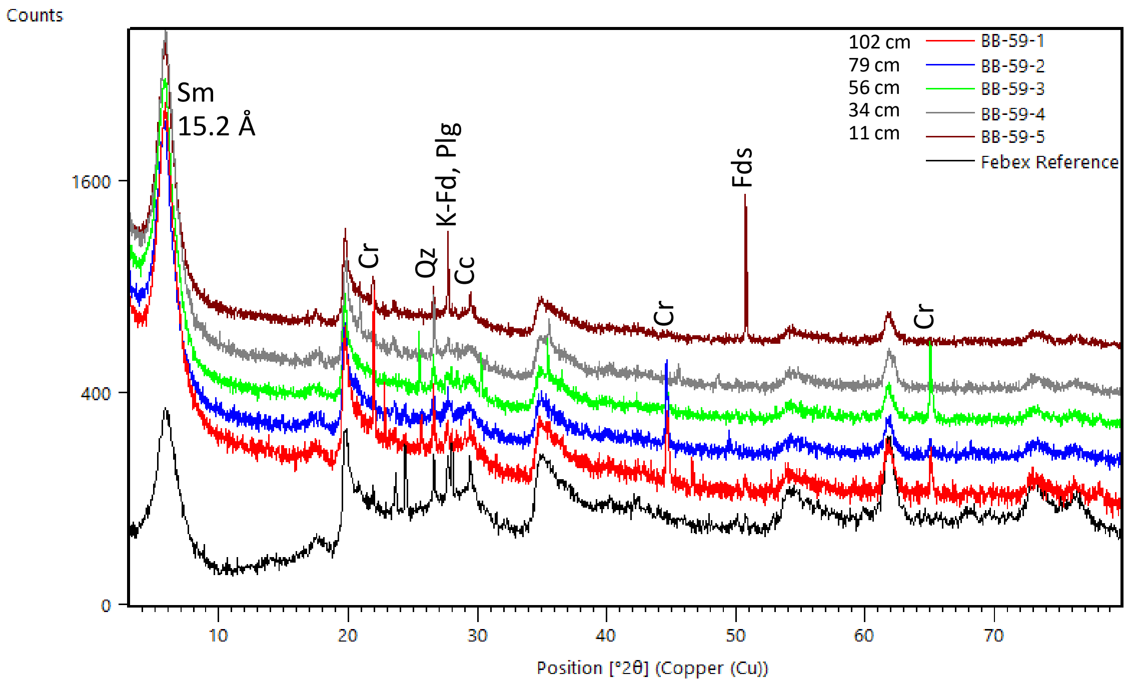

Fig. 53: XRD patterns of randomly oriented bulk bentonite samples of Section S59 (the distances from gallery axis are indicated in the legend) and of the reference bentonite obtained by CIEMAT (Sm: smectite, Cr: cristobalite, Qz: quartz, K-Fd: K-feldspars, Plg: plagioclase, Cc: calcite).

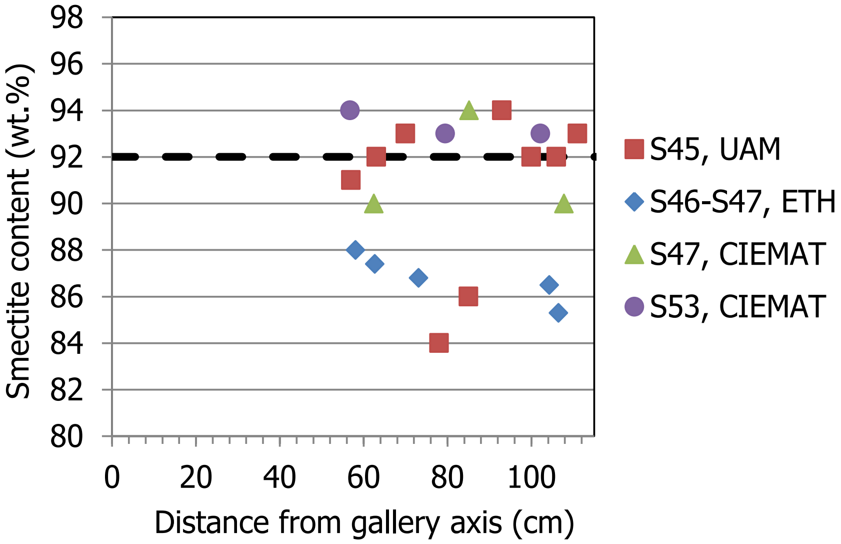

Fig. 54: Smectite content in samples from different sections around the heater determined by X-ray diffraction by different laboratories.

The dashed line indicates the content in the reference sample as determined by CIEMAT.

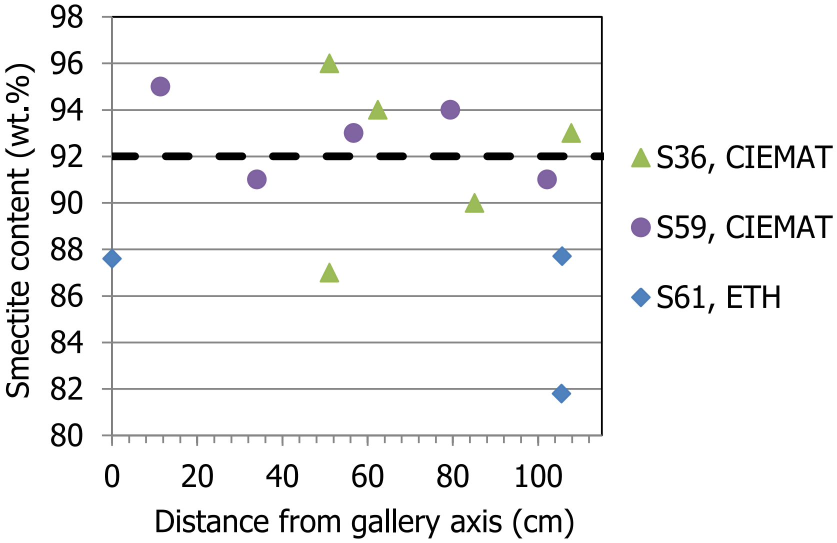

Fig. 55: Smectite content in samples from cool sections determined by X-ray diffraction by different laboratories. The dashed line indicates the content in the reference sample as determined by CIEMAT.

The samples of the fraction with grain sizes less than 2 µm was obtained by suspension and sedimentation in deionised water. CIEMAT prepared three oriented-aggregate specimens from each sample: air-dried, solvated with ethylene glycol (EG) and heated at 550 °C. Illite/smectite mixed-layers were identified according to the method of Moore & Reynols (1989) on the EG patterns, and the crystal thickness of the smectite particles was determined by the Williamson & Hall (1953) method. UAM prepared air-dried and EG oriented-aggregate specimens from samples previously homoionised with calcium or potassium. The basal reflections were treated using the

DRXWin® software. The diffraction peak positions were estimated using a deconvolution algorithm based on Pseudo-Voigt functions. The presence of collapsed smectite phases in K-homoionic high-charged montmorillonite was calculated with the Plançon & Drits (2000) (MLM "STRUCMIX") software for a hypothetical mica-di-smectite mixed layer mineral (Plançon 2013), using the Watanabe diagram (Tomita et al. 1988).

CIEMAT's analysis of the oriented-aggregate specimens showed that the smectite phases were made up of a R0 smectite-illite mixed-layer (R0 meaning that the layering was disordered), with 5 – 23 % of illite layers, although most samples had between 5 and 13 %. The main basal reflection, (001), at around 1.46 nm for all the samples indicated the Ca-Mg character of the smectite particles, and the *d*001 value at around 1.7 nm in the EG patterns showed the complete expansion of the interlayer. As an example, Fig. 56 and Fig. 57 show the results of air-dried and glycolated oriented-aggregate specimens for samples from Section S53. The crystal thickness of the smectite particles ranged between 7.65 and 10.31 nm, the number of 2 : 1 (TOT) layers in the quasicrystals being of 5 – 6. This is in agreement with previous analyses of the reference FEBEX bentonite (Fernández et al. 2004, Enresa 2006) in which the same cell dimensions of the montmorillonite particles as in the retrieved samples were measured.

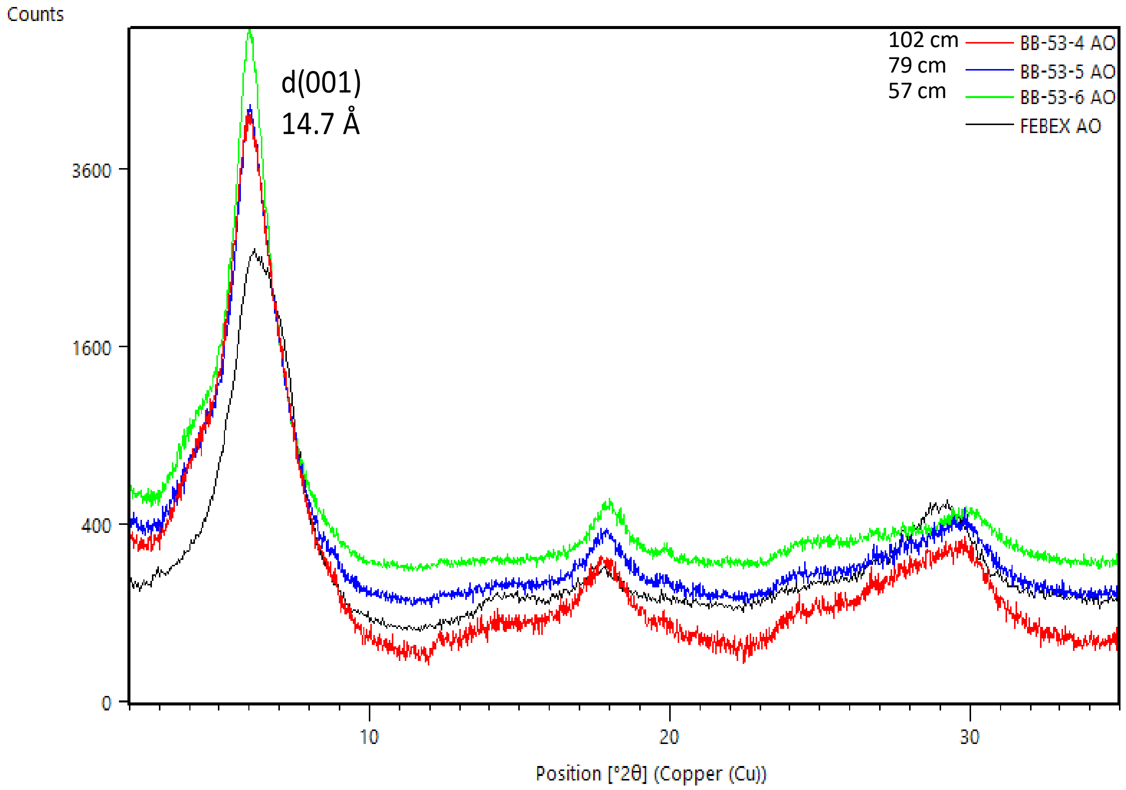

Fig. 56: XRD patterns of oriented-aggregate (AO) mounts of bentonite samples from Section S53 (the distances from gallery axis are indicated in the legend) and of the reference bentonite obtained by CIEMAT.

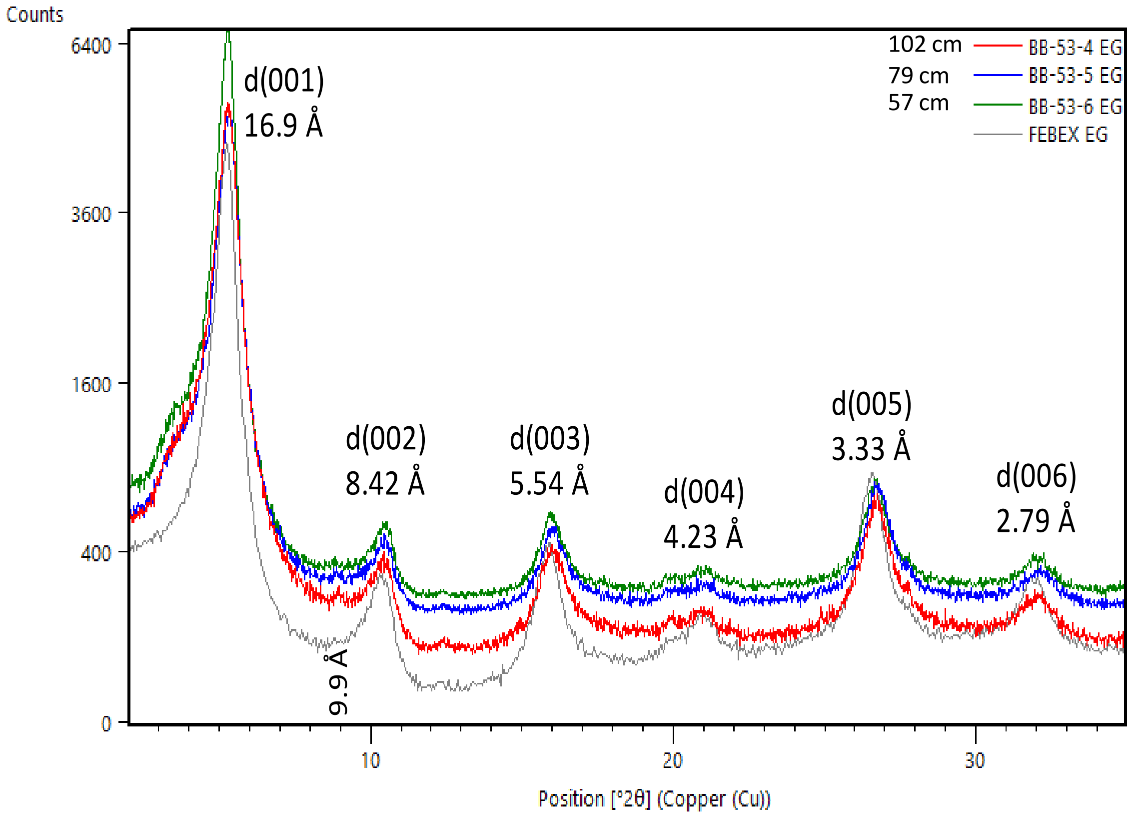

Fig. 57: XRD patterns of EG oriented-aggregate mounts of bentonite samples from Section S53 (the distances from gallery axis are indicated in the legend) and of the reference bentonite obtained by CIEMAT.

UAM analyses of the less than 2 µm fraction also showed the normal expansion behaviour of the Ca-homoionised smectite on EG treatment. No evidence of the formation of a discrete illite phase was found. However, in the K-homoinised samples the expansion upon glycolation was not complete. The basal reflection of the glycolated samples tended to increase towards the heater, from 1.46 to 1.51 nm. The changes were very subtle, but indicate higher quantities of high-charged montmorillonite towards the heater (Cuevas et al. 2016).

5.1.2 Thermal analyses

The thermal analyses are an additional diagnostic tool that provides information about the dehydration and dehydroxylation characteristics of the smectite, particularly about the kind of cations in the interlayer and the position of the OH groups, and consequently about the cis/transvacancy character of the octahedral sheet (Emmerich 2011).

CIEMAT performed the thermal analysis (thermogravimetry and differential scanning calorimetry, TG-DSC) of bulk samples of Sections S47, S53 and S59 at a heating rate of 10 °C/min and under a dynamic argon atmosphere (20 mL/min) at temperatures between 20 and 1100 °C.

UAM performed thermogravimetric analyses from 25 to 1'000 °C at a temperature increment rate of 10 °C/min on 0.5-g bulk samples from Section S45 ground to < 5 µm.

ETH performed thermogravimetric and mass spectrometric analyses (TG-MS) with a thermobalance coupled to a mass spectrometer, which allowed to investigate the evolved water, CO_2 and SO_2 as part of the mineral composition analysis. Approximately 110 mg of bulk sample were analysed in a platinum crucible over the range 25 – 1'000 °C (heating rate 10 °C/min) in a dry and CO_2-free airflow atmosphere (50 mL/min).

The analyses of CIEMAT showed that both the reference and the retrieved samples displayed typical TG-DSC curves of dioctahedral smectites with most of the OH^- groups at cis-vacant positions. The dehydration peaks (peak at 136 °C and a shoulder at 200 °C) corresponded to smectites with divalent cations in the interlayer. The dehydroxylation peak was located at around 650 °C, except in the samples taken close to the heater in Sections S47 and S53, which showed an abnormal double dehydroxylation peak (at 600 – 610 and 652 °C). This new band may indicate the presence of an illite/smectite and chlorite/smectite mixed-layer different to that observed in all the samples by XRD analysis, a larger proportion of trans-vacant or more octahedral iron (Wolters & Emmerich, 2007). The temperature of the decomposition peak was between 865 and 870 °C, increasing towards the internal part of the barrier. No accessory minerals were observed in the TG-DSC analyses. Fig. 58 shows an example of the results obtained for the reference sample and for samples taken from Section S47.

The analyses performed by UAM showed very small differences between the different samples from Section S45 and the reference bentonite. The dehydroxylation of montmorillonite took place around 600 °C, which is consistent with the trans-cis-vacant type of octahedral occupation defined by Wolters & Emmerich (2007), even in the samples closest to the heater. The peak at 129 °C indicates the presence of divalent cations (high hydration energy) and is better developed in the two samples closest to the heater. This observation would agree with the increase towards the heater in the proportion of divalent cations in the exchange complex discussed in Section 5.4. The evolved gases lost in the range of dehydroxilation (T > 450 °C) seemed to be higher in the samples closest to the heater, but this was not related to a higher carbonate content.

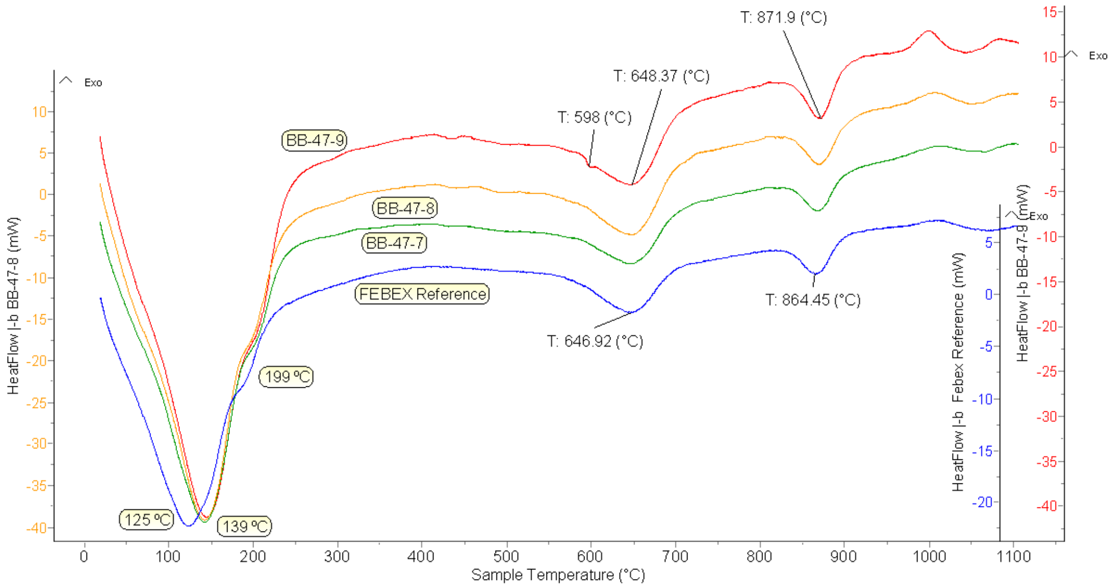

Fig. 58: DSC curves of samples from Section S47 and of the reference FEBEX obtained by CIEMAT (BB47-7: 104 cm, BB47-8: 82 cm, BB47-9: 59 cm from gallery axis).

5.1.3 Fourier Transform Infrared Spectroscopy

Fourier Transform Infrared Spectroscopy (FTIR) was used by CIEMAT as an additional method for the analysis of the mineral composition and of the chemical changes in the structure of smectite, especially at the octahedral sheets. Particularly, the ion allocation in the octahedral position in smectite was investigated (Madejová & Komadel 2001). The IR spectra were measured in the middle-infrared region (4'000 – 400 cm^{-1}). The measurements were carried out in transmission mode using KBr-pellets obtained by dispersing 2 mg of powder sample in 200 mg of KBr.

The spectra from the bulk samples analysed displayed the main typical dioctahedral smectite bands, as well as those of quartz. The spectra showed a band at 3627 cm^{-1} which corresponds to the OH-stretching region of structural hydroxyl groups for dioctahedral smectites with Al-rich octahedral sheets. In the 1'300 – 400 cm^{-1} range there was only one broad, complex Si-O-stretching vibration band at around 1030 cm^{-1}, which is typical of dioctahedral montmorillonite. The presence of peaks at 915 cm^{-1} (δAlAlOH) and 840 cm^{-1} (δAlMgOH), indicated partial substitution of octahedral Al by Mg, typical also of dioctahedral smectites. The weak band at 798 cm^{-1} was caused by the Si-O stretching of quartz. The features described can be observed in Fig. 59, in which the results obtained for the reference bulk bentonite and for bulk samples of Section S59 are shown. The spectra of the samples with the fraction less than 2 µm showed similar patterns. Hence, both the spectra of the bulk samples and of the clay fractions would indicate that no structural alteration of the smectite took place during operation.

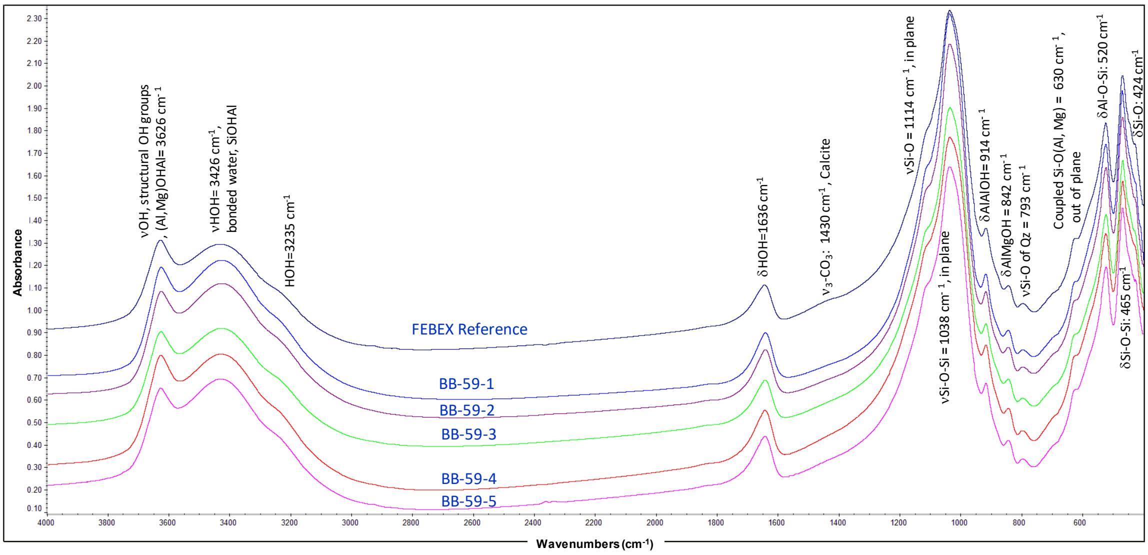

Fig. 59: FTIR spectra of bulk samples from Section S59 obtained by CIEMAT (BB59-1: 102 cm, BB59-2: 79 cm, BB59-3: 56 cm, BB59-4: 34 cm, BB59-5: 11 cm from gallery axis).

5.1.4 Scanning Electron Microscopy

The Scanning Electron Microscopy (SEM) was used by CIEMAT to define the microstructural morphology of clay minerals, possible alteration products and accessory minerals. Samples from Sections S36, S47, S53 and S59 were analysed.

The major mineral phases identified were smectite, quartz and feldspars (Fig. 60). The accessory minerals found were the same as those of the FEBEX reference bentonite: carbonates, sulphates, zircon, monacite, biotite, muscovite, ilmenite and apatite (Fig. 61). Microorganisms and organic matter were found in samples from the external and middle rings in Sections S36, S47, and S59, i.e., in the wettest part of the barrier (Fig. 62: dormant spores? bacteria?). Consistently, the microbiology studies performed on the samples retrieved showed that cells could be cultivated in large numbers in the samples from moist, low temperature positions of the barrier (Bengtsson et al. 2017). Colonies of microorganisms had systematically been found in the wettest samples from thermohydraulic tests and also in samples from oedometric tests performed under high temperature (40 – 60 °C) in which the bentonite water content was high (Fernández et al. 2001, Villar 2002). In Section S36, just at the contact with the shotcrete plug, portlandite and ettringite were found (Fig. 63, see also Turrero & Cloet 2017). Furtherome, increases in K and Mg were detected in some smectite particles of samples from this section.

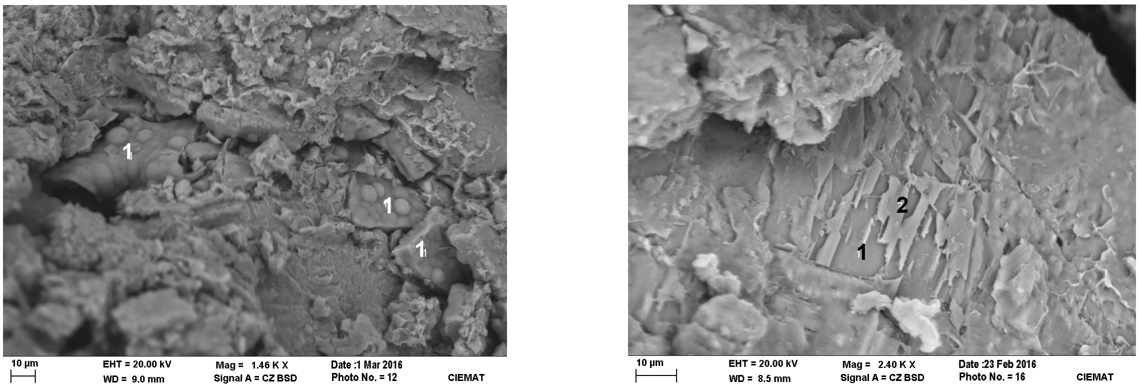

Fig. 60: SEM photomicrographs: clay matrix and silica (1) in a sample from the inner part of Section S59 (left, block BB59-4, 34 cm from the gallery axis); K-feldspars (1), plagioclase (2) in a sample from the external bentonite ring of Section S59 (right, block BB59-1, 102 cm from the gallery axis).

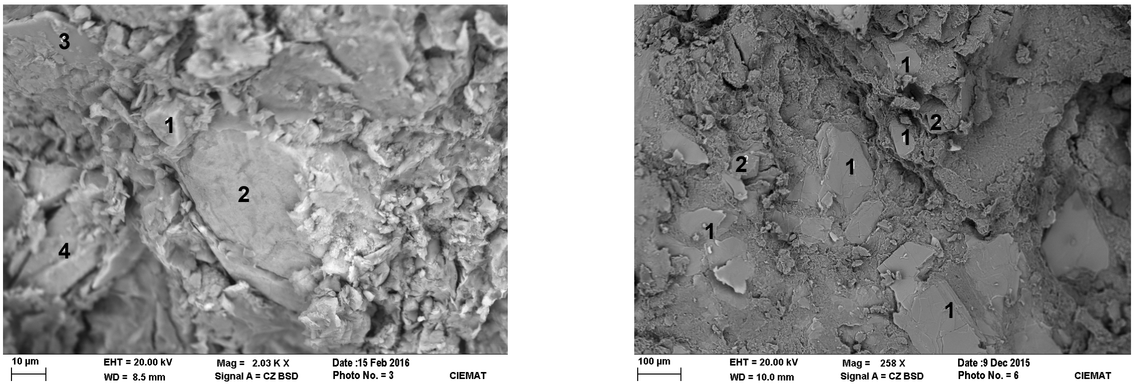

Fig. 61: SEM photomicrographs: apatite (1), Fe-oxide (2), plagioclase (3), Ti-Fe-Mn (4) in the middle bentonite ring of Section S47 (left, BB47-5, 79 cm from the gallery axis); biotite (1), plagioclase (2) in the external bentonite ring of Section S47 (right**,** BB-47-7, 102 cm from the gallery axis).

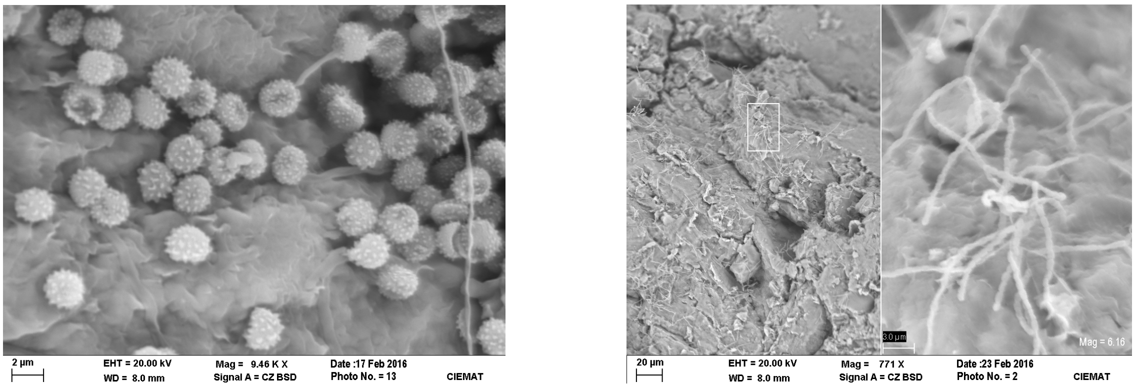

Fig. 62: SEM photomicrographs: microorganisms in the external bentonite ring of Section S47 (left, block BB47-7, 102 cm from the gallery axis) and S59 (right, block BB59-1, 102 cm from the gallery axis).

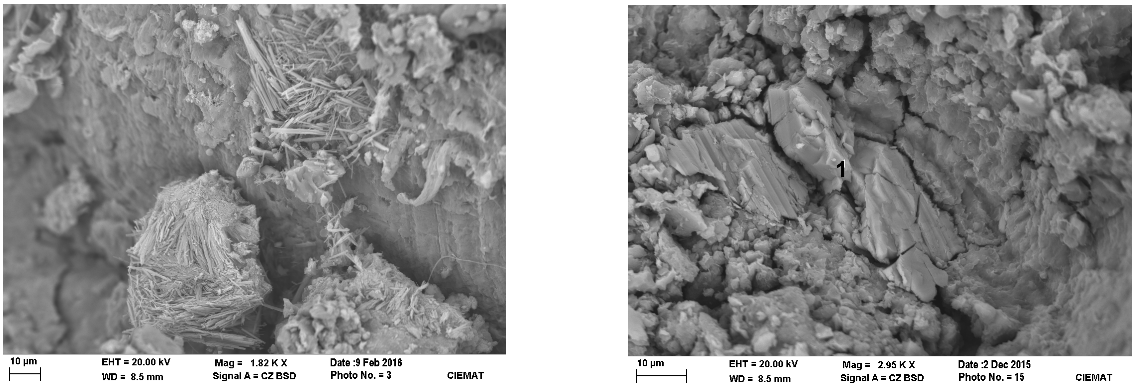

Fig. 63: SEM photomicrographs of samples at the contact with the shotcrete plug: ettringite in the middle bentonite ring of Section S36 (left, block BB36-2, 85 cm from the gallery axis) and portlandite (1) in the external bentonite ring of Section S36 (right, block BB36-1, 108 cm from the gallery axis).

5.2 Mean layer charge

Layer charge is the charge deficit caused by ionic substitutions in the structure of minerals which is balanced by the exchangeable cations in smectites. It is a significant characteristic of the 2 : 1 sheet structural unit of montmorillonite and determines cation retention and specific adsorption of water and organic polar molecules (Lagaly & Mermut 2001). In smectites, the layer charge may be different for each layer, both in terms of charge location (tetrahedral or octahedral) and charge magnitude, and the mean layer charges (MLC) represent only the statistical average of the charge classes in the layers (Olis et al. 1990).

CIEMAT, UAM and ETH determined the MLC by means of the simplified method of alkylammonium cations established by Olis et al. (1990), which uses empirical relationships between the XRD basal spacing measured in oriented-aggregate specimens of the ion-exchanged clay fractions and the mean layer charge calculated from the conventional n-alkylammonium ion-exchange technique. CIEMAT and UAM ion-exchanged the clay to sodium, whereas ETH did not homogenise the samples. The correlation between the interlayer space measured in the XRD patterns of the n-alkylammonium exchanged samples and the MLC values corresponding to the nC = 12 and nC = 18 (nC: number of carbon atoms in the alkyl chain) were used. The average of the two values is given below as the MLC of the smectite. UAM used only the values for nC = 12.

For the reference bentonite, CIEMAT and UAM found a value of 0.37 MLC/hfu (hfu = half unit cell). The values found for the retrieved samples are plotted in Fig. 64. All of them had values between 0.36 and 0.38 MLC/hfu. The observed dispersion did not seem to be related to the location of the samples (different sections or proximity to the heater). The average value for all the samples analysed by each laboratory was 0.37 MLC/hfu, i.e. the same as for the reference bentonite. Therefore, the smectite particles prior and after the FEBEX *in-situ* test can be classified as low-medium charge smectites. The location of the charge is mainly in the octahedral sheets, as shown in Section 5.3.2.

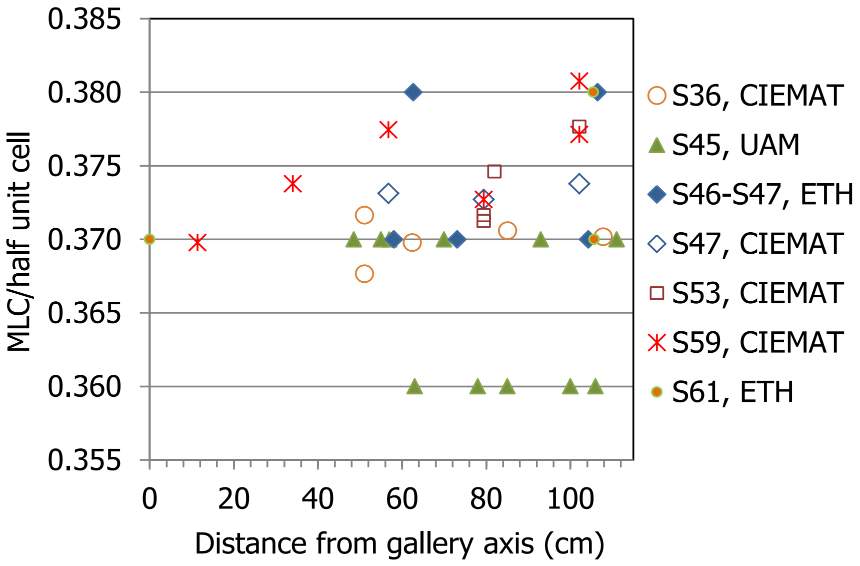

Fig. 64: Mean layer charge of the smectite determined by different laboratories in samples retrieved from different sections.

5.3 Solid chemical composition and smectite crystal chemistry

5.3.1 Chemical composition of the bulk sample

The chemical composition of the bulk sample in terms of oxide-content was analysed by X-ray fluorescence (XRF) by CIEMAT and BGR. These groups, along with ETH, also measured the content of organic carbon and total carbon. CIEMAT also determined the content of poorly crystalline and free silica, aluminium and iron.

To determine the major elements by XRF CIEMAT used 0.8 g of powdered samples (ground to < 250 µm) that were oven-dried at 105 °C and homogeneously mixed with 7.2 g of lithium tetraborate in the proportion of 34 – 66 %. The whole material was melted stepwise in a platinum crucible. The loss on ignition (LoI) was determined separately by oven-drying at 1'025 °C for 3 hours. The trace elements were also determined in molten pellets of the powdered (ground < 63 µm) samples. To produce these pellets, 12 g of dried sample (105 °C) was mixed with wax and the material was pressed at 150 kN for 1 minute. CIEMAT analysed the chemical composition of samples taken evenly along radii from Sections S36, S47, S53 and S59, a total of 19 samples, by XRF.

BGR prepared the powdered samples for XRF-analysis by mixing with a flux material (lithium metaborate) and melting into glass beads. The beads were analysed by wavelength-dispersive XRF. To determine the loss on ignition, 1'000 mg of sample material was heated to 1'030 °C for 10 min. BGR analysed two samples taken at the front of the heater (S42), two samples taken at two different distances from the heater in Section S48, samples taken along two radii in Section S45 and samples taken along a radius in Sections S50 and S53, a total of 45 samples, all of them from sections around the heater.

Neither the results by CIEMAT nor those by BGR allowed to establish clear differences between samples from different sections or taken at different distances from the heater. Hence, the average of the results obtained in the samples analysed by CIEMAT and BGR has been computed and is shown in Tab. 6, along with the chemical composition of the reference bentonite. In the case of BGR the material analysed as reference was the FEBEX bentonite used in the ABM experiment. Naturally, the major elements found by the two groups were the same and the proportions were also quite similar. The BGR analyses gave less silicon, aluminium and sodium and more loss on ignition (LoI) than determined by CIEMAT. With respect to the changes occurred during operation, they do not seem to be significant and for most elements the trend found by one laboratory was not the same as that found by the other (the changes were minor in any case). However, the two laboratories found a small increase in iron and calcium and a decrease in sodium.

The spatial distribution of the elements was quite homogeneous across the barrier and did not seem to follow any particular trend for most elements. Nevertheless, the content of magnesium increased from the granite towards the axis of the gallery, both in the sections around the heater and in the cool sections (Fig. 65). In contrast, the calcium and more notably, sodium contents increased from the internal part of the barrier towards the gallery wall (Fig. 66, Fig. 67). In the case of calcium this increase was particularly clear in the cool sections analysed by CIEMAT (S36 and S59). These trends could be mostly related to the changes in the exchangeable cations that are reported in Section 5.4. They were not found in the analyses of the less than 2 µm fraction, since it was homogenised in Ba prior to the chemical analyses (Section 5.3.2).

Tab. 6: Chemical composition by XRF of the bulk samples (the number of samples analysed is indicated in parenthesis).

Element (wt.%)	**CIEMAT**			**BGR**	
	FEBEX ref	**FEBEX ref*** (7)	**Average retrieved** (19)	**FEBEX ABM**	**Average retrieved** (45)
SiO_2	55.46	57.89 ± 1.55	57.54 ± 1.31	55.25	54.26 ± 0.38
Al_2O_3	17.28	17.95 ± 0.71	17.83 ± 0.44	17.19	17.01 ± 0.14
MgO	4.37	4.21 ± 0.21	4.49 ± 0.20	4.39	4.38 ± 0.16
Fe_2O_3	3.09	3.12 ± 0.22	3.37 ± 0.20	3.12	3.14 ± 0.07
CaO	1.75	1.83 ± 0.10	1.95 ± 0.25	1.82	1.87 ± 0.22
Na_2O	1.16	1.31 ± 0.09	1.20 ± 0.10	1.13	1.10 ± 0.11
K_2O	0.99	1.04 ± 0.05	1.10 ± 0.09	1.03	0.96 ± 0.06
TiO_2	0.15	0.23 ± 0.01	0.19 ± 0.02		0.21 ± 0.01
MnO	0.03	0.04 ± 0.00	0.04 ± 0.00		0.04 ± 0.00
SO_3	0.04	0.04	~ detec. lim.	0.07	0.05 ± 0.03
P_2O_5	0.03	0.03 ± 0.01	0.04 ± 0.00	0.00	0.04 ± 0.00
LoI	16.82	13.8 ± 2.6	11.27 ± 1.71	16.00	16.83 ± 0.47

* Obtained by acid digestion (Fernández 2004).

Regarding the trace elements, which were also analysed by CIEMAT using XRF, an increase in fluorine content with respect to the initial value was observed in all samples (Fig. 68, left). The additional fluorine probably came from the granite groundwater, which has a high content (4 – 6 mg/L, Garralón et al. 2018), and seems to have moved towards the internal part of the barrier. The chlorine content also increased towards the internal part of the barrier (Fig. 68, right), reflecting the advective movement of chlorides observed in the distribution of soluble species in the pore water (Section 5.5). In contrast, the manganese content decreased towards the axis of the gallery. Other elements whose concentration increased with respect to the FEBEX reference values were copper, phosphorus and yttrium, without a clear spatial pattern.

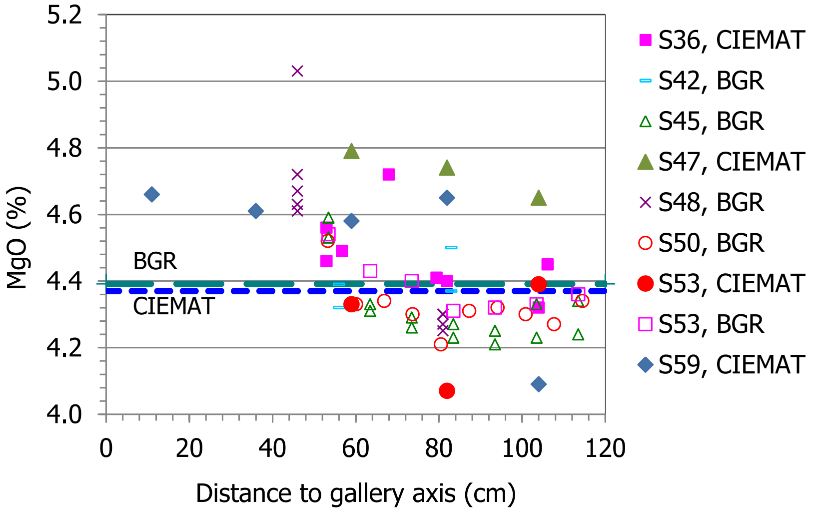

Fig. 65: Magnesium content in bulk samples from different sections analysed by BGR and CIEMAT (the horizontal dashed lines indicate the reference values).

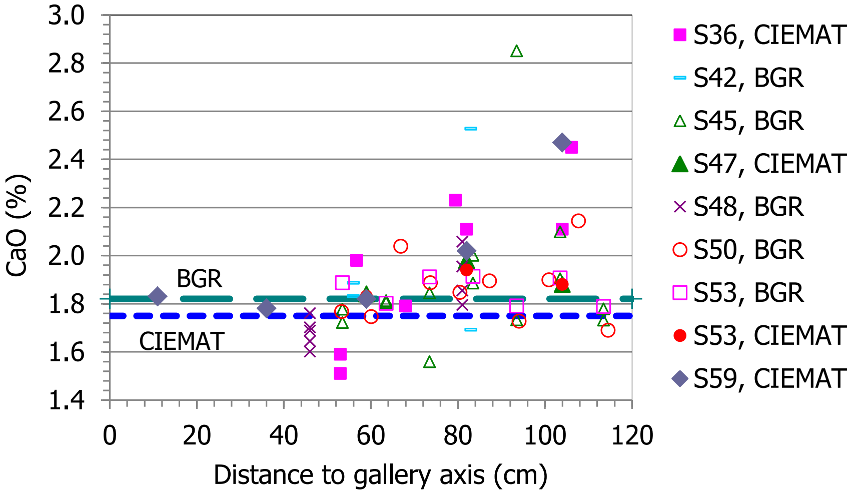

Fig. 66: Calcium content in bulk samples from different sections analysed by BGR and CIEMAT (the horizontal dashed lines indicate the reference values).

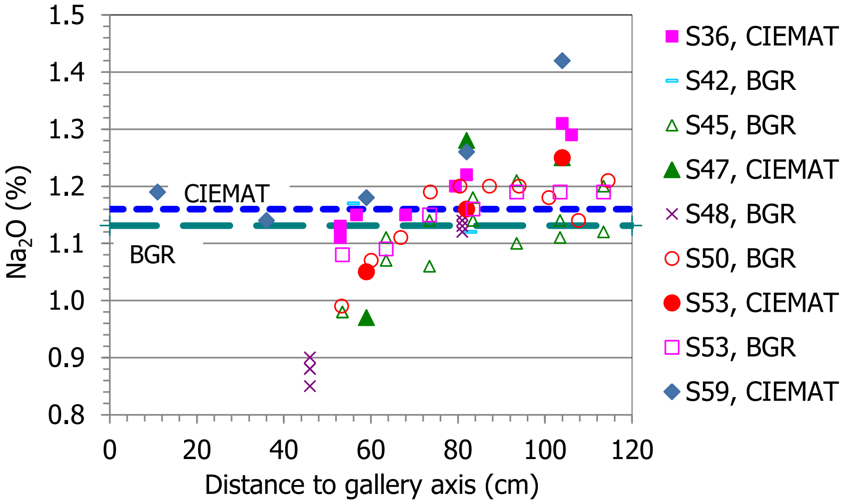

Fig. 67: Calcium content in bulk samples from different sections analysed by BGR and CIEMAT (the horizontal dashed lines indicate the reference values).

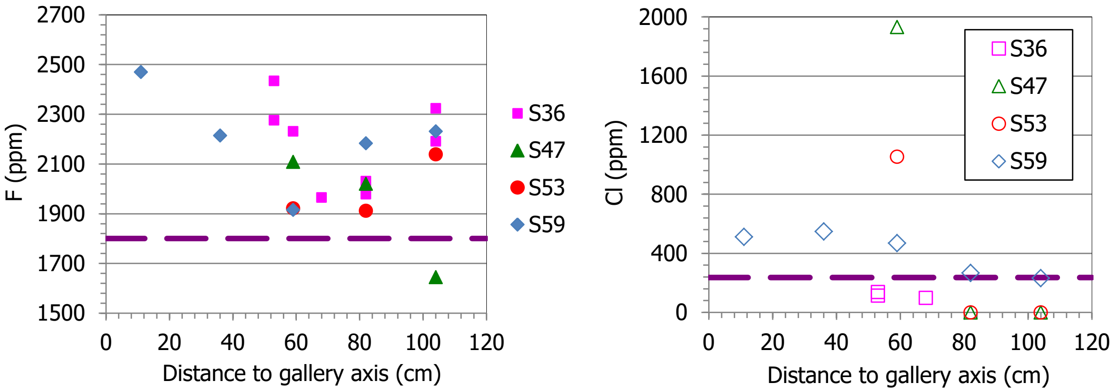

Fig. 68: Fluorine and chlorine contents in bulk samples from different sections analysed by CIEMAT (the horizontal dashed lines indicates the reference value).

CIEMAT determined the total carbon (TC) and total sulphur contents by combustion on 200 mg of sample ground to a size of less than 250 µm. The total inorganic carbon (TIC) content was independently measured from the CO_2 released during acidification with phosphoric acid. The difference between TC and TIC provides the organic carbon (OC) value. Samples taken along different radii of Sections S36, S47, S53 and S59 were analysed.

The organic carbon content was measured by BGR after dissolution of the carbonates. Carbonates had been removed by treating the samples several times at 80 °C with HCl until no further gas evolution could be observed. Samples of 170 – 180 mg of the dried material were used to measure the total carbon content. Total inorganic carbon was calculated by the difference of TC-OC. The samples were heated in the device to 1'800 – 2'000 °C in an oxygen atmosphere and the contents of CO_2 and SO_2 were determined by an infrared detector.

For the determination of the carbon content of the bentonite ETH used an elemental analytical system. TC and TIC were determined separately, and TOC was computed from the difference between both. The TIC was obtained from the CO_2 released during acidification with phosphoric acid, which is assumed to come from the dissolution of carbonates. The TOC was obtained from the CO_2 released by thermal combustion at 1'300 °C. The detection of the CO_2 gas was carried out using nondispersive infrared (NDIR) spectroscopy. The measurements were carried out in oxygen atmosphere on two specimens per sample of approx. 0.4 g of the air-dried material ground to < 400 μm.

Tab. 7 shows the average values of all the samples analysed by the three laboratories, which were in the order of the values corresponding to the reference bentonite, indicating no major changes during operation in the overall content of carbon and sulphur. The total carbon content was 0.14 % in the three cases, which is only slightly above the value for the reference bentonite. Most of the carbon measured was inorganic, and the content of organic carbon was always below 0.06 % in the analyses by ETH and below 0.10 % in the analyses by BGR. The OC did not follow any clear spatial distribution across the barrier. The TIC percentage would correspond to an average calcite content about 1 %, which agrees with the one obtained for the FEBEX-ABM reference bentonite based on XRD Rietveld analysis (Kaufhold et al. 2016). In fact, the calcite content detected by ETH using XRD correlates well with the calcite content deduced from the TIC analyses in the same samples (Fig. 70). The content of total carbon increased from the axis of the gallery towards the granite, particularly in the sections around the heater (Fig. 69).

The sulphur content was very low (lower than 0.06 %), and in many of the samples analysed by CIEMAT even below the detection limit. Its content was not related to the location of the samples in the barrier.

In the same samples CIEMAT determined the extractable and free silica and aluminium by using a Na_2CO_3 0.5 M dissolution (pH 10.5) according to the alkali dissolution method at room temperature (Follett et al. 1965, Wilson 1987). The concentration of silica and aluminium was analysed by ICP-OES. The citrate-bicarbonate-dithionite method was used for determining the extractable iron oxides following the Jackson's procedure (2005). The content of the three species was very variable among samples but did not show any clear spatial pattern. The free aluminium and iron contents were in most samples above the reference values (which were below detection limit for aluminium and 0.06 wt.% for iron), whereas the free silica content was overall below the reference value (which was 0.42 wt.%). Nevertheless, the values measured in the retrieved samples were in all cases below 0.3 wt.% for aluminium (0.07 wt.% on average) and 0.5 wt.% for iron (0.11 wt.% on average); hence, the changes with respect to the reference bentonite were not large.

Tab. 7: Total carbon (TC), total inorganic carbon (TIC), organic carbon (OC) and total sulphur (wt.%).

Lab/# samples	**TC**	**TIC**	**OC**	**S**
BGR/45	0.14 ± 0.05	0.08 ± 0.05	0.06 ± 0.01	0.03 ± 0.01
CIEMAT/39	0.14 ± 0.03	< 0.3	< d.l.	< 0.1
ETH/12	0.14 ± 0.05	0.11 ± 0.04	0.03 ± 0.02	

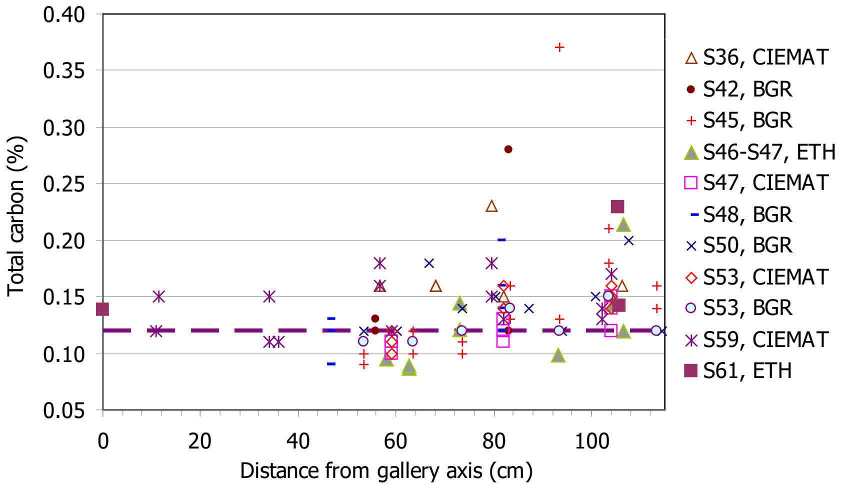

Fig. 69: Total carbon in samples from different sections as determined by three laboratories (the horizontal dashed line indicates the reference value).

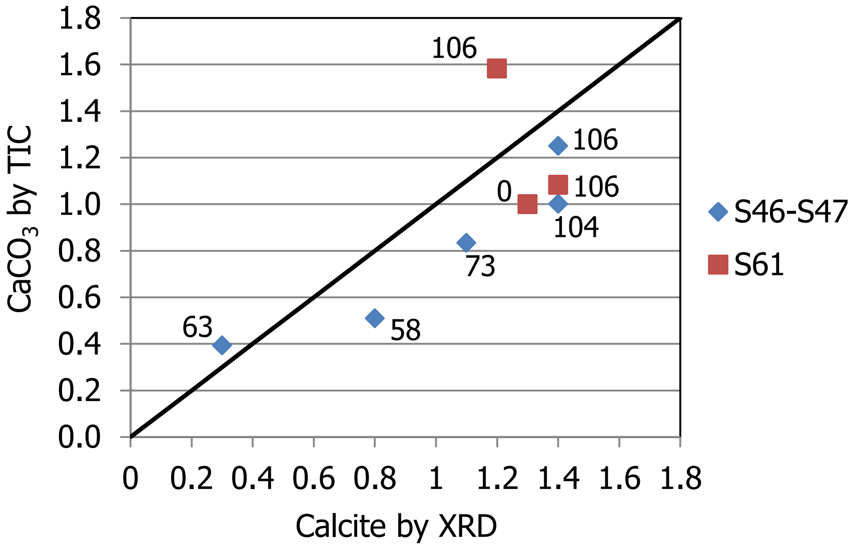

Fig. 70: Calcite content (wt.%) estimated by ETH using XRD and computed from the TIC content in samples from two sections (the distance from the gallery axis of each sample is indicated in cm).

5.3.2 Chemical composition of the less than 2 µm fraction: structural formulae

The chemical composition of the less than 2 µm fraction of the samples after homoionisation with barium and drying at 105 °C was analysed by X-ray fluorescence (XRF) by CIEMAT. The major elements found in the clay fraction were indeed the same as in the bulk sample, although the loss on ignition was higher (18 wt.% in < 2 µm fraction *vs.* 11 wt.% in bulk sample), reflecting the higher proportion of combined water in the smectites predominant in the less than 2 µm fraction (Section 5.1.1). Also, as a consequence of the lack of secondary minerals (quartz, calcite, feldspars, plagioclase) in this fine fraction, the proportion of silicon, calcium, sodium and potassium decreased with respect to the bulk sample.

From these chemical analyses, the stoichiometric elemental composition of the smectites was calculated by CIEMAT based on the assumption of 22 negative charges per half-formula unit (phfu), taking into account the measured layer charge (Section 5.2) for the calculation, as recommended by Köster (1977). CIEMAT analysed samples from Sections S36, S47, S53 and 59 and determined the structural formulae for the smectite in three samples along a radius in Sections S36, S47 and S53 and in five samples along a radius in Section S59. No significant changes were observed among the different retrieved samples and the reference bentonite. All smectites showed substantial substitution in the octahedral sheet (85 – 95 %), whereas the substitution of the tetrahedral charge was much lower (between 5 to 15 %). In the octahedral sheet, magnesium substituted mainly for aluminium, the amount of iron being low. All the samples displayed an octahedral filling below 2.05 mol/phfu, matching the dioctahedral character of the smectite. Furthermore, since the layer charge was < 0.42 MLC/hfu and the percentage of tetrahedral charge < 15 %, the smectites can be classified as Wyoming-type montmorillonites. An average structural formula of the 16 samples analysed is given in Tab. 8.

Tab. 8: Structural formulae calculated by CIEMAT from the chemical analyses of the < 2 µm of the Ba-homoionised samples.

Sample	**Structural formula**
FEBEX ref*	$(Si_{3.94}Al_{0.06})^{IV}\ (Al_{1.35}Fe^{3+}{}_{0.21}Mg_{0.49}Ti_{0.01})^{VI}\ O_{10}(OH)_2\ X_{0.29}$
Average retrieved (16)	$(Si_{3.96 \pm 0.01}Al_{0.04 \pm 0.01})^{IV}\ (Al_{1.35 \pm 0.01}Fe^{3+}{}_{0.20 \pm 0.01}Mg_{0.48 \pm 0.01}Ti_{0.01})^{VI}\ O_{10}(OH)_2\ X_{0.20 \pm 0.01}$

* Not homoionised.

UAM focussed on the crystal chemistry of samples along a radius from Section S45 and of the reference FEBEX bentonite. To accomplish this, UAM analysed the Ca^{2+}-homoionized less than 2 µm fraction of the clay by SEM. The sample was dried at 60 °C, ground and pressed in an adhesive graphite disc mount in order to obtain a flat surface. Analyses were performed on different surfaces with a coupled EDX (Energy Dispersive X-ray Spectroscopy) in order to obtain major chemical data and calculate structural formulae. As an internal standard for calibration, a < 0.5 µm fraction of the FEBEX reference montmorillonite, previously analysed by X-ray fluorescence, was used.

The montmorillonitic clay fraction analysed by UAM was highly homogeneous and revealed only a minor mineralogical alteration of the smectite component. The content of calcium atoms (related to structural formula layer charge) was virtually the same in the retrieved samples as in the reference sample, and increased towards the heater (Fig. 71), which is consistent with the trend to have more K-collapsed layers under K-EG treatment in samples close to the heater. Moreover, the irreversibly fixed potassium was negatively correlated to the increase in layer charge (therefore in calcium), which can also be observed in Fig. 71. Hence, no evidence of illitization was found. The sample closest to the liner also showed a slightly higher content of octahedral iron. An average of the structural formulae obtained for the 11 samples analysed is given in Tab. 9, along with the formula for the reference bentonite. Despite the differences in the methodologies followed by both groups, the formulae obtained are comparable.

Tab. 9: Structural formulae calculated by UAM from the analyses of the < 2 µm of the samples Ca-homoionised performed by EDX.

Sample	**Structural formula**
FEBEX ref	$(Si_{3.94}Al_{0.05})^{IV}$ $(Al_{1.41}Fe^{3+}_{0.09}Mg_{0.50})^{VI}$ $O_{10}(OH)_2Ca_{0.24}K_{0.04}$
Average retrieved (11)	$(Si_{3.96\pm0.02}Al_{0.04\pm0.02})^{IV}$ $(Al_{1.41\pm0.02}Fe^{3+}_{0.09\pm0.01}Mg_{0.50\pm0.02})^{VI}$ $O_{10}(OH)_2Ca_{0.25\pm0.02}K_{0.04\pm0.01}$

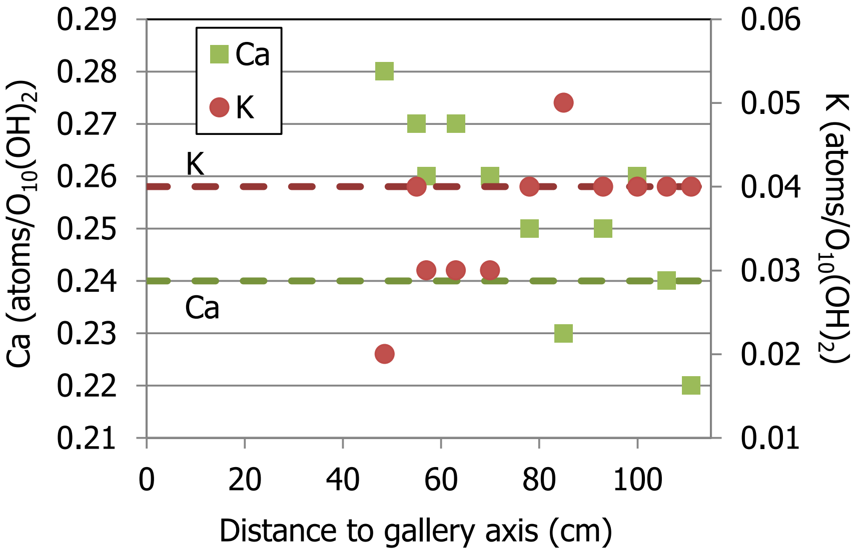

Fig. 71: Calcium and potassium atoms in the structural formula of the Ca-homoionised montmorillonite as determined by UAM.

Additionally, CIEMAT analysed the trace elements in the less than 2 µm fraction of the same 16 samples by XRF. The average values obtained for each element are compared in Fig. 72 with those obtained for the total samples discussed above in Section 5.3.1.

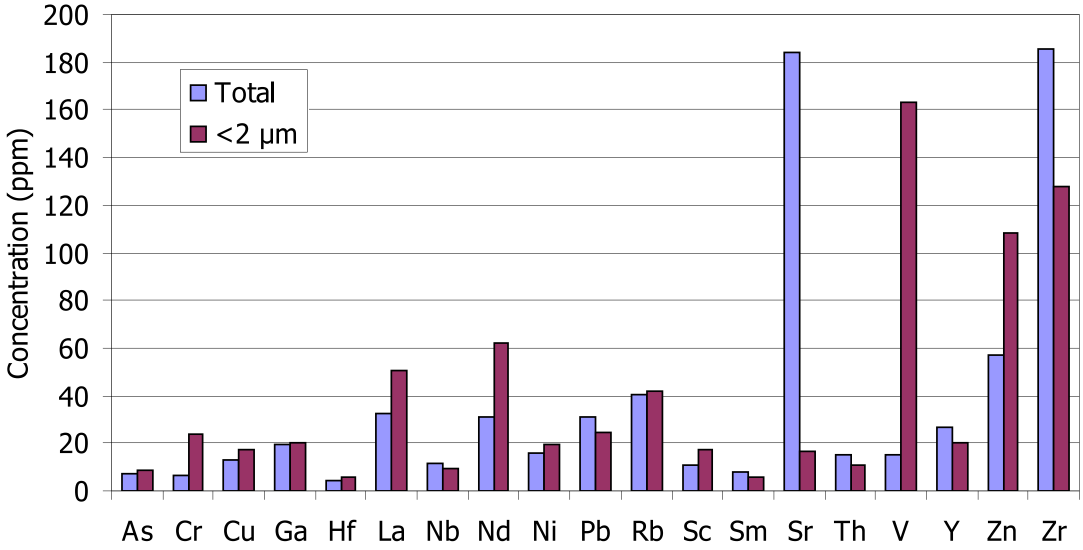

Fig. 72: Average content of trace elements found in the total sample and in the less than 2 µm fraction of samples from Sections S36, S47, S53 and S59 (average of 16 samples analysed by CIEMAT).

5.4 CEC and exchangeable cations

The Cation Exchange Capacity (CEC) is a measure of the clay surface negative charges and hence a measure of the cations' potential retention. Additionally, the concentration of the different cations in the exchange complex and the changes with respect to the reference sample gives an indication of the geochemical reactions taking place in the solid/water system, since these changes are coupled to dissolution/precipitation and transport processes. Both the CEC and the composition of the exchange complex were determined by CIEMAT, BGR, UAM, ETH and SÚRAO. CIEMAT analysed samples taken along three different radii from Sections S36 (in contact with the shotcrete plug), S47 and S53 (around the heater) and S59 (a cool section at the back of the gallery). BGR analysed two samples taken at the front of the heater (S42), two samples taken at two different distances from the heater in Section S48, samples taken along two radii in Section S45 and samples taken along a radius in Sections S50 and S53, i.e. all the samples analysed were taken around the heater. UAM analysed samples taken along a radius in the section around the heater S45. ETH analysed samples taken along a radius in Sections S46 – S47 and S61. SÚRAO performed determinations in sub-samples of sample B-S-36-3, which was a piece of a block in contact with the liner in Section S36. All the groups corrected the values obtained for CEC and exchangeable cations taking into account the water content of the samples, i.e. the values were recalculated for bentonite dry weight.

CIEMAT measured the CEC with a 0.01 M copper triethylenetetramine (Cu-trien) solution according to Ammann et al. (2005), dispersing 0.2 g of clay in 25 mL of water and 10 mL Cu-trien^{+2} (0.01 M). The standard deviation of the measurement was ± 2 meq/100 g. The determination of the exchangeable cation population was performed by using Cs as index cation (Sawhney 1970). The clay samples were equilibrated at 1 : 4 (10 g : 40 mL) solid to liquid ratio (with 0.5 M $CsNO_3$ at pH 8.2). Sodium and potassium were determined by flame atomic emission spectrometry (FAES) and the concentration of the rest of major cations was analysed by Inductively Coupled Plasma-Atomic Emission Spectrometry (ICP-OES).

BGR determined the CEC and the concentration of exchangeable cations using the Cu-trien method (Meier & Kahr, 1999). The FEBEX samples were analysed using 30 mL Cu-trien solution and no additional water. Two different sample masses (0.2 and 0.3 g) were analysed and average values were calculated. The following error (± 3 sigma) can be approximately considered: K^+ (± 0.3 meq/100 g), Mg^{2+} (± 0.8 meq/100 g), Ca^{2+} (± 0.8 meq/100 g), Na^+ (± 1.9 meq/100 g), and the CEC (± 3.1 meq/100 g).

UAM also used the Cu-trien method, but dispersing 0.15 g of clay in 50 mL of water and 10 mL $CuTrien^{+2}$ (0.01 M). This determination was only performed on the < 2 µm fraction, which was previously obtained by dispersion and sedimentation. For the displacement of the exchangeable cations, 2 g of bentonite were mixed with NH_4-O-Ac 0.050 M at pH 7 (modified from Thomas 1982). The extracted cations were analysed either by flame photometry (Na^+, K^+) or ion chromatography.

ETH used the Cu-trien method (Meier & Kahr, 1999) to determine the CEC. Approximately 0.15 g of air-dried bentonite were mixed with 50 mL of exchanging solution, constituted by 5 mL of Cu-trien solution and deionised water. The suspensions were centrifuged and the supernatant was photometrically analysed for CEC and using atomic absorption spectrometry for the analysis of cation concentrations.

SÚRAO determined the CEC and exchangeable cations using the Cu-trien method (Meier & Kahr 1999, Ammann et al. 2005, Hrušková 2008). Spectrophotometry (UV/Vis) and atomic absorption spectroscopy were used to analyse the resulting solutions.

CIEMAT corrected the concentration of exchangeable cations measured both in the retrieved and the reference samples by subtracting the soluble cations content (Ca and Na) determined in adjacent samples (Section 5.5.1), whereas the other groups did not correct the data. In this sense, the values given by the other groups would correspond to "extractable" or "leachable" cations, since they included, not only the exchangeable cations, but also the cations dissolved in the pore water and those from the soluble minerals dissolved during the exchange procedure. This has repercussions on the interpretation of results and is discussed in more detail below.

The results for the CEC obtained by CIEMAT are shown in Fig. 73, where the overall decrease with respect to CIEMAT's reference value (98.1 ± 2.0 meq/100 g, indicated by a dashed horizontal line) is clear. This value is the average of 10 determinations performed following the same methodology as for the retrieved samples. This decrease took place in all the four sections analysed, with no clear spatial trend. The results obtained by SÚRAO in a sample of Section S36 (located near the concrete plug) are also included: depending on the measurement method two considerably different values were obtained for the same subsample, which provides further evidence of the uncertainty of the analytical methods.

Fig. 74 shows the CEC results obtained by CIEMAT, BGR and ETH in samples taken from sections around the heater. The values obtained by BGR were homogeneous along the radii and higher than those of CIEMAT's, but the two laboratories recorded a slight decrease of CEC in the samples retrieved with respect to the reference bentonite. ETH's values were higher than those determined by the other laboratories but also with no clear spatial trend. ETH determined the CEC of three samples in the cool Section S61, which gave a result of 106 ± 4 meq/100 g.

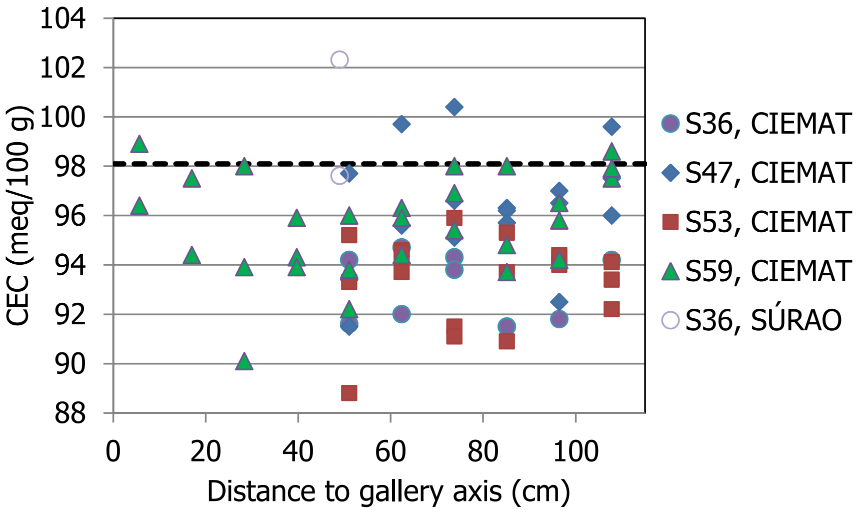

Fig. 73: Cation exchange capacity (CEC) determined along three radii of four different sections by CIEMAT (each point is the average of two subsamples) and for a sample of Section S36 by SÚRAO (average of ten subsamples measured with two different methods).

The dashed line indicates CIEMAT's value for the reference bentonite (98.1 ± 2.0 meq/100 g).

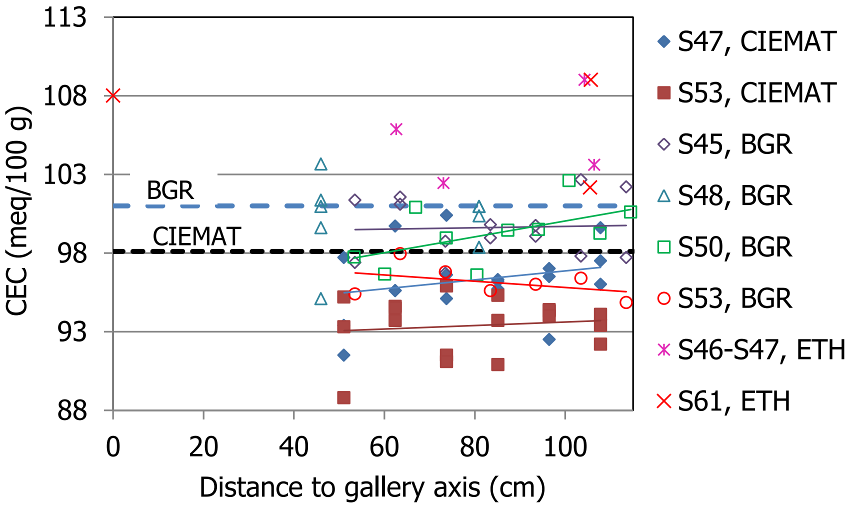

Fig. 74: Cation exchange capacity (CEC) determined in samples of different sections by CIEMAT, BGR and ETH (for CIEMAT and BGR each point is the average of two subsamples).

The dashed horizontal lines are the values determined by CIEMAT and BGR for the reference bentonite.

The results for the main exchangeable cations along with the sum of exchangeable cations obtained by CIEMAT are plotted in Fig. 75. Two of the sections analysed were located around the heater (S47 and S53), another one at the back of the gallery (cool Section S59) and Section S36 was in contact with the shotcrete plug. The results obtained by SÚRAO in a sample taken close to the liner in Section S36 are also included in the Figures. The results obtained for the three radii in each section analysed by CIEMAT were overall consistent. This means that the distribution of exchangeable cations followed a radial pattern, similar to what was observed for the water content and dry density. Fig. 75 also shows the values for the reference material. It is clear that the exchangeable cations complex changed during FEBEX operation, but the concentration of each cation was affected in a different way and the effects of high temperature or proximity to concrete were also noticeable:

- The sodium concentration in the exchange complex decreased towards the heater in Sections S47 and S53, the samples closest to the liner had concentrations as low as 12 meq/100 g. Whereas near the granite the sodium concentration was close (or slightly above) to that of the reference material (28 meq/100 g). The samples in cool Section S59 had sodium concentrations typically below the reference value and tended to decrease towards the inner part of the barrier. In Section S36 –which was subjected to a thermal gradient during the first five years of operation – the sodium concentration in the exchange complex was higher than the reference value near the granite and decreased towards the dummy canister.
- The magnesium concentration in the sections subjected to a thermal gradient, S47 and S53, increased towards the heater, where it was above the reference value. Magnesium was slightly below the reference (33 meq/100 g) in the external parts of the barrier. In the cool Section S59 the exchangeable magnesium concentration was quite homogeneous and slightly above the reference value. However, in Section S36, well away from the heater and adjacent to the shotcrete plug, the magnesium concentration was considerably lower than the reference value in all the samples, decreasing from 32 meq/100 g at the contact with the liner to 15 meq/100 g at the granite.
- The concentration of exchangeable calcium did not change in the cool Section S59 with respect to the reference FEBEX and was homogeneous all over the section. However, in the Sections S47 and S53, around the heater, the concentration of exchangeable calcium was higher than the reference value. In Section S47 there was a clear increase of exchangeable calcium towards the heater that was not seen in Section S53. Section S47 was subjected to higher temperatures than S53 during operation, because it was in the middle part of the heater, and this could be the reason for this difference. In fact, the difference in temperature between the two sections also resulted in different water contents (Fig. 8). In Section S36 the content of exchangeable calcium was much higher than the reference value, but tended to decrease towards the dummy canister.
- Finally, the sum of exchangeable cations clearly decreased with respect to the reference value (103 meq/100 g) in most of the samples. In the sections around the heater this decrease tended to be higher towards the internal part of the barrier.

Summarising the observations described above, there seems to have been an overall decrease in exchangeable cation content, which would agree with the decrease in cation exchange capacity observed (Fig. 73). The sodium concentration in the exchange complex decreased towards the internal part of the barrier, particularly in the heated sections. The distribution of exchangeable magnesium and calcium seemed to be affected by temperature, since it was quite homogeneous in the cool Section S59 whereas the exchangeable magnesium concentration increased towards the heater, as did the exchangeable calcium concentration in the hottest Section S47. Hence, both exchangeable calcium and magnesium were affected by temperature. The fact that the exchangeable sodium content decreased towards the heater, while exchangeable magnesium and calcium contents increased, made the exchangeable complex more heterogeneous towards the heater. In the section in contact with the shotcrete plug (S36) there was a drastic overall increase in calcium and a decrease in magnesium with respect to the reference values. The results obtained by SÚRAO in a sample of this section agreed with CIEMAT's, except for the content of magnesium, which was considerably higher in SÚRAO's results. This affected the sum of exchangeable cations, which resulted in a higher value in this particular location for SÚRAO. It has to be taken into account that the samples analysed from Section S36 were taken from the middle part of the blocks, and not from the contact area with the shotcrete surface. However, the studies performed specifically in the closest contact to the shotcrete (Turrero & Cloet 2017) showed an overall increase in exchangeable calcium, sodium and potassium with respect to the reference bentonite and a significant decrease in magnesium, which is consistent with the changes observed in the samples analysed here, taken farther away from the interface, and with the findings for the section closest to the concrete plug dismantled in 2002 (S7, Villar et al. 2006).

Although not shown in the Figures, Section S36 also experienced an overall increase in exchangeable potassium, particularly towards the dummy canister (the average value for all the samples of S36 was 4.5 ± 0.7 meq/100 g, whereas the reference value was 2.9 meq/100 g). The concentration of potassium was overall higher than the reference value in the rest of the sections. Very small concentrations of strontium and barium were also found in most of the samples, as well as copper in samples from Section S36.

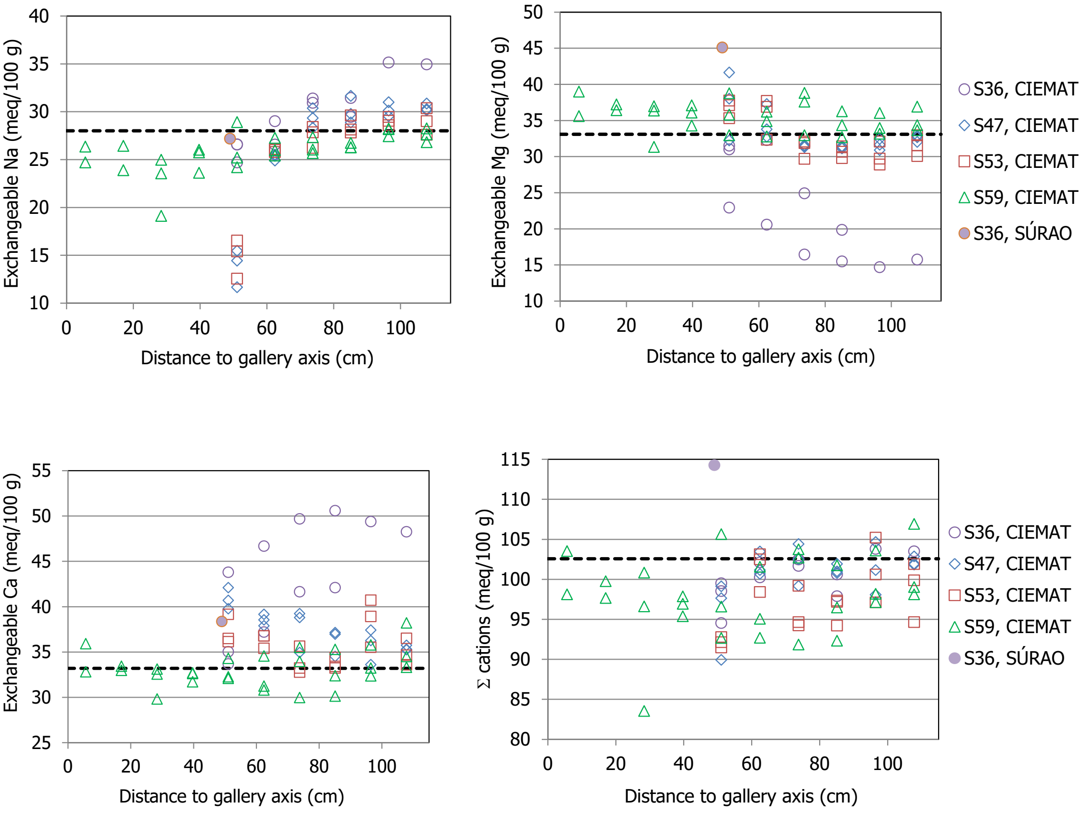

Fig. 75: Major exchangeable cations and sum of exchangeable cations determined along three radii of four different sections by CIEMAT (each point is the average of two subsamples) and SÚRAO (average of 10 subsamples).

The dashed lines indicate the values for the reference bentonite determined by CIEMAT.

The cation exchange complex of samples taken in sections around the heater is analysed in more detail in Fig. 76, where the results obtained by all the groups are plotted. All the laboratories detected the decrease in exchangeable sodium towards the heater, although in the case of BGR and UAM it was less drastic than seen in CIEMAT's results. The exchangeable magnesium concentration was seen to increase towards the heater by all laboratories, although values reported by BGR and ETH were higher than CIEMAT's and UAM values were lower and more disperse. The increase in exchangeable calcium towards the heater was clearly recorded by BGR and ETH, whose results were higher than CIEMAT's and showed an almost linear increase from the granite to the heater. The sum of exchangeable cations was higher for BGR and ETH and increased clearly towards the heater, whereas it showed no clear spatial trend in CIEMAT's results.

The differences found between the results obtained by CIEMAT and the other laboratories, which as a general rule recorded higher concentrations of all the exchangeable cations, can be explained by a different result assessment. CIEMAT also accounted for soluble cations. It considered that part of the cation concentrations measured were actually not exchangeable but soluble cations. Hence the values measured were corrected by subtracting the soluble cation content (Ca and Na) determined in adjacent samples (Section 5.5.1). In fact, if the sum of exchangeable cations is compared with the CEC measured in the same samples, it can be seen that the difference between these two show no spatial trend in CIEMAT's results; they remain around the value for the reference bentonite. However, in the case of BGR the sum of cations was considerably higher than the CEC in all the samples and increased clearly towards the heater (Fig. 77). This would be explained by an increase in soluble species found towards the heater (Section 5.5.1), that would have been extracted during the preparation of the samples for the displacement of the exchangeable cations and inaccurately taken as exchangeable. In the case of UAM, the higher concentration of exchangeable calcium can be explained not only because the contribution of soluble salts was not subtracted, but also because the method used to extract the exchangeable cations (displacement by NH_4-O-Ac) promotes the dissolution of carbonates.

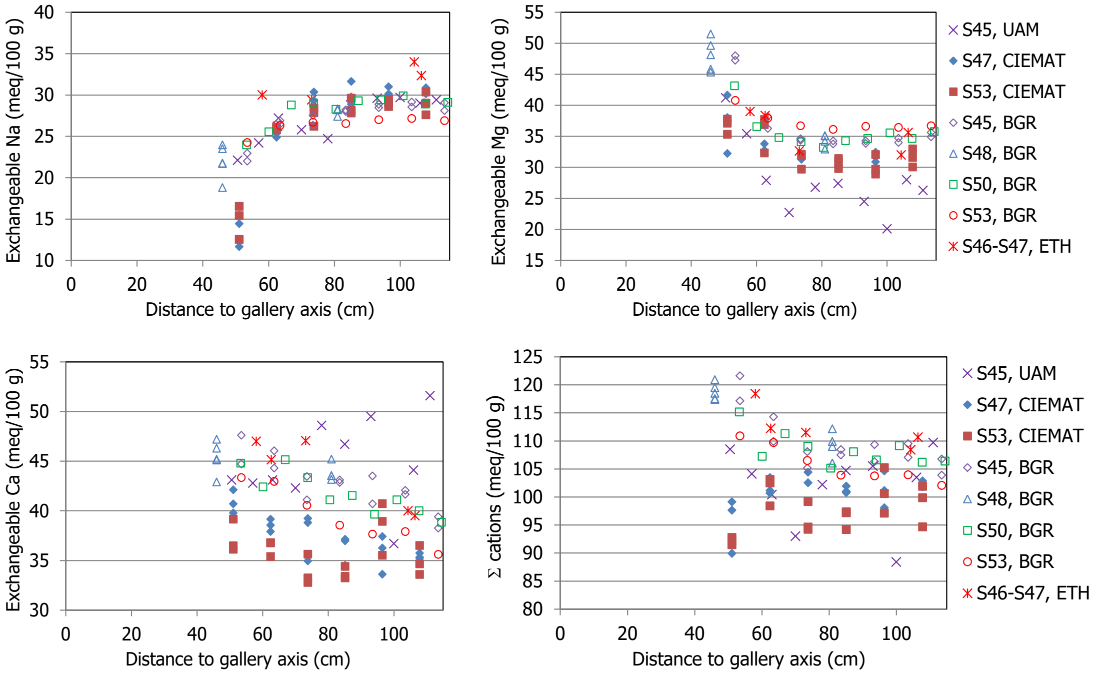

Fig. 76 Major exchangeable cations and sum of exchangeable cations determined in samples of sections around the heater by different laboratories (for BGR's results each point is the average of two subsamples).

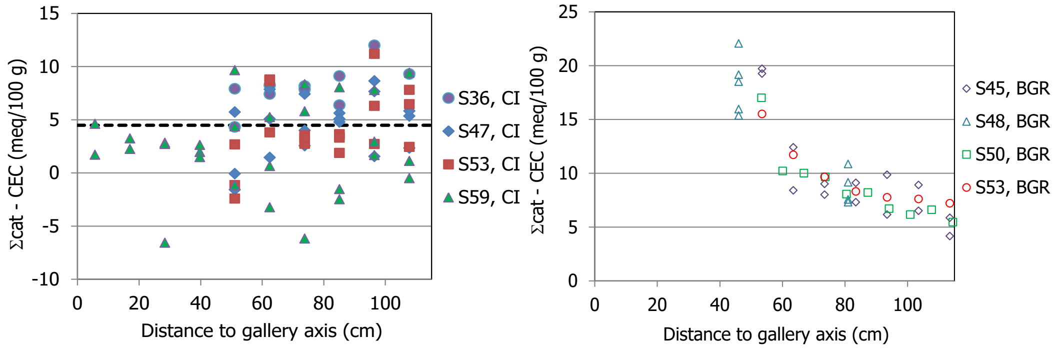

Fig. 77: Difference between the sum of exchangeable cations and the CEC of samples taken in sections around the heater: CIEMAT's results (left) and BGR's results (right).

Tab. 10 shows the average values of exchangeable cations and CEC for those sections in which a representative number of samples was analysed. These values are plotted in Fig. 78 as a function of the *x*-coordinate along the gallery. Despite the different analytical techniques among the laboratories, there seems to be a trend for the exchangeable calcium content (and to a lesser extent sodium content) to decrease towards the back of the gallery, whereas the magnesium content kept constant, except in the section in contact with the shotcrete plug (S36) where it sharply decreased.

Tab. 10: Average exchangeable cation concentration and CEC (in meq/100 g) for several sections as determined by different laboratories.

Section	**Na^+**	**K^+**	**Mg^{2+}**	**Ca^{2+}**	**Σ cations**	**CEC**
Reference	28	2.9	33.1	33.2	97.5	98.1
S36, CIEMAT	29.8 ± 3.1	4.5 ± 0.7	21.6 ± 6.4	44.7 ± 6.3	101.0 ± 2.9	101.0 ± 2.0
S45, UAM	27.1 ± 2.7	2.1 ± 0.2	28.0 ± 6.1	44.9 ± 4.3	102.0 ± 6.6	
S45, BGR	27.2 ± 2.0	2.6 ± 0.2	36.7 ± 4.4	42.8 ± 2.3	109.6 ± 4.5	99.6 ± 1.8
S47, CIEMAT	26.5 ± 6.1	3.2 ± 0.3	33.1 ± 3.5	37.4 ± 2.8	100.7 ± 4.7	100.7 ± 3.3
S50, BGR	28.2 ± 1.9	2.3 ± 0.2	35.7 ± 2.8	41.8 ± 2.1	108.4 ± 3.0	99.2 ± 1.9
S53, CIEMAT	25.8 ± 5.2	3.1 ± 0.1	32.7 ± 4.0	35.7 ± 2.5	97.6 ± 5.0	97.6 ± 4.1
S53, BGR	26.4 ± 1.0	2.6 ± 0.1	37.3 ± 1.6	39.5 ± 2.9	105.8 ± 3.3	96.1 ± 1.0
S59, CIEMAT	25.9 ± 2.0	3.1 ± 0.2	35.4 ± 2.2	33.1 ± 2.4	98.1 ± 5.3	98.1 ± 4.9

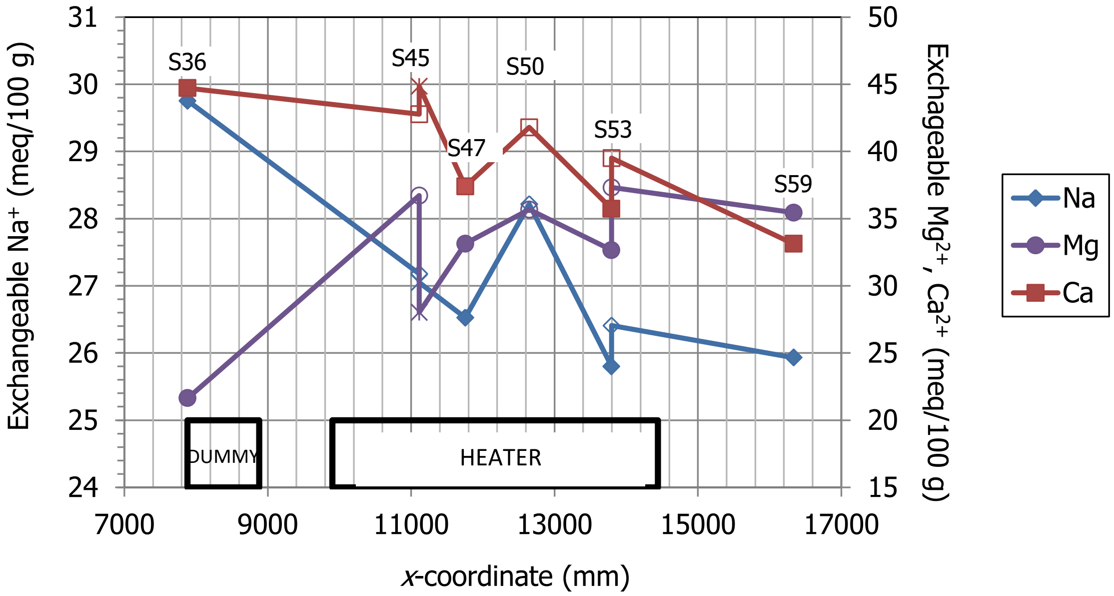

Fig. 78: Average values for exchangeable cations in sections along the gallery (filled symbols: CIEMAT, empty symbols: BGR, crosses: UAM).

5.5 Bentonite pore water

The analysis of the bentonite pore water was performed following two complementary approaches: the preparation of aqueous extracts (Section 5.5.1) and the extraction of the pore water by squeezing at high pressure (Section 5.5.2). CIEMAT used both methodologies, whereas UAM prepared just aqueous extracts and measured some parameters in them.

In fact, the aqueous extracts do not directly give the pore water composition, but just the soluble salts content. The pore water concentrations in the bentonite can only be obtained by back-calculation from the concentration of non-reactive compounds (Cl, Br, F) in the aqueous extracts taking into account the actual solid:liquid ratio of the bentonite in the barrier and the anion-accessible porosity. This value is a difficult parameter to obtain, which in bentonites is usually calculated from diffusion tests.

On the other hand, the squeezing process involves the expulsion of interstitial fluid from the saturated argillaceous material being compressed (Entwisle & Reeder 1993). The volume of water extracted depends on the water content of the sample, its properties (e.g. dry density, relative contents of easily-squeezed clays and of stiffer materials like quartz and calcite), and the experimental conditions, such as: the pressure applied, the duration time of squeezing and size of the squeezing rig (Fernández et al. 2003, 2014). The method also has limitations, for example, the squeezed pore water can be diluted because of their mixture with water from the diffuse double layers or the possible membrane effect through charged clay particles (ion filtering, anion exclusion).

5.5.1 Aqueous extracts

UAM prepared aqueous extracts of samples taken along a radius in Section S45. Solid:liquid ratios of 1 : 2.5 (with 4 g of clay) were used to measure pH and of 1 : 5 (using 4 g of clay) to measure electrical conductivity. The results obtained can be seen in Fig. 79, which shows that the electrical conductivity of the extract was below the one for the reference bentonite (908 µS/cm) in most of the barrier and increased drastically towards the liner in the 10 cm closest to it. This would be an indication of the huge concentration of soluble species in the proximity to the heater. On the contrary, the pH of the extract was higher than the initial one in the 40 cm closest to the granite and decreased sharply towards the heater.

CIEMAT analysed duplicate samples taken along three different radii from Sections S36 (in contact with the shotcrete plug), S47 and S53 (around the heater) and S59 (a cool section at the back of the gallery). To prepare the aqueous extracts CIEMAT crushed and air-dried the samples and mixed them with degassed, deionised water in a solid:liquid ratio 1 : 4 (with 10 g of clay). The suspensions were shaken and allowed to react under anoxic conditions for 24 h. After phase separation by centrifugation the supernatants were filtered through a 0.45-µm filter and the concentration of major cations analysed by ICP-AES, sodium and potassium by FAES and anions by ion chromatography. Since the concentration of most ions in the aqueous extracts is controlled by mineral dissolution processes and ion exchange reactions, the extraction conditions described aimed at suppressing mineral oxidation and avoid large modification of the cation exchange complex by calcite dissolution. The results obtained are presented and discussed in detail in Fernández et al. (2018). The analysis performed in that report showed that there were no significant differences between the three radii sampled in each section, i.e. that the concentrations measured depended basically on the distance to the gallery axis but not on the particular (y, z) coordinates inside the bentonite section. For this reason, the Figures below do not indicate the radii from which the samples were taken.

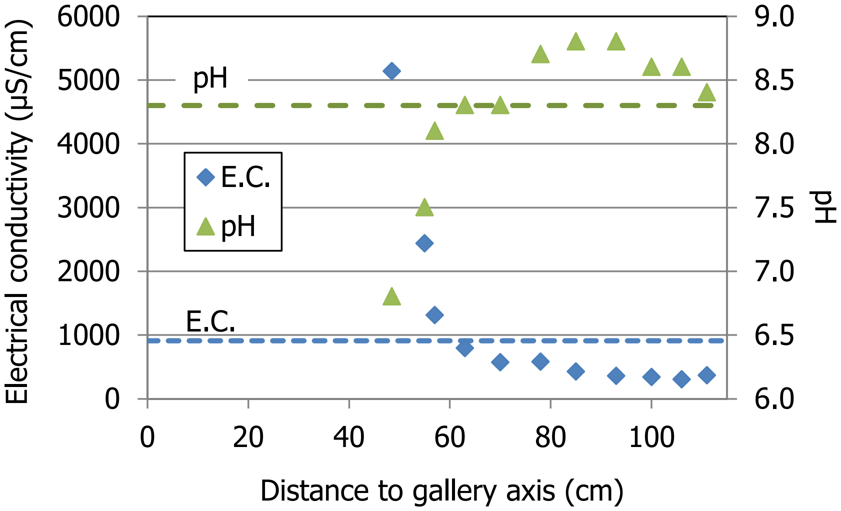

Fig. 79: Electrical conductivity and pH of aqueous extracts of solid:liquid ratio 1 : 5 (E.C.) and 1 : 2.5 (pH) prepared by UAM from samples of Section S45 taken along a radius (the dashed lines indicate the values for the reference sample).

The concentration of ions in the aqueous extracts was controlled by two factors: the advection of water coming from the granite and the thermal gradient around the heater. For this reason, the distribution pattern of most ions was different in the sections around the heater (S47 and S53) and in the cool Sections S36 and S59, particularly in the proximity to the heater.

In all the samples the main ions measured were sodium and chloride (Fig. 80), which controlled the pore water chemistry. In the external part of the barrier, close to the granite, the concentration of these ions decreased below the original values, especially in the heated sections. In particular chloride had been leached out of the 40 cm closest to the granite and concentrated in the proximity to the heater. The process was less intense for sodium and in the cool Section S59. In fact, although the relation between the concentrations of both ions was linear, the sodium content was always higher, which could be caused by ion-exchange reactions that could have been triggered by the dissolution of carbonates and sulphates. In fact, the sodium content in the exchange complex decreased on average with respect to the reference value (Tab. 10).

The distribution inside the barrier of other cations (calcium, magnesium) was similar to that observed for sodium (Fig. 81): a decrease below the initial value in the external, wettest part of the barrier and a concentration towards the axis of the gallery, very sharp in the sections around the heater. This pattern would indicate that these soluble species were transported by advection and concentrated in inner parts of the barrier (where they probably precipitated, as the comparison with the composition of the squeezed pore water shows, Section 5.5.2), but that the movement was enhanced by the thermal gradient, which points to other processes, in addition to advection, contributing to the ion concentration. The potassium concentration in the external part of the barrier was similar to the reference one, but increased towards the gallery axis, very sharply in the hot sections. Consequently, the overall potassium content increased with respect to that of the reference bentonite in a proportion much higher than for the rest of the ions.

The soluble sulphate was also depleted close to the granite and its concentration increased towards the internal part of the barrier; the maximum was found at a distance from the gallery axis that seemed to depend on temperature (Fig. 82). For the sake of clarity, the average of the measurements performed in all the samples taken at the same distance from the gallery axis in every section (i.e. along three different radii) are shown on the right hand of the Figure. The sulphate concentration front was sharpest in the two heated Sections S47 and S53 and in S36 which had been a hot section until the first dismantling. In contrast, the sulphate concentration increased in a broader central area of the cool Section S59. This pattern suggests that the water increase near the granite dissolved sulphate salts which were transported inwards, more slowly than chloride probably because of dissolution/precipitation processes. However, the high temperature seems to have hindered farther movement, and thus, the peak concentration for Section S47, the hottest one, was closer to the granite than that for Section S53.

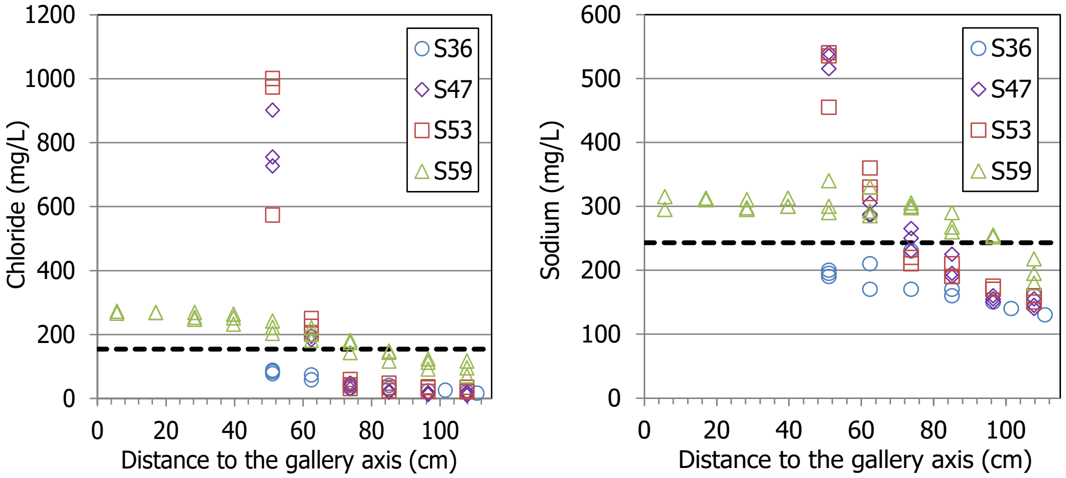

Fig. 80: Concentration of soluble chloride and sodium in 1 : 4 aqueous extracts of samples from several sampling sections (each symbol is the average of two subsamples)

The dashed horizontal lines indicate the concentration for the reference bentonite.

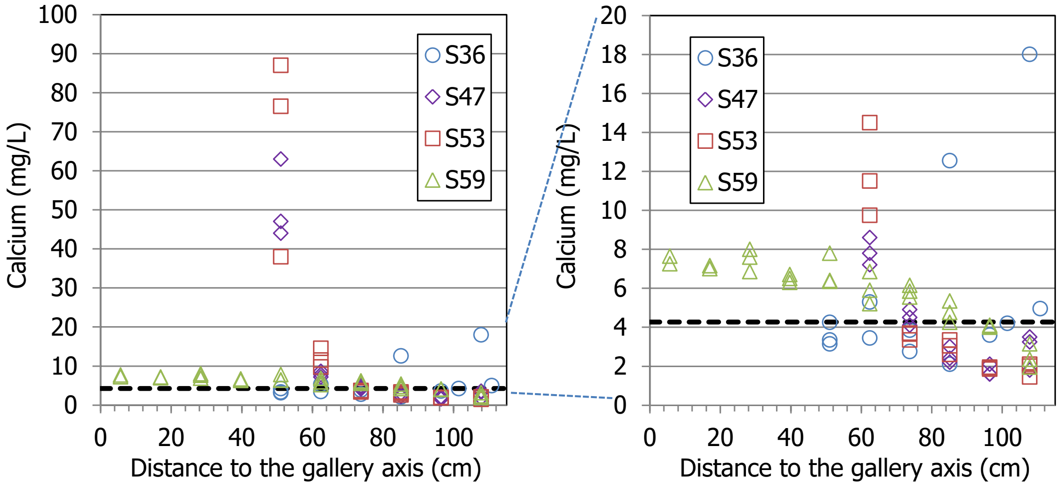

Fig. 81: Concentration of soluble calcium in 1 : 4 aqueous extracts of samples from several sampling sections (each symbol is the average of two subsamples).

The dashed horizontal lines indicate the concentration for the reference bentonite.

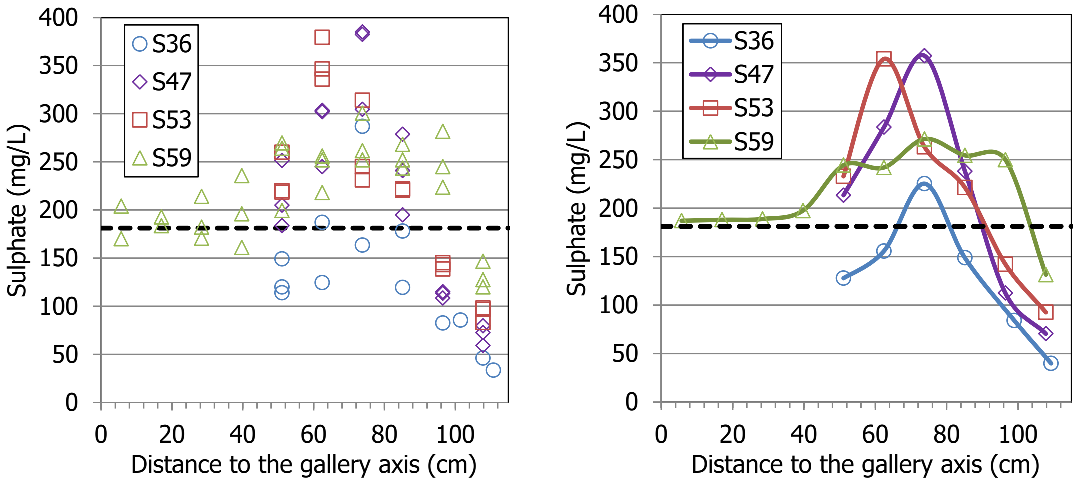

Fig. 82: Concentration of soluble sulphate in 1 : 4 aqueous extracts of samples from several sampling sections.

Left: each symbol is the average of two subsamples, right: average for all the samples taken at the same distance from the heater. The dashed horizontal line indicates the concentration for the reference bentonite.

The bicarbonate content in the aqueous extracts was higher than the reference value in all the more hydrated samples (those close to the granite). These bicarbonates could have come from the granite groundwater or from bentonite carbonates dissolution. This happened in approximately the 20 cm closest to the granite in the cool sections, from this distance inwards the bicarbonate concentration in the aqueous extracts remained at values similar to those of the reference bentonite or slightly below. In the hot sections (S47 and S53) the carbonate dissolution took place in a broader area, approximately a 35-cm thick more external part of the barrier. In contrast, from this distance inwards the bicarbonate concentration decreased with respect to the original value, which must be related to the precipitation of carbonates triggered by the decrease of their solubility with temperature. In fact, the temperature in the bentonite at distances from the heater smaller than 30 cm was higher than 70 °C (Martínez et al. 2016). The aqueous extracts' pH was alkaline, ranging from 8 to 9.2, and their changes followed similar patterns to those of bicarbonate (Fig. 83). These results agree quite well with those obtained by UAM in 1 : 2.5 aqueous extracts (Fig. 79). UAM analysed samples just at the contact with the liner, where pH dropped to values below 7.

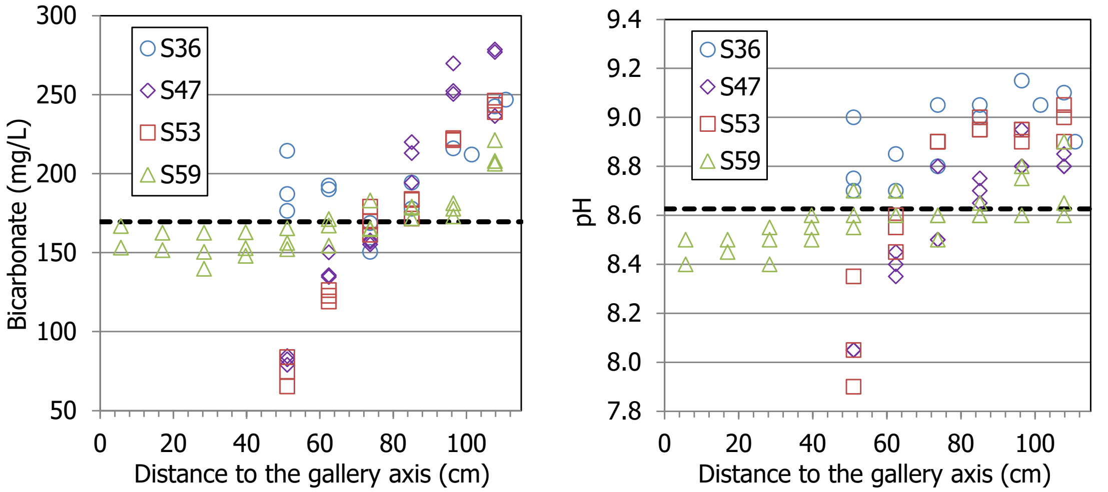

Fig. 83: Concentration of bicarbonate in 1 : 4 aqueous extracts of samples from several sampling sections and pH of the extracts (each symbol is the average of two subsamples).

The dashed horizontal line indicates the values for the reference bentonite.

The content of fluoride also increased above the reference value in the samples closest to the granite and tended to decrease below it towards the axis of the gallery. The increase was probably related to the high fluoride content in the groundwater, as was discussed in Section 5.3.1 on the bentonite's chemical composition, since an increase in fluorine content was observed (Fig. 68). Thiosulfate, which could be related to the reduction of sulphates or to the oxidation of sulphur minerals, was also found in some samples. Furthermore, acetate and formate were also found in the aqueous extracts. Both organic compounds are produced as fermentation products through the degradation of organic matter under anaerobic conditions. In particular, the acetate content increased significantly towards the heater.

The average concentration of ions in the aqueous extracts of the different sections analysed are shown in Tab. 11. An overall increase in the content of most ions took place because of the general increase in water content and the consequent dissolution of mineral species, which in some cases could have been enhanced by the high temperature. Only the bicarbonate content remained in values similar to those for the reference sample. Other ions not mentioned yet that appeared in low concentrations but almost systematically in all the samples were: bromide, nitrate, aluminium, strontium, iron and boron.

The soluble ions content and their spatial distribution was different in Section S36 as opposed to the other sections. Apart from the general trends on the chemical composition of the aqueous extracts that were commented above, Fig. 80 to Fig. 83 and the results in Tab. 11 show that the average concentrations of sodium, chloride and sulphate in Section S36 were clearly lower than those for the reference material. In contrast, unlike what happened in the other sections, the bicarbonate concentration and the pH were higher in Section S36. This section was submitted to a substantial thermal gradient during the first five years of operation, while Heater #1 was on. During this period, the ions would have been solubilised and transported according to the pattern expected under a thermal gradient as was observed in Sections S47 and S53. After Heater #1 extraction and partial dismantling, hydration of Section S36 took place under lower temperature for another 13 years. During this time, the effects of hydration under a thermal gradient that had occurred during the first five years of operation were more or less obliterated. Section S36 also showed the unique (relative to the other sections) effects of having been in contact with the shotcrete plug.

Tab. 11: Concentration of ions measured in 1 : 4 aqueous extracts (average of all the samples of a given section, in mmol/100 g).

	Chloride	Sulphate	Bicarbonate	Sodium	Calcium	Magnesium	Potasium	pH
Reference	1.98	0.83	1.29	4.79	0.05	0.05	0.03	8.6
S36	0.61	0.62	1.48	3.47	0.06	0.12	0.07	8.9
S47	2.26	1.12	1.28	5.46	0.13	0.18	0.18	8.1
S53	2.59	1.03	1.26	5.23	0.17	0.20	0.07	8.7
S59	2.48	1.04	1.26	5.65	0.07	0.08	0.06	8.6

The saturation indices computed from the modelling of the chemical composition of the aqueous extracts with PHREEQC (Parkhurst & Appelo 1999) showed that most samples were in equilibrium and/or oversaturated with calcite and dolomite; in equilibrium with quartz and chalcedony; and undersaturated with respect to gypsum, celestine, halite and fluorite.

5.5.2 Squeezing

The pore water of the bentonite samples was obtained at CIEMAT by the squeezing technique at high pressures (Fernández et al. 2018). The squeezing rig was designed to allow one-dimensional compression of the sample by means of an automatic hydraulic ram operating downwards, the squeezed water being expelled from the top and bottom of the cell through stainless steel porous disks. The compaction chamber was made of AISI 329 stainless steel with an internal diameter of 70 mm. The extraction was performed at room temperature. In order to collect the water at anoxic conditions, several cycles of Ar-flushing and vacuum were performed at the beginning of the tests and the water expelled was collected in a vacuum vial sealed by a septum (Fig. 84).

The bentonite samples for squeezing were prepared by trimming a cylindrical shape from the bentonite blocks using a knife (Fig. 85). The sample was then weighed and placed into the cell. A small stress of 1 to 10 MPa was initially applied to remove most of the atmospheric gas from the cell and allow the sample to bed in. After applying two additional Ar-flushing and vacuum cycles to the sampling circuit, the stress was progressively increased up to the selected pressure. When the maximum volume of squeezed water was obtained for a given pressure, the vial was removed, keeping the sample away from any contact with the atmosphere. The water sample collected was weighed and immediately analysed. During the squeezing test, the evolution of the pressure, axial strain and changes in the length of the sample due to consolidation were recorded over time by using a data acquisition system. At the beginning and the end of the tests, the samples were weighted, and their length and diameter were measured. The final water content and dry density were also determined.

Fig. 84: Extraction of pore water by the squeezing technique under anoxic conditions.

Fig. 85: Preparation of a sample for a squeezing test.

The water samples were filtered through 0.45 µm syringe filters, except those for pH and electrical conductivity measurements. The total alkalinity of the water samples was determined by titration; the major and trace cations and silica were analysed by Inductively Coupled Plasma-Atomic Emission Spectrometry (ICP-AES); sodium and potassium were determined by flame atomic emission spectrometry (FAES); ultra-trace elements were determined by ICP-MS; and anions were analysed by ion chromatography. Fluoride and iodide were determined with ion selective electrodes; the Fe(II)/Fe(III) ratio was determined by UV-Vis spectrophotometry with the ferrozine method. The non-purgeable organic carbon, which refers to the organic carbon present in a non-volatile form, was analysed with a TOC-VCSH analyser.

The samples analysed were taken along a radius at three sections: Section S36 (at the concrete interface), Section S47 (around the middle part of the heater) and Section S59 (at the back of the gallery). The minimum pressure necessary to obtain the quantity of water required for chemical analysis was applied. Thus, the pressure range was between 20 and 70 MPa, depending on the initial water content and dry density of the compacted samples. The amount of water extracted ranged between 6 and 17 mL for a given pressure step, when higher the higher the initial water content of the bentonite.

Some samples were squeezed at different pressures to analyse the influence of squeezing pressure on the chemical composition of the pore water. In this case, the pore waters obtained at each pressure step were collected and analysed separately. For all the ions, the concentrations measured were lower as the squeezing pressure increased. It has to be taken into account that the extractions at different pressures were performed successively in the same bentonite sample, and hence, the water sample for a higher pressure was obtained after a large quantity of pore water had already been extracted for the previous, lower squeezing pressure. In the following statement of results, only the analyses corresponding to the first extraction of each sample (the one at the lower pressure) have been considered.

The proportion of each ion in the pore water and their changes across the barrier followed similar patterns to those detected in the aqueous extracts. Indeed, the total concentrations were much higher in the pore water obtained by squeezing because of the different solid:liquid ratios and the dilution involved in aqueous extracts preparation. As in the case of the aqueous extracts, the main ions in all the pore water samples were sodium and chloride (Fig. 86). These ions, as well as calcium (Fig. 87), magnesium, strontium, bromide and nitrate, were below the reference value in the external part of the barrier and increased towards the axis of the gallery, both in the cool and hot sections.

The salt content in the aqueous extracts close to the heater was much higher in S47 than in cold Section S59 (Fig. 80). This would indicate that the soluble salts were precipitated around the heater. Sulphate was also depleted close to the granite and its concentration increased towards the internal part of the barrier; however, it was maximal at a distance from the gallery axis that was longer in the hot Section S47 (Fig. 87). In fact, near the heater the sulphate concentration was similar to the reference one. All the ions mentioned had concentrations below the reference concentration derived from samples taken in Section S36, similarly to what was found in the aqueous extracts. As observed in the aqueous extracts, the overall potassium content increased with respect to the reference value, even in Section S36.

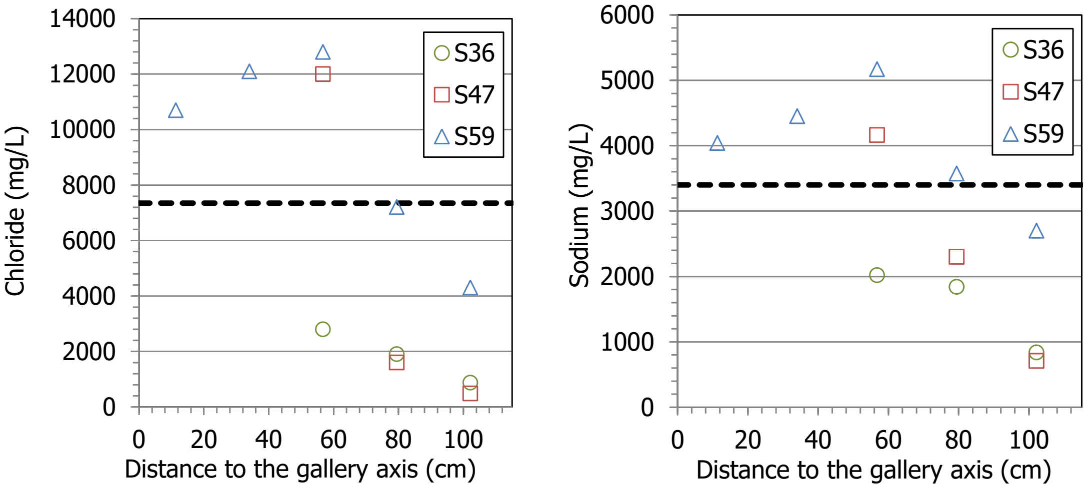

Fig. 86: Concentration of chloride and sodium in pore waters obtained by squeezing of samples from several sampling sections.

The dashed horizontal lines indicate the concentration for the reference bentonite.

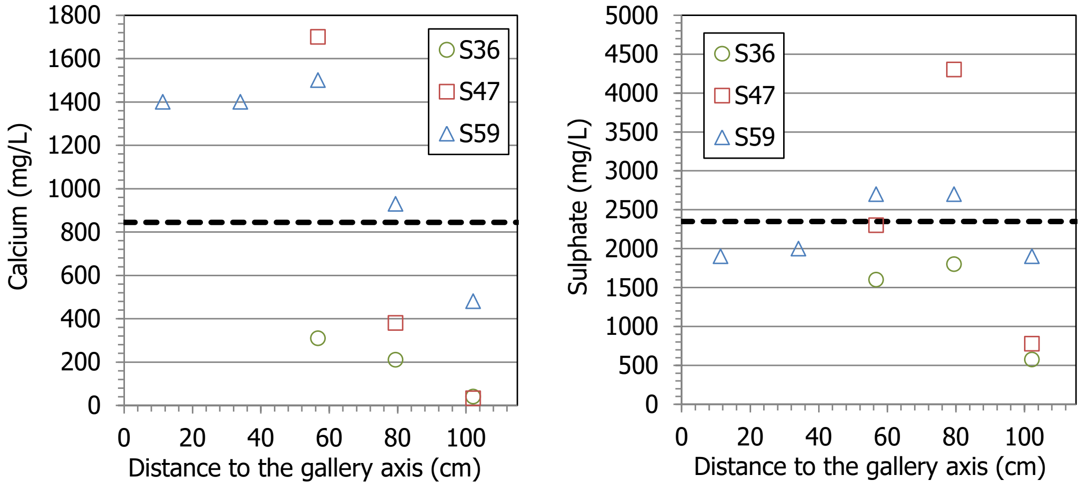

Fig. 87: Concentration of sulphate and calcium in pore waters obtained by squeezing of samples from several sampling sections.

The dashed horizontal lines indicate the concentration for the reference bentonite.

The pH values were slightly alkaline (7.6 to 7.9) and above the reference value (7.7) in the 40 cm closest to the granite in Sections S47 and S59. In the hot Section S47 the pH dropped to 6.8 in the proximity to the heater. The alkalinity was higher than the initial one in all the samples from Section S59 and in the external part of S47, i.e. in the more hydrated samples in which carbonate dissolution could have taken place.

The geochemical code PHREEQC (Parkhurst & Appelo 1999) was used for equilibrium modelling and saturation indices calculation. The pore waters were undersaturated with respect to calcite, gypsum and celestine, and saturated with respect to chalcedony and quartz in all samples, except in the central part of the buffer where pore waters were saturated with respect to gypsum in Sections S47 (heated) and S59 (non-heated).

6 Thermo-hydro-mechanical characterisation

Most thermo-hydro-mechanical properties of bentonite depend on its dry density and water content. In order to check if these properties changed during operation, two approaches were used:

- The samples to be tested were obtained by trimming the blocks to the appropriate size of the testing cells, attempting to preserve their dry density and water content, i.e. the same conditions in which they were received, and the results were compared either with those obtained in samples trimmed from a reference block (UPC, CT) or with those obtained with empirical correlations resulting from previous investigations relating these properties to the water content and dry density of the reference bentonite compacted to various dry densities and water contents (CIEMAT).
- The samples retrieved were remoulded to different dry densities and water contents and tested. The results obtained were then compared to those corresponding to samples of the reference bentonite specifically prepared in the same way (CT).

When analysing the hydro-mechanical properties of the bentonite retrieved from the FEBEX in-situ test, the changes experienced by the bentonite during on-site sampling and during preparation of specimens in the laboratory have to be taken into account. Although the samples were preserved carefully and their water content did not seem changed compared to the in-situ values during operation, the stresses in the barrier (which could be as high as 6 MPa during operation (Martínez et al. 2016)) were released upon dismantling, and this probably resulted in a decrease in the bentonite dry density. Additionally, the preparation of specimens to fit the testing rings required drilling and trimming, which caused a decrease in the final dry density of the samples tested with respect to that of the bentonite blocks from which they were taken. This decrease was not of the same magnitude in all cases, since it depended on the sample conditions and on the operator.

Nevertheless, the aim was to check if the THM properties reported here had changed irreversibly during operation with respect to those of the reference bentonite. For this reason, the values obtained are compared to those expected under the same testing conditions for the reference FEBEX bentonite. Hence, it has to be taken into account that some of the values measured (such as those concerning permeability and swelling) do not correspond to those the bentonite had in the barrier, where its dry density was higher and some boundary conditions (water availability and salinity, stress state) were different.

6.1 Thermal conductivity

The thermal conductivity (λ) of the bentonite was measured in situ by Nagra and in the laboratory by CIEMAT and ETH. The three organisations used methods based on the line source (hot wire) transient method, which is recommended for non-dry soils. The hot wire transient method is based on the exponential increase in the temperature of a thin hot wire that occurs when a constant power is applied (heat flux), while the wire is stretched in the centre of a cylindrical sample or a rectangular parallelepiped of infinite length. This allows the thermal conductivity of the material to be calculated on the basis of heat flux (power and intensity), the characteristics of the heating wire (length, radius and resistance) and the increase in temperature of the wire over a given period of time. The wire can be either inserted into the sample (needle sensor) or placed between the sample and an insulating material of known thermal conductivity (probe method). Both testing configurations are claimed to perform alike (Kyoto Electronics 1987).

The in-situ thermal conductivity measurements were performed using a handheld thermal analyser directly on the section surface in the FEBEX tunnel as soon as the surface became available (i.e., the disturbance to the material was kept as little as possible). The thermal analyser consisted of a handheld controller and a needle sensor that was inserted into the bentonite surrounded by thermal grease (Fig. 88). The laboratory measurements were performed at room temperature by placing the probe on a flat surface of the samples. In the case of ETH, the probe was pressed with a 5-kg weight on the surface of subsamples cut from the blocks (Fig. 89, left). CIEMAT measured the thermal conductivity at two different positions on the surface of the blocks, the plastic film around the blocks was removed only at the measurement position to avoid any water content changes during the measurement (Fig. 89, right).

All the in-situ measurement results (four sections, five layers) are shown in Fig. 90. The results show no clear spatial variations and no distinct difference between hot (S46, S53) and cool (S58, S61) sections. In general, the λ values were constant in the radial direction with a mean of 1.28 ± 0.06 W/m·K. The thermal conductivity measured in the two laboratories on the surface of the blocks is shown in Fig. 91. There is not a clear relation between the position of the blocks in the barrier and the thermal conductivity, which in the case of CIEMAT is mostly clustered between 1.1 and 1.3 W/m·K. The values obtained by ETH are considerably lower, ranging from 0.8 to 1.1 W/m·K. The reason could be the drying of the block during the preparation of the subsamples for measuring, since circular samples of the same surface as the probe were trimmed. Fig. 92, in which all the results are plotted together, highlights the fact that the thermal conductivities measured in situ are on average higher than those measured in the laboratory.

Fig. 88: Thermal analyser used by Nagra for the in-situ determinations during dismantling (the syringe contained the thermal grease) and needle sensor.

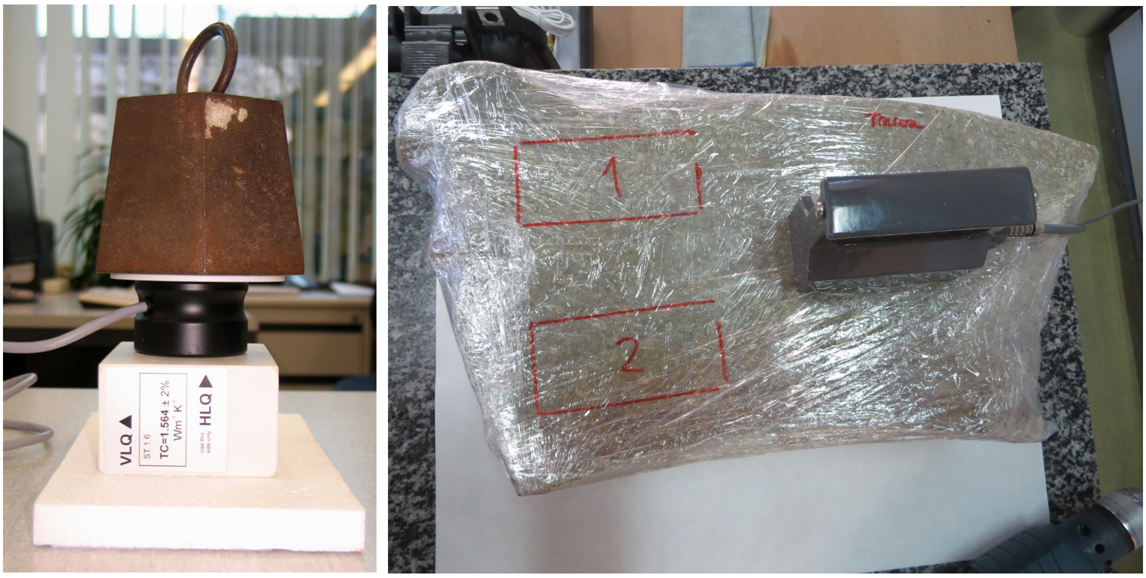

Fig. 89: Measurement of the thermal conductivity of a standard material (ETH, left) and of a bentonite block (CIEMAT, right).

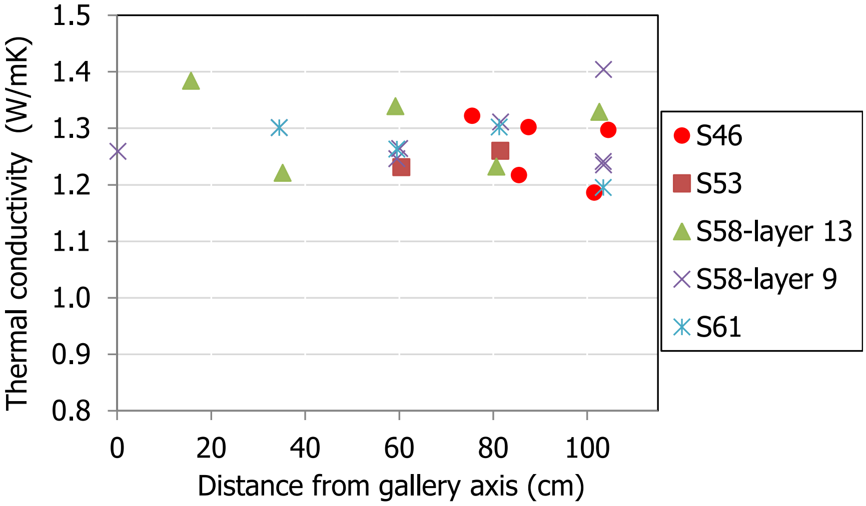

Fig. 90: Thermal conductivity measured in situ by Nagra in different sampling sections.

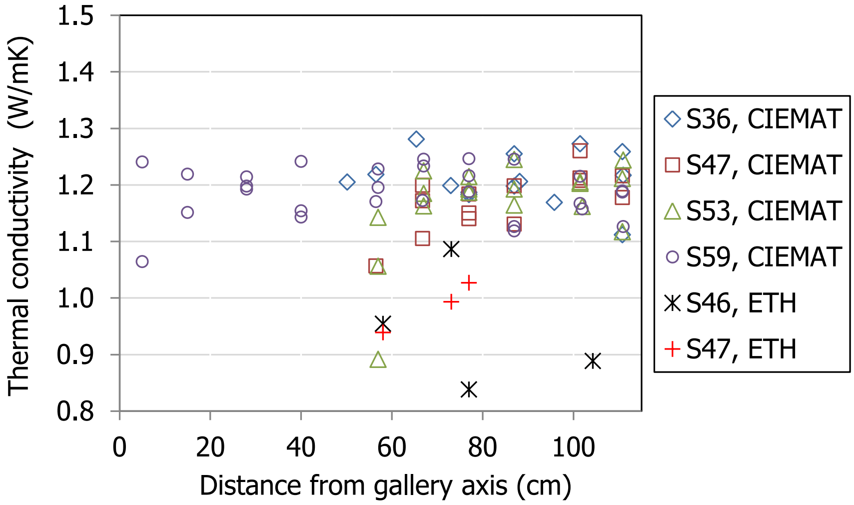

Fig. 91: Thermal conductivity measured at CIEMAT and ETH on blocks taken from different sampling sections.

It is known that thermal conductivity depends on water content and dry density and consequently on degree of saturation. For this reason, the values have been plotted again as a function of degree of saturation in Fig. 93. To plot these values the thermal conductivity measured in situ was related to the water content and dry density of samples taken as close as possible to the point where the λ was measured. For Sections S58 and S61 an interpolation of the values measured on site in these same sections (Villar et al. 2016) has been used. For Sections S46 and S53 (both layers) the water content and dry density values measured on site in the nearby Sections S45 and S52, respectively, have been interpolated. The ETH values were correlated to the degree of saturation values measured in equivalent locations in Section S47 at CIEMAT laboratories. A trend for the thermal conductivity to decrease with the degree of saturation can be observed. Also, except for samples of Section S58, there is more coherence between the values obtained in situ and in the laboratory. Nevertheless, a large dispersion is visible, possibly because the samples tested had a broad range of water content and dry density. The fact that most of the samples were close to full saturation makes it difficult to establish clear dependences, because the range of thermal conductivities measured is too narrow.

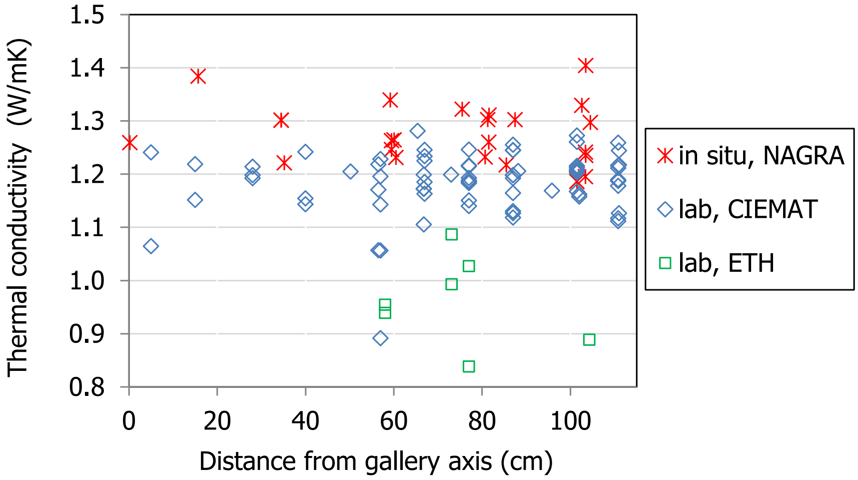

Fig. 92: Comparison of the thermal conductivity values measured in situ and in the laboratory in different sections.

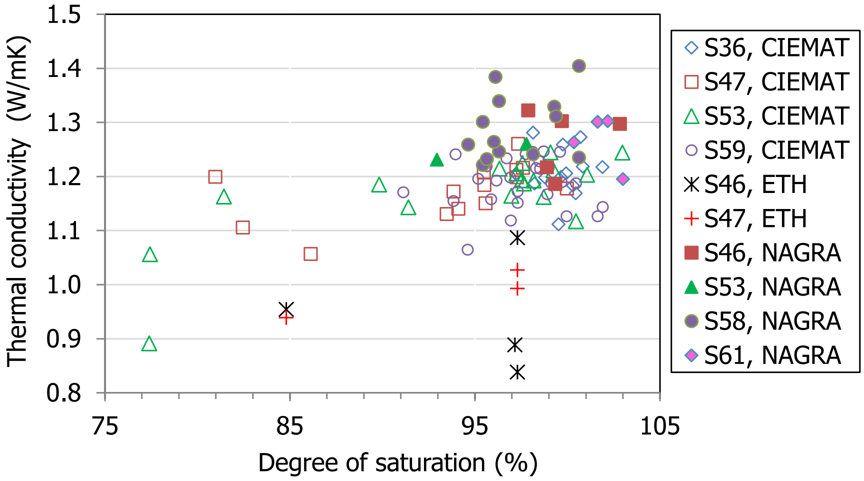

Fig. 93: Thermal conductivity measured in situ (filled symbols) and in the laboratory as a function of the degree of saturation for different sampling sections.

In Fig. 94 the values have been plotted again, grouped according to the dry density as a function of the water content of the samples. Although the dispersion is still large, it becomes clear that samples of different water content could have the same thermal conductivity, but the dry density of these samples lowers with higher water content. The Figure also highlights that for similar water contents and dry densities the thermal conductivity measured in situ was higher than that measured in the laboratory. There are two possible explanations for this difference:

- The stress state, which was higher in the measurements taken in situ since the blocks had not been released from the barrier when the measurements were done, had an effect on thermal conductivity, causing it to be higher. However, ETH measured the thermal conductivity in the lab by applying a vertical stress to the samples and the values obtained were lower than those obtained at CIEMAT with no load application. On the other hand, the samples tested at ETH experienced considerable handling and trimming to be prepared, which could have induced small micro-cracks that adversely affected the thermal conductivity.

- In Fig. 93 and Fig. 94 the thermal conductivity measured in situ was correlated to values determined on site from samples drilled in nearby locations. As it was stated in Villar et al. (2016), the degrees of saturation measured in these samples were possibly lower than those of the bentonite in the barrier, because a decrease of dry density occurred during sampling and trimming. Consequently, the actual degree of saturation and dry density of the unreleased blocks on which thermal conductivity was measured were higher than those of the samples retrieved by drilling and analysed on site. This is the preferred explanation.

In order to check if the thermal conductivity of the bentonite changed during operation, empirical relationships between thermal conductivity (λ, W/mK) and water content (w, %) as a function of the bentonite dry density (ρ_d, g/cm^3) have also been plotted in the Figure:

$$\ln \lambda = \ln (0.8826\ \rho_d - 0.8909) + 0.003\ w \qquad [1]$$

These relationships were determined from measurements performed with the same methodology as used in the laboratory by CIEMAT on samples of untreated FEBEX bentonite compacted to different dry densities with various water contents (Villar 2002). Despite the dispersion of the values, the comparison between values obtained with the same methodology (i.e. measured in the lab by CIEMAT) points to a clear preservation of the thermal conductivity of the bentonite after operation.

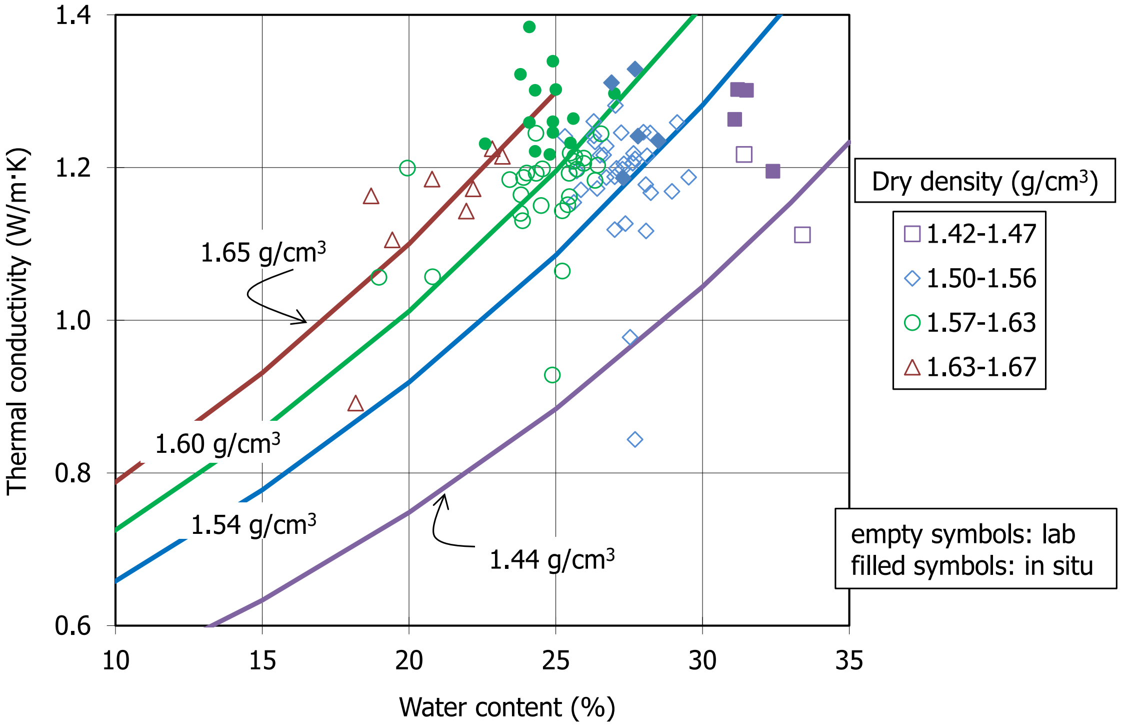

Fig. 94: Dependence of thermal conductivity of bentonite measured in situ and in the laboratory (CIEMAT) on water content and dry density and empirical relationships for the FEBEX reference bentonite.

6.2 Swelling pressure

The swelling pressure and hydraulic conductivity were determined by ClayTech using the test equipment shown in Fig. 95. The specimens were confined by a cylindrical ring with a diameter of 50 mm or 35 mm and stainless steel filters at the top and bottom. At the beginning of the test, the height of the test volume was fixed to approximately 10 mm. The swelling pressure developed by the samples on saturation was determined by the load cell placed between the piston and the upper lid. The sample was saturated by circulating deionised water first from an inlet below the specimens and then, 24 hours later, also from above. During the tests the confined volume set at the start was kept almost constant. Once a constant value of swelling pressure was reached, the hydraulic conductivity of the same samples was measured as described in Section 6.6.

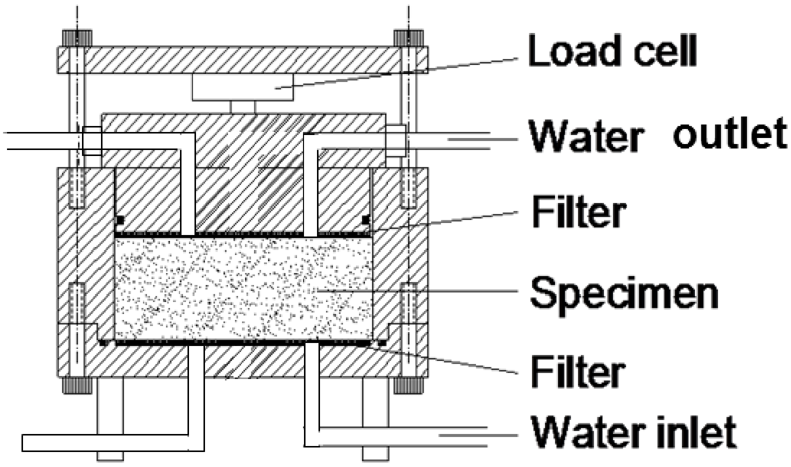

Fig. 95: Schematic drawing of the swelling pressure device used by ClayTech.

The aim of these tests was to analyse any effect of the repository-like conditions on the bentonite swelling pressure, not to determine the absolute value of the property in situ. With this objective in mind, the following samples were tested:

- Specimens trimmed from blocks from Section S47. The block from the innermost bentonite ring had a lower water content than expected (see Section 4.1) and it was difficult to trim good-shaped specimens from it. This is the reason why the dry density of some of the trimmed samples is below 1.4 g/cm^3 and hence not representative of the barrier density during operation.
- Remoulded specimens obtained by grinding the bentonite from blocks of Section S47 to a grain size less than 1.5 mm and re-compacting the granules obtained at dry densities of 1.56 to 1.60 g/cm^3. The initial water content values of the samples were between 15 and 22 %.
- Remoulded specimens obtained by grinding the bentonite from a block compacted along with the others in 1996 but not used at the installation. The material was ground to a grain size less than 1.5 mm and the granules were re-compacted at a range of dry densities. The values obtained in samples from this block were considered reference values. The swelling pressure of the retrieved samples was compared with these reference values in order to evaluate any changes.

The results are plotted in Fig. 96 as a function of the dry density of the samples after stress release and extraction out of the cell, which was determined by immersion in paraffin oil of a sample half. The exponential increase of swelling pressure with dry density is clear. When results from the material sampled from the field experiment are compared to those of the reference material, no large deviations are observed. The largest deviation in the pre- and post-FEBEX measurements is the reduction of swelling pressure found in some of the remoulded specimens from the innermost ring of the barrier.

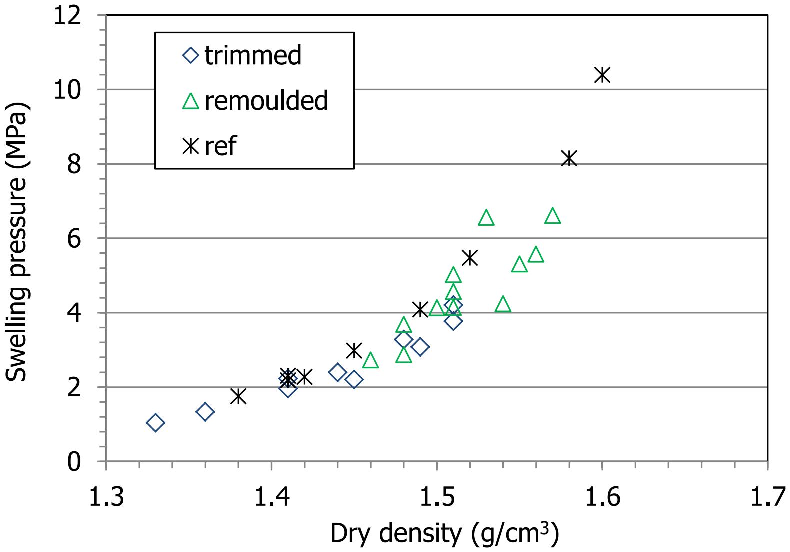

Fig. 96: Swelling pressure of trimmed and remoulded samples from Section S47 and of remoulded samples from a reference block (crosses) obtained by ClayTech (the dry density is determined after extraction of the oedometer ring).

6.3 Swelling capacity

The saturation (or swelling) under load test makes it possible to determine the strain capacity of the soil when it saturates under a previously established pressure. The swelling capacity of 20 samples taken at different distances from the heater from three different sections (S36, S47 and S53) was tested by CIEMAT.

To perform the swelling under load tests, the specimens were drilled from the blocks and subsequently trimmed, so that they fit tightly in the oedometer rings, with a diameter between 3.6 and 5.0 cm. The resulting height of the samples was between 1.2 and 1.8 cm. The trimming and fitting process meant a decrease of the density of the specimen in the oedometer ring with respect to the original dry density of the block in most cases. This implies that the swelling capacity of the samples tested was smaller than that of the blocks, because swelling capacity increases with dry density.

The tests were performed in standard oedometers following approximately ASTM D 4546-85 Method A. Once in the oedometer, a vertical pressure of 0.5 MPa was applied to the samples. After stabilisation of the deformation, the samples were saturated with deionised water at atmospheric pressure from the bottom porous plate. The swelling strain experienced by the specimens upon saturation was recorded as a function of time until stabilisation by linear strain transducers connected to a Data Acquisition System (DAS). During most of the tests, the electrical conductivity of the water in the oedometer cell's reservoir was measured with an electrical conductivity meter, which was submerged in the oedometer water every time the reservoir was refilled with deionised water. Water refilling was done to keep the water level in the cell approximately constant.

The final vertical strain (ε) was computed as the ratio between the change in height experienced by the sample and the initial height, the negative values indicating swelling. On completion of the tests, the water content of the specimen was determined by oven-drying at 110 °C for 48 hours. It was verified that all the specimens were fully saturated. The tests were performed at laboratory temperature.

As an example of the results obtained, the evolution of the vertical stress during the swelling deformation tests of samples from Section S47 is shown in Fig. 97. Note that negative strain indicates volume expansion (swelling). The dry density and water content of the samples at the beginning of the swelling tests is also indicated in the Figure. The final strains reached by all the samples tested are plotted in Fig. 98 as a function of the distance to the gallery axis. Indeed, the samples closer to the gallery wall had higher initial water content and lower initial dry density. The swelling capacity is related to both, increasing with initial dry density and decreasing with initial water content. For this reason, the final strain of the samples closer to the heater was higher. It also took longer for the deformation of these samples to stabilise.

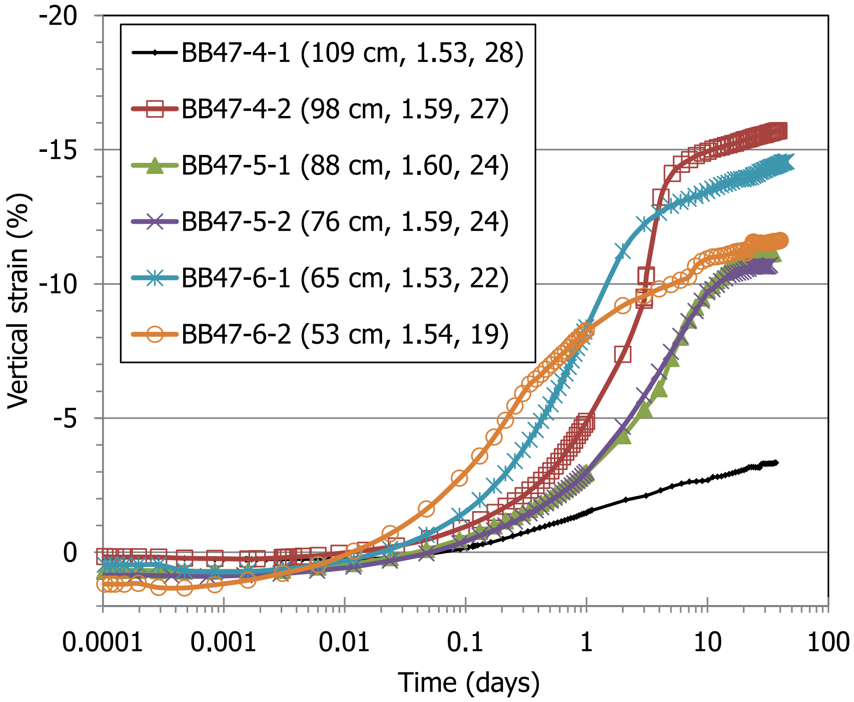

Fig. 97: Evolution of vertical strain during the swelling under 0.5 MPa stress for samples of Section S47.

The distance to the axis, and the dry density (g/cm^3) and water content (%) of each sample at the beginning of the swelling tests are indicated in the legend.

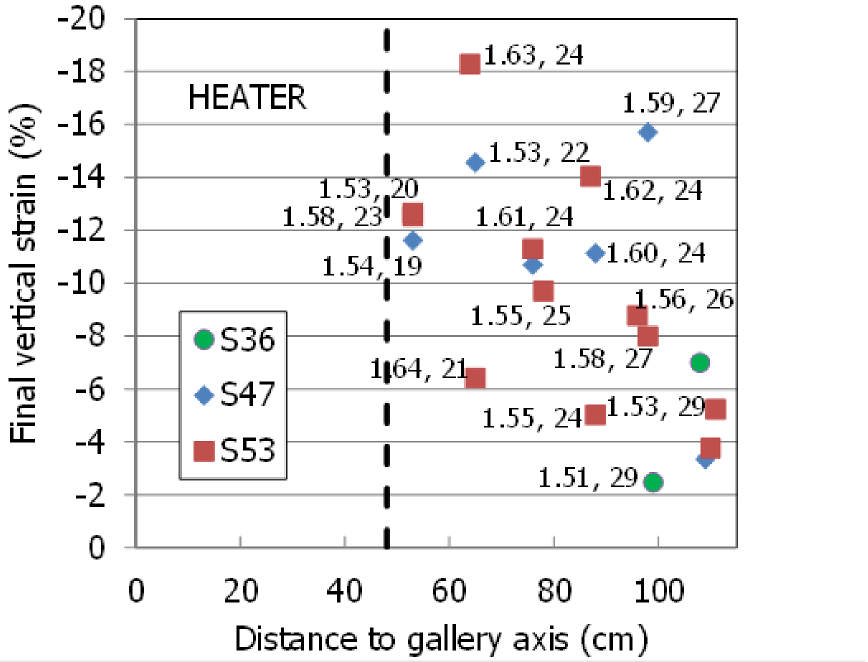

Fig. 98: Final vertical strain for samples of different sections saturated under vertical stress 0.5 MPa (the initial dry density and water content of some of the specimens is indicated in g/cm^3 and %).

In order to assess the modification of the swelling capacity of the bentonite as a result of the 18-year-long operation, the final vertical strain measured has to be compared with the final vertical strain of samples of the reference FEBEX bentonite of the same initial dry density and water content saturated under the same conditions, i.e. with the same vertical load and kind of water, since all these parameters affect the swelling capacity. Based on numerous swelling under load tests performed with the FEBEX reference bentonite compacted to different initial dry densities (ρ_{d0}, g/cm^3) with different water contents (w_0, %), an empirical relation predicting the final swelling strain (ε, %) after saturation with deionised water under vertical load of 500 kPa was found (Villar & Lloret 2008):

$$\varepsilon = (37.48\, \rho_{d0} - 50.43) \ln w_0 - 154\, \rho_{d0} + 204.24 \qquad [2]$$

The results obtained in the samples from the FEBEX-DP have been compared with the corresponding theoretical values obtained with this expression in Fig. 99. On average, the vertical strains measured were lower than the theoretical ones (-10 % *vs*. -12 %). Fig. 99 also includes the distance to the gallery axis of the samples. Most samples from the external, more saturated bentonite ring swelled less than expected, whereas the samples from the inner, drier ring tended to swell as expected or more. This could be related to their higher initial salinity, which would have brought about some osmotically-driven swelling. The higher salinity in the pore water of the samples close to the liner and the very low salinity (much lower than initial) of the samples from the external ring have been discussed in Section 5.5.1.

The electrical conductivity of the water in the oedometer cells was measured during the tests. In the tests performed with samples from the inner ring, the electrical conductivity increased considerably during the tests, which would indicate that the soluble salts in the bentonite were diffusing into the deionised water in the oedometer cell's reservoir, gradually reducing salinity in the specimen pore fluid. In contrast, the electrical conductivity of the water in the oedometer cells in which samples from the external ring were being tested barely increased during the tests, indicating that there was limited soluble salts present in their pores. Fig. 100 shows the simultaneous evolution of swelling strain and electrical conductivity of the water in the oedometer cell for two samples of Section S53, one of them obtained from the external ring and the other one from the internal ring. Because of trimming, the initial dry density of these two specimens was similar, despite the fact that the blocks from which they were obtained had considerable different densities (Fig. 14). The sample from the internal ring swelled more and for longer, with the electrical conductivity of the water in the oedometer cell increasing considerably, particularly after 10 days, when most swelling had already been developed. This could indicate that the osmotically-induced part of swelling (indicated by the increase in electrical conductivity, as the soluble species left the bentonite) was less important and was not remarkable until the crystalline swelling had been completed. This process did not take place in the reference bentonite or in the more saturated bentonite from the external ring, because in both cases the salinity was lower. It has to be highlighted that this is a process that took place because the samples were left swelling under a low vertical stress in a relatively large volume of water, these conditions were not encountered in the barrier during operation.

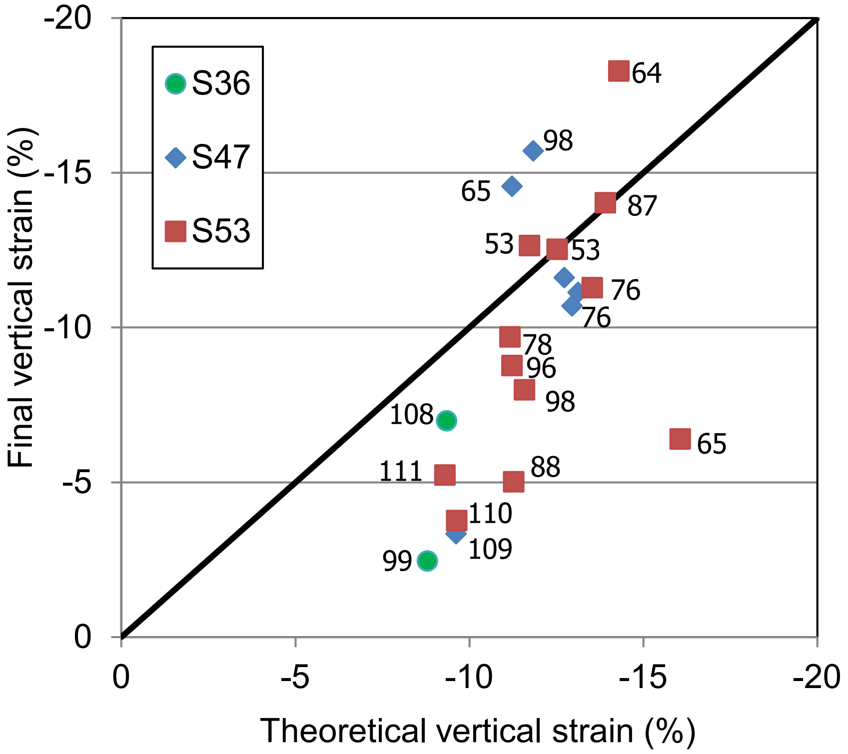

Fig. 99: Comparison between the vertical strain measured at the end of the swelling under load tests and the strain corresponding to equivalent samples of the reference bentonite tested under the same conditions obtained with the empirical relation [2].

The distance to the gallery axis of each sample is indicated in cm.

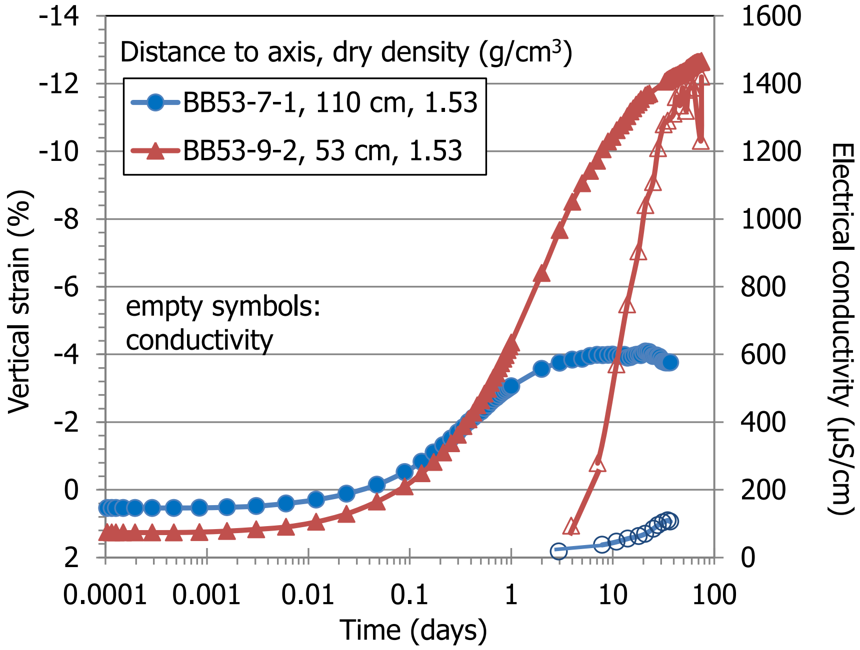

Fig. 100: Evolution of vertical strain and electrical conductivity of the water in the oedometer cell during the swelling under 0.5 MPa stress for two samples of Section S53.

6.4 Volume change behaviour on loading

The compression and consolidation tests presented in the following sections aimed at defining the pre- and post-yield compressibility parameters and the preconsolidation stress of the bentonite recovered from FEBEX under oedometric and isotropic conditions. Compression refers to the volume change behaviour on loading starting from partially saturated conditions and with virtually no outflow of pore water, whereas consolidation involves the expulsion of pore water on loading. Such data are important to complement the available information on intrinsic material parameters of FEBEX bentonite used in constitutive models. Their knowledge also allows identifying if these parameters (related mainly to volume change behaviour) underwent changes during the long-term *in-situ* experiment, and thus identifies alterations on the hydro-mechanical properties of the bentonite. The information on preconsolidation stress is important to compare and validate predicted yield loci based on the stress, suction, temperature and chemical paths followed under *in-situ* conditions with new laboratory data coming from post-mortem analyses.

6.4.1 High-stress oedometer tests

The objectives of these oedometer tests are:

- To define the preconsolidation stress (σ'_p) induced by the different stress paths followed during operation (changes in stress, temperature, suction and geochemistry)
- To determine the post-mortem pre- and post-yield compressibility parameters (compression and swelling indices)

These changes can be assessed by performing oedometer tests either at constant suction pressure or at constant water content. Compression tests at constant water content involve increasing the degree of saturation (and suction decrease) until the sample reaches full saturation with pore water expulsion on further loading. The first methodology (i.e. at constant suction pressure) was used by CIEMAT to test five samples of Section S47 (around the heater) and two samples from the reference bentonite, whereas UPC followed the second methodology (i.e. at constant water content) to test eight samples from Sections S50 (around the heater) and S57 (cool section) and a sample obtained from a reference block manufactured in 1996 along with those used in the in-situ test.

To perform these tests CIEMAT used two oedometer cells adapted to withstand the high pressure applied by an oedometric frame equipped with a load cell (Fig. 101). Cylindrical samples of a height between 1.4 and 1.8 cm and a diameter of 3.9 cm were drilled from the bentonite blocks and laterally sanded or scraped to fit the diameter of the oedometer ring. The vertical deformation of the specimen during the test was measured by two linear variable differential transformers (LVDTs).

The samples were tested under the suction measured with psychrometers or capacitive sensors (Section 4.4.2). The water content and dry density of the adjacent clay was checked. The suction inside the cells was set by means of sulphuric acid solutions. The sample was left to equilibrate at the target suction under a low vertical load. Afterwards, the sample was loaded progressively up to 32 MPa. Each loading step was kept until stabilisation of the deformation. The tests were performed at laboratory temperature.

UPC performed the consolidation tests in the oedometer shown in Fig. 102, in which three very stiff cells can be stacked and used simultaneously. The samples were trimmed to fit the oedometer rings, with a diameter of 3.0 cm and a height of 1.0 cm. The loading paths, from 0.6 to 56.6 MPa started at the as-retrieved water content. These paths may have induced matric suction changes in the bentonite, which were not recorded during loading/unloading, because only initial and final values were measured. Since all samples were close to saturation, the constant water content loading paths brought them to saturation.

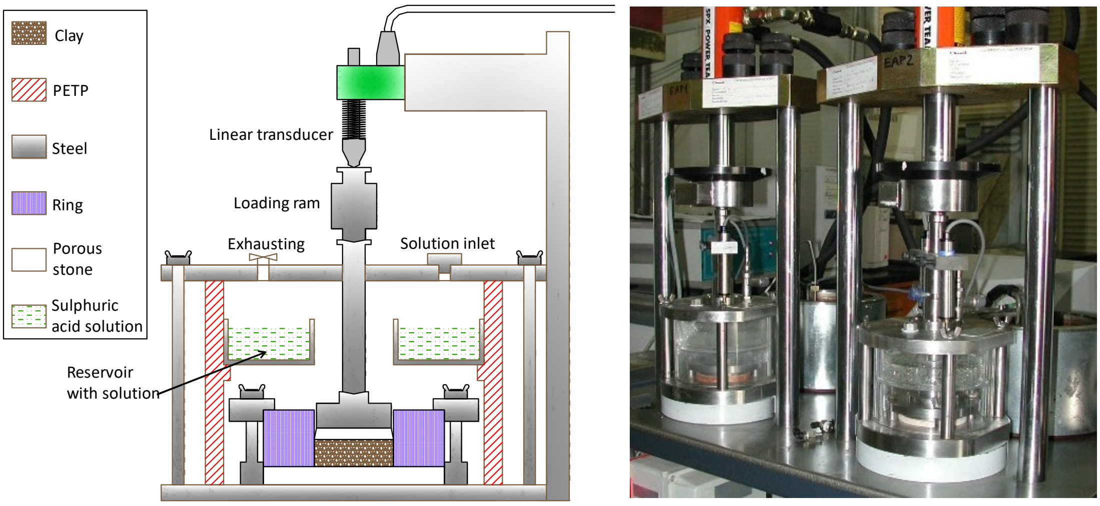

Fig. 101: Schematic cross section of an oedometric cell with vessel for solutions used by CIEMAT (left) and cells installed in the frames for high-pressure consolidation tests (right).

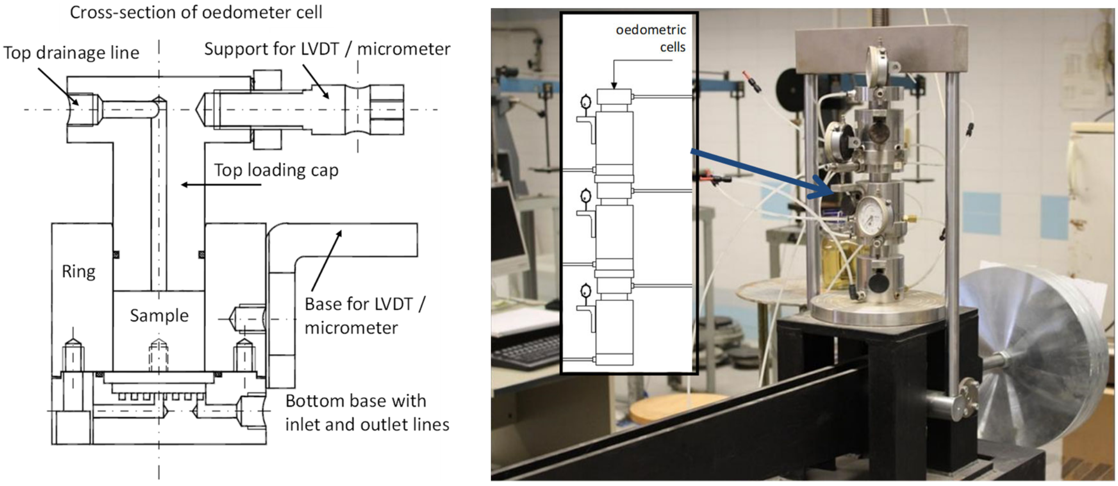

Fig. 102: Cross-section of high-stress oedometer cell and loading frame with stacked cells and lever mechanism used by UPC.

Fig. 103 shows the compression and consolidation curves for one of the tests performed by UPC, and Fig. 104 shows the same kind of results for a test performed by CIEMAT. The compression during the first steps, corresponding to the low stresses, was on average relatively fast, indicating that the material was still partially saturated. As loading proceeded, the samples became saturated and the volume change rate decreased, because the material required more time to dissipate the excess pore pressure generated on loading (consolidation stage). This happened both in the tests performed under "approximately" constant water content by UPC and in those performed under constant suction by CIEMAT. On final unloading the swelling strain was very limited, which indicates the irreversibility of the deformation occurred during loading at high stress. In the case of the UPC tests, the unloading paths were mainly carried out under water undrained conditions, although at the early unloading stage some deformation was detected associated with the limited inlet of water from the porous stones (this stored water was expelled during the loading path).

The degree of saturation computed for the different steps considering the density of water as 1 g/cm^3 turned out to be considerably higher than 100 %. In high-density bentonite there is a predominance of interlayer-adsorbed water over free water; the density of this interlayer – adsorbed water is higher than 1 g/cm^3. UPC corrected the degree of saturation values by considering a constant pore volume inside aggregates (intra-aggregate void ratio, e_m), a constant density of water inside this intra-aggregate pore volume, as well as a constant density of water (1.0 g/cm^3) at the inter-aggregate porosity equivalent to free water (Romero et al. 2017). The intra-aggregate void ratio, $e_\mathrm{m} = 0.40$, was taken as the void ratio for pore sizes below 50 nm obtained from the MIP (Section 4.3.2). With this, the average water density necessary to get values of degree of saturation of 100 % for each step in which saturation was reached was computed, and the change of water density with bentonite dry density estimated. For example, for sample BB-50-7, whose void ratio decreased during the loading stage from 0.708 to 0.437, the average water density increased from 1.14 to 1.22 g/cm^3. These values agree well with those proposed by Villar (2002) for the FEBEX bentonite.

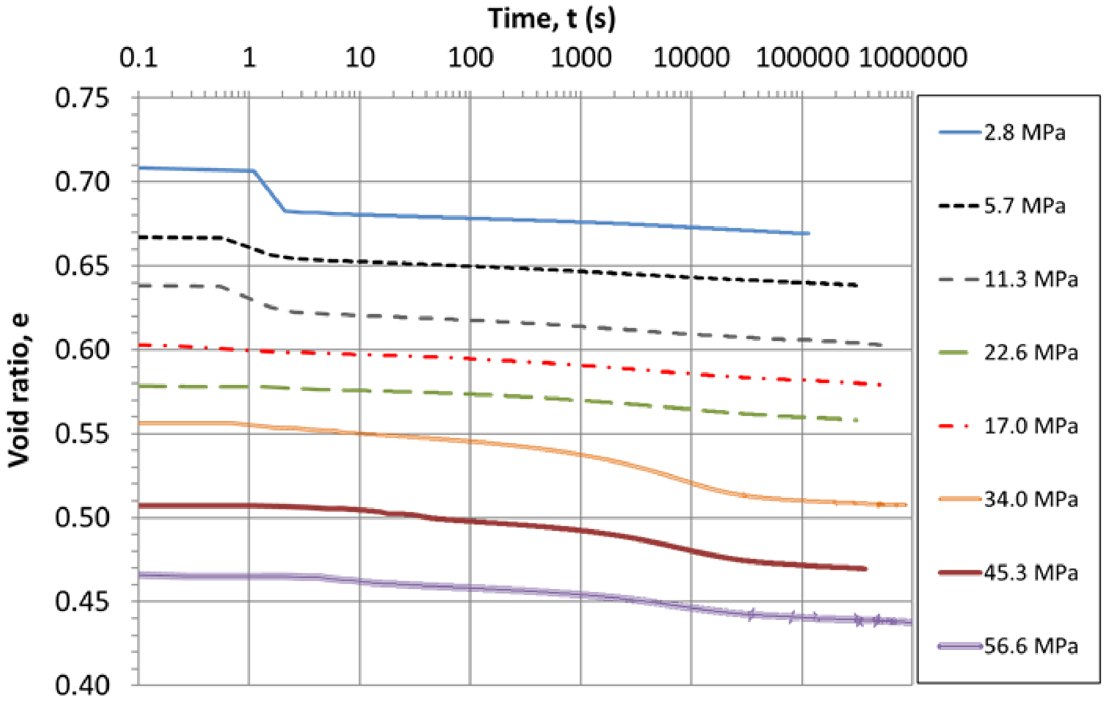

Fig. 103: Time evolution of void ratio during step loading of sample BB-50-7 (taken at 102 cm from gallery axis) at water content from 25.0 to 21.7 % (UPC).

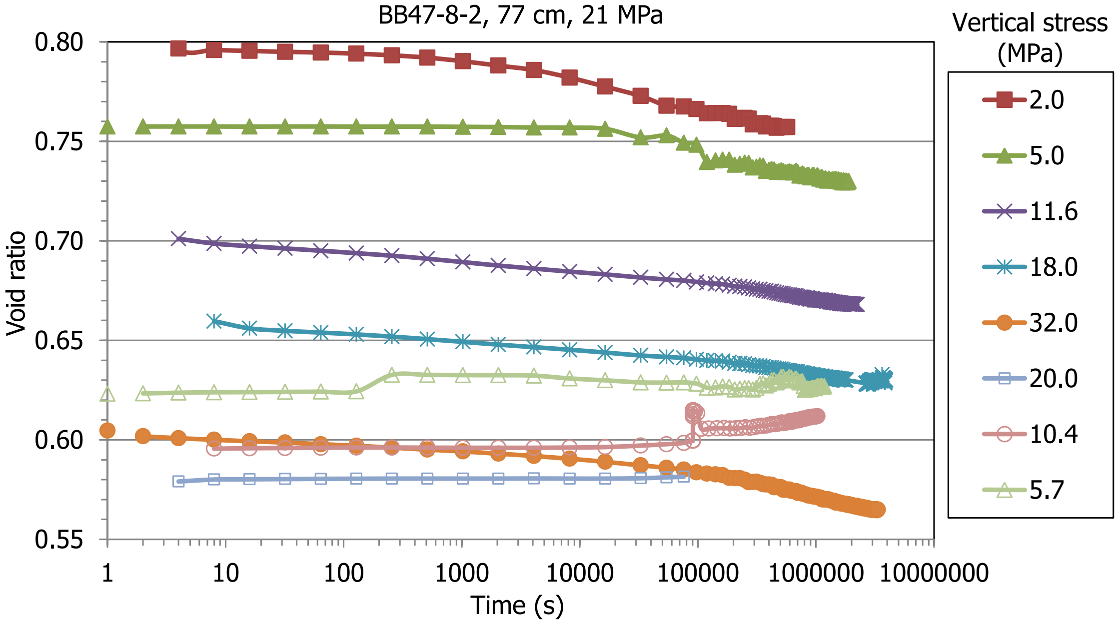

Fig. 104: Time evolution of void ratio during step loading/unloading of sample BB47-8-2 (taken at 77 cm from gallery axis) under constant suction 21 MPa (CIEMAT).

The time evolution of soil deformation under saturated conditions was interpreted by back-analysis to determine the different parameters used in consolidation analysis following Terzaghi's theory (Romero et al. 2017). These parameters are: d_o (initial displacement mainly due to cell deformability), E'_m (drained constrained modulus of elasticity), c_v (coefficient of consolidation), C_α (coefficient of secondary consolidation), t_{90} (time required for 90 % of average consolidation) and k_w (water permeability determined using c_v and E'_m results). As an example, the parameters found by UPC for each loading/unloading step for sample BB50-7 are shown in Tab. 12. The coefficient of consolidation decreased as the vertical stress increased until approximately 30 MPa. For further loading/unloading steps, the coefficient of consolidation remained approximately constant and around 0.004 mm^2/s. The coefficients of consolidation found by CIEMAT were at least one order of magnitude lower.

The values fitted by CIEMAT and UPC for water permeability have been plotted in Fig. 105. The fitted values correspond only to the higher load steps in which the computed degree of saturation indicated full saturation. The values measured under constant hydraulic gradient by CIEMAT in retrieved, trimmed samples and the empirical correlation for the reference bentonite and its range of variation are also shown in the Figure (see Section 6.6). In the UPC test of sample BB50-7, as the vertical stress increased from 17 to 57 MPa, the water permeability decreased irreversibly from 1×10^{-13} to 1.8×10^{-14}. Hence, the values obtained by UPC at the beginning of the consolidation were higher than those expected for the reference bentonite, whereas for the higher consolidation stresses (and consequently lower void ratios), the values obtained were in the order of those expected for the reference, untreated bentonite. In contrast, the permeability values fitted from the consolidation tests performed by CIEMAT were lower than expected for the reference bentonite with the same void ratio, as a consequence of the low back-analysed coefficients of consolidation.

Tab. 12: Fitted consolidation parameters for sample BB50-7 (UPC).

Vertical stress, σ_v (MPa)	***e***	**d_o** (µm)	**E'_m** (MPa)	**c_v** (mm^2/s)	**C_α**	**k_w** (m/s)	**t_{90}** (s)
17.0	0.579	30.54	1'623	0.0163	0.0010	9.8×10^{-14}	3'440
22.6	0.558	18.69	1'840	0.0156	0.0014	8.3×10^{-14}	3'470
33.9	0.508	51.85	991	0.0039	0.0013	3.9×10^{-14}	13'600
45.3	0.469	20.00	1'150	0.0040	0.0015	3.4×10^{-14}	12'300
56.6	0.437	39.53	2'034	0.0038	0.0011	1.8×10^{-14}	12'400
22.6	0.472	-10.00	2'962	0.0028	0.0000	9.1×10^{-15}	16'300
11.3	0.483	-6.00	3'900	0.0041	0.0000	1.0×10^{-14}	11'400
0.6	0.491	-6.00	4'511	0.0033	0.0000	7.1×10^{-15}	14'600

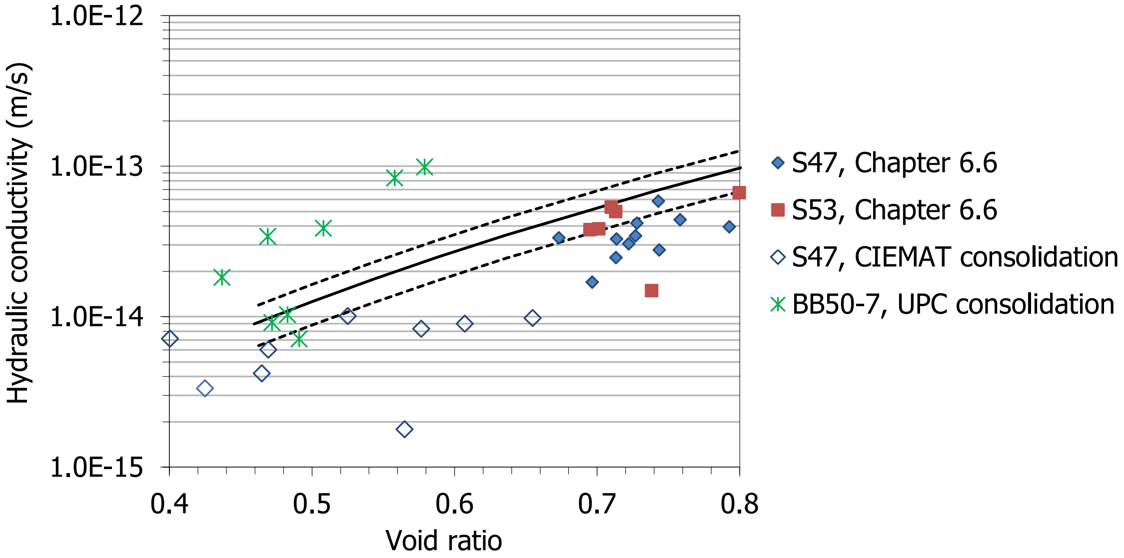

Fig. 105: Water permeability obtained from the consolidation tests (UPC, CIEMAT) and by direct measurement under controlled gradient (CIEMAT, Section 6.6).

The lines correspond to the empirical relation for untreated FEBEX bentonite (Eq. 6).

The compressibility curves obtained in the tests performed by UPC are shown in Fig. 106 and Fig. 107; the results obtained for the reference block have also been included. Those obtained by CIEMAT are shown in Fig. 108. The initial void ratios of the retrieved samples consistently increased with increasing distance from the canister and were higher than initial void ratio of the reference sample tested by UPC. Sample BB-57-14B displayed an anomalously low pre-yield compressibility and a high preconsolidation stress (this sample absorbed some water from the porous stones during the initial loading stage that explains the swelling response). On loading at high stresses, the compressibility curves tended to follow the compression curve of the reference block. The swelling strains on unloading in the UPC tests were small as a consequence of water following undrained paths (only some expansion occurred due to some inlet of water from the porous stones).

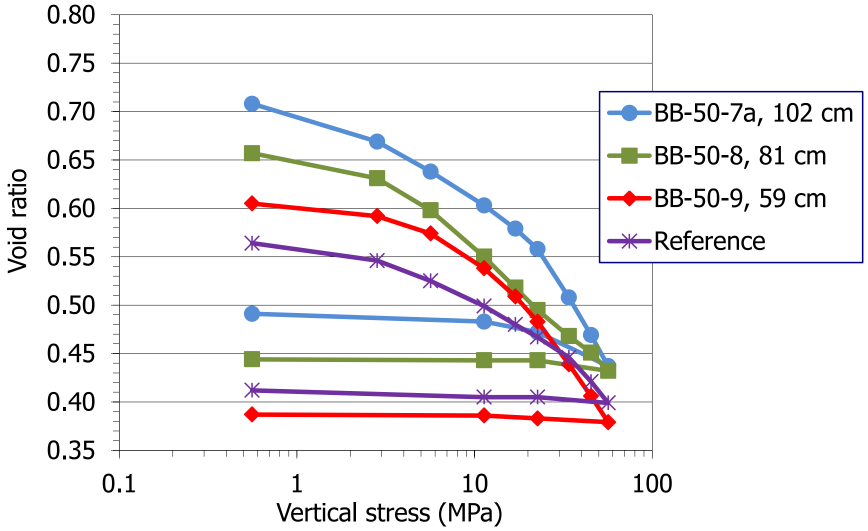

Fig. 106: Compressibility curves obtained by UPC for samples from Section S50 and for the reference block tested keeping the water content approximately constant.

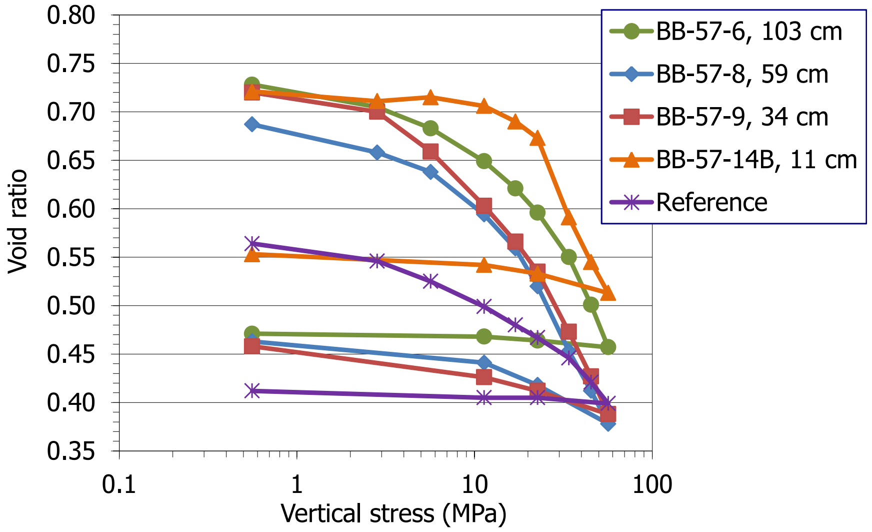

Fig. 107: Compressibility curves obtained by UPC for samples from Section S57 and for the reference block tested keeping the water content approximately constant.

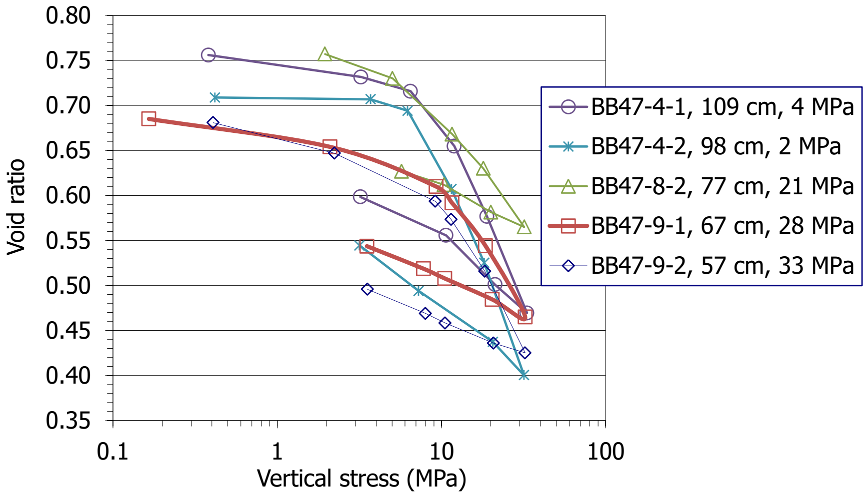

Fig. 108: Compressibility curves obtained by CIEMAT for samples from Section S47 tested under constant suction (indicated in the legend).

From these curves the vertical preconsolidation stress (σ_v*), the pre-yield compressibility for vertical stresses below 11 MPa (κ=-Δe/$\Delta \ln\sigma_v$) and the post-yield compressibility (λ=-Δe/$\Delta \ln\sigma_v$) were obtained and the results are compiled in Tab. 13. The vertical preconsolidation stress was estimated from the cumulated work input to the soil per unit of initial volume, as described in Tavenas et al. (1979).

UPC estimated the total suction at yield using Eq. 3 ($s_{\max}$ = 2'530 MPa, a = -21.4), which was obtained by fitting the initial suction measurements and the water content results from the oedometer and isotropic tests (Romero et al. 2017). To determine the degree of saturation from this curve a constant void ratio of e = 0.75 was used. These values also are included in Tab. 13, and it is observed that the degree of saturation at the yield point was systematically higher (total suction was lower) with the increase in distance from the gallery axis.

$$s = s_{\max}\, e^{aw} \qquad [3]$$

Tab. 13 also presents the results obtained by UPC in the reference block (RBS) and by CIEMAT in two tests performed with the untreated reference bentonite compacted to an initial dry density of 1.7 g/cm^3. The CIEMAT's specimens were prepared applying a compaction pressure of 30 MPa to bentonite at its hygroscopic water content (14 %) and they were tested under the suction corresponding to these conditions (116 MPa). These two tests were intended to simulate the initial conditions of the blocks in the barrier. However, because of the different geometry and size of the compacting moulds, the pressures applied to manufacture the blocks for the *in-situ* test were higher, between 40 and 45 MPa (Fuentes-Cantillana & García-Siñeriz 1998). These compaction pressures can be assumed to approximately correspond to the initial preconsolidation stress of the samples. Although the apparent preconsolidation pressures measured in the two reference samples tested by CIEMAT and in the RBS tested by UPC were actually lower than the compaction pressures, they were clearly higher than the apparent preconsolidation stresses measured in the retrieved samples through the oedometer tests reported in this Chapter. The decrease in the apparent preconsolidation pressure of the retrieved samples with respect to the reference ones can be explained by the volume increase experienced by the bentonite during hydration and the decrease in suction. The apparent preconsolidation pressure values of the field samples, plotted in Fig. 109, tended to be lower as the initial void ratio was higher and the suction was lower. The values obtained by CIEMAT, both for the reference and for the retrieved samples, were lower than those obtained by UPC.

Tab. 13: Apparent preconsolidation stress (σ_v*), pre-yield (κ) and post-yield (λ) compressibility determined from the consolidation tests under constant suction (CIEMAT) and constant water content (UPC) for untreated and retrieved samples.

Test	**Distance to gallery axis** (cm)	e_0	**Suction**[a] (MPa)	S_r **at** σ_v*	σ_v* (MPa)	κ	λ
CIEMAT							
EAP17_47[b]	Reference	0.587	116		16.5	0.012	0.116
EAP17_47_2[b]	Reference	0.579	116		16.0	0.009	0.099
BB-47-4-1	109	0.746	3.7		12.3	0.015	0.142
BB-47-4-2	98	0.706	1.6		12.0	0.025	0.175
BB-47-8-2	77	0.823	21		11.3	0.029	0.089
BB-47-9-1	67	0.679	28		13.5	0.017	0.103
BB-47-9-2	57	0.684	33		13.1	0.026	0.118
UPC							
RBS-C[c]	Reference	0.564	95.1	0.75	24.0	0.027	0.091
BB-50-9-C	59	0.605	19.4	0.82	17.3	0.029	0.114
BB-50-8-C	81	0.657	9.5	0.94	14.5	0.032	0.083
BB-50-7-C	102	0.708	≤ 6.7	1.00	18.4	0.034	0.133
BB57-14B-C	11	0.721	14.4	0.87	20.8	0.014	0.165
BB-57-9-C	34	0.720	12.8	0.89	17.5	0.036	0.162
BB-57-8-C	59	0.687	9.5	0.94	17.1	0.036	0.154
BB-57-6-O	103	0.728	7.5	0.98	19.5	0.032	0.152

[a] For UPC tests this is the suction at yield (except for RBS, for which the value given is the initial suction).

[b] Samples compacted from the reference bentonite.

[c] Sample trimmed from a reference block.

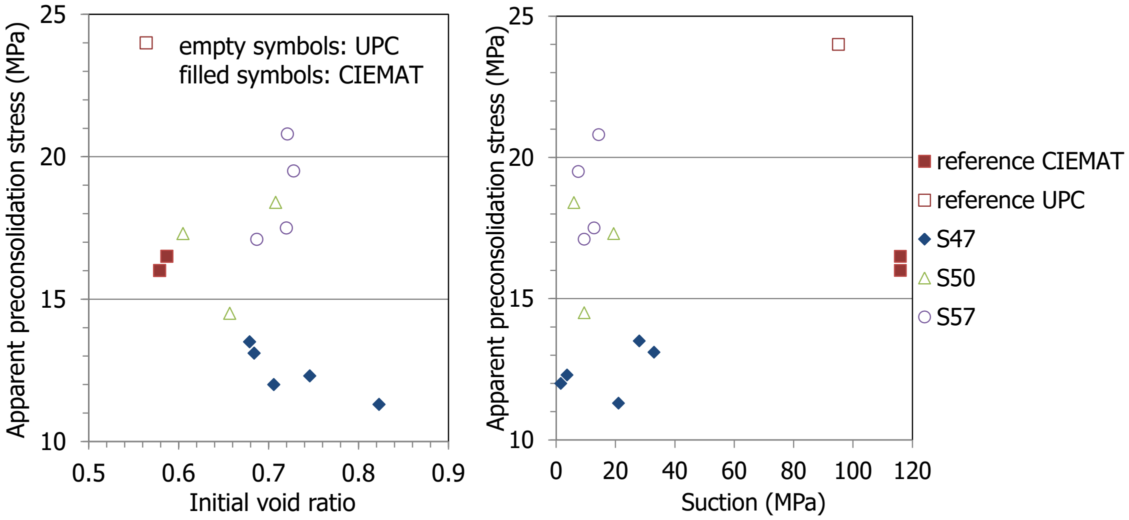

Fig. 109: Apparent preconsolidation stresses estimated from the oedometer tests for samples trimmed from the blocks retrieved from different sampling sections, for a reference block (UPC) and for compacted samples of the reference bentonite (CIEMAT).

The pre- and post-yield compressibility values are plotted in Fig. 110. The compressibility of the samples retrieved was higher compared to the reference sample both in the elasto-plastic and the elastic zones, because of their increase in the degree of saturation and the corresponding decrease in suction. The post-yield compressibility (λ) particularly increased for the samples that reached the lowest suction during barrier operation, i.e. those from Section S57 or taken closest to the granite. As reported in Tab. 13, the post-yield compressibility of samples from a section around the heater (S50) was lower than that of samples from a cold section (S57), which could be related to the higher degree of saturation of the latter. The pre-yield compressibility was slightly lower for heated samples. Although the decrease was minor, a likely cause for it could be that some cementation occurred as a consequence of the chemical changes reported in Section 5.5.

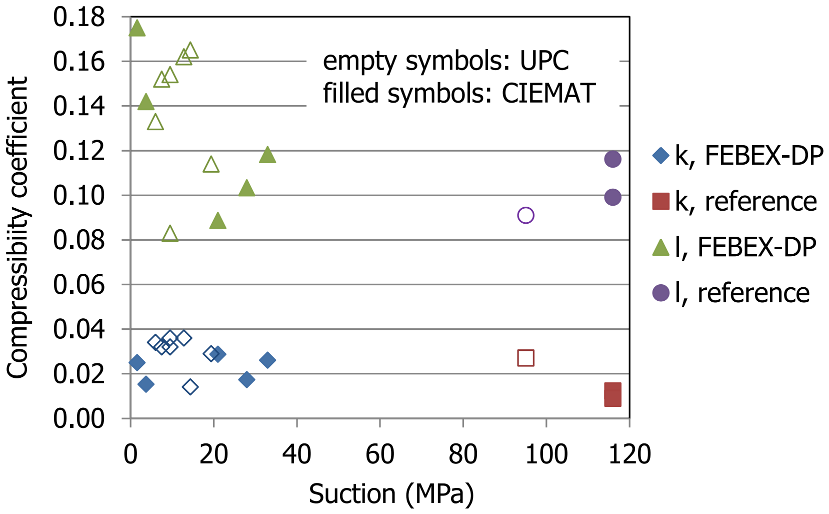

Fig. 110: Pre (k) and post-yield (l) compressibility parameters estimated from oedometer tests.

6.4.2 Isotropic conditions

High-stress isotropic tests were performed by UPC using a high-pressure triaxial system (Pineda et al. 2014) updated to apply isotropic stresses up to 30 MPa using a controlled stress rate and with new transducers for axial and radial deformations. The axial deformation of the specimen was registered by an external linear variable differential transformer (LVDT) installed in an independent frame that was specifically designed for the tests. A pressure compensated radial strain-gauge extensometer (± 5 mm range) was physically attached to the specimen by self-supporting contacts that were held in place with a spring (Fig. 111). Each cap of the isotropic cell had inlet and outlet lines, which were kept under atmospheric conditions during the loading stages. Heater bands were installed in the external four columns of the cell to allow setting up a good contact between top and bottom platens with the cell (the columns were first heated, before the platens were installed, and afterwards they were allowed to cool down to pre-stress the columns). A pressure/volume controller up to 32 MPa was used to apply the isotropic stress rate.

The tests were performed in samples from Sections S50 and S57 (hot and cold, respectively), obtained by trimming from the blocks. The specimens were 50 mm in diameter and 30 mm high and were wrapped in several neoprene membranes. They were loaded at constant water content to a mean net stress (*p*) between 15 MPa and 25 MPa. Mean stress rates were set below 1 MPa/hour. Since most samples were initially close to saturated conditions (the minimum degree of saturation was around 0.82), it was expected that constant water content loading paths would bring some of them to saturation. Dissipation of any excess pore water pressure was allowed at the maximum stress state (after the loading path at controlled stress rate) for a maximum of 24 hours.

As an example of the results obtained, Fig. 112 presents the time evolution of axial ε_1, radial ε_3 and volumetric $\varepsilon_v = \varepsilon_1 + 2\varepsilon_3$ strains along the constant water content loading path followed in sample BB50-9. Despite the isotropic loading path, the sample displayed an anisotropic deformation response with lower radial straining. This behaviour was observed in some other samples and could be inherited from the uniaxial compaction used to manufacture the blocks. Upon saturation and volume increase the initial anisotropy should tend to disappear, but this did not systematically happen in all the samples.

Fig. 113 summarises the compressibility curves on isotropic loading for all the samples tested by UPC. A good agreement is observed between the different tests, although the compressibility of 57-14B was somehow low at the early loading stage. This could be because the loading path at the defined rate was not fully drained during the first step. Nevertheless, at the final stage of the loading path the sample reached a volumetric strain consistent with the other tests.

From these tests the mean preconsolidation stress (p^*) was determined using the strain energy method (Tavenas et al. 1979), i.e. from the evolution of the cumulative work input to the soil per unit of initial volume, as was done for the oedometer tests (Romero et al. 2017). The evolution of stiffness was also determined from these curves and from it, the maximum compressibility ($-\Delta e/\Delta \ln p$). The values obtained for both parameters in all the tests are summarised in Tab. 14. The mean preconsolidation stresses obtained from the isotropic loading tests (p^*) can be related to those obtained from the oedometer tests (σ_v^*, Tab. 13) through a lateral coefficient at rest, K_0, which is also included in the Table:

$$\frac{1+2K_0}{3} = \frac{p*}{\sigma_v *} \qquad [4]$$

In saturated conditions the expected K_0 value for a normally consolidated soil should be around 1-senϕ' (around 0.77 for a drained friction angle of $\phi'\approx 13°$) and slightly lower for partially saturated conditions. The maximum compressibility values ($-\Delta e/\Delta \ln p$) were between 0.06 and 0.07, which are much lower than the post-yield compressibility values reported for oedometer tests (0.083 – 0.175 in Tab. 13). The reason could be that larger mean stresses would have been required to better define the post-yield compressibility under isotropic conditions. In this sense, the parameters estimated from the oedometer tests would be more reliable, but the combination of the two allows establishing bounding values. Additionally, the isotropic tests revealed certain anisotropy in the hydro-mechanical behaviour.

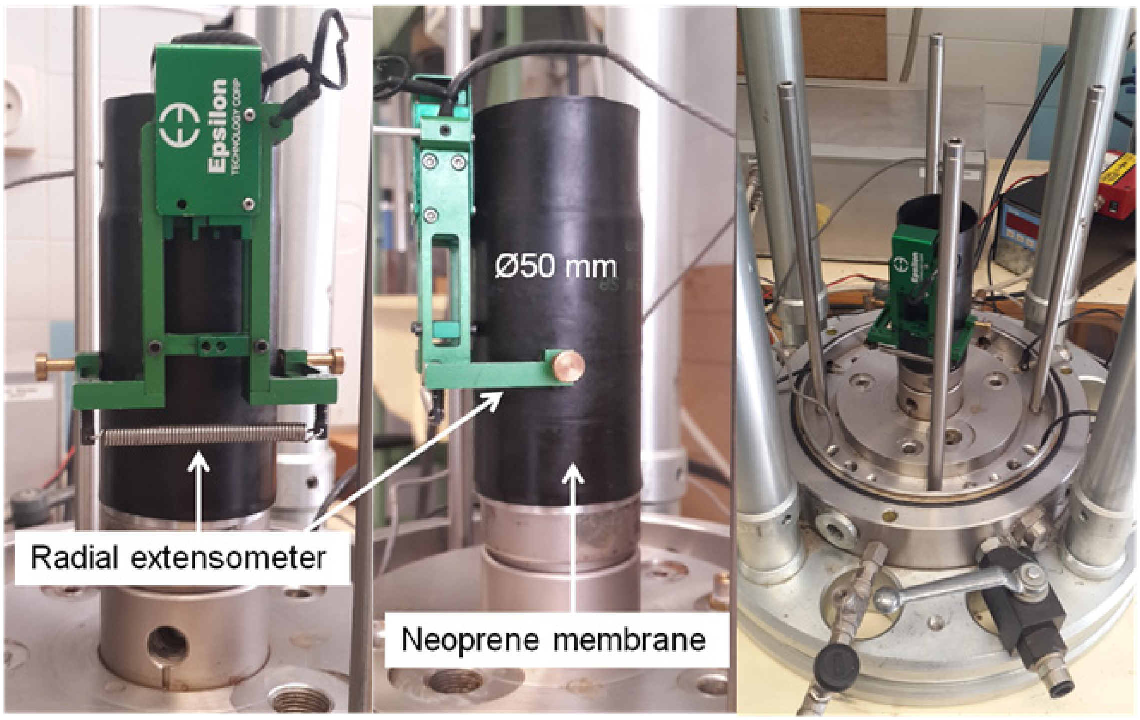

Fig. 111: Radial strain-gauge extensometer attached to the membrane surrounding the specimen in the high-stress isotropic cell.

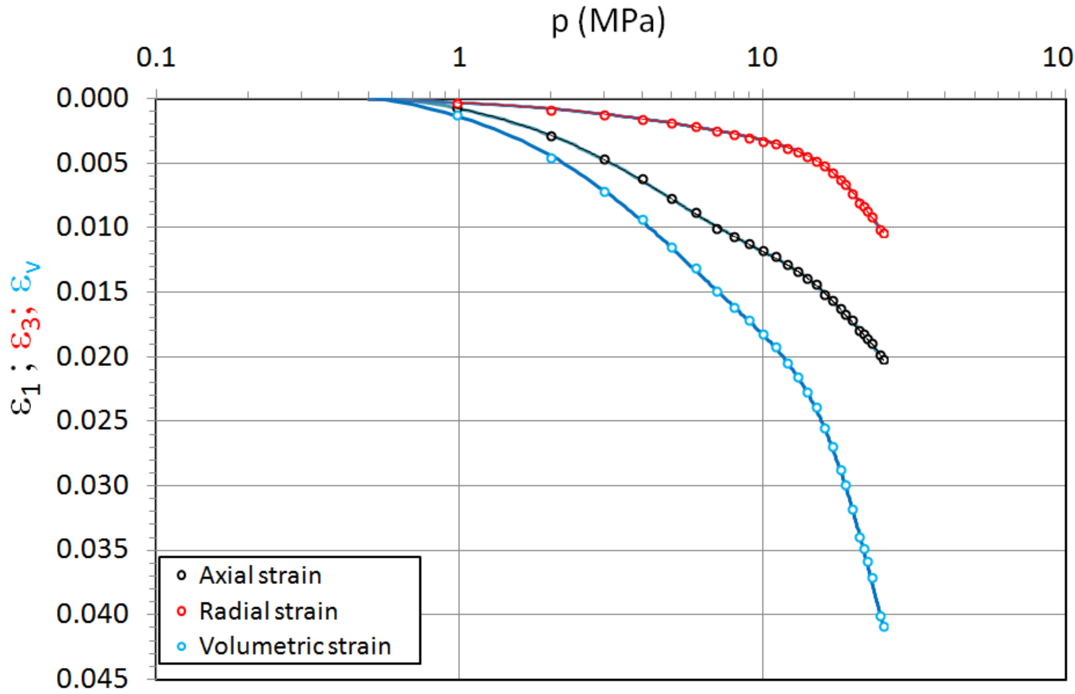

Fig. 112: Evolution of axial, radial and volumetric strains on isotropic loading for sample BB-50-9 tested by UPC.

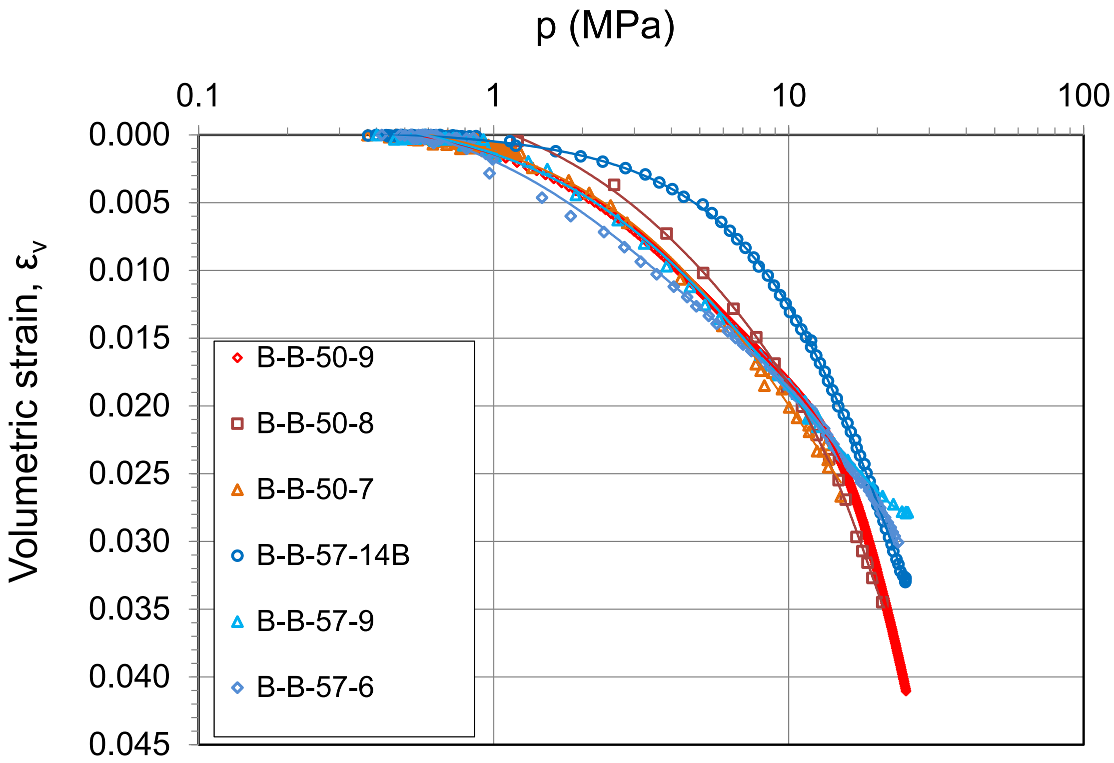

Fig. 113: Evolution of volumetric strains on isotropic loading performed by UPC on samples of Sections S50 (around the heater) and 57 (cold section).

Tab. 14: Summary of initial characteristics and parameters deduced from the isotropic consolidation tests.

Test	**Distance to gallery axis** (cm)	e_0	S_{r0}	**Initial** s (MPa)	p^* (MPa)	$-\Delta e/\Delta \ln p$	K_0
B-B-50-9	59	0.595	0.82	67.9	14.4	0.070	0.75
B-B-50-8	81	0.668	0.90	18.0	13.3	0.055	0.88
B-B-50-7	102	0.740	0.99	7.6	n.d.	-	
57-14-B	11	0.632	0.95	20.5	13.1	0.073	
B-B-57-9	34	0.640	0.99	15.5	n.d.	0.020[a]	
B-B-57-6	103	0.659	0.99	15.8	15.0	0.058	0.65[a]

[a] Anomaly low.

6.5 Mechanical strength

The unconfined compressive strength of specimens from Section S47 was determined by ClayTech by means of the unconfined compression test, which is an experimentally simple method where a cylindrical specimen is compressed axially with a constant rate of strain with no radial confinement or external radial stress. The main objective was to compare results from specimens sampled from the field experiment with those from reference bentonite performed under the same experimental conditions.

Tests were made on material from the field experiment and from the reference material. From the field experiment two specimens from each position were prepared by sawing and trimming. The reference material was prepared by grinding and re-compaction of material drilled from the reference block. The diameter of the specimens was 20 mm and the height were 20 mm. This size was chosen to increase the possibility of taking intact specimens. The strength is commonly determined on specimens having the height equal to double the size of the diameter to allow the failure surface to fully develop. To minimise the end effect on short specimens, end surfaces were lubricated. Short specimens were used in previous studies (such as the CRT and TBT projects) and it was concluded that the influence of using short specimens was small when considering deviator stress but larger when considering the corresponding strain (Dueck et al. 2011, Åkesson et al. 2012). All specimens were saturated in the saturation device before the compression test by circulating deionised water from both above and below the specimens over a short period of time at a regular basis. The time used for the saturation was two weeks. After saturation, the specimens were removed from the saturation device at least 12 h before the shearing to allow for stress relaxation and density homogenisation while protected from evaporation.

The specimens were placed in a mechanical press (Fig. 114) and the compression was run at a constant deformation rate of 0.16 mm/min which corresponds to a strain rate of 0.8 %/min. The strain rate is within the range recommended in the ASTM standard D2166/D2166M and has been repeatedly used by ClayTech to test bentonite samples. The specimens were placed between lubricated end plates and were surrounded by a thin plastic film to minimise evaporation during shearing. During the tests the deformation and the applied force were measured by means of a load cell and a deformation transducer. The specimens were undrained during shearing and no volume change was taken into account to compute deviator stress and strain. After failure, the water content and density were determined on all specimens.

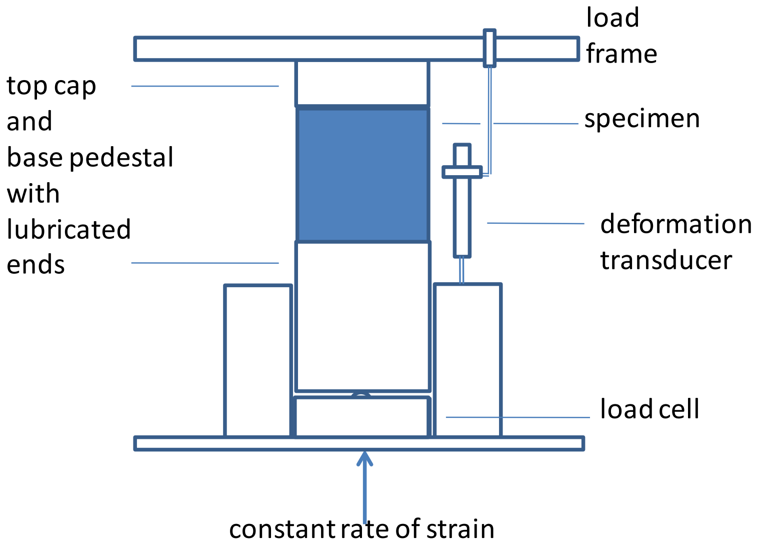

Fig. 114: Setup for the unconfined compression tests (ClayTech).

The results obtained in terms of maximum deviator stress and strain for the trimmed samples are shown in Fig. 115 as a function of the distance to the gallery axis. Most samples had strengths between 1000 and 1800 kPa, but the changes did not seem to be related to the position of the samples in the barrier. However, the vertical strain at failure decreased clearly from the gallery wall towards the liner, which would indicate a more brittle behaviour in samples that had been subjected to a higher temperature. The lower strain at failure observed on some of the specimens from the field experiment is consistent with results seen in other large-scale field tests such as the CRT and Prototype Repository, where similar temperature conditions prevailed but where the exposure time was less than half (e.g. Dueck et al. 2011).

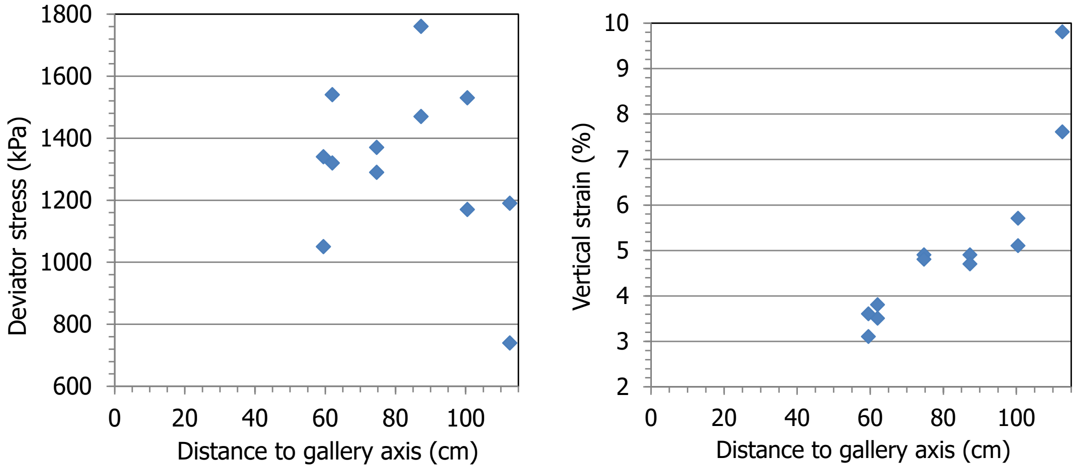

Fig. 115: Maximum deviator stress and corresponding strain for samples trimmed along a radius of Section S47 tested by ClayTech.

If the results are plotted in terms of dry density (Fig. 116), the increase of strength with dry density becomes clear. The comparison of the results obtained in samples trimmed from the retrieved blocks with those obtained in the remoulded samples prepared from the reference block, showed that the retrieved samples had lower strength than the reference sample, but the values for both groups of samples were in the same order of magnitude. The strain at failure, which tended to decrease with dry density for the reference samples, was lower for all the retrieved samples. Nevertheless, the comparison between reference and retrieved samples must be treated cautiously because the samples used in both cases were prepared differently.

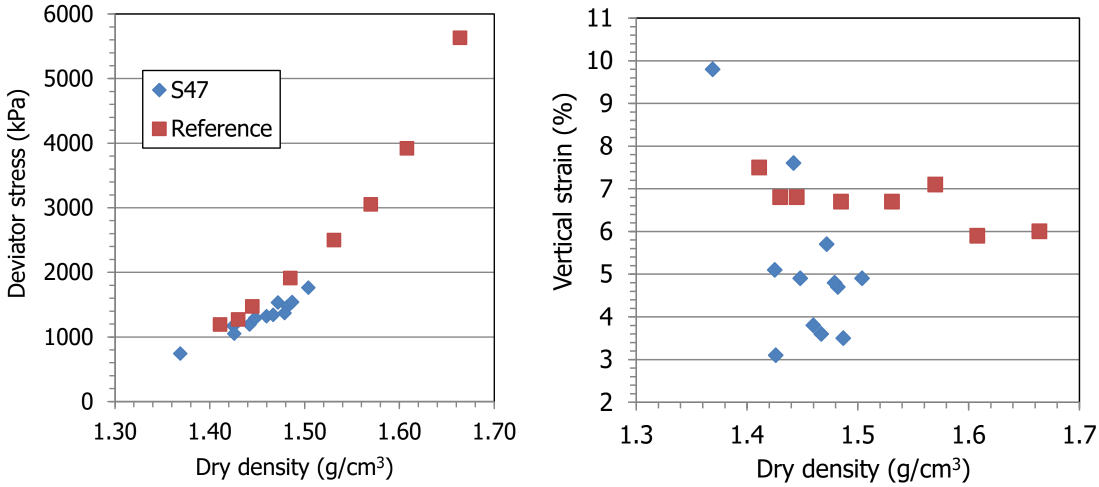

Fig. 116: Maximum deviator stress and corresponding strain for samples trimmed along a radius of Section S47 and samples recompacted from a reference block tested by ClayTech.

6.6 Hydraulic conductivity

The hydraulic conductivity of bentonite samples was measured in 17 samples from Sections S47 and S53 by CIEMAT and in samples from Section S47 by ClayTech. In both cases, cylindrical samples were trimmed from the blocks to fit the cell rings. In the tests by ClayTech the diameter of the specimens was 50 or 35 mm and the height 10 mm, and in the tests by CIEMAT the diameter was 50 mm and the height 25 mm. In addition to the tests performed in samples trimmed from the blocks, ClayTech measured the hydraulic conductivity of specimens obtained by grinding the bentonite to a grain size less than 1.5 mm and re-compacting the granules obtained at dry densities of 1.56 to 1.60 g/cm^3. These remoulded samples were obtained both from blocks of Section S47 and from a block that was not used at the installation but was compacted along with the others in 1996. The values obtained in samples from this block are considered reference values, along with the empirical correlation for the FEBEX untreated bentonite obtained by CIEMAT (Villar 2002, Eq. 5 and 6):

For $\rho_d < 1.47$ g/cm^3: $\log k_w = -6.00\ \rho_d - 2.96$ [5]

For $\rho_d > 1.47$ g/cm^3: $\log k_w = -2.96\ \rho_d - 8.58$ [6]

where k_w is the hydraulic conductivity in m/s and ρ_d is the dry density in g/cm^3.

The samples were initially saturated under constant volume using deionised water. The setup used by ClayTech allowed the measurement of swelling pressure during this phase (Fig. 95), as it was already described in Section 6.2. Although many samples had a high initial degree of saturation, they all absorbed additional water because, once in the cell, their density decreased with respect to the original value, due to the filling of some irregularities that could have been created during trimming. In fact, there was a clear decrease in dry density of the samples tested in the permeability cells with respect to that of the blocks from which they were trimmed (Fig. 117). This effect was particularly significant in the samples trimmed by ClayTech, especially those from the innermost block, which was drier and more brittle and did not allow obtaining good-shaped specimens from it. Consequently, the values measured do not correspond to the permeability of the bentonite at the moment it was retrieved, not only because the dry densities were lower and swelling of the samples could allow for disruption of the field conditions, but also because the samples were saturated with deionised water to perform the determinations, and permeability depends greatly on the degree of saturation. Hence, the aim of these tests was not to determine the absolute value of the property in situ but evaluate any potential substantial changes in the hydraulic conductivity of the bentonite that may have occurred during the FEBEX operation. This is why the values measured in the samples retrieved are compared to those of reference, untreated samples of the same dry density, which is the main parameter controlling permeability in expansive materials.

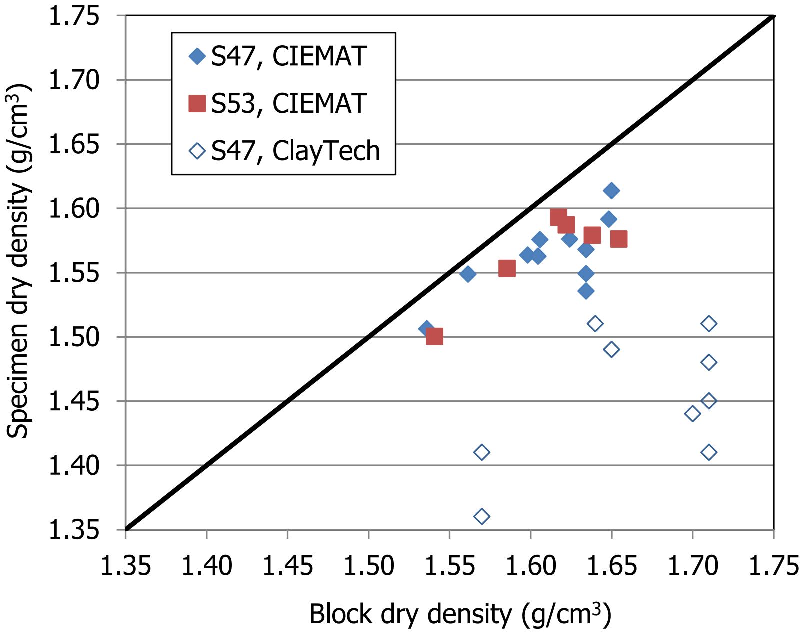

Fig. 117: Comparison of the dry density of the specimens trimmed for permeability tests and the dry density measured in adjacent samples (reported in Section 4.1).

The method used by both laboratories to determine the hydraulic conductivity was based on that of the constant head permeameter (Fig. 118). After saturation of the specimens a water pressure gradient was applied between top and bottom of the samples, and the outflow volume of water was measured. The tests ran over a time period sufficiently long to determine a volume of water passing through the specimen that was linear and stable with time for a given hydraulic gradient. The hydraulic conductivity was then calculated according to Darcy's law. During the measurements, the specimens were confined in rigid cells preventing them from deforming. The complete saturation of the specimen and associated swelling guaranteed tight contact with the walls of the cell, preventing the flow of water between these and the sample. Some details of the tests are given in Tab. 15.

The tests were performed at room temperature. At the end of the test the samples were weighed, measured and their actual water content and dry density were checked according to the methods given in Tab. 3. At ClayTech half of each specimen was used for the determination of water content and the other half was used for the determination of bulk density. The samples were fully saturated at the end of the tests.

Tab. 15: Characteristics of the hydraulic conductivity tests performed.

	CIEMAT	**ClayTech**
Saturation time (days)	13 – 86	16 – 55
Saturation pressure (MPa)	0.6	0.1
Hydraulic gradient	1'600 – 11'700	2'090 – 19'590
# gradients per sample	2 – 3	1
Duration (days)	28 – 106	5 – 11
Outflow measurement	P/V controller (mm^3)	2-mm ϕ tube (mm^3)

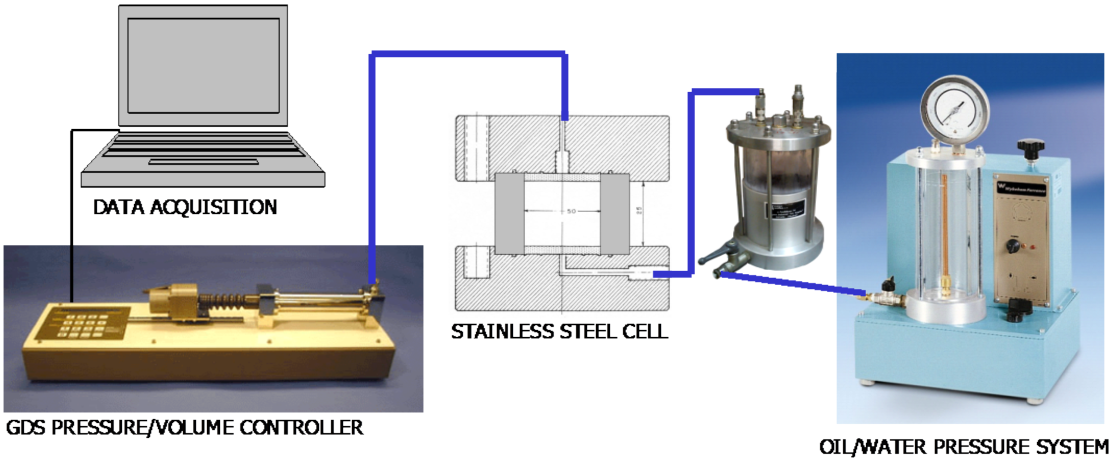

Fig. 118: Schematic representation of the assembly for permeability measurement of expansive soils used by CIEMAT (using an oil/water pump to apply injection pressure and a pressure/volume controller for backpressure application and outflow measurement).

The hydraulic conductivities measured are plotted in Fig. 119 as a function of the final dry density of the samples. The decrease of hydraulic conductivity with dry density is highlighted. It is remarkable that the reference values obtained by the two laboratories agreed quite well, the values of ClayTech (crosses) being slightly lower than those of CIEMAT (lines) but inside the expected range of variation. The reference samples for ClayTech were obtained for this investigation from a reference block compacted in 1996 along with the other blocks produced for the in-situ test but not installed. The empirical relationship for the reference FEBEX bentonite was obtained for compacted samples of different dry densities permeated with deionised water (Villar 2002). The values measured by ClayTech using remoulded retrieved materials were mostly within the expected range of variation of this property. This would indicate that no irreversible changes in the flow properties of the bentonite took place as a result of its installation in FEBEX.

Concerning the trimmed samples, for those measured at CIEMAT the values were in the order of 10^{-14} m/s, whereas for the samples measured at ClayTech the values were an order of magnitude higher. As it has been explained above, because of trimming the dry density of the samples used for the hydraulic conductivity tests was lower than those measured in adjacent samples of the same blocks (Fig. 117), and this difference was higher for the samples prepared at ClayTech, which explains the differences in the ranges of dry density tested. For the samples of dry densities below 1.5 g/cm^3 (most of those measured by ClayTech) the hydraulic conductivity was higher than the values for reference samples, whereas for higher dry densities the hydraulic conductivity measured in retrieved samples tended to be lower, even below the expected range of variation of this property. In this sense, CIEMAT checked that, for a given sample, the hydraulic conductivity measured with hydraulic gradients below 4000 was generally lower than that measured with higher hydraulic gradients. This would justify the lowest hydraulic conductivities measured in Section S47 by CIEMAT, since some of these samples were measured applying hydraulic gradients below 4000. In fact, a previous investigation analysing the effect of hydraulic gradient on hydraulic conductivity of the FEBEX bentonite found that –in some cases– the hydraulic conductivity tended to be slightly lower as the hydraulic gradient decreased (Villar & Gómez-Espina 2009). Hence, it is considered that the lowest hydraulic conductivities measured in the present work can be a consequence of having used hydraulic gradients close to the critical ones in some samples. The critical gradient, as defined by Olsen (1962), would be the hydraulic gradient below which flow occurs, but is non-Darcian (i.e. the relationship between flow and hydraulic gradient is not linear), because of the strong clay-water interactions. In contrast, in the tests performed with the reference bentonite used to establish the empirical correlations of Eq. 5 and 6, the hydraulic gradients used were higher, on average 15200 (Villar 2002).

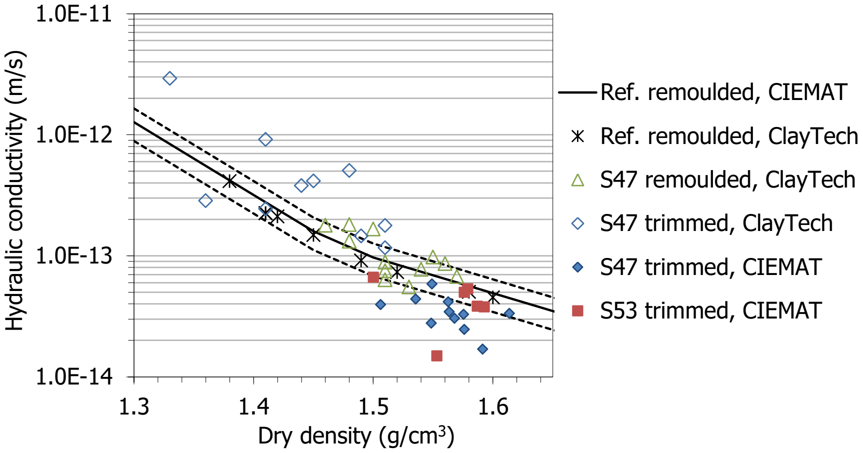

Fig. 119: Hydraulic conductivity of trimmed and remoulded samples from different sections determined by two laboratories, values for samples remoulded from a reference block (crosses) obtained by ClayTech and empirical correlation for untreated FEBEX bentonite (lines, Eq. 5 and 6).

The results obtained in trimmed samples have been plotted as a function of the location of the samples during operation in Fig. 120. Because of the difficulties in obtaining trimmed specimens of the same density as that of the block from which they were trimmed, there is no clear relation between these two variables. The samples from Section S47 showed a slight decrease in hydraulic conductivity towards the heater, which would be related to the higher density of the bentonite in this area. The higher hydraulic conductivities were measured in the samples trimmed from a block of the internal ring of Section S47 by ClayTech. As a result of the brittleness of this block, the specimens trimmed had low dry densities, which partly explains the higher hydraulic conductivity measured for materials close to the liner. Since the deviation in hydraulic conductivity of the innermost trimmed specimens from the field experiment was not coupled to a corresponding reduction in swelling pressure (Section 6.2), it might be that the specimens were not fully homogenized from the mainly radial swelling of these specimens.

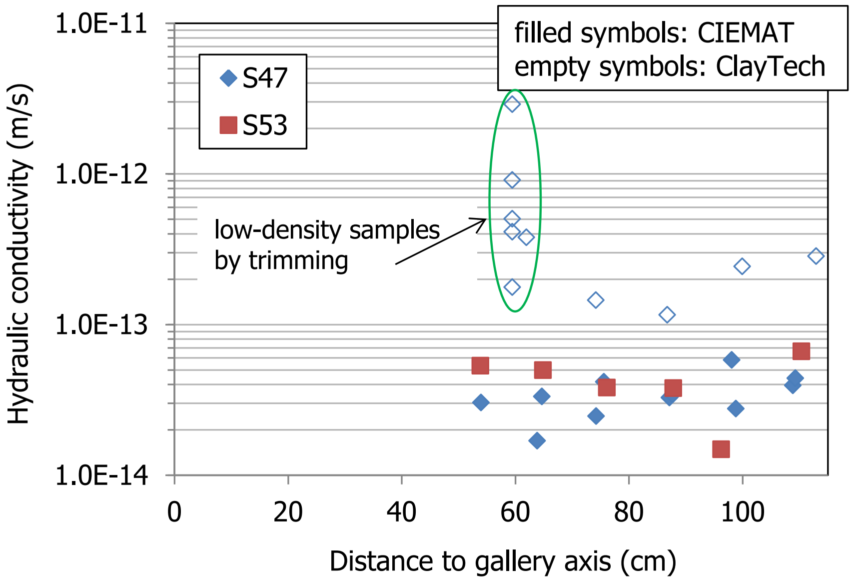

Fig. 120: Hydraulic conductivity values measured in trimmed samples as a function of their position in the barrier.

6.7 Gas permeability

Two different experimental setups were used to determine the gas permeability, a low-pressure and a high-pressure one. The aim of the tests performed in the low-pressure equipment was to determine the influence of water content and degree of saturation on gas permeability, whereas the aim of the tests performed using the high-pressure permeameter was to analyse the effect of boundary conditions, such as gas pressure and confining pressure, on gas permeability.

When there are two fluids present in the porous material (gas and water in this case), the permeability of each fluid depends upon the saturation of the material in each fluid: these are called apparent (or effective) permeabilities. Hence, the value obtained in the determinations (apart from the gas permeability, k_g) is the intrinsic permeability measured with gas flow, k_{ig}, multiplied by the relative permeability to gas, k_{rg}. In turn, the relative permeability to gas is the ratio of the apparent (effective) permeability of gas at a particular saturation to the absolute permeability of gas at total gas saturation, i.e. in completely dry material, where the k_{rg} value would be 1. Since most of the samples were close to saturation, it was expected that the permeabilities would be very low or even zero.

Most of the samples tested were drilled in the same sections where the blocks for THM and THG characterisation were taken, i.e. S36, S44, S47, S50, S53, S57 and S59. Half of them were drilled in the middle of blocks and the other half at the contact between two blocks, so as to have an interface along the core (Fig. 121, left). To prepare the samples, the core diameter was fit to that of the testing cells (36 or 50 mm) by using a cutting ring and a knife (Fig. 121, right) and sand paper in some cases. The cylindrical surface of the samples was smoothed and the parallelism of the cylinder's ends was assured. The resulting specimens were between 2.4 and 5 cm in height and 10 – 20 cm^2 in surface area. The interface between blocks was clear in those samples from the internal ring of the barrier, but it was difficult to identify in wetter samples (Fig. 122), In some cases the interface along the core became evident only after preparing the specimen (Fig. 123). In order to determine the initial water content and dry density of the samples, a small spare fragment resulting from the sample preparation was used.

Fig. 121: Sample drilled on site at the contact between blocks (left), adjusting the diameter during sample preparation (right).

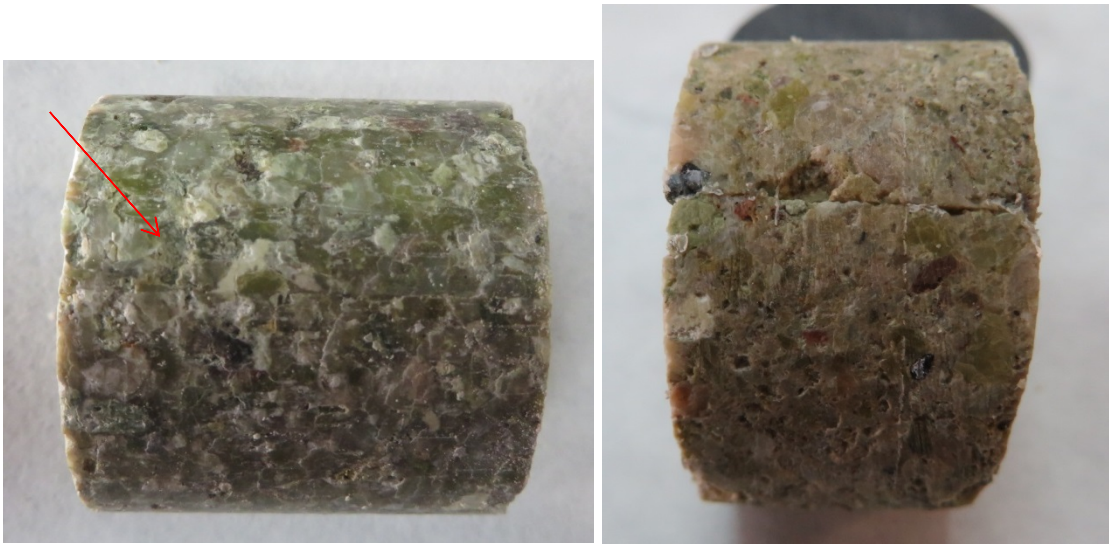

Fig. 122: Interface in a sample from the external ring (indicated by an arrow, BC-44-6) and from the inner ring (BC-44-2).

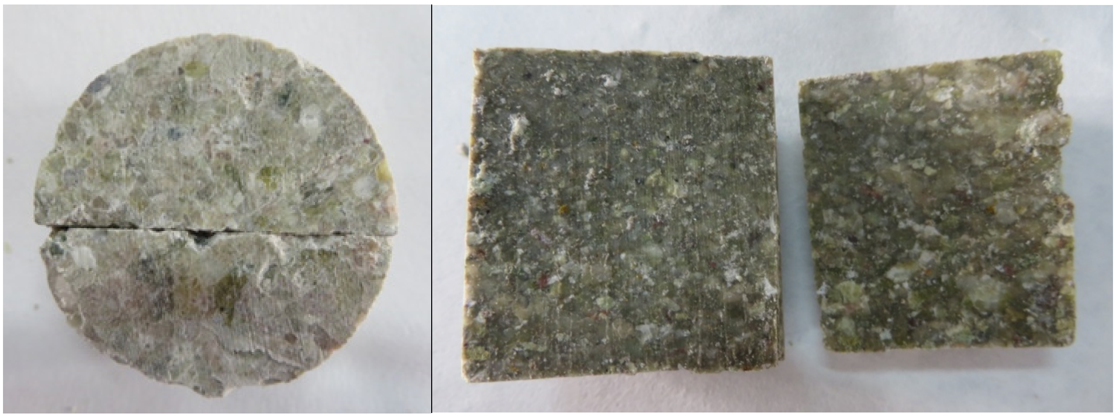

Fig. 123: Appearance of a specimen prepared for gas test with interface between blocks.

The samples wrapped in double latex membranes were placed in triaxial cells that were filled with water and pressurised to ensure perfect adherence of the membranes to the surface of the sample. Most samples were initially tested in a low-pressure equipment and afterwards in high-pressure equipment. The first device worked as an unsteady-state (or falling-head) permeameter in which only pressure was measured (LP). The second one (HP) had the configuration of a steady-state permeameter (constant-head) in which pressure and gas flow were measured. The description of each setup and testing procedure is given below.

Low-pressure equipment (LP)

Once the triaxial cell was filled with water and pressurised, the inlet at the lower part of the sample was connected to an airtight tank of known volume, in which nitrogen gas was injected at a pressure slightly higher than atmospheric. The tank was instrumented with a pressure sensor connected to a data acquisition system which recorded the pressure of the fluid contained inside. The inlet at the upper part of the sample was left open to the atmosphere. The test consisted of allowing the air in the tank to go out to the atmosphere through the specimen, while the decrease in pressure in the tank was measured as a function of time. The tests were performed at constant, room temperature.

The permeability to gas was calculated in accordance with the following equation (Yoshimi & Osterberg 1963):

$$k_{\mathrm{ig}} \cdot k_{rg} = 2.3 \times \frac{V \times L \times \mu_g}{A \times \left(P_{atm} + \frac{P_0}{4} \right)} \times \frac{-Log_{10}\left(\frac{P(t)}{P_0} \right)}{t - t_0} \qquad [7]$$

where $k_{\mathrm{g}} \cdot k_{rg}$ is the effective permeability to gas (m^2), V the volume of the tank (m^3), L the length of the sample (m), A the surface area of the sample (m^2), μ_{g} the dynamic viscosity of nitrogen ($1.78 \cdot 10^{-5}$ Pa·s), P_{atm} is atmospheric pressure (Pa), P_0 is the excess pressure over atmospheric pressure in time t_0 (s) and P(t) is the excess over atmospheric pressure in the tank at time t. The volume of the spherical tank used was $2.21 \cdot 10^{-2}$ m^3 and the gas used for the tests was nitrogen, for which a density of 1.12 kg/m^3 was taken.

Taking into account the density of nitrogen (ρ_{g}, 1.12 kg/m^3), the following relation between permeability to gas (k_{g}, m/s) and the product of intrinsic permeability measured with nitrogen gas (k_{ig}, m^2) times the relative permeability to gas (k_{rg}) is obtained:

$$k_g = \frac{\rho_g \times g}{\mu_g} \times k_{ig} \cdot k_{rg} = 6.2 \cdot 10^5 \times k_{ig} \cdot k_{rg} \qquad [8]$$

The triaxial cell was initially pressurised to 0.6 MPa and gas was injected at a pressure close to 0.1 MPa through the bottom of the sample. If flow took place, the confining pressure was increased to 1 MPa, and the test was repeated. Afterwards, the cell with the sample was moved to the high-pressure equipment.

High-pressure equipment (HP)

The HP tests were performed by keeping constant confining and injection pressures and atmospheric backpressure, i.e. following the working principle of a steady-state (constant-head) permeameter (Fig. 124). The injection pressure could reach 24 MPa and the confining pressure could be increased to as high as 33 MPa. Outflow gas rates (Q_{m}, measured by gas mass flowmeters), upstream and downstream pressure (P_{up}, P_{dw}), confining pressure and temperature were monitored online. To compute the apparent (or effective) permeability ($k_{\mathrm{g}} \cdot k_{rg}$), the inflow or outflow measurements could be used in Eq. 9 (symbols are as in Eq. 7 and Eq. 8). The values computed from the outflow have been used in this work. In this kind of test, P_{m} is the atmospheric pressure due to the SPT conditions of the gas mass flowmeters.

$$k_{\mathrm{ig}} \cdot k_{\mathrm{rg}} = \frac{Q_{\mathrm{m}} \times \mu_{\mathrm{g}} \times L \times 2\, P_{\mathrm{m}}}{A \times (P_{\mathrm{up}}^2 - P_{\mathrm{dw}}^2)} \qquad [9]$$

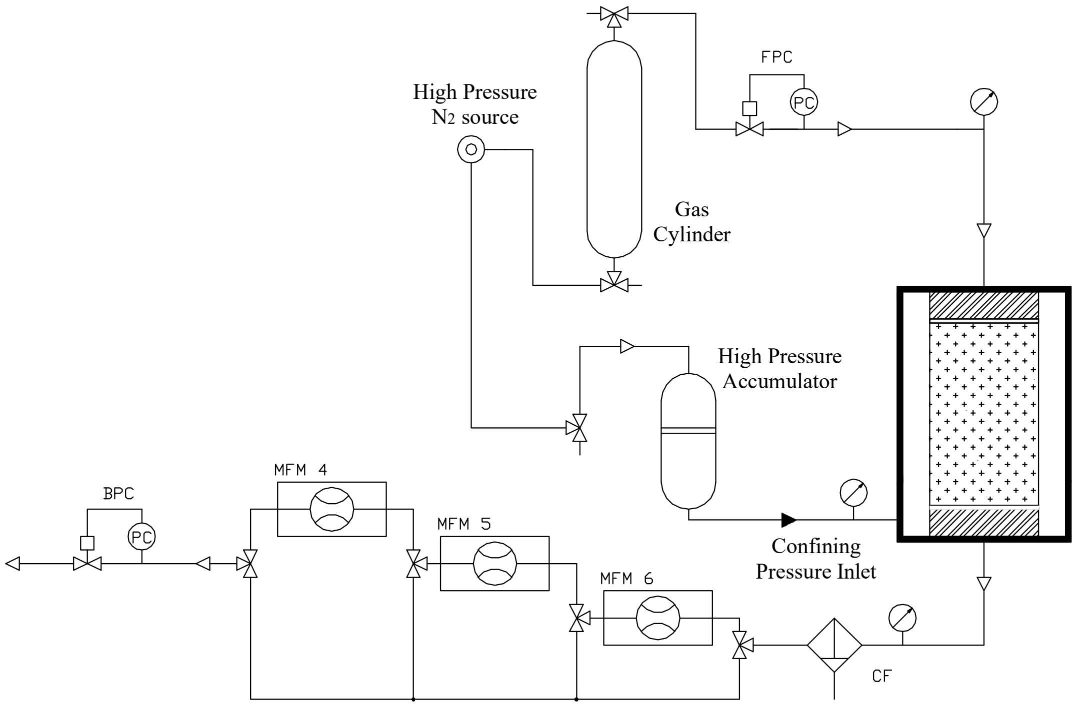

Fig. 124: Experimental setup of the high pressure line (HP) (CF: coalescing filter, FPC: forward-pressure controller, BPC: back-pressure controller, MFM: mass flow meter).

Twelve gas permeability tests were performed in triaxial cells with bentonite samples obtained by on-site drilling. The average dry density of the samples was 1.58 ± 0.04 g/cm^3 and water content 24.6 ± 2.7 % (S_r = 93 ± 6 %). The "as-retrieved" conditions of the samples were preserved during gas testing, i.e. the samples were carefully trimmed in order to minimise change in their dry density and water content. All the tests started with a confining pressure of 0.6 or 1 MPa, depending on which was the last value applied in the LP equipment. If the initial confining pressure was 0.6 MPa, it was subsequently increased to 1 MPa. Then the injection pressure was slowly increased until a notable flow was reached and then the confining pressure was increased. Finally, the confining pressure was reduced to the initial values in most of the tests. The precise pressure path followed depended on the characteristics of the samples and consequently they were quite heterogeneous.

Final checking of water content at different levels along the samples showed that the differences in water content inside the samples were smaller than 0.4 %, which indicates that the samples did not dry during gas testing.

In the range of pressures tested, no clear effect of the injection pressure on the permeability value obtained was observed. The values obtained in both setups (LP and HP) showed that, for a constant confining pressure, the gas permeability was essentially constant despite the injection pressure changes. This can be seen in Fig. 125 and Fig. 126, in which the results obtained for different samples tested consecutively under confining pressures 0.6 and 1 MPa have been plotted. Only in a few cases did the gas permeability increase slightly with the increase in injection pressure, since this implied an increase in void sizes. The figures show also that the highest gas permeabilities for these confining pressures were measured in the samples with interface (empty symbols).

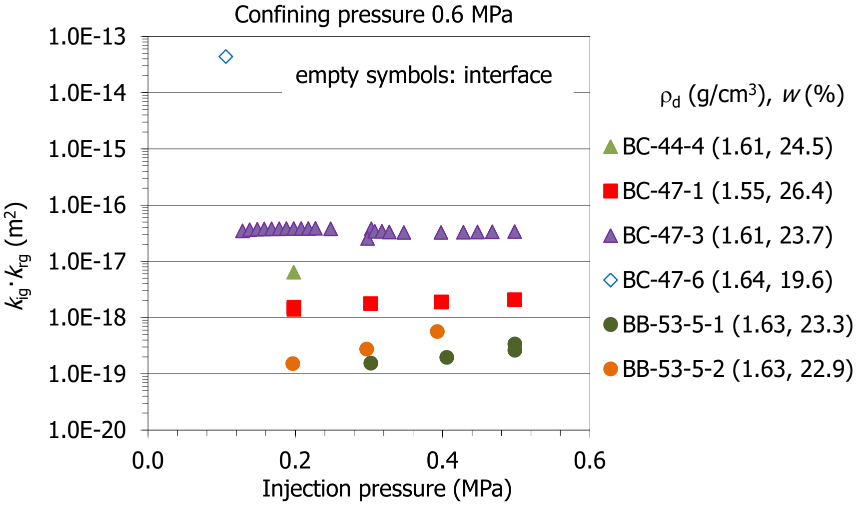

Fig. 125: Effective gas permeability measured at constant confining pressure of 0.6 MPa in the HP setup.

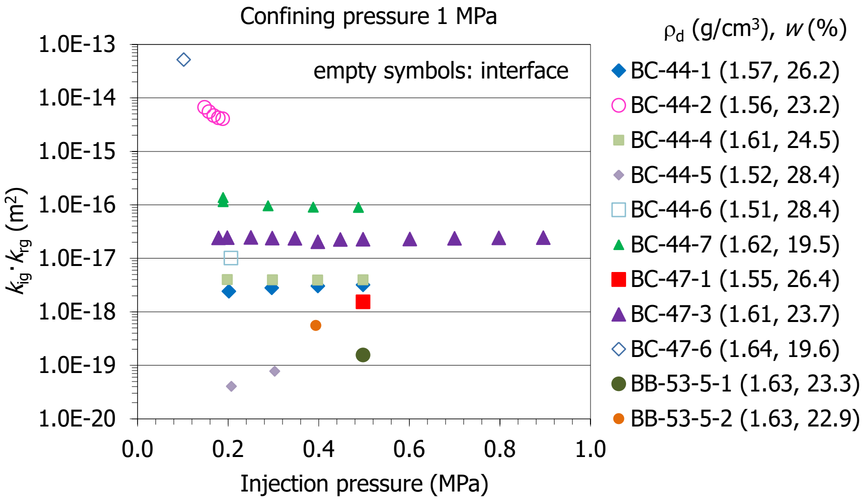

Fig. 126: Effective gas permeability measured at constant confining pressure of 1 MPa in the HP setup.

Since the injection pressure did not substantially affect the permeability values obtained for a given confining pressure, the average gas permeability obtained for all the steps performed under the same confining pressure was computed. Fig. 127 and Fig. 128 show the average gas permeability values measured for each confining pressure in material recovered from two sampling sections. The decrease of gas permeability with confining pressure is clear. The distance from the sample to the axis of the gallery is also indicated in the Figures. Overall, the samples closest to the gallery axis, which were drier and had lower degrees of saturation (Villar et al. 2016a), had higher gas permeability. The decrease of gas permeability with confining pressure was significant even for samples with a high degree of saturation. The confining stress probably reduced the size of the gas pathways, also increasing their tortuosity. In the case of the highly-saturated samples there was no need of applying a high confining pressure to completely block the air passages, whereas in the less saturated samples the gas found ways out until the confining pressure was enough to sufficiently reduce the air-filled pore space. The highest decrease of permeability (of 3 or 4 orders of magnitude) took place for confining pressures below 4 MPa. For higher confining pressures the decrease was less significant, always smaller than one order of magnitude, except when the sample had an interface or a relatively low degree of saturation. The samples with interface taken from the inner bentonite ring (distances to the gallery axis around 60 cm) had higher permeability than neighbouring samples drilled in the middle of a block, and this permeability decreased suddenly for confining pressures higher than the 4 MPa previously mentioned. The permeability of sample BC-44-2, drilled between two blocks of the internal ring of Section S44 (Fig. 122), decreased three orders of magnitude when the confining pressure was increased to 6 MPa, and the permeability of sample B-C-47-4, which was drilled in an equivalent location in Section S47, decreased four orders of magnitude when the confining pressure increased from 4 to 7 MPa. However, the samples from the external ring with and without interface behaved similarly, experiencing a clear decrease of permeability for confining pressures lower than 4 MPa. There was no flow through these samples when the confining pressure increased above 2 – 4 MPa.

During most of the gas permeability tests the dry density of the samples increased, which is consistent with the decrease in effective gas permeability occurring during the tests. Only in those tests in which the maximum confining pressure applied was low (below 1.6 MPa), the dry density of the sample did not increase after testing. In fact, there was a positive linear correlation between the change in dry density and the maximum pressure applied ($R^2 = 0.7$).

After reaching a maximum confining pressure, generally corresponding to a value above which no flow took place, the samples were progressively unloaded. During unloading, as the confining pressure decreased, the effective permeability increased, but the initial higher permeability values were never recovered. Fig. 129 and Fig. 130 show the changes in permeability during loading-unloading for samples of two sections (same samples as in Fig. 127 and Fig. 128). Overall, the samples that had higher initial permeability –either because their degree of saturation was low or because they had an interface– had to be submitted to higher confining pressures to stop flow. Also, the permanent decrease in gas effective permeability after loading was higher in the samples with an interface (namely BC-44-2 and BC-47-4). The appearance of the interface of one of these samples is shown in Fig. 131, where the closing of the interface can be observed. In contrast, sample BC-44-6, which was drilled in the outer ring of the barrier and had a high degree of saturation, behaved similarly to other samples, despite the fact that it had an interface a, indicating that the interface was no longer a preferred pathway for gas movement.

When flow occurred under a given pressure situation, the duration of the steps was generally short (1 – 2 hours). In many cases, it was observed that, if the same pressure situation was kept for longer, flow decreased, and the permeabilities computed were lower. This aspect has not been analysed in detail but could have some effect on the results obtained.

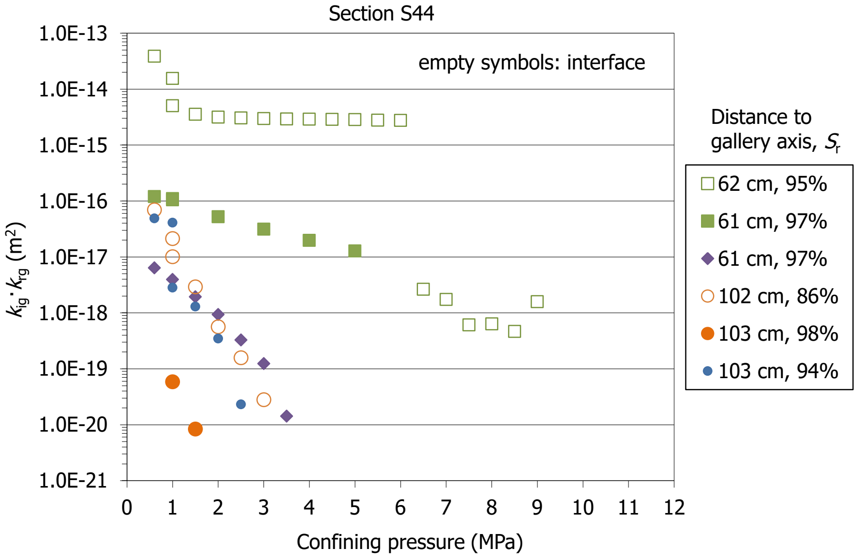

Fig. 127: Change of effective permeability with increasing confining pressure in samples of Section S44 (the values are the average of all the steps in which confining pressure was the same, irrespective of the injection pressure).

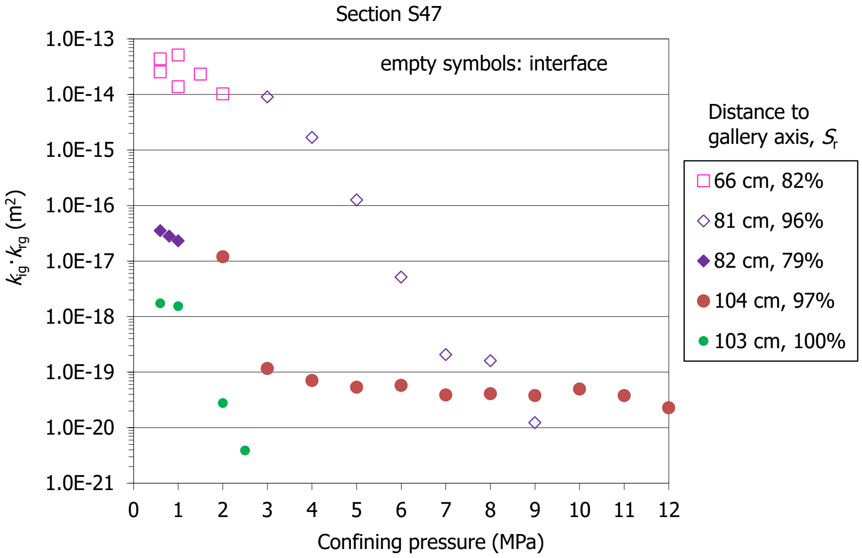

Fig. 128: Change of effective permeability with increasing confining pressure in samples of Section S47 (the values are the average of all the steps in which confining pressure was the same, irrespective of the injection pressure).

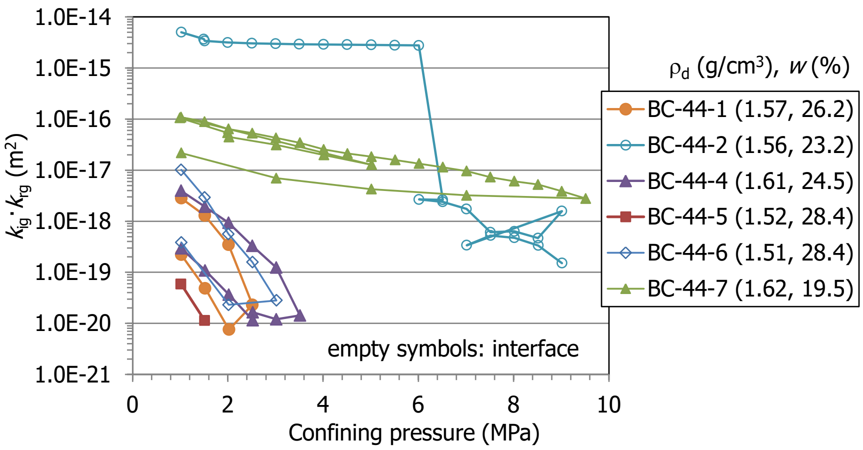

Fig. 129: Change of gas effective permeability with increase/decrease of confining pressure for samples of Section S44.

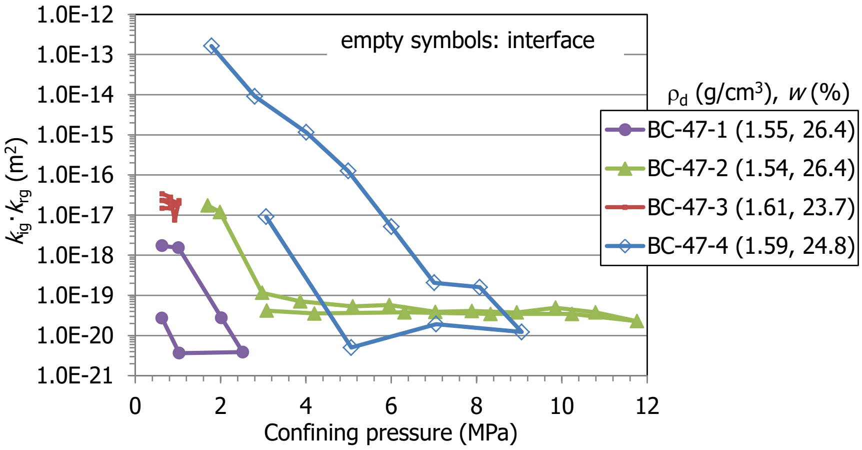

Fig. 130: Change of gas effective permeability with increase/decrease of confining pressure for samples of Section S47.

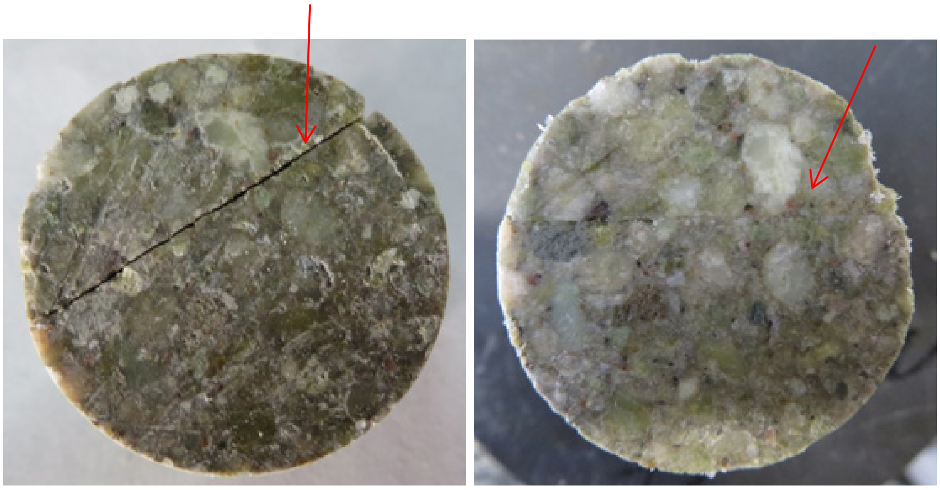

Fig. 131: Initial and final appearance of sample BC-47-4 (the arrows indicate the same position before and after testing).

The gas transport in the untreated FEBEX bentonite was analysed in previous research (the FEBEX and FORGE projects: Villar & Lloret 2001, Villar 2002, Villar et al. 2013), and gas permeability was seen to decrease with the decrease in accessible-void ratio –which is computed as e (1-S_r)– following potential expressions with exponents between 3 and 4. The permeability values measured in the FEBEX-DP retrieved samples for different confining pressures have been plotted in Fig. 132 as a function of their accessible-void ratio. The accessible-void ratio values of the samples tested were below 0.15, and the permeability was clearly higher with higher accessible-void ratio. The scatter in the data is high because the range of dry densities and water contents involved was large. There were also samples with and without interface. Figure 132 also shows the effect of confining pressure on gas effective permeability for samples of different accessible-void ratio with and without interface included in the data set. In the range of confining pressures from 0.6 to 7 MPa, the permeability decreased with increasing confining pressure, as discussed above. Overall, for similar values of accessible-void ratio the samples with an interface had higher permeability for all the range of confining pressures analysed, although the difference tended to be lower towards the smaller accessible-void ratios.

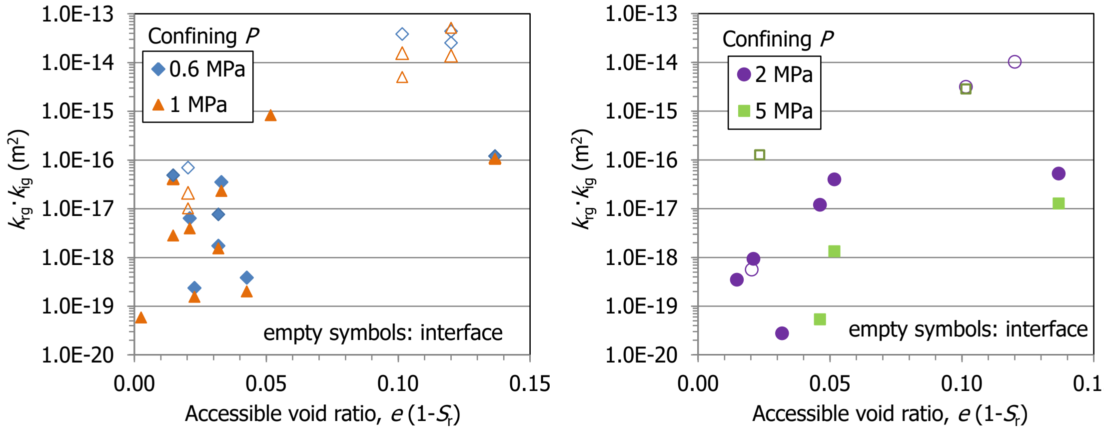

Fig. 132: Effect of confining pressure on gas effective permeability for samples with and without interface (The accessible-void ratio plotted is the initial one.

The values for confining pressure 0.6 and 1 MPa were obtained in the LP and HP setups).

The gas permeability of samples of the reference FEBEX bentonite compacted to different dry densities with various water contents was measured during the FEBEX project in the same LP setup used in the current research (Villar 2002) and during the FORGE project in the same HP setup used in this work (Villar et al. 2013). In the first case (falling-head or unsteady-state permeameter) the confining pressure applied was 0.6 MPa and the injection pressure decreased during the tests from an initial value of 0.1 MPa. In the second case (constant pressure or steady-state permeameter), confining pressures of 0.6 and 1 MPa were applied. For gas pressures below 1.2 MPa no effect of the injection or confining pressures on the value of permeability was detected. The results obtained in FEBEX and in FORGE are plotted in Fig. 133, along with the correlation curve between gas effective permeability, $k_{ig} \cdot k_{rg}$ (m^2), and accessible-void ratio, $e(1-S_r)$, which has the following expression (Villar et al. 2013):

$$k_{ig} \cdot k_{rg} = 1.25 \cdot 10^{-12} \, (e(1-S_r))^{3.22} \qquad [10]$$

The values measured in the samples retrieved during the FEBEX-DP have also been plotted in Fig. 133 and are more clearly seen in the enlargement presented in Fig. 134. In order to make the results strictly comparable, only those values obtained under confining pressures of 0.6 and 1 MPa have been presented. These values were obtained in the exact same setups as the values obtained for the reference sample. The accessible-void ratio of the FEBEX-DP samples is in the low range, because their degree of saturation was very high. Nevertheless, the values obtained for materials recovered in FEBEX-DP are generally consistent with those of the reference bentonite. The exceptions are the samples containing a block interface, with overall gas permeabilities clearly higher than those obtained with Eq. 10. The samples with an interface that had a very low accessible-void ratio (high saturation), such as BC-44-6, drilled in the external ring of the barrier, had permeabilities closer to that of the reference bentonite. This can be interpreted as evidence of effective sealing of this interface as the result of water uptake and clay swelling.

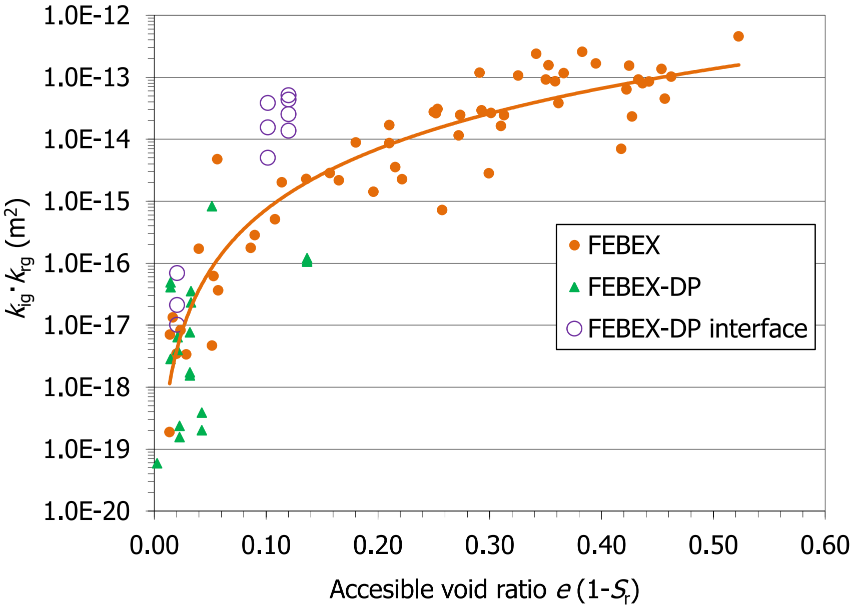

Fig. 133: Gas permeability as a function of the accessible-void ratio for FEBEX samples tested during the FEBEX and FORGE projects and for FEBEX-DP samples with and without interface.

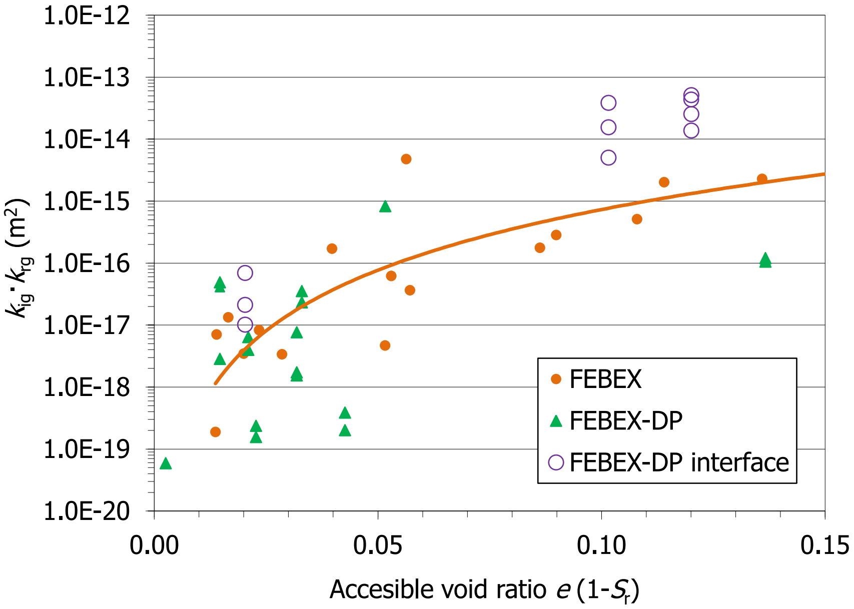

Fig. 134: Gas permeability as a function of the accessible-void ratio for FEBEX samples tested during the FEBEX and FORGE projects and for FEBEX-DP samples with and without interface (enlargement of Fig. 133).

7 Summary and conclusions

The aim of the FEBEX project (Full-scale Engineered Barriers Experiment) was to study the behaviour of components in the near-field of a repository in crystalline rock according to the Spanish reference concept for geological disposal of nuclear waste. As part of this project an *in-situ* test, under natural conditions and at full scale, was performed at the Grimsel Test Site (Switzerland), an underground laboratory managed by Nagra (the Swiss agency for nuclear waste management). The heating stage of the test began in 1997. After five years of operation, half of the experiment was dismantled. The remaining part of the experiment continued until April 2015, when the final and complete dismantling of the experiment was undertaken.

A summary of the results obtained by different laboratories on the characterisation of the bentonite retrieved during the dismantling was presented in this report. At the time of dismantling, i.e. spring-summer 2015, the test had been in operation for 18 years. During this time:

- The bentonite barrier was hydrated with groundwater coming from the granitic host rock.
- Part of the barrier around Heater #2 – whose surface temperature was 100 °C – had been submitted to a steep thermal gradient for the entire test.
- The bentonite slices at the front of the gallery surrounding a dummy canister that replaced Heater #1 after five years of operation (i.e. after the first, partial dismantling) had been exposed to 13 years of heating. The surface temperature of the outer Heater #1 (removed in 2002) had also been set at 100 °C during its operation. This means that these bentonite slices were submitted to a thermal gradient during the first five years of operation and then continued hydrating under isothermal, cooler conditions. In addition, the front bentonite slice (sampling Section S36) had been in contact for the last thirteen years of operation with the shotcrete plug constructed after the partial dismantling.

Information about the temperatures measured in the bentonite during the last part of the test is given in Tab. 1. The concrete/bentonite interaction is dealt with in detail in NAB 16-18 (Turrero & Cloet 2017), but the analyses of the bentonite blocks of Section S36 (although not the parts of the blocks in direct contact with concrete) have been reported here. Likewise, the interaction of the bentonite with the metallic elements of the experiment (sensors, liner) is specifically analysed in NAB 16-16 (Wersin & Kober 2017).

During dismantling numerous bentonite samples, in the form of blocks, cores or irregular fragments, were taken, carefully vacuum-packed and sent to the laboratories. These samples are called FEBEX-DP or retrieved samples in the discussion below. The current report presents results obtained by the Centro de Investigaciones Energéticas, Medioambientales y Tecnológicas (CIEMAT), that carried out an exhaustive characterisation detailed in NAB 16-24 (Villar et al. 2018) and NAB 16-25 (Fernández et al. 2018), and by Clay Technology (ClayTech), Universitat Politècnica de Catalunya (UPC), Bundesanstalt für Geowissenschaften und Rohstoffe (BGR), Universidad Autónoma de Madrid (UAM), Eidgenössische Technische Hochschule Zürich (ETH), Saitama University, Lawrence Berkeley National Laboratory (LBNL) and Správa Úlozist Radioaktivních Odpadú (SÚRAO). Each of these laboratories issued a complete report as listed in the Introduction, and the complete results obtained by each of them are included as Tables in the Annex of this report.

The methodologies followed by each laboratory were in many cases different, and this has an impact on the results obtained. In most cases, it was possible to assess how the experimental procedures affected the results. The study report has focussed on evaluation of the effect of temperature and hydration on the properties and characteristics of the barrier. For this reason, the analysis of results performed has taken into account the position of the samples in the barrier: if they were taken from a cool section or a section around the heater and also at which distance to the granite wall. This was done because these conditions would influence the degree of hydration reached by the sample and the temperature it was submitted to during operation. Additionally, in order to assess the potential changes that occurred during the FEBEX operation on the properties investigated, the values obtained in the FEBEX-DP samples have been compared to those of the reference, untreated FEBEX bentonite.

7.1 Physical state and microstructure

Most of the laboratories determined the water content and dry density of the samples received before any other testing. Despite the fact that there was a large difference in time since retrieval at GTS and sampling in the laboratories, and that different methodologies were followed (particularly for the determination of dry density), the values obtained were comparable. The laboratory determinations showed a clear radial distribution pattern: water content decreased from the granite towards the axis of the gallery whereas dry density increased. Hence, the void ratio of the samples (inversely related to dry density) was lower closer to the gallery axis. There was also consistency between the results obtained in the laboratories and on-site tests (those reported in NAB 16-12); the laboratory determinations even reflected the variations along the gallery that were observed in situ. This suggests that the packing and transport conditions were appropriate to preserve the in-situ state of the blocks even several months after their retrieval.

The specific weight of the bentonite was determined in 22 FEBEX-DP samples by CIEMAT and an average value of 2.70 ± 0.04 g/cm^3 was measured, in the same range of variation as for the reference bentonite. The values determined or used by ClayTech and Saitama were within this range.

The water content of all the samples was above the initial condition (14 %) and in fact most of them were saturated. To analyse the hydration state from a microstructural point of view, CIEMAT measured the basal reflection (*d*001 value) by X-ray diffraction, which gives a measure of the interlayer distance between smectite particles. All the values were above the initial one (~1.48 nm). Most of them were in the range from 1.50 to 1.65 nm, which, despite the changes in the exchangeable cation complex observed, would correspond mostly to a completely developed 2-layer hydrate in transition to a 3-layer hydrate. The samples taken at less than 20 cm from the heater with a water content below 25 % had lower basal spacings. Above this water content the basal reflection tended to increase with water content, i.e. as the distance from the axis of the gallery increased. A few samples had basal reflections close to those corresponding to the 3-layer hydrate. The values obtained for the FEBEX-DP samples for a water content below 27 % were similar to those measured in FEBEX bentonite samples of the same water content saturated with deionised water.

The pore size distribution was analysed by CIEMAT, ETH and UPC with the mercury intrusion porosimetry (MIP) technique. The results obtained by the three groups consistently showed two major pore families in all the samples: a macropore family, with sizes between 10 and 60 µm, and a mesopore family, with sizes between 8 and 20 nm. The diameter modes of these families were higher than those of the reference material (which were 17 ± 3 µm and 9 ± 2 nm, respectively), which was probably related to the overall increase in the water content of the bentonite during operation and the associated swelling. Although there was no good agreement in the exact sizes of the pore families determined by the three groups, the results were very consistent in terms of proportion and evolution of each of them.

All the MIP results indicated a clear increase in the proportion of void ratio corresponding to pores smaller than 50 nm (mesopores and micropores) at the end of FEBEX. More than 65 % of the void ratio corresponded to this pore size at the end of FEBEX, a notable increase from the original 54 %. The reason for these changes is assumed to be the hydration that occurred during FEBEX, which brought about an increase in the percentage of micropores, i.e. those that cannot be intruded by mercury. This agrees with the average increase in interlayer space noted in the previous paragraph and would point towards the ongoing homogenisation of the pore sizes towards the smaller size range.

The pore size distribution also changed as a function of the distance to the gallery axis. It must be remembered that the total void ratio was higher for the samples from the external part of the barrier than for those in the internal part, because there was a decrease in dry density during operation towards the granite. In fact, the overall decrease in void ratio observed towards the axis of the gallery was mostly "absorbed" by the macropores, since the void ratio corresponding to pores larger than 50 nm clearly decreased towards the internal part of the barrier in cool sections, at the same time that the size of the mesopores tended to decrease (ETH's results). CIEMAT's MIP results indicated the presence of a new pore family of larger size in the more saturated samples taken in the external part of the barrier. Close to the heater, where the samples had been dried, there was only a small relative increase in the macropore void ratio.

Computerized tomography was used to analyse the texture of the samples at a larger scale than that investigated by the techniques mentioned above. In particular, to study the fracture network of the retrieved bentonite, LBNL used the non-destructive Synchrotron X-Ray Micro Computerized Tomography (SXR-μCT) technique to look at the interior of the sample, undisturbed as much as possible. The samples showed a network of thin fractures, with sizes in the order of a few tens of microns. The fractures were present in the clay matrix (pure desiccation cracks), some cut across larger crystalline particles (quartz, feldspar, etc.) and some fractures were located along the interfaces of the crystals with the clay-rich matrix (aggregate-matrix detaching). From these observations, it seems reasonable to assume that there were several origins of these fractures. There was also a small amount of microporosity apparently not related to modifications in the microstructure of the material, but made up of aggregate particles in the bentonite. Cracks larger than 45 μm were uncommon, but the samples closer to the granite tended to have a larger amount of large fractures compared to the samples close to the heater or to the centre of the section. This observation agrees with the higher proportion of macropores (> 50 nm) found in the MIP analyses towards the gallery wall and again suggests that the increase in water content brought about the creation of larger voids. In contrast, the sample closest to the heater had the largest relative amount of the smallest microfractures of all the samples.

The interfaces between blocks were studied at Saitama University by means of a Microfocus X-Ray Computerized Tomography (MFX-CT) system. The study of the interfaces inside the barrier was motivated by the implications that unhealed block boundaries might have on density homogenisation, fluid transport, and consequently on the performance assessment of the barrier system. The images clearly showed the interfaces between blocks close to the heater, where conditions were drier. However, the interfaces between blocks recovered from the external, wettest part of the barrier were generally not visible. This indicates that the original block joints had closed up tightly during the long period of water adsorption in the barrier. No significant heterogeneity was observed near the joints. The apertures measured, which were affected by the stress relief upon extraction, were between 0.36 and 0.47 mm.

The external specific surface area, which represents the surface of the intra-aggregate and inter-aggregate voids but not that of the interlayer space, was determined by CIEMAT, ETH and UAM using the BET method. In the FEBEX-DP samples analysed, this parameter was related to the water content the samples had after dismantling. The BET surface areas of samples with a water content above 22 % increased slightly with water content but remained in the order of the reference value. Thus, in the cool sections and in the external part of the barrier in sections around the heater the values found were close to, or slightly higher than the reference one (55 – 56 m^2/g). However, for water content values below 22 % the external specific surface area decreased sharply as water content decreased. In fact, the measured external specific surface area dropped towards the heater, to values as low as 22 m^2/g. This effect could be attributed to aggregation of smectitic particles under shrinkage induced by the initial thermal impact in the barrier.

The total specific surface area, which is a parameter related to the water absorption and swelling capacity of bentonite, was determined by CIEMAT and ETH. The values found by CIEMAT were lower than the 655 m^2/g determined for the reference bentonite, ranging from 510 to 660 m^2/g, but they did not show a consistent trend across the barrier. The same is true for the results obtained by ETH.

The water adsorption capacity of the bentonite, analysed by CIEMAT and ClayTech by determining the water adsorption isotherms of ground samples, remained unchanged for most of the material recovered. Only the samples closest to the heater showed a higher water adsorption capacity for a higher relative humidity, i.e. lower suction.

Additionally, the suction of the bentonite blocks was measured with psychrometers or capacitive sensors by CIEMAT and UPC. Consistent with the changes in water content and dry density observed, the bentonite sections around the heater showed a clear increase of suction from the external part of the barrier towards the heater. The materials recovered from the cooler sections showed the same inwards increase but changes were less substantial. By relating the suction values measured with the degree of saturation or water content of the samples in which it was measured, water retention curves (WRC) were obtained. For a degree of saturation lower than approximately 95 % – corresponding to suctions above 10 MPa –, suction decreased linearly as the degree of saturation increased. The suction did not drop to zero when the clay approached full saturation. This remaining total suction was mainly a consequence of the block retrieval operation, which had the effect of an undrained unloading on the material. The relationship between suction and water content for suctions below 7 MPa was basically dependent on dry density: the higher the dry density the lower the water content for a given suction. The water retention curves obtained from the suction measured agreed very well with those obtained following different methods in the reference bentonite. This corroborates the preservation of the water adsorption capacity of the bentonite as was also confirmed by the determination of the water adsorption isotherms and the interlayer space discussed above.

7.2 Mineralogy and geochemistry

7.2.1 Mineralogy

The mineralogical composition of the bentonite was determined by X-ray diffraction by CIEMAT, ETH and UAM. Overall, it did not change during operation. Depending on the sample and laboratory, the proportion of smectite found was between 82 and 96 %, and K-feldspars, quartz, cristobalite, calcite and plagioclase, appeared in proportions lower than 5 %. ETH found also contents of illite around 3 % in all the samples, whereas UAM found traces of illite in the reference sample and in those samples taken at less than 30 cm from the granite. The accessory minerals detected by SEM by CIEMAT in the samples retrieved were the same as those found in the reference bentonite: carbonates, sulphates, zircon, monacite, biotite, muscovite, ilmenite and apatite.

According to CIEMAT's analyses the smectite phases were made up of a R0 smectite-illite mixed-layer (R0 meaning that the layering was disordered), with 5 – 23 % of illite layers, although most samples had between 5 and 13 %. The smectite had a basal reflection around 1.46 nm, typical of a predominantly divalent montmorillonite. The crystal thickness of the smectite particles ranged between 7.65 and 10.31 nm and the number of TOT layers in the quasicrystals was of 5 – 6. The smectite particles prior to and after the FEBEX in-situ test can be classified as low-charge smectites with the location of the charge mainly in the octahedral sheets. The mean layer charge of the retrieved samples determined by three laboratories (CIEMAT, UAM, ETH) was on average 0.37 MLC/hfu, the same as for the reference bentonite. The structural formulae of the smectite in the samples retrieved did not show changes with respect to the reference bentonite. With a substitution in the tetrahedral sheets between 5 and 15 % these confirmed their classification as Wyoming-type montmorillonites. Hence, the results of all these analyses seem to indicate that no structural changes took place in the montmorillonite during the FEBEX operation. The crystal-chemical analyses performed by UAM showed a subtle increase in layer charge of the montmorillonite towards the heater, but no evidence of illitization.

7.2.2 Solid chemistry

The chemical composition of the bentonite, which was determined by CIEMAT and BGR did not show significant changes among the different samples analysed and with respect to the reference bentonite. There was a small apparent increase in iron and calcium and a decrease in sodium.

The general spatial distribution of the elements was quite homogeneous across the barrier and did not seem to follow any particular trend for most elements. Nevertheless, the content of magnesium increased from the granite towards the axis of the gallery, both in the sections around the heater and in the cool sections, whereas calcium and specially sodium contents increased from the internal part of the barrier towards the gallery wall. These trends were not found in the analyses of the less than 2 μm fractions, which would indicate that they do not respond to changes in the smectite, but in other secondary minerals.

Among the trace elements, the increase in chlorine from the granite towards the gallery axis was clear, and agreed well with the soluble salts analyses, which also showed the increase of chloride towards the internal part of the barrier. The fluorine content, probably coming from the granite groundwater, increased overall above the reference value.

Most of the carbon measured was inorganic and seemed to be related to the calcite content. The total carbon content increased from the axis of the gallery towards the granite, particularly in the sections around the heater. However, microorganisms and organic matter were observed by SEM in samples from the external and middle rings of some bentonite sections, i.e. in the wettest part of the barrier, although it is not possible to assess if these were alive or viable microorganisms. In this context, the microbiology studies showed that cells could be cultivated in large numbers in the samples from moist, low temperature positions of the barrier (Bengtsson et al. 2017).

The results for the cation exchange capacity by CIEMAT showed an overall decrease with respect to the reference value: the retrieved samples had CECs from 89 to 100 meq/100 g (average 95 ± 2 meq/100 g) whereas the reference value is ~ 98 meq/100 g. Despite the uncertainty of the analytical methods and the differences among laboratories (CIEMAT, BGR), no spatial trends were found for this property. The validity of the conclusion of a slight decrease in CEC is supported by the changes in the exchangeable cation complex described below.

Differences in methodology used by the different groups (CIEMAT, BGR, ETH, UAM, SÚRAO) to assess the composition of the exchangeable cation complex have to be taken into account. Most groups determined the "extractable" or "leachable" cations, including not only the exchangeable cations, but also the cations dissolved in the pore water and those from the very soluble minerals dissolved during the exchange procedure. In contrast, CIEMAT corrected the concentration of exchangeable cations measured by subtracting the soluble cations content (Ca and Na) determined in adjacent samples. This has a clear repercussion on the results, because the soluble salt content was not homogeneous across the barrier (see below), and consequently the proportion of "soluble" cations was not the same in all samples. Nevertheless, the trends found by the different groups were consistent.

There was an overall decrease in exchangeable cation positions (as determined by the sum of exchangeable cations), which would agree with the apparent slight decrease in cation exchange capacity observed. The sodium concentration in the exchange complex decreased towards the internal part of the barrier, particularly in the heated sections. The decrease in exchangeable sodium towards the internal part of the barrier in hot sections, agrees with the decrease in water uptake capacity detected by ETH by the Enslin-Neff method. The distribution of exchangeable magnesium and calcium seemed to be affected by temperature, since it was quite homogeneous in the cool Section S59 whereas the exchangeable magnesium and calcium concentration increased towards the heater in the hottest Section S47. Hence, both exchangeable calcium and magnesium responded to temperature. The fact that the exchangeable sodium content decreased towards the heater, while exchangeable magnesium and calcium contents increased, made the exchangeable complex more heterogeneous towards the heater. The concentration of exchangeable potassium was overall higher than the reference value.

7.2.3 Pore water chemistry

The pore water composition was studied by CIEMAT by preparing aqueous extracts and direct pore water extraction by squeezing. The chemical analyses of the water obtained do not give the actual pore water composition in either method, particularly in the case of the aqueous extracts, because of the dilution involved in their preparation. On the other hand, the squeezed pore water can be affected by ultrafiltration processes. Thus, although the water obtained by squeezing is more representative, in both cases it is necessary to perform modelling and make some assumptions to get to the pore water composition of the bentonite in the barrier (not addressed in this report). Nevertheless, the results obtained with both methodologies were very consistent and showed clear patterns. An overall increase in the content of most soluble ions took place because of the general increase in water content and the consequent dissolution of mineral species, which in some cases could have been enhanced by the high temperature.

The overall increase in ionic content was particularly significant for soluble potassium, which agrees with the overall increase with respect to the reference sample found in the chemical analyses of the bulk solid samples. The main soluble ions in the bentonite were sodium and chloride. In the external part of the barrier, close to the granite, the concentration of these ions decreased below the original values, especially in the heated sections. In particular sodium, and mainly chloride, were leached out of the 40 cm closest to the granite and concentrated in the proximity to the heater, where they precipitated. The process of ionic redistribution was similar but less intense in the cool Section S59. Calcium, magnesium and potassium behaved similarly, with increases of their concentration towards the axis of the gallery that were remarkably sharp in the proximity to the heater. This pattern indicates that these soluble species were dissolved in the wettest part of the barrier (because of the water content increase), transported by advection and concentrated in inner parts of the barrier. The movement was enhanced by the thermal gradient, indicating that processes other than advection were also active in concentrating these ions. The soluble species precipitated close to the heater, because of their high concentration and the lower water content in this area.

Sulphate was also depleted close to the granite and its concentration increased towards the interior of the barrier, with a maximum at a temperature-determined distance from the gallery axis. The high temperature seems to have hindered movement of sulphate towards the gallery axis, perhaps as a result of dissolution/precipitation processes.

The bicarbonate content showed an opposite trend and was higher than the reference value in all the more hydrated samples. The bicarbonate could come from the granitic groundwater or from carbonate dissolution from the clay. Towards the interior of the barrier the bicarbonate concentration in the aqueous extracts remained at values similar to those of the reference bentonite in cool sections. In the hot sections the bicarbonate concentration decreased with respect to the original value. These differences must be related to the precipitation of carbonates triggered by the decrease of their solubility with increase of temperature. The pH ranged from 8 to 9.2 (7 in the contact with the liner, as determined by UAM) in the aqueous extracts and from 7.9 to 6.8 in the pore water extracted by squeezing, and the changes in pH followed similar patterns to those of bicarbonate, with a sharp decrease towards the heater.

A special case is Section S36. This section was subjected to a substantial thermal gradient during the first five years of operation followed by being in close contact with the shotcrete plug during the last thirteen years of isothermal, cooler hydration. Hence, for five years dissolution/precipitation, transport processes and exchange reactions would have taken place according to the pattern expected caused by a thermal gradient, which was then more or less obliterated during the subsequent thirteen years of hydration at lower temperature. This lower temperature is derived from its position 1.9 m from the front of Heater#2, around which a thermal gradient was generated during all of FEBEX operation. Temperatures between 40 and 88 °C were measured in Section S42 and between 30 and 44 °C in Section S38 (Tab. 1). In this sense, S36 can be considered as the coolest part of a section submitted to a thermal gradient and hence its behaviour was similar to what was observed in other external parts of the barrier (e.g. those in contact with granite). This is the reason why this section had a distinctive geochemical behaviour, despite the fact that the samples analysed were not those in direct contact with the shotcrete. In fact, the proximity to the concrete plug does not seem to have affected the characteristics of the section, which had geochemical characteristics similar to those of the external part of the barrier in the other vertical sections. To summarise, there was a depletion of soluble elements which would have moved towards the heater, i.e. towards the back of the gallery. In particular, the average concentrations of soluble sodium, sulphate and chloride (confirmed by the lower content of chlorine in the chemical analysis of the bulk samples) in section 36 were clearly lower than those for the reference value. This region unlike other sections, had higher bicarbonate concentration and pH. Also, similar to what happened in the external part of Sections S47 and S53, in Section S36 there was a drastic overall decrease in exchangeable magnesium and an increase in exchangeable calcium with respect to the reference values.

7.3 Thermo-hydro-mechanical properties

Most thermo-hydro-mechanical properties in bentonites depend on their dry density and water content. In order to check if these properties changed during operation, which was the main aim of the THM studies, two approaches were used:

- Samples were obtained by trimming the blocks to the appropriate size of the testing cells, attempting to preserve their dry density and water content, i.e. the same conditions in which they were received. The results were compared either with results obtained in samples trimmed from a reference block (UPC, ClayTech), or with those obtained with empirical correlations resulting from previous investigations relating these properties to the behaviour of a reference bentonite compacted to various dry densities and water contents (CIEMAT).

- The samples retrieved were remoulded to different dry densities and water contents and tested. The results obtained were then compared to those corresponding to samples of the reference bentonite obtained from a reference block and specifically prepared in the same way (ClayTech).

When analysing the hydro-mechanical properties of the bentonite retrieved from the FEBEX in-situ test, the changes experienced by the bentonite during sampling on site and during preparation of specimens in the laboratory have to be kept in mind. Although the samples were preserved carefully and their water content did not seem changed with respect to that their in-situ value, the stresses in the barrier (which at some points were as high as 6 MPa during operation [Martínez et al. 2016]) were released on dismantling. This probably resulted in a decrease of dry density. Additionally, the preparation of specimens to fit the testing rings required drilling and trimming, causing a decrease in the final dry density of the samples tested with respect to that of the bentonite blocks from which they were taken. This decrease was not of the same magnitude in all cases, since it depended on the sample conditions and on the operator.

7.3.1 Thermal properties

The thermal conductivity of the bentonite blocks was measured in situ (Nagra) during dismantling and in the laboratory (CIEMAT, ETH). The thermal conductivity increased with water content and dry density in the same way as it was observed for the reference bentonite. Hence, the thermal conductivity of the bentonite was preserved after operation. The values obtained in situ ranged between 1.2 and 1.4 W/m·K, with no clear spatial variation, probably because the degree of saturation was very high almost everywhere in the bentonite barrier.

7.3.2 Swelling properties

The swelling pressure was determined by ClayTech in the saturated samples (both trimmed and remoulded) kept at constant volume. In both cases, as well as in the samples obtained from the reference block, swelling pressure increased exponentially with dry density. Overall no significant deviations were found with respect to the reference values. The exception to this was a slight swelling pressure reduction observed in some of the remoulded specimens from the innermost ring of the barrier.

The swelling capacity of the samples was tested by CIEMAT by letting the trimmed samples saturate with deionised water in oedometers under a vertical load of 0.5 MPa. The final strain of the samples closer to the heater was higher, because these samples had higher dry density and lower water content, and the swelling capacity is related to both. It also took longer for the deformation of the specimens from dryer regions to stabilise. The comparison of these results with those obtained for the reference bentonite tested under the same conditions showed that on average the vertical strains measured in the FEBEX-DP samples (- 10 %) were lower than the theoretical ones (- 12 %). Most samples from the external, more saturated bentonite ring swelled less than expected, whereas the samples from the inner, drier ring tended to swell as expected or more. As explained in the pore water analyses discussed in the previous Chapter, the samples close to the heater had higher salinity, and this could have brought about some osmotically-driven swelling, because the soluble salts in the bentonite were dissolved by the deionised water in the oedometer cell and leached into it. This effect was remarkable once the more important crystalline swelling had been completed and did not take place in the samples from the external part of the barrier where salinity was below the salinity of the reference bentonite.

7.3.3 Compression testing

The high-stress oedometric and isotropic consolidation tests carried out allowed for determination of the post-mortem pre- and post-yield compressibility and the preconsolidation stress of the bentonite. CIEMAT performed the tests under oedometric conditions and at constant suction applying vertical pressures of up to 32 MPa and UPC performed the tests under constant water content applying pressures of up to 57 MPa in oedometric conditions and 25 MPa in isotropic conditions.

The coefficient of consolidation decreased as the vertical stress increased until approximately 30 MPa. For further loading/unloading steps, the coefficient of consolidation was kept approximately constant. The difference between the coefficients obtained by UPC and CIEMAT reflects the higher rigidity of samples tested under controlled suction. As the vertical stress increased from 17 to 57 MPa the water permeability decreased irreversibly, but the relationship between the values calculated from the consolidation tests and those directly measured in other FEBEX-DP samples was not clear.

On loading at high stresses the compressibility curves tended to move towards matching that of the reference block. The minimum preconsolidation stress determined for the samples retrieved was 11 MPa, and hence the pre-yield compressibility for vertical stresses below 11 MPa (κ) and the post-yield compressibility (λ) for higher vertical stresses were determined. The apparent preconsolidation stresses determined in the samples retrieved were between 11 and 24 MPa. The blocks installed in the FEBEX in-situ test at Grimsel were manufactured by applying uniaxial vertical pressures of between 40 and 45 MPa, which should correspond approximately to the preconsolidation stress of the clay. This decrease in the apparent preconsolidation pressure of the retrieved samples with respect to the reference ones can be explained by the volume increase experienced by the bentonite during hydration and the decrease in suction. The apparent preconsolidation pressure values tended to be lower as the initial void ratio was higher and the suction was lower. According to UPC's estimations, the degree of saturation at the yield point was systematically higher (total suction was lower) with the increase in distance to the gallery axis. Logically, the compressibility of the samples retrieved was higher both in the plastic and the elastic zone, because of their higher initial void ratio. The post-yield compressibility particularly increased for the samples that reached the lowest suction during barrier operation, i.e. those from cool sections or taken closest to the granite. Also, both the pre- and post-yield compressibility of samples from a section around the heater were lower than those of samples from a lower temperature section, which could be related to the higher degree of saturation and void ratio in these cooler regions.

The consolidation tests performed under isotropic conditions showed that some samples displayed an anisotropic deformational response with lower radial straining. This behaviour could be inherited from the uniaxial compaction used to manufacture the blocks. Upon saturation and volume increase the initial anisotropy tended to disappear in some cases. The mean preconsolidation stresses determined from these tests were between 13 and 15 MPa.

The unconfined compressive strength of specimens from a section around the heater was determined by ClayTech by means of unconfined compression tests on pre-saturated samples obtained by trimming. The compressive strengths were between 1000 and 1800 kPa and increased exponentially with the dry density of the samples. The vertical strain at failure clearly decreased from the gallery wall towards the liner, indicating a more brittle behaviour in the samples that had been subjected to higher temperature. The lower strain at failure observed for some of the specimens from the field experiment is consistent with results seen in other large scale field tests (e.g. Dueck et al. 2011).

7.3.4 Hydraulic properties

The hydraulic conductivity of samples saturated with deionised water obtained by trimming from the blocks and by remoulding was measured by CIEMAT and ClayTech. The values obtained were clearly related to the dry density of the samples, with hydraulic conductivity decreasing with increasing dry density. For the trimmed samples of dry densities below 1.5 g/cm^3, once they were allowed to hydrate and swell into a homogeneous specimen (most of those measured by ClayTech), the hydraulic conductivity was higher than the values that would be expected for reference bentonite at the same dry density. For higher dry densities, where less swelling of the recovered samples occurred, the hydraulic conductivity measured in retrieved samples by CIEMAT tended to be lower than the expected range of variation of this property. So, given the lack of clear conclusion regarding change in hydraulic conductivity, all that can be drawn from these tests is that the saturated permeability of the bentonite remained very low ($< 10^{-13}$ m/s at the end-of-test densities).

The gas permeability of the FEBEX-DP samples was determined by CIEMAT in samples taken at different positions across the barrier, some of which were taken between two blocks, i.e. they were crossed by an interface. Two-phase flow seems to have been the main gas transport mechanism under the testing conditions. Overall the gas permeability depended on the accessible-void ratio of the samples, $e(1\text{-}S_r)$, in the same way as was to be expected for the FEBEX reference bentonite, potentially decreasing with accessible-void ratio. Consequently, it seems no changes on the gas transport properties occurred as the result of the THM conditions that the bentonite was exposed to. The gas permeability of the samples was also related to their position in the barrier, tending to be lower towards the granite, where the degree of saturation was higher, and hence, the accessible-void ratio lower. The void ratio accessible for gas flow was below 0.15 in all the samples tested, given their high degree of saturation. If the correlation between accessible-void ratio and gas permeability is extrapolated towards a value close to zero accessible-void ratio (say 0.002), an almost completely saturated sample, the intrinsic permeability would be in the order of 10^{-21} m^2. This is the same order of magnitude as the intrinsic permeability for a dry density of 1.6 g/cm^3 measured in saturated samples with water flow.

The gas permeability of the samples also depends on their stress state, decreasing noticeably as the confining pressure increased up to 4 MPa. As the confining stress increased, the tortuosity of the gas pathways would increase, which would have caused the decrease in gas permeability, and eventually the closing of pathways. In fact, beyond a confining stress of 4 MPa no gas flow took place through any of the wetter samples. For higher confining pressures the decrease of gas permeability with stress was less significant, except in samples with a vertical block interface present. The decrease in permeability occurred during loading was not reversible, and the gas permeability of the samples after unloading was lower than the initial one. Samples with an interface had higher gas permeability than samples of similar accessible-void ratio with no interface, and it was necessary to apply higher confining pressures to reduce or supress gas flow through them. Nevertheless, the samples drilled along interfaces of the external ring of the barrier had permeabilities closer to those corresponding to the same accessible-void ratio in the reference bentonite, which would indicate the closing and healing of the interface, resulting in gas transport properties that are dominated by the matrix structure and not by the interface. The closing of interfaces in the more hydrated samples of the external part of the barrier was also confirmed by the MFX-CT studies presented previously.

7.4 Closure

The FEBEX-DP investigations undertaken by several laboratories confirmed the good performance and stability of the bentonite barrier over a time period of 18 years. As was observed during the partial dismantling in 2002, the swelling capacity of the bentonite was able to fill all the construction gaps after a further 13 years. It provided a continuous barrier, in which, once saturated, the interfaces between blocks did not have any role on the water content and density distribution or fluid transport. The mineralogy of the bentonite, and in particular the montmorillonite crystal-chemistry, remained unchanged, as well as its physico-chemical and surface properties and its water adsorption capacity. Because of the inwards groundwater movement and the thermal gradient caused by the heater, changes in the pore water chemistry and the cation exchange complex were observed. The thermal, hydraulic and mechanical properties analysed were consistent with the range expected for the reference bentonite, although because of the dry density gradients generated in the barrier, these properties were not homogeneous across the barrier.

8 References

Abós, H. & Martínez, V. (2015): AN 15-578 Sample Log Book 34 to 62 FEBEX-DP (document avialbale on request).

AITEMIN (2014): FEBEX-e. Sensors Data Report (In Situ Experiment) #8. Full report. Madrid, 119 pp.

Åkesson, M., Olsson, S., Dueck, A., Nilsson, S., Karnland, O., Kiviranta, L., Kumpulainen, S. & Lindén, J. (2012): Temperature Buffer Test. Hydro-mechanical and chemical/ mineralogical characterizations. SKB Report P-12-06. Svensk Kärnbränslehantering AB.

Alonso, J., García-Siñeriz, J.L., Bárcena, I., Alonso, M.C., Fernández Luco, L., García, J.L., Fries, T., Pettersson, S., Bodén, A. & Salo, J.-P. (2008): ESDRED. Deliverable 9 of Module 4, WP4. Module 4 (Temporary Sealing Technology). Final Technical Report. 84 pp.

Ammann, L., Bergaya, F. & Lagaly, G. (2005): Determination of the cation exchange capacity of clays with copper complexes revisited. Clay Minerals 40: 441 – 453.

ASTM D2166/D2166M-16. (2016): Standard test method for unconfined compressive strength of cohesive soil. ASTM International, West Conshohocken, PA.

ASTM D4531-15. (2015): Standard test methods for bulk and dry density of peat and peat products. ASTM International, West Conshohocken, PA.

ASTM D4546-85. (2003): Standard test methods for one-dimensional swell or settlement potential of cohesive soils. ASTM International, West Conshohocken, PA.

Bárcena, I & García-Siñeriz, J.L. (2015): FEBEX-DP (GTS) Full Dismantling Sampling Plan (in situ Experiment). Nagra Arbeitsbericht NAB 15-14. 103 pp.

Bárcena, I., Fuentes-Cantillana, J.L. & García-Siñeriz, J.L. (2003): Dismantling of the Heater #1 at the FEBEX "in situ" test. Description of operations. Publicación Técnica Enresa 09/2003, Madrid, 134 pp.

Bárcena, I., García-Siñeriz, J.L. & Huertas, F. (2006): FEBEX Project Final Report. Addendum sensors data report. In situ experiment. Publicación Técnica Enresa 05-5/2006. Madrid, 157 pp.

Bengtsson, A., Blom, A., Taborowski, T., Schippers, A., Edlund, J., Kalinowski, B. & Pedersen, K. (2017): FEBEX-DP: Microbiological Report. Nagra Arbeitsbericht NAB 16-15. 49 pp.

Brunauer, S., Emmett, P.H. & Teller, E. (1938): Adsorption of gases in multimolecular layers. Journal of the American chemical society, 60, 309 – 319.

Cervinka, R. & Kolomá, K. (2016): Determination of CEC and exchangeable cations on sample B-S-36-3. Technical Report XY/2015. Prague, 14 pp.

Chávez-Páez, M., Van Workum, K., de Pablo, L. & de Pablo, J.J. (2001): Monte Carlo simulations of Wyoming sodium montmorillonite hydrates. Journal of Chemical Physics 114(3): 1405 –1413.

Cuevas, J., Ruiz, A.I., Ortega, A. & Fernández, R. (2016): Bentonite laboratory program and report. Contribution to mineralogical and geochemical characterization: S45, mineralogy, crystal-chemistry. UAM, Madrid, 30 pp.

Cuevas, J., Villar, M.V., Martín, M., Cobeña, J.C. & Leguey, S. (2002): Thermo-hydraulic gradients on bentonite: distribution of soluble salts, microstructure and modification of the hydraulic and mechanical behaviour. Applied Clay Science 22 (1 – 2): 25 – 38.

Dohrmann, R., Olsson, S., Kaufhold, S. & Sellin, P. (2013): Mineralogical investigations of the first package of the alternative buffer material test – II. Exchangeable cation population rearrangement. Clay Minerals 48: 215–233.

Dougherty, R. & Kunzelmann, K.H. (2007): Computing local thickness of 3D structures with Image J. Microscopy and Microanalysis 13(S02): 1678 – 1679.

Dueck, A., Johannesson L.-E., Kristensson O. & Olsson S. (2011): Report on hydro-mechanical and chemical-mineralogical analyses of the bentonite buffer in Canister Retrieval Test. SKB Technical Report TR-11-07. Svensk Kärnbränslehantering.

Dueck, A., Nilsson, U. & Åkesson, M. (2016): FEBEX-DP, Hydro-mechanical analyses of the bentonite buffer. Clay Technology AB, 33 pp.

Emmerich, K. (2011): Thermal analysis in the characterization and processing of industrial minerals. In: Christidis, G.E. (Ed.): Advances in the Characterization of Industrial Minerals. European Mineralogical Union and the Mineralogical Society of Great Britain & Ireland, London. pp. 129 – 170.

Enresa (1995): Almacenamiento geológico profundo de residuos radiactivos de alta actividad (AGP). Diseños conceptuales genéricos. Publicación Técnica Enresa 11/95. 105 pp. Madrid.

Enresa (2000): FEBEX Project. Full-scale engineered barriers experiment for a deep geological repository for high level radioactive waste in crystalline host rock. Final Report. Publicación Técnica Enresa 1/2000, Madrid, 354 pp.

Enresa (2006): FEBEX Full-scale Engineered Barriers Experiment, Updated Final Report 1994 – 2004. Publicación Técnica Enresa 05-0/2006, Madrid, 590 pp.

Entwisle, D.C. & Reeder, S. (1993): New apparatus for pore fluid extraction from mudrocks for geochemical analysis. In: Manning, D.A.C., Hall P.L., C.R. Hughes (eds): Geochemistry of clay-pore fluid interactions, Chapman and Hall, London. pp. 365 – 388.

Fernández A.M., Bath A., Waber H.N. & Oyama T. (2003): Water sampling by squeezing drillcores (Annex 2). In: Pearson, F.J., Arcos, D., Bath A., Boisson J.-Y., Fernández, A.M., Gäbler, H.-E., Gaucher, E., Gautschi, A., Griffault, L., Hernán, P., Waber, H.N. (Eds.): Mont Terri Project – Geochemistry of water in the Opalinus Clay formation at the Mont Terri Rock Laboratory. Federal Office for Water and Geology (FOWG). Geology Series No. 5, pp. 171 – 199.

Fernández, A.M. (2004): Caracterización y modelización del agua intersticial en materiales arcillosos: Estudio de la bentonita de Cortijo de Archidona. Ph. D. Thesis. CIEMAT, Madrid, 505 pp.

Fernández, A.M., Baeyens, B., Bradbury & M., Rivas, P. (2004): Analysis of the pore water chemical composition of a Spanish compacted bentonite used in an engineered barrier. Physics and Chemistry of the Earth 29: 105 – 118.

Fernández, A.M., Sánchez-Ledesma, D.M., Tournassat, C., Melón, A., Gaucher, E.C., Astudillo, J. & Vinsot, A. (2014) : Applying the Squeezing Technique to Highly Consolidated Clayrocks for Pore Water Characterisation: Lessons Learned from Experiments at the Mont Terri Rock Laboratory. Applied Geochemistry 49: 2 – 21.

Fernández, A.M., Sánchez-Ledesma, D.M., Melón, A., Robredo, L. M., Rey, J.J., Labajo, M., Clavero, M.A., Carretero, S. & González, A.E. (2018): Thermo-hydro-geochemical behaviour of a Spanish bentonite after of the FEBEX in situ test at the Grimsel Test Site. Technical report CIEMAT/DMA/2G216/03/16. Nagra Technical Report NAB 16-25.

Fernández, A.M., Villar, M.V., Tsige, M. & Pérez del Villar, L. (2001): Estudio de la microfábrica y mineralogía de la bentonita del Cortijo de Archidona. Proyecto Barra I: Efecto salinidad. Informe Técnico CIEMAT/DIAE/54341/2/00. Madrid, 113 pp.

Follett, E.A.C., Mchardy, W.J., Mitchell, B.D. & Smith, B.F.L. (1965): Chemical dissolution techniques in the study of soil clays: Parts I and II. Clay Minerals 6: 23 – 34.

Fuentes-Cantillana, J.L. & García-Siñeriz, J.L. (1998): FEBEX. Final design and installation of the "in situ" test at Grimsel. Publicación Técnica Enresa 12/98. Madrid, 184 pp.

García-Siñeriz, J.L., Abós, H., Martínez, V., de la Rosa, C., Mäder, U. & Kober, F. (2016): FEBEX-DP Dismantling of the Heater #2 at the FEBEX "in situ" test. Description of operations. Nagra Arbeitsbericht NAB 16-11.

Garralón, A., Gómez, P., Turrero, M.J., Torres, E., Buil, B., Sánchez L. & Peña, J. (2018): Hydrogeochemical characterization of the groundwater in the FEBEX gallery. Nagra Arbeitsbericht NAB 16-14.

Hrušková, M. (2008): Analytical characterization of the surface properties of clay minerals – A critical evaluation of the Cu-trien method for CEC determination. Thesis. Charles University in Prague, Faculty of Natural Science, Department of Analytical Chemistry, 141 pp.

Huang, W.-L., Bassett, W.A. & Wu, T.C. (1994): Dehydration and hydration of montmorillonite at elevated temperatures and pressures monitored using synchrotron radiation. American Mineralogist 79: 683 – 691.

Jacinto, A., Villar, M.V. & Ledesma, A. (2012): Influence of water density on the water-retention curve of expansive clays. Géotechnique 62 (8): 657 – 667.

Jackson, M.L. (2005): Soil chemical analysis. Advanced course. Revised Second Edition. Parallel Press. University of Wisconsin-Madison Libraries. Madison, Wisconsin, 930 pp.

Kaufhold, S. & Dohrmann, R. (2008): Comparison of the traditional Enslin-Neff method and the modified Dieng method for measuring water-uptake capacity. Clays and Clay Minerals 6: 686 – 692.

Kaufhold, S., Dohrmann, R. & Ufer, K. (2016): FEBEX Experiment – Geochemistry and Mineralogy. 20 pp.

Kaufhold, S., Dohrmann, R., Sandén, T., Sellin, P. & Svensson, D. (2013): Mineralogical investigations of the alternative buffer material test – I. Alteration of bentonites. Clay Minerals 48: 199–213.

Kawamoto, K. (2016): Microfocus X-Ray Computerized Tomography on selected FEBEX-DP samples at Saitama University. Internal Report.

Keeling, P.S. (1961): The examination of clays by IL/MA. Transactions of the British Ceramic Society 60: 217 – 244.

Keeling, P.S., Kirby, E.C. & Robertson, R.H.S. (1980): Moisture adsorption and specific surface area. Journal of the British Ceramic Society 79: 36 – 40.

Kober, F. & Van Meir, N. (2017): FEBEX-DP – Dismantling related supplementary documents. Nagra Arbeitsbericht NAB 16-68.

Kober, F. (2018): Additional reports on the FEBEX-DP post-mortem THM/THG analysis. Unpubl. Nagra Interner Bericht.

Köster, H.M. (1977): Die Berechnung kristallchemischer Strukturformeln von 2 : 1-Schichtsilikaten unter Berücksichtigung der gemessenen Zwischenschichtladungen und Kationenumtauschkapazitäten, sowie die Darstellung der Ladungsverteilung in der Struktur Mittels Dreieckskoordinaten. Clay Minerals 12: 45 – 54.

Kyoto Electronics Manufacturing C. (1987): Kemtherm QTM-D3 Quick Thermal Conductivity Meter Instruction Manual. Tokyo, 19 pp.

Lagaly, G. & Mermut, A.R. (2001): Baseline studies of the Clay Minerals Society source clays: layer-charge determination and characteristics of those minerals containing 2 : 1 layers. Clays and Clay Minerals 49(5): 393 – 397.

Lanyon, G.W. & Gaus, I. (2016): Main outcomes and review of the FEBEX In Situ Test (GTS) and Mock-Up after 15 years of operation. Nagra Arbeitsbericht NAB 15-04, 79 pp.

Lloret, A. & Villar, M.V. (2007) Advances on the knowledge of the thermo-hydro-mechanical behaviour of heavily compacted FEBEX bentonite. Physics and Chemistry of the Earth Parts A/B/C 32 (8-14): 701 – 715.

MacDowell, A.A., Parkinson, D.Y., Haboub, A., Schaible, E., Nasiatka, J.R., Yee, C.A., Jameson, J.R., Ajo-Franklin, J.B., Brodersen, C.R. & McElrone, A.J. (2012): X-ray micro-tomography at the Advanced Light Source. In: Stock, S.R. (ed.): Developments in X-Ray Tomography VIII. Proc. SPIE 8506: 850618. International Society for Optics and Photonics.

Madejová, J. & Komadel, P. (2001): Baseline studies of the Clay Minerals Society Source Clays: Infrared methods. Clays and Clay Minerals 49(5): 410 – 432.

Marcial, D. (2003) : Comportement hydromécanique et microstructural des matériaux de barrière ouvragée. Ph.D. Thesis. École Nationale des Ponts et Chausées, Paris, 316 pp.

Martínez, V., Abós, H. & García-Siñeriz, J.L. (2016): FEBEX-e: Final Sensor Data Report (FEBEX In Situ Experiment). Nagra Arbeitsbericht NAB 16-19.

Meier, L.P. & Kahr, G. (1999): Determination of the cation exchange capacity (CEC) of clay minerals using the complexes of copper (II) ion with triethylenetetramine and tetraethylenepentamine. Clays and Clay Minerals 47: 386 – 388.

Monsalvo, R., De Pablo, L. & Chávez, M.L. (2006) : Hydration of Ca-Montmorillonite at basin conditions: a Monte Carlo molecular simulation. Revista Mexicana De Ciencias Geológicas 23(1): 84 – 95.

Moore, D. & Reynolds, R. (1989): X-Ray diffraction and the identification and analysis of clay minerals. Oxford University Press, New York, 332 pp.

Olis A.C., Malla P.B. & Douglas, L.A. (1990): The rapid estimation of the layer charges of 2 : 1 expanding clays from a single alkylammonium ion expansion. Clays and Clay Minerals 25: 39 – 50.

Olsen, H.W. (1962): Hydraulic flow through saturated clays. 9th Nat. Conf. On Clays and Clay Minerals. Pergamon. Oxford. 170 – 182.

Parkhurst, D.L. & Appelo, C.A.J. (1999): Users guide to PHREEQC (Version 2): a computer program for speciation, batch reactions, one dimensional transport and inverse geochemical calculations. Water Resources Investigations Report 99-4259, US Geological Survey.

Pineda, J.A., Romero, E., Alonso, E.E. & Pérez, T. (2014): A new high-pressure triaxial apparatus for inducing and tracking hydro-mechanical degradation of clayey rocks. Geotechnical Testing Journal 37(6): 933 – 947.

Plançon A. & Drits, V.A. (2000) : Phase analysis of clays using an expert system and calculation programs for X-ray diffraction by two- and three-component mixed-layer minerals. Clay and Clay Minerals 48: 57 – 62.

Plançon, A. (2013): Identification and characterization of mixed-layer clay minerals by means of XRD of oriented clay mounts. In: Fiore, S., Cuadros, J., Huertas, F.J.(Eds.): Interstratified clay minerals: origin, characterization and geochemical significance. AIPEA Educational Series.

Plötze, M. (2015): FEBEX DP Bentonite characterization. IGT Report CL 1053/1. 15 pp.

Plötze, M. (2017): FEBEX DP Bentonite characterization. IGT Report CL 1053/2.

Romero, E., Alvarado, C. Lloret, A. & Mirsalehi, S. (2017): Laboratory tests on the post mortem hydro-mechanical characterisation of FEBEX bentonite. CIMNE-UPC-GEOLAB, 84 pp.

Sakaki, T. (2016): FEBEX-DP: In-situ measurement of thermal conductivity of bentonite blocks during dismantling and a comparison with CIEMAT laboratory results. Nagra AN 16-505 (Included in NAB 16-68). 25 pp.

Sawhney, B.L. (1970): Potassium and cesium ion selectivity in relation to clay mineral microstructure. Clays and Clay Minerals 18: 47 – 52.

Schindelin, J., Arganda-Carreras, I., Frise, E., Kaynig, V., Longair, M., Pietzsch, T., Preibisch, S., Rueden, C., Saalfeld, S., Schmid, B. & Tinevez, J.Y. (2012): Fiji: an open-source platform for biological-image analysis. Nature Methods 9(7): 676 – 682.

Skipper, N.T., Refson, K. & McConnell, J.D.C. (1991) : Computer simulation of interlayer water in 2 : 1 clays. Journal of Chemical Physics 94 (11): 7434 – 7445.

Sposito, G. (1992): Characterization of particle surface charge. In: Buffle J, van Leeuwen (eds.): Environmental particles. Chelsea, MI: Lewis Publ. p 291 – 314.

Svensson D., Dueck, A., Nilsson, U., Olsson, S., Sandén, T., Lydmark, S., Jägerwall, S., Pedersen, K. & Hansen, S. (2011): Alternative Buffer Material, Status of the ongoing laboratory investigation of reference materials and test package 1. SKB Technical Report TR-11-06. Svensk Kärnbränslehantering.

Tambach, T.J., Hensen, E.J.M. & Smit, B. (2004): Molecular simulations of swelling clay minerals. Journal of Chemical Physics B 108: 7586 – 7596.

Tavenas, F., des Rosiers, J.-P., Leroueil, S., La Rochelle, P. & Roy, M. (1979) : The use of strain energy as a yield and creep criterion for lightly overconsolidated clays. Géotechnique 29(3): 285 – 303.

Thomas, G. W. (1982): Exchangeable cations. In: Page, A. L., Miller, R. H., Keeney, D. R. (Eds.): Methods of soil analysis. Part II. 2nd edition. America Society of Agronomy and Soil Science of America. Madison, USA. pp 159 – 165.

Tomita, K., Takahashi, H. & Watanabe, T. (1988): Quantification curves for mica/smectite interstratifications by X-Ray poder diffraction. Clays and Clay Minerals 36: 258 – 262.

Turrero M.J. & Cloet, V. (Eds.). (2017): FEBEX DP Concrete ageing and concrete-bentonite interaction studies. Nagra Arbeitsbericht NAB 16-18.

Villar, M., Fernández, A.M., Martín, P.L., Barcala, J.M., Gómez-Espina, R. & Rivas, P. (2008): Effect of Heating/Hydration on Compacted Bentonite: Tests in 60-cm Long Cells. Colección Documentos CIEMAT. 72 pp. ISBN 978-84-7834-597-4.

Villar, M.V. & Gómez-Espina, R. (2009): Report on thermo-hydro-mechanical laboratory tests performed by ciemat on febex bentonite 2004 – 2008. Informes Técnicos CIEMAT 1178. Madrid, 67 pp. Agosto 2009.

Villar, M.V. & Lloret, A. (2001): Variation of the intrinsic permeability of expansive clay upon saturation. In: ADACHI, K. & FUKUE, M.(eds.): Clay Science for Engineering. Balkema, Rotterdam. 259 – 266.

Villar, M.V. & Lloret, A. (2008): Influence of dry density and water content on the swelling of a compacted bentonite. Applied Clay Science 39: 38 – 49.

Villar, M.V. (2002): Thermo-hydro-mechanical characterisation of a bentonite from Cabo de Gata. A study applied to the use of bentonite as sealing material in high level radioactive waste repositories. Publicación Técnica Enresa 01/2002, Madrid, 258 pp.

Villar, M.V. (Ed.) et al. (2006): FEBEX Project Final report. Post-mortem bentonite analysis. Publicación Técnica Enresa 05-1/2006, Madrid, 183 pp.

Villar, M.V., Gómez-Espina, R. & Gutiérrez-Nebot, L. (2012): Basal spacings of compacted bentonite. Applied Clay Science 65 – 66: 95-105.

Villar, M.V., Gutiérrez-Rodrigo, V., Iglesias, R.J., Campos, R. & Gutiérrez-Nebot L. (2016b): Changes on the microstructure of compacted bentonite caused by heating and hydration. Proceedings of the 3rd European Conference on Unsaturated Soils (E-UNSAT 2016). E3S Web of Conferences 9, 18001. DOI: 10.1051/e3sconf/20160918001.

Villar, M.V., Gutiérrez-Rodrigo, V., Martín, P.L., Romero, F.J. & Barcala, J.M. (2013): Gas transport in bentonite. Informes Técnicos CIEMAT 1301. Madrid, 63 pp.

Villar, M.V., Iglesias, R.J., Abós, H., Martínez, V., de la Rosa, C. & Manchón, M.A. (2016a): FEBEX-DP onsite analyses report. NAB 16-12. 106 pp.

Villar, M.V., Iglesias, R.J., Gutiérrez-Alvarez, C., Carbonell, B., Campos, R., Campos, G., Martín, P.L. & Castro, B. (2018): FEBEX-DP: Thermo-hydro-mechanical postmortem analysis of bentonite performed at CIEMAT. Technical report CIEMAT/DMA/2G216/2/16. NAB 16-24. Madrid.

Wersin, P. & Kober, F. (eds.) (2017): FEBEX-DP. Metal corrosion and iron-bentonite interaction studies. Nagra Arbeitsbericht NAB 16-16.

Williamson, G.K. & Hall, W.H.. (1953): X-ray line broadening from filed aluminium and wolfram. Acta Metallurgica 1: 22 – 31.

Wilson, M.J. (1987): A handbook of determinative methods in clay mineralogy. Blackie. 308 pp.

Wolters, F. & Emmerich, K. (2007): Thermal reactions of smectites - relation of dehydroxylation temperature to octahedral structure. Thermochimica Acta 462: 80 – 88.

Yoshimi, Y. & Osterberg, J.O. (1963): Compression of partially saturated cohesive soils. J. Soil Mechanics and Foundations Division. ASCE 89, SM 4, 1 – 24.

Zheng, L., Rutqvist, J., Xu, H., Kim, K., Voltolini, M. & Cao, X. (2017): Investigation of coupled processes and impact of high temperature limits in argillite rock: FY17 Progress. Lawrence Berkeley National Laboratory, June 23, 2017, SFWD-SFWST-2017-000040, LBNL No. 2001014.

Appendix: FEBEX-DP postmortem THM/THC analysis report

ETHZ

Tab. A-1: Summary of basic properties. ETHZ.

Sample	**Distance** (cm)	W (%)	ρ_d (g/cm^3)	S_r (%)	λ (W/m·K)
BC-46-1A	106	26.8	1.50	97	
BC-46-2A	93	25.0	1.50	91	
BC-46-3A	77	23.4	1.56	93	0.8381
BC-46-4A	63	20.7	1.60	88	
BC-46-5A	104	29.8	1.40	91	0.8885
BC-46-6A	85	24.9	1.49	89	
BC-46-7A	73	23.8	1.52	89	1.0864
BC-46-8A	58	19.4	1.64	88	0.9543
BC-46-9A	93	25.0	1.55	97	
BC-46-10A	102	26.1	1.52	97	
BC-46-1B	106	26.1	1.56	104	
BC-46-2B	93	24.5	1.50	89	
BC-46-3B	77	23.0	1.60	98	1.027
BC-46-4B	63	20.7	1.62	91	
BC-46-5B	104	30.6	1.37	90	
BC-46-6B	85	25.1	1.55	98	
BC-46-7B	73	23.8	1.56	94	0.993
BC-46-8B	58	19.5	1.62	85	0.939
BC-46-9B	93	25.0	1.52	93	
BC-46-10B	102	25.5	1.51	94	
BD-61-1	106	33.6	1.38		
BD-61-5	0	24.3	1.38		
BD-61-6	106	31.8	1.32		
BD-61-8	60	30.4	1.40		

Tab. A-2: Mercury intrusion porosimetry results. ETHZ.

Sample	**Distance** (cm)	***W*** (%)	***e***	**Intruded *e*** (%)	**> 50 nm** (%)	**Mode > 50 nm** (nm)	**50-2 nm** (%)	**Mode 50-2 nm** (nm)	**e > 50 nm**	**e < 50 nm**
BC-46-1Aa	106	27.3	0.742	45	18	3'034	24	17.2	0.130	0.612
BC-46-1Ab	106	27.3	0.742	51	27	2'599	25	13.5	0.201	0.541
BC-46-1Ba	106	27.3	0.742	44	23	2'904	22	34.2	0.173	0.569
BC-46-1Bb	106	27.3	0.742	48	26	3'456	23	13.2	0.192	0.550
BC-46-4Aa	63	21	0.646	44	26	3'227	16	14.1	0.166	0.480
BC-46-4Ba	63	21	0.646	46	26	3'228	17	31.6	0.169	0.477
BC-46-4Bb	63	21	0.646	48	29	2'744	18	14.0	0.188	0.458
BC-46-7Ab	73	23.5	0.667	45	26	2'966	19	28.7	0.172	0.494
BC-46-8A-f	58	21	0.646	57	25	2'239	25	16.0	0.160	0.486
BD-46-5A-a	59	21	0.646	64	34	107'911	31	22.8	0.256	0.390
BD-46-5A-b	59	21	0.646	68	36	76'780	24	14.3	0.235	0.411
BD-46-8A-a	88	25	0.688	54	28	2'505	23	14.4	0.191	0.497
BD-61-1a	103	32.4	0.862	46	35	1'619	26	29.1	0.299	0.563
BD-61-1b	103	32.4	0.862	48	36	3'456	26	36.5	0.307	0.555
BD-61-5-b	0	25.5	0.837	56	35	3'452	18	16.2	0.293	0.544
BD-61-5-c	0	25.5	0.837	55	37	95'249	18	17.4	0.311	0.526
BD-61-6-a	103	32.4	0.824	50	36	54'683	18	7.5	0.299	0.525
BD-61-6-b	103	32.4	0.824	50	35	1'517	18	11.3	0.293	0.532
BD-61-8 a	60	31.1	0.812	46	32	91'836	24	26.3	0.262	0.550
BD-61-8 c	60	31.1	0.812	47	30	3'457	24	9.9	0.234	0.578

Tab. A-3: Total and BET specific surface areas, water uptake (Enslin-Neff) and mean layer charge. ETHZ.

Sample	**Distance** (cm)	**BET** (m^2/g)	**Total *a*$_s$** (m^2/g)	**Water uptake**[b] (%)	**M.L.C.** (mlc/hfu)
BC-46-1A	106.4	56.3*		167	0.38
BC-46-4B	62.7	43.5*		116	0.38
BC-46-5A	104.3	53.1	665		0.37
BC-46-7A	73.1	49.1*		131	0.37
BC-46-8A	58	38.7	665		0.37
BD-61-1	105.5	52.3*		159	0.38
BD-61-5	0	53.1	660		0.37
BD-61-6	105.7	51.9	675		0.37

[a] Average of two subsamples.

[b] Average of two or three subsamples.

Tab. A-4: Mineralogy by X-ray diffraction (wt%). ETHZ.

Sample	**Distance** (cm)	**Calcite**	**Cristob.**	**Ca-Sm**	**K-Felds**	**Na-Plag**	**Quartz**	**Illite**
BC-46-1A	106	1.4 ± 0.2	0.8 ± 0.3	85.3 ± 2.8	2.1 ± 0.3	5.2 ± 0.4	2.3 ± 0.2	2.9 ± 0.4
BC-46-4B	63	0.3 ± 0.2	0.9 ± 0.1	87.4 ± 2.9	1.8 ± 0.3	4.2 ± 0.4	2.2 ± 0.2	3.2 ± 0.5
BC-46-5A	104	1.4 ± 0.2	0.5 ± 0.4	86.5 ± 2.9	2.9 ± 0.3	3.5 ± 0.4	2.1 ± 0.2	3.1 ± 0.5
BC-46-7A	73	1.1 ± 0.2	1.2 ± 0.3	86.8 ± 2.8	2.0 ± 0.4	3.7 ± 0.4	2.2 ± 0.2	3.0 ± 0.5
BC-46-8A	58	0.8 ± 0.2	1.0 ± 0.3	88.0 ± 2.9	1.7 ± 0.4	3.7 ± 0.4	1.5 ± 0.2	3.3 ± 0.5
BD-61-1	106	1.2 ± 0.2	1.2 ± 0.3	81.8 ± 2.9	3.4 ± 0.4	5.9 ± 0.4	3.6 ± 0.2	2.9 ± 0.4
BD-61-5	0	1.3 ± 0.2	1.5 ± 0.3	87.6 ± 2.9	1.5 ± 0.4	3.0 ± 0.4	1.9 ± 0.2	3.2 ± 0.5
BD-61-6	106	1.4 ± 0.2	1.0 ± 0.3	87.7 ± 2.9	1.5 ± 0.4	3.2 ± 0.4	1.7 ± 0.2	3.5 ± 0.5

Tab. A-5: Total inorganic carbon (TIC), equivalent $CaCO_3$ and total organic carbon (TOC). ETHZ.

Sample	**Distance** (cm)	**TIC** (%)	**$CaCO_3$** (%)	**TOC** (%)
BC-46-1A	106	0.15	1.2	0.06
BC-46-4A	63	0.08	0.6	0.01
BC-46-5A	104	0.12	1	0.02
BC-46-7A	73	0.1	0.8	0.02
BC-46-8A	58	0.06	0.5	0.03
BC-46-9A	93	0.08	0.7	0.01
BC-46-1B	106	0.12	1	0.00
BC-46-4B	63	0.05	0.4	0.04
BC-46-7B	73	0.12	1	0.02
BD-61-1	106	0.19	1.6	0.04
BD-61-5	0	0.12	1	0.02
BD-61-6	106	0.13	1.1	0.01

Tab. A-6: Exchangeable cations and cation exchange capacity (meq/100g). ETHZ.

Sample	**Distance** (cm)	**Ca^{2+}**	**Mg^{2+}**	**Na^{+}**	**K^{+}**	**Fe**	**CEC**
BC-46-1A	106	39.5	35.6	32.4	3.2	0	104[a]
BC-46-5A	104	40	32	34	2.4	0	109
BC-46-7A	73	47.1	32.7	29.4	2.4	0	102[a]
BC-46-8A	58	47	39	30	2.4	0	
BC-46-4B	63	45.2	38.4	26.2	2.6	0	106[a]
BD-61-1	106	40.3	36.2	29.9	3.4	0	102[a]
BD-61-5	0	41	34	31	2.4	0	108
BD-61-6	106	41	35	31	2.4	0	109

* Average of two subsamples.

UAM

Tab. A-7: Water content, BET specific surface area and mean layer charge. UAM.

Sample	**Distance** (cm)	w^a (%)	**BET** (m^2/g)	**M.L.C.** (mlc/huc)
FEBEX			56.0	0.37
BC-45-13	111.5	30.0 ± 2.5	55.3	0.37
BC-45-14	106	30.2 ± 0.3	50.2	0.36
BC-45-15	100	26.9 ± 0.7	57.8	0.36
BC-45-16	93	26.1 ± 0.1	53.9	0.37
BC-45-17	85	24.0 ± 0.5	55.7	0.36
BC-45-18	78	22.9 ± 0.3	51.0	0.36
BC-45-19	70	22.7 ± 0.5	45.9	0.37
BC-45-20	63	21.7 ± 0.0	41.4	0.36
BC-45-21	57	19.9 ± 0.7	30.3	0.37
BC-45-22	51	18.2 ± 0.5	21.9	0.37

Tab. A-8: Mineralogy by X-ray diffraction (%). UAM.

Sample	**Distance** (cm)	**Cristob.**	**Mn**	**Ort**	**Plag**	**Cal**	**Qtz**	**Il**	**Alb**
FEBEX Reference		2	94	< 1	1	1	1	1	-
BC-45-13	111	1	93		2		2	< 1	-
BC-45-14	106	1	92	2	1	1	3	< 1	-
BC-45-15	100	1	92	1	2	1	2	< 1	-
BC-45-16	93	1	94	1	1		2	< 1	-
BC-45-17	85	2	86	1	3	1	7	< 1	-
BC-45-18	78	1	84	2	6	4	3		-
BC-45-19	70	2	93	1	2	-	3		-
BC-45-20	63	2	92	1	2	1	3		-
BC-45-21	57	2	91	2	3	-	2		+
BC-45-22	55	1	77	2	2	1	2		16

Tab. A-9: Structural formula of the montmorillonite obtained from the chemical analysis of the < 2 µm homoionised in calcium. UAM.

Sample	**Distance** (cm)	**Montmorillonite structural formulae**
FEBEX		$K_{0.04 \pm 0.01}Ca_{0.24 \pm 0.06}(Fe_{0.09} Al_{1.41} Mg_{0.50}) Si_{3.94} Al_{0.05}(O_{10} (OH)_2)$
BC-45-13	111	$K_{0.04 \pm 0.01}Ca_{0.22 \pm 0.02}(Fe_{0.09} Al_{1.43} Mg_{0.47}) Si_{3.99} Al_{0.01}(O_{10} (OH)_2)$
BC-45-14	106	$K_{0.04 \pm 0.01}Ca_{0.24 \pm 0.03}(Fe_{0.09} Al_{1.42} Mg_{0.48}) Si_{3.98} Al_{0.02}(O_{10} (OH)_2)$
BC-45-15	100	$K_{0.04 \pm 0.01}Ca_{0.26 \pm 0.03}(Fe_{0.10} Al_{1.41} Mg_{0.49}) Si_{3.93} Al_{0.07}(O_{10} (OH)_2)$
BC-45-16	93	$K_{0.04 \pm 0.01}Ca_{0.25 \pm 0.05}(Fe_{0.09} Al_{1.42} Mg_{0.49}) Si_{3.95} Al_{0.05}(O_{10} (OH)_2)$
BC-45-17	85	$K_{0.05 \pm 0.01}Ca_{0.23 \pm 0.07}(Fe_{0.09} Al_{1.42} Mg_{0.48}) Si_{3.98} Al_{0.02}(O_{10} (OH)_2)$
BC-45-18	78	$K_{0.04 \pm 0.01}Ca_{0.25 \pm 0.04}(Fe_{0.10} Al_{1.41} Mg_{0.50}) Si_{3.96} Al_{0.04}(O_{10} (OH)_2)$
BC-45-19	70	$K_{0.03 \pm 0.01}Ca_{0.26 \pm 0.06}(Fe_{0.09} Al_{1.40} Mg_{0.50}) Si_{3.95} Al_{0.05}(O_{10} (OH)_2)$
BC-45-20	63	$K_{0.03 \pm 0.01}Ca_{0.27 \pm 0.07}(Fe_{0.09} Al_{1.41} Mg_{0.51}) Si_{3.94} Al_{0.06}(O_{10} (OH)_2)$
BC-45-21	57	$K_{0.03 \pm 0.01}Ca_{0.26 \pm 0.08}(Fe_{0.09} Al_{1.41} Mg_{0.50}) Si_{3.94} Al_{0.06}(O_{10} (OH)_2)$
BC-45-22	55	$K_{0.04 \pm 0.01}Ca_{0.27 \pm 0.09}(Fe_{0.09} Al_{1.40} Mg_{0.51}) Si_{3.94} Al_{0.06}(O_{10} (OH)_2)$
BC-45-52	48.5	$K_{0.02 \pm 0.01}Ca_{0.28 \pm 0.05}(Fe_{0.11} Al_{1.37} Mg_{0.53}) Si_{3.95} Al_{0.05}(O_{10} (OH)_2)$

Tab. A-10: Exchangeable cations in the bulk sample and cation exchange capacity of the < 2 µm fraction (cmol(+)/kg). UAM.

Sample	**Distance** (cm)	**Ca^{2+}**	**Mg^{2+}**	**Na^+**	**K^+**	**CEC**
FEBEX		36.0	37.0	26.0	2.3	122.4
BC-45-13	111	51.6	26.3	29.4	2.4	108.6
BC-45-14	106	44.1	28.0	29.0	2.4	105.4
BC-45-15	100	36.7	20.1	29.7	1.9	120.6
BC-45-16	93	49.5	24.5	29.6	1.8	106.5
BC-45-17	85	46.7	27.4	28.8	1.8	112.9
BC-45-18	78	48.6	26.8	24.7	2.1	123.5
BC-45-19	70	42.3	22.7	25.8	2.1	114.1
BC-45-20	63	43.1	27.9	27.2	2.2	127.6
BC-45-21	57	42.8	35.4	24.2	1.7	117.8
BC-45-22	51	43.1	41.2	22.1	2.1	122.7
BM-S-43-P52	48					113.3

Tab. A-11: pH and electrical conductivity of aqueous extracts of solid:liquid ratios 1 : 2.5 and 1 : 5, respectively. UAM.

Sample	**Distance** (cm)	**pH**	**EC** (µs/cm)
FEBEX	-	8.3	908 ± 45
BC-45-13	111.5	8.4	363 ± 5
BC-45-14	106	8.6	301 ± 85
BC-45-15	100	8.6	338 ± 40
BC-45-16	93	8.8	353 ± 27
BC-45-17	85	8.8	423 ± 11
BC-45-18	78	8.7	575 ± 101
BC-45-19	70	8.3	568 ± 40
BC-45-20	63	8.3	788 ± 8
BC-45-21	57	8.1	1'308 ± 321
BC-45-22	55	7.5	2'432 ± 238
BM-S-43-P52	Liner (50)	6.8	5'132 ± 89

BGR

Tab. A-12: Chemical composition of the bulk sample obtained by XRF (%). BGR.

Sample	Distance (cm)	SiO_2	TiO_2	Al_2O_3	Fe_2O_3	MnO	MgO	CaO	Na_2O	K_2O	P_2O_5	(SO_3)	LOI
Ref. ABM	0	55.2		17.2	3.1		4.4	1.8	1.1	1.0	0.00	0.07	16.0
BS-42-1	83	55.1	0.2	17.1	3.2	0.04	4.5	1.7	1.1	0.9	0.04	0.05	15.9
BS-42-1	83	54.1	0.2	17.0	3.1	0.04	4.4	2.5	1.1	1.0	0.04	0.05	16.3
BS-42-2	56	54.3	0.2	17.1	3.3	0.04	4.3	1.9	1.2	0.9	0.04	0.10	16.6
BS-42-2	56	54.7	0.2	17.2	3.2	0.04	4.4	1.8	1.2	0.9	0.04	0.05	16.1
BC-45-23	114	54.1	0.2	17.2	3.1	0.05	4.3	1.7	1.1	0.9	0.03	0.01	17.2
BC-45-24	104	53.8	0.2	17.0	3.1	0.05	4.3	1.9	1.1	0.9	0.04	0.02	17.5
BC-45-25	94	54.4	0.2	17.1	3.1	0.03	4.2	1.7	1.2	1.0	0.04	0.04	16.8
BC-45-26	84	54.2	0.2	17.1	3.3	0.04	4.3	2.0	1.2	1.1	0.04	0.08	16.4
BC-45-27	74	54.2	0.2	17.0	3.4	0.04	4.3	1.8	1.1	1.0	0.04	0.08	16.7
BC-45-28	64	54.7	0.2	16.9	3.1	0.04	4.3	1.8	1.1	0.9	0.04	0.07	16.7
BC-45-29	54	53.8	0.2	16.9	3.1	0.04	4.5	1.8	1.0	0.9	0.04	0.05	17.6
BC-45-48	114	54.2	0.2	17.2	3.1	0.04	4.2	1.8	1.2	1.0	0.04	0.02	16.8
BC-45-49	104	53.8	0.2	16.9	3.1	0.04	4.2	2.1	1.1	0.9	0.04	0.03	17.3
BC-45-50	94	53.0	0.2	16.6	3.0	0.04	4.3	2.9	1.1	0.9	0.04	0.05	17.7
BC-45-51	84	54.4	0.2	16.9	3.1	0.04	4.2	1.9	1.1	1.0	0.04	0.07	16.9
BC-45-52	74	54.7	0.2	16.8	3.1	0.03	4.3	1.6	1.1	1.0	0.03	0.05	17.1
BC-45-53	64	54.1	0.2	17.0	3.2	0.04	4.3	1.8	1.1	1.0	0.04	0.06	17.2
BC-45-54	54	54.3	0.2	16.6	3.1	0.04	4.6	1.7	1.0	1.0	0.04	0.03	17.2
BM-S-48-2 1	46	53.5	0.2	17.0	3.0	0.04	4.7	1.8	0.9	0.8	0.03	0.03	17.8
BM-S-48-2 2	46	53.8	0.2	17.0	3.1	0.04	4.6	1.6	0.9	0.9	0.03	0.04	17.7
BM-S-48-2 3	46	53.6	0.2	17.2	3.0	0.03	4.6	1.6	0.9	0.9	0.04	0.03	17.7
BM-S-48-2 4	46	54.2	0.2	17.0	3.1	0.04	4.7	1.7	0.9	0.9	0.04	0.04	17.1
BM-S-48-2 5	46	54.2	0.2	16.7	3.1	0.04	5.0	1.7	0.8	0.9	0.04	0.04	17.1
BM-S-48-3 1	81	54.2	0.2	16.8	3.1	0.04	4.3	2.0	1.1	0.9	0.04	0.05	17.1
BM-S-48-3 2	81	54.2	0.2	17.1	3.1	0.04	4.3	1.8	1.1	1.1	0.04	0.08	16.8
BM-S-48-3 3	81	54.4	0.2	17.0	3.2	0.04	4.3	1.9	1.1	0.9	0.04	0.09	16.8
BM-S-48-3 4	81	54.7	0.2	16.9	3.2	0.04	4.3	2.1	1.2	1.0	0.04	0.09	16.3
BS-50-1	115	54.7	0.2	17.0	3.1	0.04	4.3	1.7	1.2	1.0	0.04	0.02	16.6
BS-50-2	108	54.4	0.2	16.9	3.2	0.04	4.3	2.1	1.1	1.0	0.04	0.03	16.6
BS-50-3	101	54.1	0.2	17.2	3.1	0.05	4.3	1.9	1.2	0.9	0.04	0.03	16.9
BS-50-4	94	54.7	0.2	17.0	3.2	0.04	4.3	1.7	1.2	1.0	0.03	0.04	16.5
BS-50-5	87	54.2	0.2	17.1	3.2	0.04	4.3	1.9	1.2	1.0	0.04	0.06	16.6
BS-50-6	81	54.4	0.2	17.1	3.1	0.04	4.2	1.8	1.2	1.1	0.04	0.08	16.5
BS-50-7	74	54.3	0.2	17.1	3.1	0.04	4.3	1.9	1.2	1.0	0.04	0.12	16.5
BS-50-8	67	54.0	0.2	16.9	3.1	0.03	4.3	2.0	1.1	0.8	0.04	0.10	17.2
BS-50-9	60	54.7	0.2	17.0	3.2	0.04	4.3	1.7	1.1	0.9	0.04	0.08	16.6

Tab. A-12: Cont.

Sample	**Distance** (cm)	**SiO_2**	**TiO_2**	**Al_2O_3**	**Fe_2O_3**	**MnO**	**MgO**	**CaO**	**Na_2O**	**K_2O**	**P_2O_5**	**(SO_3)**	**LOI**
BS-50-10	53	53.8	0.2	17.1	3.2	0.04	4.5	1.8	1.0	0.9	0.04	0.06	17.2
BC-53-13	114	54.5	0.2	17.2	3.2	0.04	4.4	1.8	1.2	1.1	0.04	0.02	16.4
BC-53-14	104	54.5	0.2	17.2	3.2	0.04	4.3	1.9	1.2	1.0	0.04	0.03	16.3
BC-53-15	94	54.3	0.2	17.0	3.2	0.04	4.3	1.8	1.2	1.0	0.04	0.04	16.8
BC-53-16	84	54.1	0.2	17.0	3.1	0.04	4.3	1.9	1.2	1.0	0.04	0.04	17.0
BC-53-17	74	54.3	0.2	17.1	3.2	0.04	4.4	1.9	1.2	1.0	0.05	0.05	16.6
BC-53-18	64	54.5	0.2	17.1	3.1	0.04	4.4	1.8	1.1	0.9	0.04	0.07	16.6
BC-53-19	54	54.6	0.2	17.1	3.2	0.04	4.5	1.9	1.1	1.0	0.04	0.07	16.2

Tab. A-13: Trace elements in the bulk sample by XFR (mg/kg). BGR.

Sample	**Distance** (cm)	**Ag**	**Ba**	**Cd**	**Ce**	**Cs**	**I**	**In**	**La**	**Nd**	**Sb**	**Sm**	**Sn**	**Te**
BS-50-1	115	< 0.5	168.6	< 0.5	74.1	4.7	< 0.5	< 0.5	32.8	28.9	0.9	6.2	7.7	< 0.5
BS-50-2	108	< 0.5	157.5	< 0.5	74.4	4.4	< 0.5	< 0.5	32.9	28.0	< 0.5	6.2	7.8	< 0.5
BS-50-3	101	< 0.5	134.2	< 0.5	74.0	4.9	< 0.5	< 0.5	35.0	28.2	< 0.5	6.2	8.1	0.7
BS-50-4	94	< 0.5	150.2	< 0.5	73.7	4.1	< 0.5	< 0.5	33.0	27.2	0.6	5.6	8.2	< 0.5
BS-50-5	87	< 0.5	126.9	< 0.5	73.1	4.6	< 0.5	< 0.5	34.5	28.2	< 0.5	7.0	7.6	0.6
BS-50-6	81	< 0.5	112.9	< 0.5	71.6	4.9	< 0.5	< 0.5	33.6	26.4	0.8	6.0	8.4	< 0.5
BS-50-7	74	< 0.5	142.9	< 0.5	73.6	5.2	< 0.5	< 0.5	34.5	28.3	0.6	6.1	7.7	< 0.5
BS-50-8	67	< 0.5	123.4	< 0.5	78.4	4.8	< 0.5	< 0.5	35.4	29.2	0.5	6.7	8.0	0.5
BS-50-9	60	< 0.5	159.5	< 0.5	72.6	4.8	< 0.5	< 0.5	33.2	29.1	< 0.5	6.5	7.8	< 0.5
BS-50-10	53	< 0.5	131.3	< 0.5	70.0	4.4	< 0.5	< 0.5	33.0	25.7	< 0.5	6.7	8.1	0.5

Tab. A-14: Total, organic and inorganic carbon and total sulphur (%). BGR.

Sample	**Distance** (cm)	C_{total}	C_{org}	C_{carb}	S_{total}
Ref. ABM	0	0.14	0.06	0.08	0.03
BS-42-1	83	0.12	0.06	0.06	0.03
BS-42-1	83	0.28	0.05	0.23	0.03
BS-42-2	56	0.13	0.06	0.07	0.06
BS-42-2	56	0.12	0.05	0.07	0.03
BC-45-23	114	0.14	0.07	0.07	0.02
BC-45-24	104	0.18	0.07	0.11	0.01
BC-45-25	94	0.13	0.07	0.06	0.02
BC-45-26	84	0.16	0.07	0.09	0.03
BC-45-27	74	0.11	0.06	0.05	0.02
BC-45-28	64	0.10	0.06	0.04	0.04
BC-45-29	54	0.10	0.07	0.03	0.03
BC-45-48	114	0.16	0.07	0.09	0.02
BC-45-49	104	0.21	0.07	0.14	0.01
BC-45-50	94	0.37	0.10	0.27	0.01
BC-45-51	84	0.13	0.06	0.07	0.01
BC-45-52	74	0.10	0.06	0.04	0.01
BC-45-53	64	0.12	0.06	0.06	0.05
BC-45-54	54	0.09	0.06	0.03	0.03
BM-S-48-2 1	46	0.13	0.05	0.08	0.03
BM-S-48-2 2	46	0.09	0.05	0.04	0.02
BM-S-48-2 3	46	0.09	0.06	0.03	0.02
BM-S-48-2 4	46	0.09	0.06	0.03	0.02
BM-S-48-2 5	46	0.12	0.07	0.05	0.03
BM-S-48-3 1	81	0.20	0.07	0.13	0.03
BM-S-48-3 2	81	0.12	0.06	0.06	0.05
BM-S-48-3 3	81	0.14	0.06	0.08	0.04
BM-S-48-3 4	81	0.16	0.06	0.10	0.04
BS-50-1	115	0.12	0.07	0.05	0.02
BS-50-2	108	0.20	0.05	0.15	0.02
BS-50-3	101	0.15	0.06	0.09	0.02
BS-50-4	94	0.12	0.09	0.03	0.02
BS-50-5	87	0.14	0.07	0.07	0.02

Tab. A-14: Cont.

Sample	**Distance** (cm)	C_{total}	C_{org}	C_{carb}	S_{total}
BS-50-6	81	0.15	0.06	0.09	0.02
BS-50-7	74	0.14	0.06	0.08	0.03
BS-50-8	67	0.18	0.06	0.12	0.04
BS-50-9	60	0.12	0.06	0.06	0.04
BS-50-10	53	0.12	0.06	0.06	0.04
BC-53-13	114	0.12	0.05	0.07	0.02
BC-53-14	104	0.15	0.05	0.10	0.03
BC-53-15	94	0.12	0.06	0.06	0.03
BC-53-16	84	0.14	0.05	0.09	0.03
BC-53-17	74	0.12	0.05	0.07	0.03
BC-53-18	64	0.11	0.05	0.06	0.04
BC-53-19	54	0.11	0.05	0.06	0.04

Tab. A-15: Exchangeable cations and cation exchange capacity (meq/100g). BGR.

Block Sample	**Distance** (cm)	Ca^{2+}	Mg^{2+}	Na^{+}	K^{+}	**CEC**
BS-42-1	83	39.4	39.2	28.5	2.5	98.9
BS-42-1	83	41.3	38.1	28.2	2.6	99.3
BS-42-2	56	42.4	38.9	26.9	2.5	97.0
BS-42-2	56	40.2	38.1	27.3	2.5	98.7
BC-45-23	114	39.4	35.6	29.1	2.3	102.2
BC-45-24	104	42.1	34.7	29.2	3.3	102.7
BC-45-25	94	40.7	33.9	28.9	2.5	99.8
BC-45-26	84	42.9	33.8	28.0	2.5	99.8
BC-45-27	74	43.5	34.4	27.5	2.5	98.8
BC-45-28	64	44.3	36.3	26.5	2.5	101.1
BC-45-29	54	47.6	48.0	23.0	2.5	101.4
BC-45-48	114	38.3	34.9	28.1	2.3	97.7
BC-45-49	104	41.7	34.0	28.6	2.5	97.8
BC-45-50	94	43.5	34.3	28.5	2.7	99.1
BC-45-51	84	43.1	34.3	28.2	2.5	99.0
BC-45-52	74	41.1	34.6	26.4	2.7	96.7
BC-45-53	64	46.1	38.2	26.9	2.8	101.6

Tab. A-15: Cont.

Block Sample	**Distance** (cm)	**Ca^{2+}**	**Mg^{2+}**	**Na^{+}**	**K^{+}**	**CEC**
BC-45-54	54	44.7	47.3	22.0	2.7	97.4
BM-S-48-2 1	46	47.2	45.4	24.0	2.5	103.7
BM-S-48-2 2	46	45.1	45.8	23.5	2.5	101.0
BM-S-48-2 3	46	46.3	49.7	21.7	2.9	101.4
BM-S-48-2 4	46	45.2	48.2	21.8	3.0	99.6
BM-S-48-2 5	46	42.9	51.5	18.8	4.0	95.1
BM-S-48-3 1	81	45.2	35.1	28.3	3.3	101.0
BM-S-48-3 2	81	43.6	35.1	28.2	2.7	100.4
BM-S-48-3 3	81	43.6	34.2	28.3	2.5	101.0
BM-S-48-3 4	81	43.2	33.0	27.4	2.2	98.4
BS-50-1	115	38.9	35.8	29.1	2.4	100.6
BS-50-2	108	40.0	34.7	28.9	2.3	99.3
BS-50-3	101	41.1	35.6	29.9	2.2	102.6
BS-50-4	94	39.7	34.7	29.4	2.5	99.5
BS-50-5	87	41.6	34.3	29.3	2.5	99.5
BS-50-6	81	41.1	33.2	28.3	2.1	96.6
BS-50-7	74	43.4	34.1	29.0	2.2	99.0
BS-50-8	67	45.2	34.8	28.8	2.2	100.9
BS-50-9	60	42.4	36.6	25.6	2.4	96.7
BS-50-10	53	44.8	43.2	24.0	2.9	97.8
BC-53-13	114	35.6	36.7	26.9	2.9	94.9
BC-53-14	104	37.9	36.5	27.2	2.5	96.4
BC-53-15	94	37.7	36.6	27.0	2.5	96.0
BC-53-16	84	38.6	36.1	26.6	2.7	95.6
BC-53-17	74	40.6	36.7	26.7	2.5	96.8
BC-53-18	64	43.0	37.9	26.3	2.5	98.0
BC-53-19	54	43.4	40.8	24.3	2.5	95.4

SÚRAO

Tab. A-16: Exchangeable cations and cation exchange capacity obtained with two methods for a sample taken at 51 cm from the gallery axis (meq/100g). SÚRAO.

Sample	**Ca^{2+}**	**Mg^{2+}**	**Na^{+}**	**K^{+}**	**CEC_{VIS}[a]**	**CEC_{Cu}[a]**
BS-36-3-4	37.4	41.8	26.9	3.1	102.5 ± 4.7	106.8 ± 0.6
BS-36-3-5	31.1	41.6	26.3	3.4	96.4 ± 6.6	104.0 ± 3.2
BS-36-3-6	43.0	45.4	26.3	3.2	99.1 ± 6.6	102.8 ± 1.8
BS-36-3-7	40.5	44.5	28.7	3.9	97.3 ± 21.2	103.1 ± 23.3
BS-36-3-8	41.1	45.0	27.6	4.2	97.0 ± 6.4	101.6 ± 5.5
BS-36-3-9	40.8	49.7	27.7	3.7	100.9 ± 4.4	103.9 ± 1.9
BS-36-3-10	35.3	48.1	27.7	3.9	96.0 ± 8.7	99.3 ± 7.4
BS-36-3-11	37.4	46.3	27.1	3.9	96.6 ± 5.8	101.4 ± 3.5
BS-36-3-12	38.9	43.6	27.9	3.4	94.9 ± 4.9	100.7 ± 1.6
BS-36-3-13	38.2	45.2	25.5	3.3	95.4 ± 18.7	99.5 ± 13.3

[a] Average of three subsamples.

Clay Technology

Tab. A-17: Summary of basic properties. ClayTech.

Sample	**Distance** (cm)	***W*** (%)	**ρ_d** (g/cm^3)	***S*r** (%)
BB-47-12	50	16.9	1.71	76
BB-47-12	52	16.9	1.69	75
BB-47-12	54	16.8	1.71	77
BB-47-12	56	17.5	1.71	79
BB-47-12	58	17.3	1.71	79
BB-47-12	60	18	1.71	82
BB-47-12	62	18.2	1.70	81
BB-47-11	71	22.6	1.65	95
BB-47-11	73	22.6	1.65	94
BB-47-11	75	22.2	1.66	93
BB-47-11	77	23	1.65	95
BB-47-11	79	23.2	1.65	96
BB-47-11	81	23.6	1.64	97
BB-47-11	83	23.5	1.64	96
BB-47-11	85	23.6	1.64	96
BB-47-11	87	23.6	1.64	96
BB-47-11	89	24.1	1.63	98
BB-47-11	91	23.8	1.63	96
BB-47-10	92	24.1	1.65	100
BB-47-10	93	25.1	1.62	99
BB-47-10	94	25.5	1.62	101
BB-47-10	95	24.8	1.61	97
BB-47-10	96	25.6	1.61	101
BB-47-10	97	24.9	1.62	98
BB-47-10	98	24.3	1.62	97
BB-47-10	100	26.5	1.57	98
BB-47-10	102	25.6	1.60	98
BB-47-10	104	25.9	1.59	99
BB-47-10	106	26.6	1.59	101
BB-47-10	108	26.5	1.58	100
BB-47-10	110	27.8	1.56	102
BB-47-10	112	27.1	1.57	100

Tab. A-18: Water sorption isotherms determined on ground samples of the reference bentonite and in a sample taken at 49 cm from the gallery axis. ClayTech.

Sample	**Ref -No17**	**Ref-No18**	**Ref-No19**	**BB47-12-9**
Initial *w* (%)	14.2	61.9	1.2	16.1
RH (%)	*w* (%)			
0	0.2	0.8	0.6	1.9
11	7.6	8.0	4.7	8.2
33	12.7	13.1	11.2	12.3
58	16.0	17.7	15.5	15.7
75	19.3	21.4	18.9	18.9
84	21.3	23.5	20.6	21.6
93	25.3	28.8	24.3	29.1
97	30.6	35.0	31.2	48.0

Tab. A-19: Swelling pressure and hydraulic conductivity of samples remoulded from a FEBEX reference block. ClayTech.

Sample	ρ_d (g/cm^3)	W (%)	P_s (MPa)	**Hyd. Grad.** (m/m)	k_w (m/s)
Ref-No01	1.41	35.3	2.3	2'950	2.2×10^{-13}
Ref-No02	1.42	34.8	2.3	2'930	2.1×10^{-13}
Ref-No03	1.41	35.7	2.2	4'550	2.2×10^{-13}
Ref-No04	1.45	33.2	3.0	4'620	1.5×10^{-13}
Ref-No05	1.49	31.2	4.1	9'060	9.1×10^{-14}
Ref-No06	1.52	29.8	5.5	9'080	7.3×10^{-14}
Ref-No07	1.58	27.1	8.2	11'260	5.0×10^{-14}
Ref-No08	1.60	26.7	10.4	11'060	4.5×10^{-14}
Ref-No20	1.38	36.3	1.8	5'040	4.1×10^{-13}
Ref-No21	1.67	23.7	18.7	19'590	2.7×10^{-14}

Tab. A-20: Swelling pressure and hydraulic conductivity of remoulded samples. ClayTech.

Sample	**Distance** (cm)	**ρ_d** (g/cm^3)	***W*** (%)	**P_s** (MPa)	**Hyd. Grad.** (m/m)	**k_w** (m/s)
BB47-10-3	113	1.53	29.6	6.6	8'140	5.5×10^{-14}
BB47-10-4	101	1.51	30.6	5.0	8'140	6.3×10^{-14}
BB47-11-3	87	1.51	30.4	4.1	6'820	7.5×10^{-14}
BB47-11-4	75	1.51	30.9	4.6	6'820	8.8×10^{-14}
BB47-12-3	62	1.54	29	4.2	8'140	7.7×10^{-14}
BB47-12-4	60	1.57	27.2	6.6	8'140	6.7×10^{-14}
BB47-12-10	60	1.56	28.4	5.6	4'940	8.6×10^{-14}
BB47-12-19	60	1.55	27.7	5.3	7'890	9.7×10^{-14}
BB47-12-14	50	1.48	31.5	3.7	6'070	1.3×10^{-13}
BB47-12-15	50	1.46	32.2	2.7	4'330	1.8×10^{-13}
BB47-12-16	50	1.48	30.5	2.9	4'290	1.8×10^{-13}
BB47-12-18	50	1.50	30.4	4.1	7'600	1.7×10^{-13}

Tab. A-21: Swelling pressure and hydraulic conductivity of trimmed samples. ClayTech.

Sample	**Distance** (cm)	**ρ_d** (g/cm^3)	***W*** (%)	**P_s** (MPa)	**Hyd. Grad.** (m/m)	**k_w** (m/s)
BB47-10-1	113	1.36	37.5	1.3	3'550	2.8×10^{-13}
BB47-10-2	100	1.41	35.2	2.0	3'000	2.4×10^{-13}
BB47-11-1	87	1.51	30.8	3.8	7'100	1.2×10^{-13}
BB47-11-2	74	1.49	31.4	3.1	7'240	1.5×10^{-13}
BB47-12-1	62	1.44	32.7	2.4	3'490	3.8×10^{-13}
BB47-12-2	60	1.41	34.6	2.2	3'110	9.1×10^{-13}
BB47-12-11	60	1.33	38	1.0	2'090	2.9×10^{-12}
BB47-12-12	60	1.51	29.1	4.2	5'150	1.8×10^{-13}
BB47-12-13	60	1.45	32.4	2.2	2'290	4.1×10^{-13}
BB47-12-17	60	1.48	30.5	3.3	4'260	5.0×10^{-13}

Tab. A-22: Unconfined compressive stress of samples remoulded from a FEBEX reference block. ClayTech.

Sample	ρ_d (g/cm^3)	W (%)	q_{max} (MPa)	ε (%)
Ref-No09	1.43	33.3	1'270	6.8
Ref-No10	1.41	34.0	1'190	7.5
Ref-No11	1.45	33.0	1'470	6.8
Ref-No12	1.49	31.0	1'910	6.7
Ref-No13	1.53	29.4	2'500	6.7
Ref-No14	1.57	27.1	3'050	7.1
Ref-No15	1.61	25.9	3'920	5.9
Ref-No16	1.66	23.2	5'630	6.0

Tab. A-23: Unconfined compressive stress of trimmed samples. ClayTech.

Sample	**Distance** (cm)	ρ_d (g/cm^3)	W (%)	q_{max} (MPa)	ε (%)
BB-47-10-5	113	1.37	36.5	740	9.8
BB-47-10-6	113	1.44	32.9	1'190	7.6
BB-47-10-7	101	1.47	31.7	1'530	5.7
BB-47-10-8	101	1.43	34.1	1'170	5.1
BB-47-11-5	87	1.50	29.9	1'760	4.9
BB-47-11-6	87	1.48	30.6	1'470	4.7
BB-47-11-7	75	1.45	32.6	1'290	4.9
BB-47-11-8	75	1.48	30.4	1'370	4.8
BB-47-12-5	62	1.49	30.6	1'540	3.5
BB-47-12-6	62	1.46	32.3	1'320	3.8
BB-47-12-7	60	1.47	31.2	1'340	3.6
BB-47-12-8	60	1.43	33.2	1'050	3.1

Nagra

Tab. A-24: Thermal conductivity measured on site (the water and dry density have been estimated from the on site measurementes reported in NAB 16-12). Nagra.

Section	**Layer**	***Y*** (cm)	***Z*** (cm)	**Distance** (cm)	***W*** (%)	ρ_d (g/cm^3)	λ (W/m·K)	***T*** (°C)
S46	45	1	102	102	27.3	1.55	1.19	19.4
	45	1	86	86	24.8	1.61	1.22	19.3
	45	1	76	76	23.8	1.63	1.32	20.0
	45	1	61	61	22.1	1.66		21.7
	45	99	-34	105	27.0	1.58	1.30	18.7
	45	83	-28	88	25.0	1.61	1.30	18.9
	45	72	-24	76	23.5	1.63		20.7
	45	55	-19	59	21.0	1.66		21.8
S53	29	60	-11	61	22.6	1.63	1.23	18.9
	29	82	0	82	24.9	1.60	1.26	18.7
	29	102	10	103	26.7	1.58		18.9
S58	13	88	52	16	24.1	1.61	1.38	19.5
	13	70	41	35	24.3	1.60	1.22	19.0
	13	51	30	59	24.9	1.59	1.34	18.9
	13	30	18	81	25.5	1.57	1.23	18.6
	13	13	9	103	27.7	1.54	1.33	18.4
	9	0	2	0	24.1	1.60	1.26	19.1
	9	30	17	35	24.3	1.60	1.30	18.4
	9	52	30	60	24.9	1.59	1.25	18.3
	9	70	41	81	25.6	1.57		18.1
	9	90	52	103	27.8	1.53	1.24	18.0
	9	-60	0	60	25.6	1.57	1.26	18.2
	9	-82	0	82	26.9	1.56	1.31	17.9
	9	-104	0	104	28.5	1.53	1.40	18.2
	9	-104	0	104	28.5	1.53	1.24	18.0
S61	4	-26	23	35	31.5	1.47	1.30	18.1
	4	-47	36	60	31.1	1.47	1.26	18.0
	4	-65	49	81	31.2	1.48	1.30	17.8
	4	-82	60	103	32.4	1.46	1.20	17.7

UPC

Tab. A-25: Summary of basic properties. UPC.

Sample	**Distance** (cm)	***W*** (%)	ρ_d (g/cm^3)	S_r *(%)*	***e***	**Suction** (MPa)
BB-50-9	59	19.2	1.67	84	0.619	38.8
BB-50-8	81	21.8	1.67	95	0.617	17.0
BB-50-7	102	26.7	1.58	102	0.708	8.8
BB-57-14B	11	24.9	1.57	94	0.720	12.7
BB-57-9	34	23.5	1.65	99	0.640	15.5
BB-57-8	59	25.5	1.60	100	0.686	11.9
BB-57-7	79	24.7	1.59	95	0.698	10.0
BB-57-6	103	28.1	1.54	101	0.748	8.4

Tab. A-26: Mercury intrusion porosimetry results. UPC.

Sample	**Distance** (cm)	***W*** (%)	***e***	**Intruded *e*** (%)	**> 50 nm** (%)	**Mode > 50 nm** (nm)	**50-2 nm** (%)	**Mode 50-2 nm** (nm)	**e > 50 nm**	**e < 50 nm**
FEBEX		15.5	0.564	55	32	31'345	23	9.4	0.193	0.371
B-B-50-9	59	19.2	0.619	54	31	31'345	23	9.4	0.193	0.426
B-B-50-8	81	21.8	0.617	53	27	31'345	26	9.4	0.168	0.449
B-B-50-7	102	26.7	0.708	53	23	14'747	30	9.4	0.162	0.546
57-14-B	11	24.9	0.720	49	23	31'345	26	9.4	0.169	0.551
B-B-57-8	59	25.5	0.686	55	27	22'426	28	9.4	0.187	0.499
B-B-57-6	103	28.1	0.748	54	28	22'426	26	17.8	0.208	0.540

Tab. A-27: Results of the high-stress oedometer tests performed in a sample trimmed from a FEBEX reference block. UPC.

Vertical stress, σ_v (MPa)	***e***	***W*** (%)	**Average ρ$_w$** (Mg/m^3)	***S*$_r$**
0.6	0.564	15.5	1.17	0.63
2.8	0.546	15.5	1.18	0.65
5.7	0.525	15.5	1.18	0.67
11.3	0.499	15.5	1.19	0.70
17.0	0.480	15.5	1.20	0.73
22.6	0.467	15.5	1.21	0.74
34.0	0.446	15.5	1.22	0.77
45.3	0.421	15.5	1.23	0.81
56.6	0.399	15.5	1.24	0.85
22.6	0.405	15.5	1.24	0.84
11.3	0.405	15.5	1.24	0.84
0.6	0.412	15.5	1.23	0.82

Tab. A-28: Results of the high-stress oedometer tests performed in samples trimmed from blocks of Section S50. UPC.

Vertical stress, σ_v (MPa)	***e***	***W*** (%)	**Average ρ$_w$** (Mg/m^3)	***S*$_r$**
BB-50-7a, 102 cm				
0.6	0.708	25.1	1.14	0.84
2.8	0.669	25.1	1.14	0.88
5.7	0.638	25.1	1.15	0.92
11.3	0.603	25.1	1.16	0.97
17.0	0.579	25.0	1.17	1.00
22.6	0.558	24.2	1.17	1.00
34.0	0.508	22.4	1.19	1.00
45.3	0.469	21.0	1.20	1.00
56.6	0.437	19.8	1.22	1.00
22.6	0.472	21.0	1.20	1.00
11.3	0.483	21.4	1.20	1.00
0.6	0.491	21.7	1.20	1.00

Tab. A-28: Cont.

Vertical stress, σ_v (MPa)	***e***	***W*** (%)	**Average ρ_w** (Mg/m^3)	***S*$_\mathrm{r}$**
BB-50-8, 81 cm				
0.6	0.657	21.8	1.15	0.78
2.8	0.631	21.8	1.15	0.81
5.7	0.598	21.8	1.16	0.85
11.3	0.55	21.8	1.18	0.91
17.0	0.518	21.8	1.19	0.96
22.6	0.495	21.8	1.19	1.00
34.0	0.468	20.9	1.21	1.00
45.3	0.451	20.2	1.21	1.00
56.6	0.432	19.5	1.22	1.00
22.6	0.443	20.0	1.22	1.00
11.3	0.443	20.0	1.22	1.00
0.6	0.444	20.0	1.22	1.00
BB-50-9, 59 cm				
0.6	0.605	18.2	1.16	0.70
2.8	0.592	18.2	1.16	0.71
5.7	0.574	18.2	1.17	0.73
11.3	0.538	18.2	1.18	0.78
17.0	0.509	18.2	1.19	0.81
22.6	0.483	18.2	1.20	0.85
34.0	0.439	18.2	1.22	0.92
45.3	0.406	18.2	1.24	0.98
56.6	0.379	17.4	1.24	1.00
22.6	0.383	17.6	1.24	1.00
11.3	0.386	17.7	1.24	1.00
0.6	0.387	17.8	1.24	1.00

Tab. A-29: Results of the high-stress oedometer tests performed in samples trimmed from blocks of Section S57. UPC.

Vertical stress, σ_v (MPa)	***e***	***W*** (%)	**Average ρ_w** (Mg/m^3)	S_r
BB-57-14B, 11 cm				
0.6	0.721	24.9	1.13	0.82
2.8	0.711	24.9	1.14	0.83
5.7	0.715	24.9	1.13	0.83
11.3	0.706	24.9	1.14	0.84
22.6	0.673	24.9	1.14	0.88
34.0	0.591	24.9	1.16	0.98
45.3	0.545	23.7	1.18	1.00
56.6	0.513	22.6	1.19	1.00
22.6	0.533	23.3	1.18	1.00
11.3	0.542	23.6	1.18	1.00
0.6	0.553	24.0	1.17	1.00
BB-57-9, 34 cm				
0.6	0.72	21.8	1.13	0.72
2.8	0.7	21.8	1.14	0.74
5.7	0.659	21.8	1.15	0.78
11.3	0.603	21.8	1.16	0.84
17.0	0.566	21.8	1.17	0.89
22.6	0.535	21.8	1.18	0.94
34.0	0.473	21.1	1.20	1.00
45.3	0.427	19.4	1.23	1.00
56.6	0.388	17.8	1.24	1.00
22.6	0.412	18.8	1.23	1.00
11.3	0.426	19.3	1.23	1.00
0.6	0.458	20.5	1.21	1.00
BB-57-8, 59 cm				
0.6	0.687	22.9	1.14	0.79
2.8	0.658	22.9	1.15	0.82
5.7	0.638	22.9	1.15	0.84
11.3	0.594	22.9	1.16	0.89
17.0	0.559	22.9	1.17	0.94
22.6	0.52	22.8	1.19	1.00

Tab. A-29: Cont.

Vertical stress, σ_v (MPa)	***e***	***W*** (%)	**Average ρ_w** (Mg/m^3)	***S*r**
34.0	0.453	20.4	1.21	1.00
45.3	0.412	18.8	1.23	1.00
56.6	0.378	17.3	1.24	1.00
22.6	0.418	19.1	1.23	1.00
11.3	0.441	19.9	1.22	1.00
0.6	0.463	20.7	1.21	1.00
BB-57-6, 103 cm				
0.6	0.728	25.7	1.13	0.84
2.8	0.705	25.7	1.14	0.87
5.7	0.683	25.7	1.14	0.89
11.3	0.649	25.7	1.15	0.93
17.0	0.621	25.7	1.16	0.97
22.6	0.596	25.6	1.16	1.00
34.0	0.55	23.9	1.18	1.00
45.3	0.501	22.1	1.19	1.00
56.6	0.457	20.5	1.21	1.00
22.6	0.464	20.8	1.21	1.00
11.3	0.468	20.9	1.21	1.00
0.6	0.471	21.0	1.20	1.00